Non-Natural Elements for Peptide-Based Molecular Design, Structural Analysis, and Functional Modifications

Dissertation

Daichi Nasu
Clemens-Schöpf-Institut für Organische Chemie und Biochemie

TECHNISCHE UNIVERSITÄT DARMSTADT

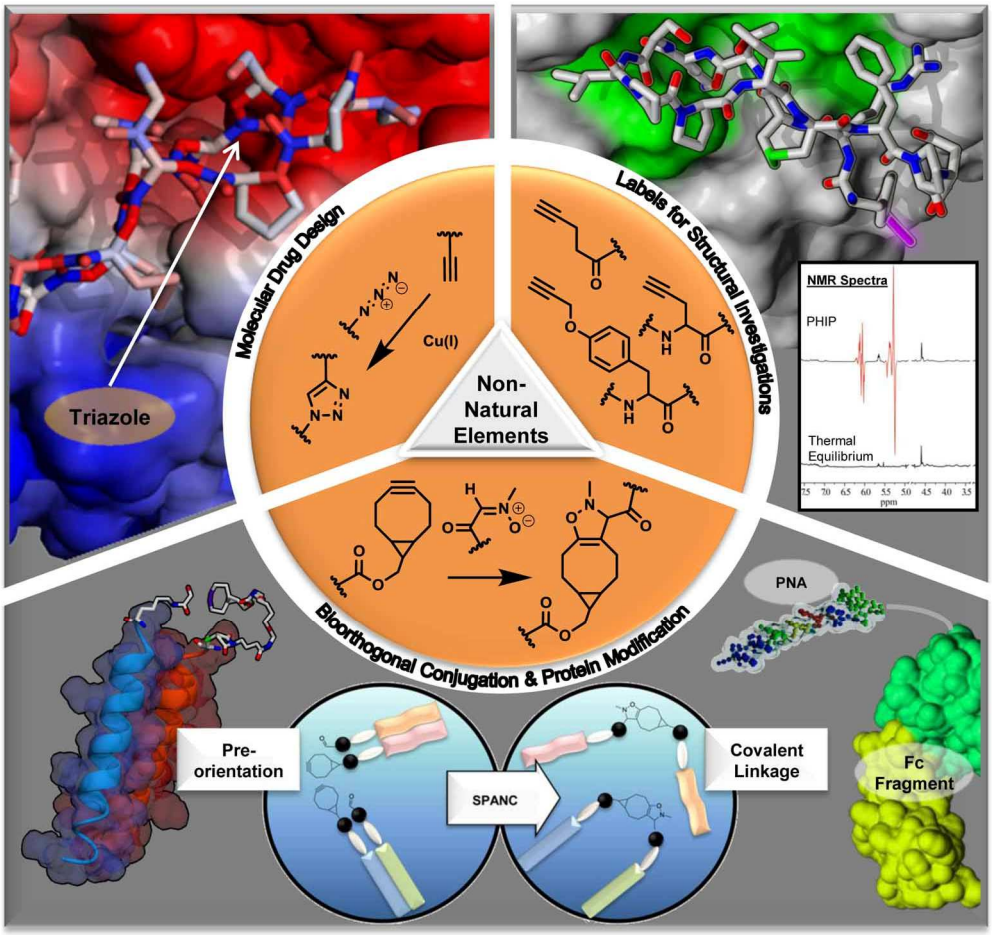

Non-Natural Elements for Peptide-Based Molecular Design, Structural Analysis, and Functional Modifications

Nicht-natürliche Struktur- und Funktionselemente für peptidbasiertes molekulares Design, Strukturaufklärung und funktionelle Modifizierung

TECHNISCHE UNIVERSITÄT DARMSTADT

Clemens-Schöpf-Institut für Organische Chemie und Biochemie

Vom Fachbereich Chemie

der Technischen Universität Darmstadt

zur Erlangung des akademischen Grades eines Doktor-Ingenieurs (Dr.-Ing.)

genehmigte

Dissertation

vorgelegt von

Dipl.-Ing. Daichi Nasu
aus Frankfurt am Main

Referent: Prof. Dr. Harald Kolmar

Korreferent: Prof. Dr. Gerd Buntkowsky

Tag der Einreichung: 28. Oktober 2015
Tag der mündlichen Prüfung: 14. Dezember 2015

Darmstadt 2016

D17

Die vorliegende Arbeit wurde unter der Leitung von Herrn Prof. Dr. Harald Kolmar am Clemens-Schöpf-Institut für Organische Chemie und Biochemie der Technischen Universität Darmstadt von November 2011 bis Oktober 2015 angefertigt.

Deutsche Zusammenfassung

In der vorliegenden Dissertation sind die Ergebnisse von drei unabhängigen Forschungsprojekten zusammengefasst, die das übergeordnete Thema „Anwendung von unnatürlichen Strukturelementen zur Design und Synthese von bioaktiven Peptiden, Peptidomimetika und Biomakromolekülen“ umfassen. In den jeweiligen Projekten wurden nicht natürliche Strukturelemente für folgende Ziele in unterschiedlichen Biomolekülen eingebaut: 1. Zum molekularem Design von therapeutisch relevanten Wirkstoffen, 2. Zur Markierung für Strukturaufklärung, 3. Zur funktionalen Modifizierungen von Biomakromolekülen. Diese drei Themen wurden individuell bearbeitet und haben Gemeinsamkeiten in der generellen Strategie (Strukturierung in Design, Synthese und Aktivitätsuntersuchung) und der verwendeten Methoden zur Synthese (Peptid-Festphasensynthese, „Click“-Chemie) und Charakterisierung (HPLC, Massen-Spektrometrie, Enzymassays).

Projekt 1: Proteaseinhibitor mit einer Triazolgruppe im Peptid-Rückgrat

Ein synthetischer Proteaseinhibitor mit einer Triazolgruppe im Peptid-Rückgrat wurde entwickelt und es wurde der Einfluss auf die Bioaktivität und proteolytische Stabilität durch diese Modifikation untersucht. Dazu wurde über rationales Design ein Inhibitor der humanen Neutrophil-Elastase (HNE), basierend auf dem Strukturgerüst der *Sunflower Trypsin Inhibitor-1* (SFTI-1) mit einer 1,4-disubstituierten Triazolgruppe als *trans*-Amidgruppen-Ersatz an der fiktiven proteolytischen Spaltungsposition (P1-P1‘ Position = „*Scissile Bond*“) neben weiteren Referenzpeptiden synthetisiert.
Durch chromatographische und massenspektrometrische Analysen wurde mit dem synthetischen Inhibitor bzw. mit Vergleichspeptiden und deren Zielproteasen gezeigt, dass der Einbau einer 1,4-disubstituierten Triazolgruppe als unspaltbarer Ersatz der „Scissile Bond“ dient, was zu einer erhöhten Stabilität gegen die Proteolyse durch das Zielenzym führte. Bei 24 stündiger Inkubation des synthetischen Inhibitors mit HNE konnte keine Spaltung an der entsprechenden Position nachgewiesen werden, wohingegen sein Ursprungspeptid bei gleicher Reaktionskondition mehr als 15 % abgebaut wurde. Gleiche Experimente mit der linearen Vorstufe des synthetischen Inhibitors zeigten proteolytische Spaltungen an alternativen Spaltungspostionen mit deutlich geringerer Reaktionsgeschwindigkeit als das entsprechende Ursprungspeptid, welches hauptsächlich an der „Scissile Bond“ gespalten wurde.
Weiterhin wurde in Enzym-Inhibitions-Assays gezeigt, dass die Einführung der Triazolgruppe zu einer leichten Verschlechterung der Inhibitionskonstante im Vergleich zum Ursprungspeptid (von 144.48 nM auf 563.63 nM, Faktor 3.8) führte. Dieses Verhältnis von K_i der Inhibitoren mit und ohne Triazolgruppe an der fiktiven Spaltposition entspricht den ermittelten Werten von bisherigen, vergleichbaren Arbeiten[a] und ist deutlich besser als die Werte von ähnlichen Studien über Proteaseinhibitoren mit Prolin- oder Azitidin-Derivaten.[b] Daher wird vermutet, dass der Austausch der genannten Amid-Bindung durch eine Triazolgruppe als effektive Strategie zur Verbesserung der pharmakokinetischen Eigenschaften von proteolyseempfindlichen Proteaseinhibitoren angewendet werden kann. Die Strategie könnte von besonderem Nutzen zur Synthese von linearen Inhibitoren mit

intrinsischer Empfindlichkeit gegen proteolytischen Verdau oder für die Herstellung von Inhibitoren aus hochaffinen Substraten sein. Allerdings benötigt die Studie noch weitere Untersuchungen mit zusätzlichen Modell-Peptiden und Zielproteasen um die Hypothese verallgemeinern zu können.

Projekt 2: PHIP-aktive funktionale Peptide

Zusammen mit der Arbeitsgruppe von Prof. Buntkowsky (TU Darmstadt) wurde eine systematische Studie über Parawasserstoff induzierte Polarisierung (parahydrogen-induced polarization, PHIP), die eine effektive Methode zur Verstärkung von NMR-Signalen darstellt, von funktionalen Peptiden durchgeführt. Dazu wurden drei unterschiedliche Alkinderivate Propargylglycin (Pra), 4-Pentinsäure und *O*-Propargyltyrosin (Tyr(*O*-propargyl)), die als Zielfunktionalitäten der homogen katalysierten Hydrierung und somit als Markierungsbausteine dienen, in das Grundgerüst vom monozyklischem SFTI-1 eingebaut. Über einfache *in silico* Modellierung bzw. Simulationen und vorläufige Experimente erwies sich der *N*-Terminus als am besten geeignet für den Einbau der PHIP-Markierungen. Anschließend wurde der Einfluss auf die Signalverstärkung und die Bioaktivität durch diese Modifizierung untersucht

Aus den Ergebnissen von Vorarbeiten[c] wurde eine Hypothese erstellt, dass starke Elektronen-Donatoren in räumlicher Nähe der zu hydrierenden ungesättigten Bindungen die Hydrierungseffizienz beeinträchtigen und dadurch zur Verschlechterung der PHIP-Aktivität führen. Dies wurde durch eine Reihe von PHIP-NMR-Experimenten bestätigt, da bei keinen der Pra markierten SFTI-Derivaten, bei denen nur eine Methyleneinheit zwischen Dreifachbindung und Peptid-Rückgrat vorhanden war, eine signifikante Signalverstärkung festgestellt werden konnte. Ähnliche Einschränkung der PHIP-Aktivität wurde auch bei einem SFTI-Derivat, was mit 4-Pentinsäure markiert wurde, beobachtet, obwohl der Baustein alleine eine extrem hohe intrinsische Signalverstärkung von Faktor 900 erwies. Dahingegen wurden hohe Signalverstärkungen um den Faktor 70 bei den SFTI-Derivaten mit Tyr(*O*-propargyl) als räumlich isolierte Markierung, selbst in wässrigen Lösungen, beobachtet.

Ein weiterer Gegenstand der Studie war die Untersuchung des Einflusses von bestimmten Funktionalitäten im Peptid, die möglicherweise zur Vergiftung des Hydrierungskatalysators führen. Dazu wurden ausgewählte Funktionalitäten (Disulfidbrücke, freier Aminoterminus) durch alternative Gruppen ersetzt oder komplett entfernt. Jedoch führte die Einführung von 1,5-disubstituiertem Triazol als Disulfidbrückenersatz und die Acylierung vom freien *N*-Terminus zu keiner eindeutigen Verbesserung der PHIP-Aktivität. Daher wird vermutet, dass die Katalysatorvergiftung aus einem komplexen Zusammenspiel von mehreren Faktoren resultiert und somit nicht einer bestimmten funktionellen Gruppe zugeordnet werden kann.

Interessanterweise führte die Einführung der PHIP-Markierung in das Gerüst von SFTI-1 zu keiner bzw. nur zu minimalen Verschlechterung der Inhibitionsaktivität gegen Trypsin (in einigen Fällen auch zu minimaler Verbesserung). Selbst bei Verwendung vom sterisch anspruchsvolleren Tyr(*O*-popargyl) als Markierung wurde keine merkliche Beeinträchtigung der Bioaktivität beobachtet, sodass alle synthetisierte PHIP markierte Inhibitoren eine hervorragende Inhibition gegen Trypsin im „Tight-binding Inhibitor“-Bereich aufwiesen. Dieses Ergebnis ist von besonderer Wichtigkeit für Folgestudien, die sich mit PHIP-Experimenten an Enzym-Inhibitor-Komplexen beschäftigen und die zur Strukturaufklärung

von komplexen Biomolekülen oder zur Mechanismenaufklärung von Bioprozessen dienen können. Die Ergebnisse dieses Teilprojektes sind bereits in einer Publikation veröffentlicht.[d]

Projekt 3: Affinität gesteuerte chemische Ligation zur Multifunktionalisierung von biomolekularen Strukturgerüsten

Die Affinität-gesteuerte Ligation als Strategie zur Synthese von komplexen biomolekularen Konjugaten wurde anhand von oligopeptidischen Modellsystemen und einem Proteingerüst, das aus einem Fc-Fragment eines IgG Antikörpers stammt, untersucht. Im Konzept der Affinität-gesteuerten Ligation werden die reaktiven Gruppen einer bioorthogonalen Reaktion durch nichtkovalent wechselwirkende Einheiten („Guiding Units“) in räumlicher Nähe vororientiert. Die Reaktion wird anschließend manuell durch einen „Trigger“ gestartet, sodass durch erhöhte lokale Konzentration der reaktiven Funktionalitäten eine Beschleunigung der Reaktionsgeschwindigkeit und Verbesserung der Selektivität zu erwarten ist. In der vorliegenden Arbeit wurden als „Guiding Units“ komplementäre α-helikale Peptide („Coiled Coil“ Peptide) und peptidische Nukleinsäuren („Peptide Nucleic Acid“ = PNA) verwendet.
Als schaltbare bioorthogonale Reaktion wurde die Alkin-Nitron-Zykloaddition („Strain-promoted Alkyne-Nitrone Cycloaddition“=SPANC) eingesetzt. Dazu wurde eine Bicyclononin-(BCN-) Einheit und eine Aldehydgruppe, die *in situ* zur reaktiven Nitron-Komponente umgesetzt wird, an den Aminotermini von komplementeren „Coiled Coil“-Peptiden mit 3 bzw. 5 repetitiven Einheiten oder unterschiedlichen PNA-Oligomeren installiert. In einer Reihe von Testreaktionen mit unterschiedlichen Reaktionskonditionen wurde gezeigt, dass die Affinität-gesteuerte SPANC zwischen diesen Modellpeptiden bzw. -PNAs einen signifikanten Vorteil bezüglich Reaktionskinetik und Selektivität gegenüber nicht-gesteuerten bzw. –geschalteten Konjugationen mit analogen Molekülen besitzen. Interessanterweise wurde bei den SPANC-Reaktionen mit dem „Coiled Coil“-Peptiden mit 5 repetitiven Einheiten als „Guiding Unit“ ein besserer Reaktionsumsatz und eine erhöhte Reaktionsgeschwindigkeit als analoge Reaktion mit PNAs nachgewiesen. Daher wird vermutet, dass die Stärke der nicht kovalenten Wechselwirkungen in diesem Modelsystem keine primäre Rolle spielt. Während den Testreaktionen wurde eine unerwartete, bislang nicht beschriebene Nebenreaktion von SPANC-Reaktionen beobachtet, was zu einer Verschlechterung des Reaktionsumsatzes führte. Für Folgearbeiten muss daher eine Methode zur Unterdrückung dieser Nebenreaktion oder zur Isolation vom unerwünschten Nebenprodukt gefunden werden.
Anschließend wurde die Konjugation von PNA-Oligomeren an das Fc-Gerüst durch Sortase A katalysierte Transpeptidierung untersucht. Das dabei entstandene Fc-PNA-Konjugat wurde in einem Folgeprojekt von Stephan Dickgießer (Arbeitskreis Kolmar, TU Darmstadt) als modulares Grundgerüst für die Herstellung von einem bioaktivem Bindermolekül verwendet, was mit einem nicht-peptidischen Binder gegen einem therapeutisch relevanten Zielrezeptor und einer Fluoreszenzmarkierung funktionalisiert wurde. Zusammen mit der Strategie der Affinität-gesteuerten Ligation, die eine selektive und effiziente Konjugation von mehreren Ligandeinheiten ermöglicht, dienen die Methoden, die in dieser Studie entwickelt und untersucht worden sind, als Grundlage für die Herstellung von komplexen, multivalenten Antikörper-Toxin-Konjugaten.

Die Ergebnisse, die in der der vorliegenden Dissertation zusammengefasst sind, wurden in zwei wissenschaftlichen Publikationen veröffentlicht[d,e]. Sie können als Orientierungspunkte für nachfolgende Forschungen dienen, die die praktische Anwendung der jeweiligen Konzepte und Strategien im Blick haben werden.

Literaturverzeichnis der deutschen Zusammenfassung

[a] M. Tischler, D. Nasu, M. Empting, S. Schmelz, D. W. Heinz, P. Rottmann, H. Kolmar, G. Buntkowsky, D. Tietze, O. Avrutina, *Angew. Chem., Int. Ed.* **2012**, *51*, 3708-3712.

[b] A. Legowska, D. Debowski, R. Lukajtis, E. Sztabkowska, M. Aneta, K. Brzozowski, M. Wysocka, A. Lesner, K. Rolka, *Protein Pept. Lett.* **2011**, *18*, 1158-1167.

[c] M. Körner, G. Sauer, A. Heil, D. Nasu, M. Empting, D. Tietze, S. Voigt, H. Weidler, T. Gutmann, O. Avrutina, H. Kolmar, T. Ratajczyk*, G. Buntkowsky*,. *Chem. Comm.* **2013**, *49*, 7839-7841.

[d] G. Sauer, D. Nasu, D. Tietze, T. Gutmann, S. Englert, O. Avrutina, H. Kolmar*, G. Buntkowsky*, *Angew. Chem., Int. Ed. Engl.* **2014**, *53*, 12941-5.

[e] S. Dickgiesser, N. Rasche, D. Nasu, S. Middel, S. Hörner, O. Avrutina, U. Diederichsen, H. Kolmar*, *ACS Chemical Biology*, **2015** (im Druck).

Teile der vorliegenden Arbeit sind bereits veröffentlicht:

1. M. Tischler[†], **D. Nasu**[†], M. Empting[†], S. Schmelz, D. W. Heinz, P. Rottmann, H. Kolmar, G. Buntkowsky*, D. Tietze*, O. Avrutina*, Braces for the Peptide Backbone: Insights into Structure–Activity Relationships of Protease Inhibitor Mimics with Locked Amide Conformations, *Angew. Chem., Int. Ed. Engl.* **2012**, *51*, 3708-3712.

Deutsche Version: Peptid in Ketten: Einblicke in die Struktur-Aktivität-Beziehungen von Proteaseinhibitormimetika mit fixierten Amidkonformationen. *Angew. Chem*. **2012**, *124*, 3768-3772.

2. M. Körner, G. Sauer, A. Heil, **D. Nasu**, M. Empting, D. Tietze, S. Voigt, H. Weidler, T. Gutmann, O. Avrutina, H. Kolmar, T. Ratajczyk*, G. Buntkowsky*, PHIP-Label: Parahydrogen-Induced Polarization in Propargylglycine-Containing Synthetic Oligopeptides. *Chem. Comm.* **2013**, *49*, 7839-7841.

3. G. Sauer, **D. Nasu**, D. Tietze, T. Gutmann, S. Englert, O. Avrutina, H. Kolmar*, G. Buntkowsky*, Effective PHIP Labeling of Bioactive Peptides Boosts the Intensity of the NMR Signal. *Angew. Chem., Int. Ed. Engl.* **2014**, *53*, 12941-5.

Deutsche Version: Effektive Markierung von bioaktiven Peptiden mit PHIP-Markern zur Steigerung der Empfindlichkeit von NMR-Signalen, *Angewandte Chem.* **2014**, *126*, 13155–13159.

4. S. Dickgiesser, N. Rasche, **D. Nasu**, S. Middel, S. Hörner, O. Avrutina, U. Diederichsen, H. Kolmar*, Self-Assembled Hybrid Aptamer-Fc Conjugates for Targeted Delivery: A Modular Chemoenzymatic Approach. *ACS Chemical Biology*, **2015** (im Druck).

Weitere Publikationen, die im Rahmen dieser Doktorarbeit veröffentlicht wurden:

5. M. Reinwarth[†], **D. Nasu**[†], H. Kolmar*, O. Avrutina*, Chemical Synthesis, Backbone Cyclization and Oxidative Folding of Cystine-Knot Peptides — Promising Scaffolds for Applications in Drug Design. *Molecules* **2012**, *17*(11), 12533-12552.

6. C. Schroeter, R. Guenther, L. Rhiel, S. Becker, L. Toleikies, A. Doerner, J. Becker, A. Schoenemann, **D. Nasu**, B. Neuteboom, H. Kolmar*, B. Hock*, A Generic Approach to Engineer Antibody pH-Switches Using Combinatorial Histidine Scanning Libraries and Yeast Display. *mAbs.,* **2015**, *7*, 138-151.

[†] Gemeinsame Erstautorenschaft
* Korrespondenzautoren

重要なことは、たえず　転んだ方がベスト」と思えること。

この信条さえあれば、自分がどの道に転ぼうと、最後は　自分の選んだ道は正しかった」と思えるようになります。

藤田誠

Chem-Station 化学者へのショートインタビュー

The important thing is to think always that the stumbling way is the best way.
If you possess this creed, it doesn't matter where you stumble to as you can ultimately believe that the way you have chosen by yourself was the right one.

Makoto Fujita (1957-)
Chemist, Professor in Institute of Technology, Tokyo University

Danksagung

Zunächst möchte ich an folgenden Personen meinen aufrichtigen Dank aussprechen:

Als erstes bedanke ich mich selbstverständlich bei meinem Doktorvater **Prof. Dr. Harald Kolmar** für unzählige Unterstützungen, beginnend mit meiner Aufnahme als Doktorand und Mitarbeiter, Bereitstellung unterschiedlicher, interessanter Projekte und Gelegenheiten diese präsentieren zu dürfen, bis hin zur Beratung bei fachlichen und vor allem fächerübergreifenden Fragen. Einen herzlichen Dank dafür, dass ich überhaupt die Chance bekommen habe die Promotion anzufangen und bis zum Ende durchziehen zu können.

Mein zweiter großer Dank geht an **Dr. Olga Avrutina**. Vielen Dank für die außerordentliche Sorgfalt und Geduld bei fachlichen Beratungen und vor allem bei der Korrektur von allen wissenschaftlichen Texten in Englisch, einschließlich der vorliegenden Arbeit. Ohne dich wäre keine von mir abgelegte Arbeit überhaupt verständlich gewesen. Ich weiß, dass in meinem Englisch noch ein großer Raum für Verbesserungen besteht, jedoch habe ich durch dich viele Grundlagen für das fachlich korrekte Schreiben erlernen können.

Ein weiterer Dank geht an **Prof. Dr. Gerd Buntkowsky** für die Übernahme des Korreferats und der Bereitstellung eines sehr interessanten und gelungenen Kooperationsprojektes. Außerdem will ich mich dafür bedanken, dass ich einige Laborgeräte und Einrichtungen auch für weitere Projekte verwenden durfte. Bei meinen direkten Mitforschern aus dem Arbeitskreis Buntkowsky, **Dr. Marco Körner**, **Grit Sauer** und **Dr. Daniel Tietze** möchte ich mich für die angenehme und gelungene Zusammenarbeit bedanken.

Ebenfalls bedanke ich mich für eine gelungene Kooperation bei **Prof. Dr. Ulf Diederichsen** aus der Georg-August-Universität Göttingen und den Mitarbeitern seines Arbeitskreises, **Dr. Cornelia Panse** und **Stephen Middel**, die einen Großteil der PNAs, die in dieser Arbeit verwendet worden sind, bereitgestellt haben.

Bei **Dr. Alesia Tietze** bedanke ich mich für die externe MALDI-MS Messungen.

Aus dem Arbeitskreis von Prof. Kolmar bedanke ich mich zuerst bei **Stephan Dickgießer**, für die unterhaltungsreiche Zusammenarbeit, Bereitstellung von einigen Ergebnissen für meine Arbeit und die gelungene Weiterführung von dem gemeinsamen Forschungsprojekt.

Ebenfalls bedanke ich mich bei meinem Bench-Nachbarn **Heiko Fittler** für seine Hilfsbereitschaft und die spaßige Atmosphäre in unserem kleinen, aber angenehmen Peptidlabor.

Bei meinen großen Vorgängern, **Dr. Martin Empting** und **Michael Reinwarth** bedanke ich mich dafür, dass sie mir alle wichtigen Grundlagen für einen Peptidchemiker beigebracht haben und bei Problemen stets entgegengekommen sind.

Allen weiteren Mitarbeiter des Arbeitskreises von Prof. Kolmar möchte ich mich für zahlreiche Hilfestellungen und die angenehme Arbeitsatmosphäre bedanken.

Meinen Eltern, **Shinobu** und **Hideyuki Nasu** und meinem Bruder **Takumi Nasu** bin ich sehr dankbar für die sowohl seelisch-moralische als auch finanzielle Unterstützung, die überhaupt mein Chemiestudium und die Promotion ermöglicht haben.

Zuletzt bedanke ich mich bei **Freunden und Bekannten** aus meinem privaten Umfeld, die mich stets gut beraten und motiviert haben. Besonderen Dank an **Tatsuya Shimizu.**, **Masaru** und **Mikako Tanabe**, **Natsuko Takashima**, **Toshiyuki. Ohno**, **Takaomi Ichijou**, **Alexander** und **Martina Montag**, **Shohei Fujiwara** und vielen weiteren Leuten.

Table of Contents

1 Introduction

1.1 Preface

Engineering of natural compounds is used in drug discovery since decades. Bioactive products isolated from microorganisms, fungi, or plants often serve as lead compounds for synthetic or recombinantly produced therapeutics.[1] In the field of rational drug design, two approaches are of especial value, the installation of non-natural functional moieties into compounds of biological origin and the substitution of structural elements of biomolecules by non-biological surrogates.

Depending on their chemical and biological characteristics, non-natural motifs can be of benefit in several application fields. Thus, they can modulate ligand-receptor binding, target specificity, ADMET (absorption, distribution, metabolism, excretion, and toxicity) and a number of other issues.[2] Moreover, they allow for the introduction of the *de-novo* functions such as labels, toxins or orthogonally addressable binding sites in biomolecules, thus converting them into potential agents for therapy, diagnostics, and structural or mechanistic investigations.

Since a majority of biomolecules which are directly involved in the physiological processes are products of the cellular translation machinery, the chemical intervention is mostly preferred on post-translational level and relies on the chemistry of the amino acid building blocks. Till the end of 50s, only qualitative assessment of protein modification was possible due to the lack of sensitive and accurate methods to determine the precise amino acid composition, as well as efficient procedures to separate, purify, and characterize the modified products.[3] The development of advanced protein analytics, including radioactive labeling, automated amino acid analysis,[4] micro gel electrophoresis, X-ray crystallography, ESI and MALDI mass spectrometry, as well as ion-exchange and size-exclusion chromatography facilitated the characterization of modified proteins.[5]

After the elaborated analytical base has been established, the research focus shifted towards the development of selective chemical transformations to obtain site-specific, pinpoint protein modifications. Starting with the labeling of the antigen-combining site of a rabbit anti-*p*-azobenzenearsonate antibody with the *p*-azonylbenzenediazonium ion (Wofsey et al., 1962)[6] and the active-site labeling of chymotrypsin using TPCK (Schoellmann et al., 1963),[7] a large number of so-called affinity labeling reagents has been reported. However, this approach required detailed information on the structure and mechanism of the parent protein. Therefore, chemical conjugations using the side chains of amino acids followed, among them iodination of Tyr,[8] dicarbonyl conjugations to Arg,[9] or carboxymethylation of Cys by bromoacetate.[10] Unfortunately, due to the fact that amino acids are present in proteins in multiple copies this approach suffers from insufficient selectivity.[3]

Two milestones have to be mentioned in view of the selective incorporation of non-natural elements in biomolecules. The first is the invention of “click” chemistry by Sharpless et al. in 2001,[11] which describes a set of powerful, highly reliable, and selective reactions for rapid synthesis of desired compounds and combinatorial libraries. Although a number of transformations matching the criteria emphasized for “click” reactions has been already known, they were applied to modify biomolecules much later. Thus, within the recent ten

years, revision of “the last century” reactions towards biocompatible orthogonal ligations became a trend and resulted in molecular constructs with multiple functions or tailor-made characteristics. Details about “click” chemistry will be discussed in chapter 1.4.1.
The second milestone was the development of the solid-phase peptide synthesis (SPPS) reported by Merrifield in 1963.[12] This epochal strategy facilitated, on the one hand, the access to highly pure synthetic peptides that can be used to model or mimic protein fragments or even proteins.[13] On the other hand, it enabled the preparation of peptides and peptidomimetics with pre-installed non-natural motifs for orthogonal conjugations or directly acting as labels. Even the installation of artificial elements in the backbone of the biopolymers became possible.[14] A large number of non-canonical amino acids and functional building blocks are to date commercially available as SPPS-compatible derivatives.
With the keywords “click-chemistry”, “SPPS”, and “protein/peptide modification”, the research summarized in this work deals with synthetic biomolecules possessing non-natural structural elements for three applications:

1. Molecular design of therapeutically relevant agents;
2. Labels for structural investigations and diagnostics;
3. Addressable sites for bioorthogonal conjugations.

Each subject was elaborated as an individual project lacking direct interconnections, besides the philosophy and methodology of the used approach. In this chapter, the theoretical background of the concepts, strategies, and model components/systems discussed in the presented work are summarized.

1.2 Non-Natural Elements for Peptide-Based Molecular Design

1.2.1 Rational Drug Design

Directed evolution and rational design are the two major strategies in the modern, target-based pharmacology and drug discovery.[15] In contrast to directed evolution which is based on substance libraries comprising more than 10^7 randomized proteins and does not require detailed knowledge on the target,[16] in rational design novel molecules with defined functions are generated relying on the prediction of molecular behavior as a function of the structure by using physical or knowledge-based models.[17] Thus, more explicit information on structure and mechanism of the biomolecule is presumed. While the improvement of directed evolution strategy is strongly supported by the development of several high-throughput screening (HTS) techniques, the rational design made a rapid progress along with the rise of computational modeling and simulation methods. These are closely connected with powerful methods to analyze protein structure (e.g. X-ray crystallography, solid-state NMR, electron microscopy). Interestingly, the most popular trend in directed evolution, the pinpoint mutation of single protein domains, is based on the combination of amino acid randomization and structure- and knowledge-based drug design.
One major advantage of the classic rational design strategy over random mutagenesis-based techniques is that the access to non-natural fragments in the target agent is much more

facilitated. While the scope of lead compounds found by directed evolution is often limited to peptides and proteins expressible in living cells, with the exception of glycoproteins and introduction of non-canonical amino acids by genetic code expansion, in rational design the rich arsenal of chemical transformations is available to manipulate molecules as long as the synthetic procedure is realistic and practicable.

1.2.2 Biomimetics with Non-Natural Structural Elements

How do non-natural structural elements tailor the properties of biomolecules? In this chapter, only the surrogates of the native functionalities of proteins and peptides are discussed; non-natural elements acting as labels or giving the biomolecule a contrived function (e.g. toxins, carriers) will be addressed in chapter 1.3.1.

Since the beginning of human history, mankind has taken benefits from mimicking biological systems. Starting from the macro-scaled objects, e.g. fluid systems for city planning or the "tunneling shield" technique for tunnel construction,[18] and followed by examples from the daily life as "hook and loop fasteners"[18-19] or medical bionics (implants, prosthetic devices), the interest to imitate biological motifs and to substitute them with artificial elements extended to the molecular level of peptidomimetics. These are rather short protein- or oligopeptide-like chains or small molecules designed to mimic natural peptides, proteins, or elements thereof in 3D space.[20] Peptidomimetics differ from canonical peptides by the backbone architecture as they can comprise non-α- or D-amino acids as well as bioisosteric groups.

In some cases, regular peptides with special modifications in their side chains (peptide analogs) are also referred to as peptidomimetics. In general, peptidomimetics are designed to have similar biological effects as the original model peptides, but they often possess advantaged pharmacokinetic properties as enhanced resorption in physiological systems, higher stability against proteolytic degradation, *in vivo* distribution or even optimized/advanced pharmacodynamic characteristics.[20] Thus, mimicking peptides by small isosteric/isoelectronic groups is an important issue in the development of drug-like compounds.

Peptidomimetics can be roughly classified in four types depending on their composition and the strategy of synthesis (**Table 1**).[21] Type-I peptidomimetics, also called pseudopeptides, are very similar to the original counterparts. Only pinpoint modifications of the backbone are performed while retaining the most functional groups to assure important contacts with the binding sites of the target protein. The modifications are restricted to only some motifs of the secondary structures as p-turns or β-hairpins. In general, for type-I peptidomimetics structure-based design is used. Thus, a number of protease inhibitors were established as the structural mimics of the peptide bond in a transition state or product state for the enzyme-catalyzed reaction. Type-II peptidomimetics, also known as functional mimetics, are small non-peptidic molecules derived by molecular modeling, often in combination with high-throughput screening of chemical libraries. Type-II peptidomimetics have no or only limited structural similarity to the parental peptides and their classification as peptidomimetics has mainly historical reasons. In contrast, type-III peptidomimetics, also called topographical mimetics, possesses a novel scaffold, often unrelated to the parental peptide, but still retaining the

essential functional group for receptor binding. Hence, topographical mimetics are exclusively gained by structure-based design. Type-IV peptidomimetics or non-peptide peptidomimetics are constructed by the so-called Group Replacement Assisted Binding (GRAB) technique of drug design and they share structural and functional features of type-I peptidomimetics while bearing no obvious resemblance to a parent peptide or its isosters.[22]

Table 1. Classification of peptidomimetics in four different types according their molecule class and design/synthesis route defined by Kharb et al.[21]

Peptidomimetics	Type-I	Type-II	Type-III	Type-IV
Synonym	Pseudopeptides	Functional mimetics	Topographical mimetics	Non-peptide mimetics
Design/Synthesis	Structure-based design	Molecular modeling & HTS	Structure-based design	GRAB technique
Molecule class	Oligo-/poly-pseudopeptides	Small molecules	Small molecules	Small molecules
Example	Peptide-based protease inhibitors	G-protein-coupled receptor antagonists	Small molecule-based protease inhibitors	Piperidine inhibitors[22]

A classic example for rational drug design using a natural peptide as starting point is the development of several integrin-like receptor agonists mimicking the Arg-Gly-Asp peptide motif (RGD motif). The RGD motif has been found in numerous extracellular proteins (vitronectin, collagen, or fibronectin), and plays an important role in intracellular recognition and adhesion.[23] Since several transmembrane proteins of the integrin super families were found to be overexpressed in diverse diseased cells,[24] they attracted attention as therapeutic and diagnostic targets. To that end, a number of approaches was developed, among them the structure-based design of selective small-molecule ligands.[25] In **Table2**, the structures and bioactivity of selected RGD peptidomimetics acting as GPIIb/IIIa ($\alpha_{2b}\beta_3$) receptor and the vitronectin ($\alpha_v\beta_3$) receptor inhibitors are listed. [26] As seen from **Table 2**, in the RGD mimetic 1 (derived from the 3D structure of a cyclic RGD peptide) the essential structural elements of the original amino acid residues can still be recognized. Based on the structure of this lead compound, further highly specific receptor antagonists could be synthesized by simple modifications (RGD mimetic 2ab).[26]

Table 2. Chemical structure of native RGD motif and the synthetic peptidomimetics reported by Keenan et al. with corresponding inhibition constant K_i against GPIIb/IIIa ($\alpha_{2b}\beta_3$) receptor and the vitronectin ($\alpha_v\beta_3$) receptor.[26]

	Chemical structure	Inhibitioin constant K_i against: $\alpha_{2b}\beta_3$	$\alpha_v\beta_3$
native RGD motif	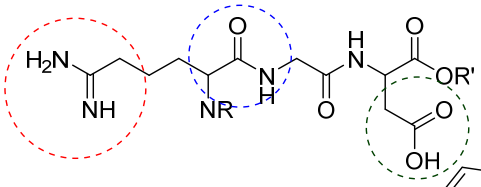	-	-
RGD mimetic 1	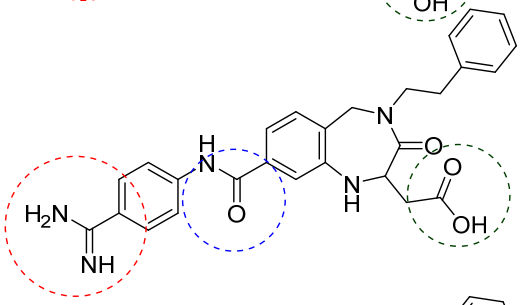	2.8 nM	-
RGD mimetic 2a	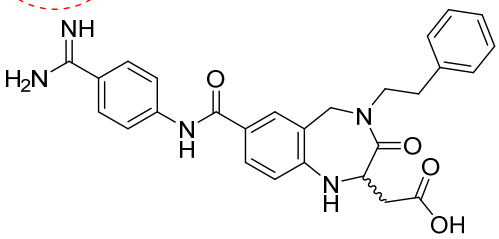	26 nM	56,000 nM
RGD mimetic 2b	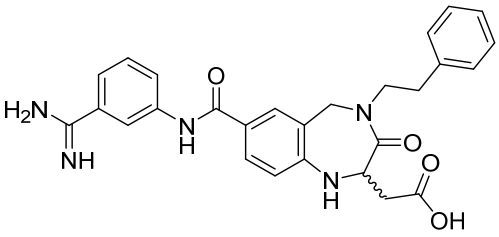	4,500 nM	510 nM

A further example for drug design comprising a small organic molecule and using a short peptide as starting point for tuning is shown in **Scheme 1**. Captopril is a non-peptidic mimic of the bradykinin potentiating peptide (BPP_{5a}). $BPP_{5a,}$ isolated from snake species like vipers and taipans, inhibits the natural angiotensin-converting enzymes (ACE) by competitive binding to the active site.[27] Though BPP_{5a} regulates blood pressure, its resorption upon oral administration is not possible. However, its non-peptidic mimetic ensures easier uptake of the agent and leads to a higher *in vivo* stability.[28] Therefore, captopril became a commercially available therapeutic for treatment of hypertension. In the chemical structure of captopril, a construct resembling the amino acid sequence Ala-Pro can be found which is supposed to be the essential element for its bioactivity. These small molecule-based peptidomimetics can be classified to the type-III ones.[26]

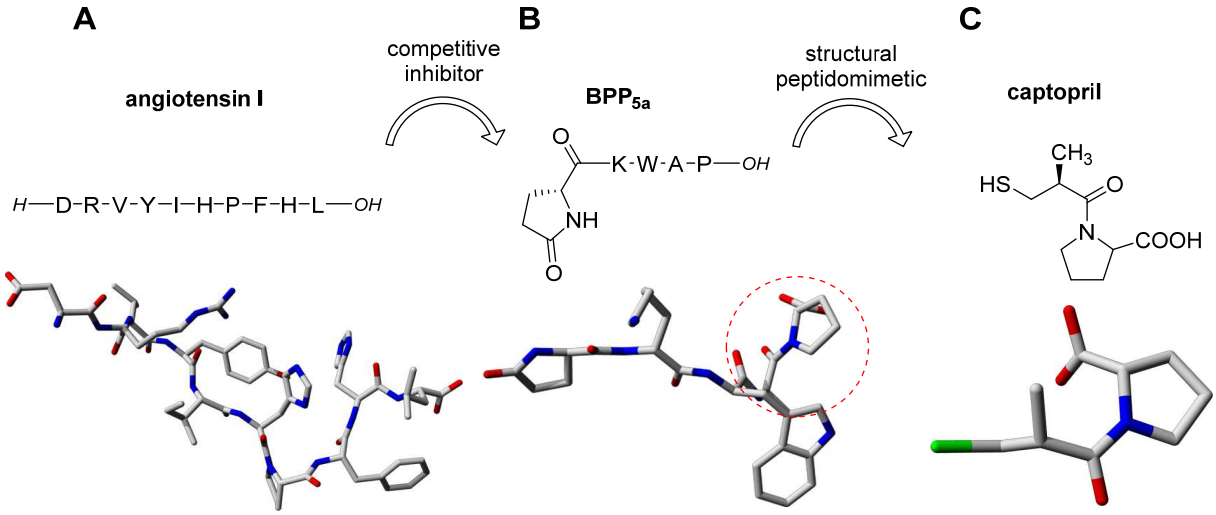

Scheme 1. Amino acid sequence and chemical structure of **A**: ACE-binding substrate angiotensin I, **B**: its competitive inhibitor BPP_{5a}, and **C**: its topographic mimetic captopril and the corresponding 3D structure depicted as stick with red = oxygen, blue = nitrogen, green = sulfur, and grey = carbon. Models derived from the crystal structure of angiotensin (PDB: 1N9V), ACE-BPP_{5a} complex: (PDB: 4AA2), and ACE-captopril complex (PDB: 4C2P).

For some special therapeutically relevant targets, the similarity in topography of target-binding regions is not sufficient for the selective binding of a peptidomimetic. In such cases, preserving the original scaffold of the model peptide can positively influence target recognition by electrostatic or non-polar interactions with the surface of target enzymes, or by enhancing the conformational rigidity upon intramolecular hydrogen bonding. Thus, the investigations towards the development of pseudopeptides and peptide analogs using therapeutically relevant model peptides as starting point has always been of high interest.[29] Often the rationale behind the replacement of a peptidic backbone element by a non-peptidic surrogate is to obtain conformationally constrained peptides which are often used to study the ligand-receptor interactions.[14a] Typical surrogates acting as mimics of amide bonds or dipeptide units with conformationally constrained architecture are shown in **Scheme 2**. *N*-Substituted peptoids and depsipeptides bearing an ester bond instead of the amide one are peptide surrogates found in natural products. Along with D- and β-amino acids, they contribute to enhanced proteolytic stability and can also influence the peptide architecture. The ε-caprolactam[14b] and the 1,4-dusubtituted triazole are condensation products of two peptide fragments and act as conformationally constrained dipeptide mimics at the same time. The 1,2,3-triazole motif possessing topologic and electronic similarity to the original amide bond is preferentially used since the invention of efficient Cu(I)-catalyzed click reaction.[30] Valverde et al. recently reported the synthesis of a bombesin derivative, a protease-resistant gastrin-releasing peptide receptor antagonist, by introduction of a triazolyl backbone mimic with preserved affinity to its target receptor.[31]

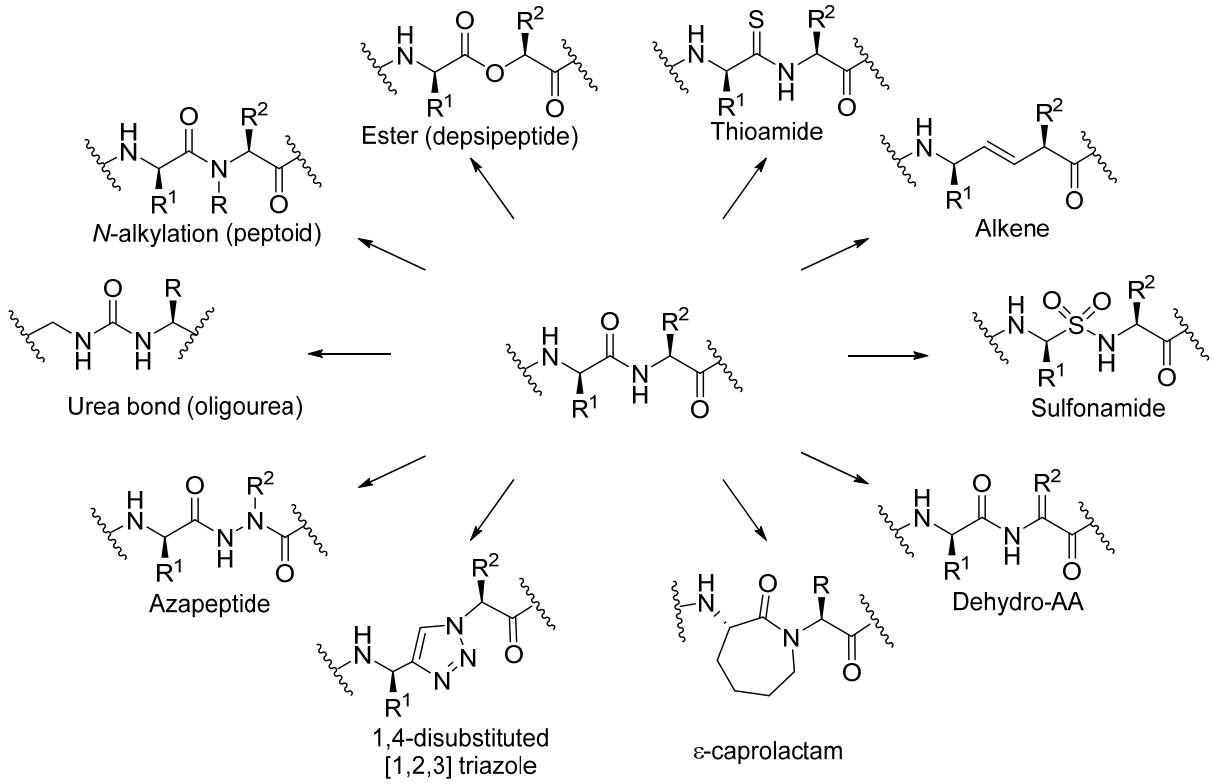

Scheme 2. Commonly used amide surrogates.

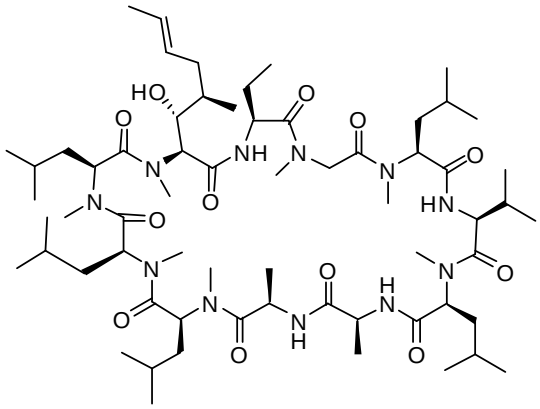

Figure 1. Cyclosporine A.

A "nonstandard peptide"[32] which belongs to cyclosporines and comprises several nonproteinogenic amino acids as well as non-standard structural elements, is a prominent example for the Nature-derived peptide mimetics. Cyclosporine A (**Figure 1**) possesses a highly modified peptide scaffold including two various nonproteinogenic side chains, diverse *N*-methylated peptide bonds, a D-amino acid and a head-to-tail macrocyclization pattern. These structural elements contribute to the proteolytic stability, oral availability, membrane permeability, and highly specific receptor binding.[33]

1.2.3 Synthesis of Peptidomimetics and Peptide Analogs

Traditionally, peptidomimetics are synthesized chemically. In the case of small molecules, all methods of organic synthesis could be applied. For the pinpoint-modified oligo- or polypeptides a solid-phase approach utilizing non-canonical amino acids or non-natural building blocks in combination with in-solution chemistry is the standard procedure (**Scheme**

3A). Only in few special cases, peptidomimetics could be obtained from recombinantly produced peptide scaffolds *via* enzymatic reactions.[34]
The installation of non-natural amino acids upon recombinant expression was enabled along with the development of the technique for genetic code expansion and became popular in the last decade. This strategy exploits the gap of the 64 codons-to-20-amino acids map by the introduction of an orthogonal pair of tRNA and aminoacyl tRNA synthetase in combination with the amber stop codon introduced in a gene of interest. That enabled the direct access to long-chain peptide analogs and alloproteins (**Scheme 3B**).[35] In addition, Suga and coworkers reported a so-called genetic code reprogramming technique which allowed a cell-free translational synthesis of backbone-modified peptidomimetics.[32] A main advantage of this method based on specially screened, flexible ribozymes for RNA-aminoacylation (flexyzimes) is the fact that the installation of non-natural moieties is not limited to a single modification, making possible the synthesis of highly sophisticated, modified peptidomimetics as e.g. cyclosporine A (chapter 1.2.2 **Figure 1**).

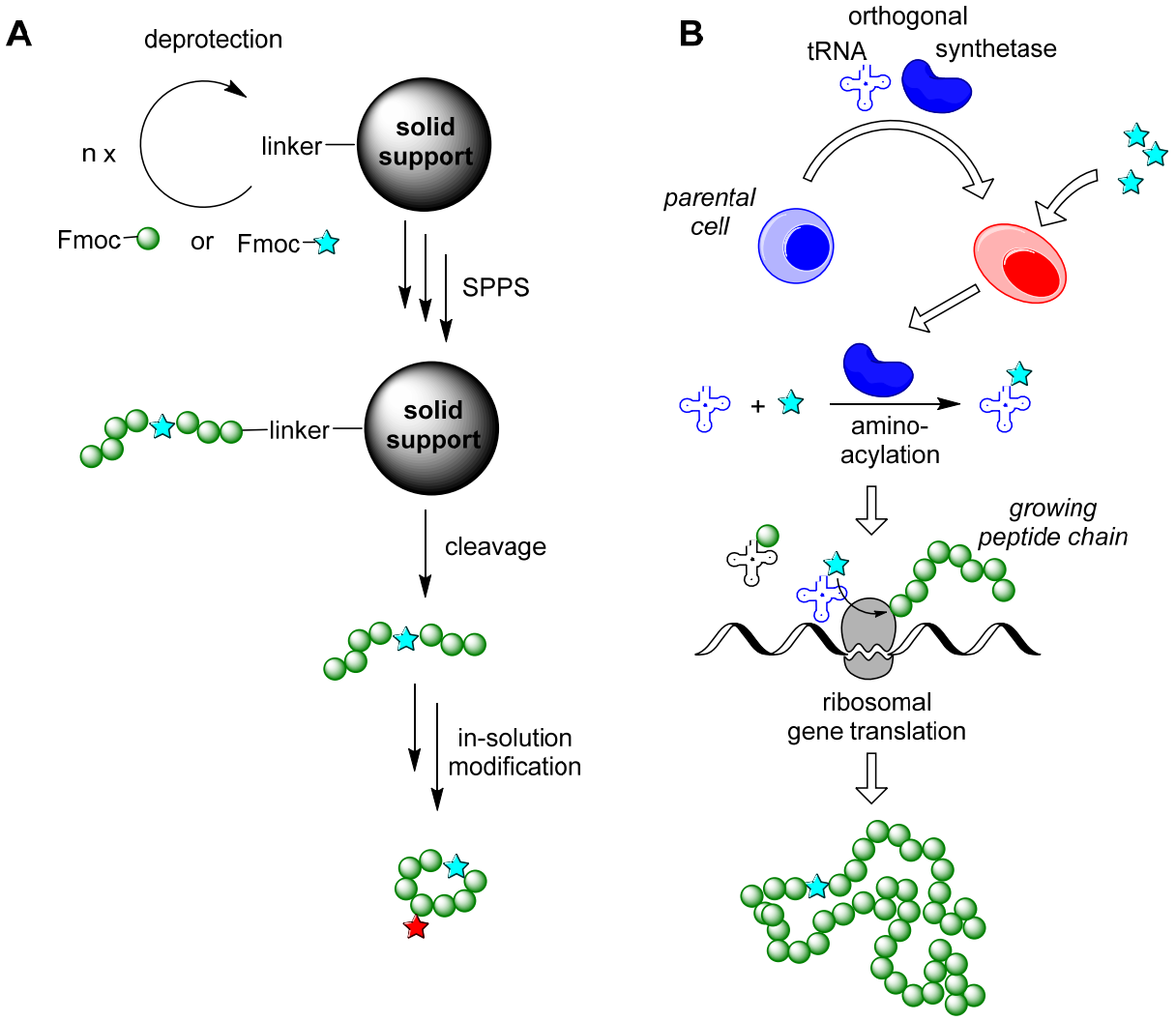

Scheme 3. Strategies towards peptidomimetics. **A**: Fmoc-SPPS and subsequent in-solution chemistry; **B**: recombinant expression *via* gene code expansion. Canonical amino acids are depicted as green balls. Non-natural amino acids or building blocks are depicted as stars.

Since recombinant production of peptidomimetics is still limited due to the need of sophisticated equipment and optimized cells, as well as unpredictable efficacy, the conventional synthetic methods were chosen in the present study.

1.3 Non-Natural Elements for Structural Investigations

1.3.1 Labels and Biomarkers for Diagnosis, Structural, and Mechanical Investigations

The installation of non-natural structural elements into peptides and proteins to bring a new function in the parent biomolecule is one of the basic strategies in biochemical/biomedical research. It can result in direct therapeutic effects (conjugation to antimicrobial or apoptosis-inducing agents), promote enhanced target binding (oligomerization, immobilization, or multifunctionalization), or act as markers, making the biomolecule distinguishable from environment or other components. Being strongly dependent on the chosen analytical method, protein labeling can provide insights to the mechanisms of bioprocesses and structure of biomolecules, as well as to the distribution of diverse agents in physiological systems, etc. For instance, a fluorescent dye can act as label for direct or indirect visualization of cells, for protein structure analysis using fluorescence polarization techniques, for investigation of protein-protein interactions using fluorescence resonance energy transfer (FRET), or for quantification of diverse molecules in physiological systems by fluorescence spectroscopy. Radioisotope labels commonly bound to the biomolecule *via* DOTA or similar chelators, can be used for visualization of drug distribution and accumulation by single-photon emission computed tomography (SPECT) or positron emission tomography (PET).[36] In wide sense, selenomethionine (Sem) can also be categorized to labels for advanced structure elucidation by X-ray crystallography (indeed, Sem is a naturally existing amino acid).[37] Certain diagnostic labels possess also a therapeutic function, e.g. alpha-particle emitting isotopes (^{213}Bi or ^{225}Ac) for radioimmunotherapy[38] or near-infrared-activated photosensitizer (phthalocyanine derivatives) for photoimmunotherapy.[39] Isotope labeling of peptides and proteins is a popular technique in the field of protein structure elucidation *via* nuclear magnetic resonance spectroscopy (NMR),[40] whereby the most popular isotopic labels, ^{15}N and ^{13}C, are often incorporated *via* bacterial expression in proteins and chemically indistinguishable from the common isotopes of these elements.[41]

1.3.2 NMR Hyperpolarization Techniques in Biochemistry

Although NMR spectroscopy has become the most common method for structural analysis in organic chemistry and life science, the application of magnetic resonance-based methods to complicated biological systems still has limitations due to low inherent sensitivity leading to an insufficient signal-to-noise ratio (SNR) or poor resolution caused by the anisotropic nuclear interactions. To overcome these drawbacks, several techniques for protein NMR were developed. Thus, decoupling (e.g. magic-angle spinning) and recoupling of the spin

interactions in solid-state NMR (ssNMR) influence the chemical shift anisotropy, and isotope labeling using ^{13}C, ^{15}N, ^{19}F, or ^{31}P minimize the background noise.[40, 42]
The NMR signals S (or the magnetization M) are proportional to the nuclear polarization P and the total number of nuclei N_0 in an NMR sample

$$S \propto N_0 P \tag{1}$$

and the polarization of an atomic nucleus with the quantum number $I = \frac{1}{2}$ is dependent on the differences between the two energy state populations N_{up} and $N_{\text{down.}}$ These originate from the orientation of the magnetic moment μ of the nucleic spins to the external magnetic field B_0 (parallel to field: μ_{up}, antiparallel to field: μ_{down}).[43]

$$P \equiv \frac{N_{\text{up}} - N_{\text{down}}}{N_{\text{up}} + N_{\text{down}}} \tag{2}$$

A small difference in the population of each energy level results in a weak polarization and, conclusively, to weak signals which is the case at thermal equilibrium. The population of the energy levels under thermal equilibrium can be described by the Boltzmann distribution:

$$N_{\text{m}} = \frac{\exp(-E_{\text{m}}/k_{\text{B}}T)}{\sum_{i=-1}^{+1} \exp(-E_{\text{m}}/k_{\text{B}}T)} \tag{3}$$

where N_{m} is the population of the nuclei in state m, k_{B} is the Boltzmann constant, T is the temperature, and E_{m} is the magnetic quantum energy of the state m given by the formula:

$$E_{\text{m}} = -\mu \times B_0 \tag{4}$$

By combination of the equations (2) – (4), it follows that P can be expressed as:

$$P = tanh\left(\frac{-\mu B_0}{2k_B T}\right) \tag{5}$$

and it becomes obvious that the NMR signal intensity is strongly dependent on the strength of the external magnetic field B_0 and the temperature T.[43] Thus, the classical way to obtain intense signals in NMR experiments is the application of a stronger magnetic field, which can be accomplished by utilizing a larger magnet or by reduction of the temperature near to absolute zero. Thereby, the equal distribution of the nuclei in the energy states is rescinded and the sample is “hyperpolarized” (**Figure 2**).
Since both strategies are associated with drawbacks in view of costs and application to biomolecular probes, more feasible methods for hyperpolarization were established.

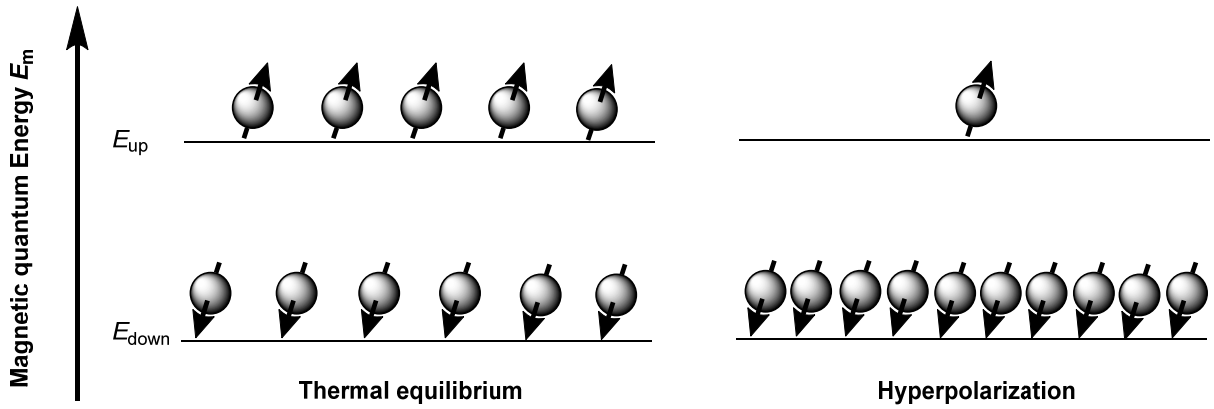

Figure 2. Orientation of the nuclei at thermal equilibrium and in the hyperpolarized state. The magnetic field (B_0) is directed vertically upwards. Figure modified from [44].

Hyperpolarization techniques using no "brute-force" approaches[45] were first reported in the 1960s. They utilized transfer of the electron spins from optically pumped Rb atoms (ground-state electron were pumped selectively to the $\pm \frac{1}{2}$ state *via* irradiation with circularly polarized laser light) to the nuclear spins of noble gases as ^{3}He or ^{129}Xe.[46] Another method used metastability exchange by the electron shell exchange of metastable atoms while collision with a ground-state noble gas atom.[47] Furthermore, the dynamic nuclear polarization (DNP) technique was invented 1978 by Abragam and Goldman, which uses the transfer of electronic spin polarization from free radicals added to the probe under microwave irradiation near the electron paramagnetic frequency to enhance the polarization of nuclear spins.[48] This method is now well-established and applied to the structure elucidation of several biomolecules in ssNMR and even in solution NMR analysis.[49] Nevertheless, DNP-enhanced NMR requires sophisticated equipments, high energy costs for cooling the probes, generation of a strong magnetic field, the microwave irradiation, and long polarization times.[50]
In general, hyperpolarization of biomolecules opened the door for structural characterization of complex biomolecular analytes and investigation of biochemical processes *via* NMR or the magnetic resonance imaging (MRI).

1.3.3 NMR PHIP Experiments with Biomolecules

In 1986, Bowers and Weitekamp theoretically predicted that a strong nuclear spin polarization can be obtained upon homogeneously catalyzed addition of molecular parahydrogen (para-H_2) to unsaturated hydrocarbons.[51] One year later, the same authors have experimentally confirmed their hypothesis.[52] Molecular hydrogen exists in two isomeric forms that differ in their nuclear spin conformation and the population of rotational states: molecular hydrogen with anti-symmetric nuclear states (para-H_2) and hydrogen molecules with symmetric nuclear states (ortho- with an ortho-to-para ratio of 3:1 at ambient temperature. The thermodynamic equilibrium of the rotational and nuclear states is strongly dependent on the temperature, thus an enrichment of para-H_2 can be accomplished at low temperature (e.g. by cooling with liquid nitrogen) and catalytically accelerated, for instance by charcoal.[53] Since para-H_2 has due to its symmetric character an overall nuclear spin of zero, in the hydrogenation product exclusively the symmetry-matched nuclear spin energy

level becomes populated. This leads to significant deviation of the product spin system from that in a system at thermal equilibrium and, finally, to the observed signal enhancement (SE) and an antiphase doublet signal.[53]

These characteristic signals can be explained by a simplified population model shown in **Scheme 4**: In an AX-type spin system at thermal equilibrium (**Scheme 4A**), four energy states $\alpha\alpha$, $\alpha\beta$, $\beta\alpha$, and $\beta\beta$ are equally populated, where α and β are corresponding spin functions and the nuclear wave function of para-H_2 is described as:

$$\psi = \frac{1}{\sqrt{2}}(\alpha\beta - \beta\alpha) = 0 \qquad (6)$$

Upon radiofrequency radiation in an NMR experiment four transitions shown in **Scheme 4A** yield the typical two-doublet signals centered at the corresponding chemical shift. If a catalytic hydrogenation of an unsaturated bond with para-H_2 is performed inside the NMR magnet (experiment called PASADENA = Parahydrogen And Synthesis Allow Dramatically Enhanced Nuclear Alignment)[52, 54] and the para-H_2 nuclei are transferred to into the AX-type spin system, the symmetry of the anti-aligned state of para-H_2 abruptly breaks and induces a chemical distinction between the two hydrogen atoms. Hence, only the levels $\alpha\beta$ and $\beta\alpha$ become populated and a large gap between the population numbers of each energy level arises resulting in an unusual, highly polarized pair of proton spins. The characteristic antiphase signals during the experiment are caused by the selective population transfer of the energy levels (**Scheme 4B**).

.

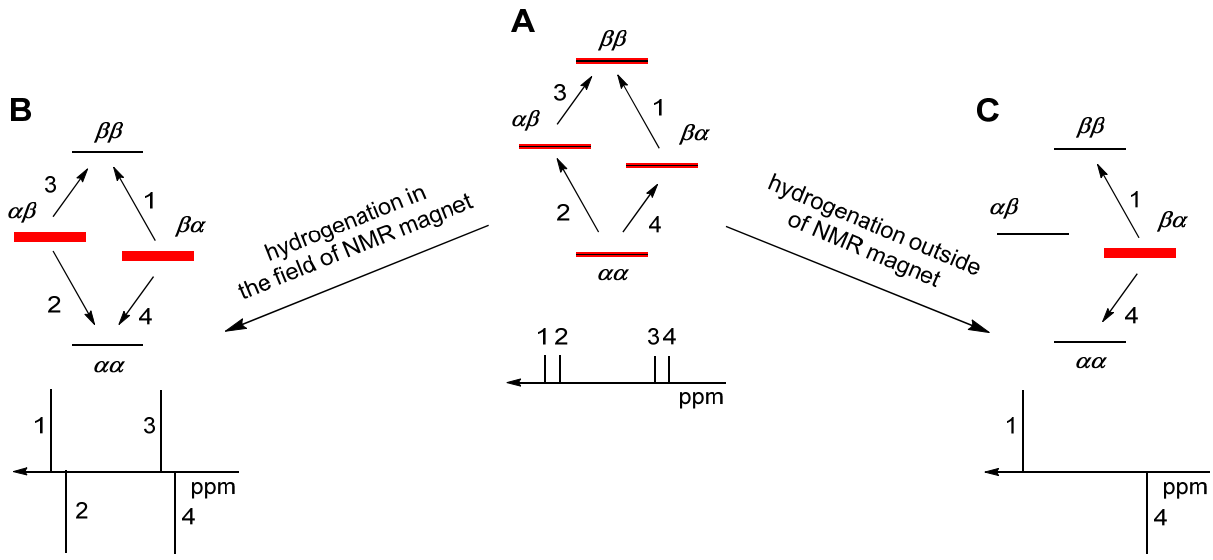

Scheme 4. Population models for an AX-type two-spin system and expected NMR signals in **A**: Standard NMR system (thermal equilibrium), **B**: during PASADENA experiment, **C**: during ALTADENA experiment. Expected NMR signals are numbered with corresponding nuclear spin transitions. Population numbers of spins are expressed as the width of red lines. Figure modified from [53].

When the catalytic hydrogenation of an unsaturated bond with para-H_2 is performed outside the NMR magnet and subsequently transferred into the magnetic field under adiabatic condition (experiment called ALTADENA = Adiabatic Longitudinal Transport After

Dissociation Engenders Nuclear Alignment),[55] only one of the energy levels of $\alpha\beta$ or $\beta\alpha$ will be populated leading to only two possible transitions during measurement, graphically shown in **Scheme 4C**. More detailed quantum mechanical explanations and models for these observations are omitted in the presented work and can be found in certain books and reviews on hyperpolarization methods.[53] Covering both experiments, PASADENA and ALTADENA, the term Parahydrogen-induced polarization (PHIP) was introduced.[56]

Furthermore, a method closely related to PHIP, Signal Amplification By Reversible Exchange (SABRE), was described by Adams et al. 2009. It takes the advantage of the fact that in special cases a transient metal complexation of para-H_2 together with the substrate of interest is sufficient to break the symmetry of para-H_2, thus realizing a polarization transfer from the hydrogen molecule without direct hydrogenation, while the chemical structure of the analyte is kept unaltered.[57] Along with the already mentioned DNP, hyperpolarized Xenon biosensor (HP/Xe),[58] Chemically Induced Dynamic Nuclear Polarization (CIDNP),[59] PHIP and SABRE became well-established techniques for the signal enhancement in NMR experiments. A major advantage of PHIP NMR experiments is their feasibility with no need for sophisticated and expensive equipment.

In contrast to DNP methods which have already gained recognition for the detection and the structural investigation of complicated biomolecules as e.g. membrane proteins, the application of para-H_2-enhanced NMR techniques to bio-related targets is currently limited to a small number of small biomolecules: derivatives of glucose, barbituric acid, non-natural amino acids, and short oligopeptides.[60] The requirement of an unsaturated bond in the molecule of interest strongly narrows the spectrum of analytes. On the contrary, the development of SABRE enabled the signal enhancement provided by para-H_2 for molecules without olefin or alkyne moieties. However, this technique utilizes a pyridine motif or a moiety with similar structural and electronic properties within the substrate to obtain successful hyperpolarization. Therefore, its application is hampered in case of complex biomolecules. For these reasons, the development of a viable PHIP label which could be easily installed in biomolecules and enables strong hyperpolarization without affecting bioactivity is in demand.[50b]

1.4 Non-Natural Elements for Bioorthogonal Conjugation

1.4.1 "Click" Chemistry

According to the original definition given by Sharpless, a chemical reaction has to match the next criteria to be referred to as "click chemistry": it has to be modular, wide in scope, regio- and stereospecific, high-yielding, generating no or only easily removable side products, performable in simple reaction conditions, with educts and starting materials being easily available, and solvents easily removable. Moreover, it must be compatible with atmospheric oxygen and aqueous conditions.[11] Along with the fact that the majority of the reactions matching the scope are bioorthogonal and compatible with biological systems, "click chemistry" finds wide application for the labeling of biomolecules and the generation of combinatorial chemical libraries for fragment-based drug screening.

Sharpless has classified three types of “click” reactions: 1) the nucleophilic opening of small, strained heterocyclic electrophiles (e.g. epoxides, azyridines, azyridinium, and episulfonium ions), 2) some special mild condensation reactions of carbonyl compounds (e.g. 1,3-dioxirane formation with 1,3-diols, oxime and hydrazone ligations using hydroxyamines and hydrazides, and Michael-type additions), 3) cycloadditions, especially reactions involving heteroatoms and 1,3-dipoles.[11] Few of these “click” reactions are listed in **Scheme 5** whereby not all of the reactions do perfectly match the initial requirements of “click” chemistry.

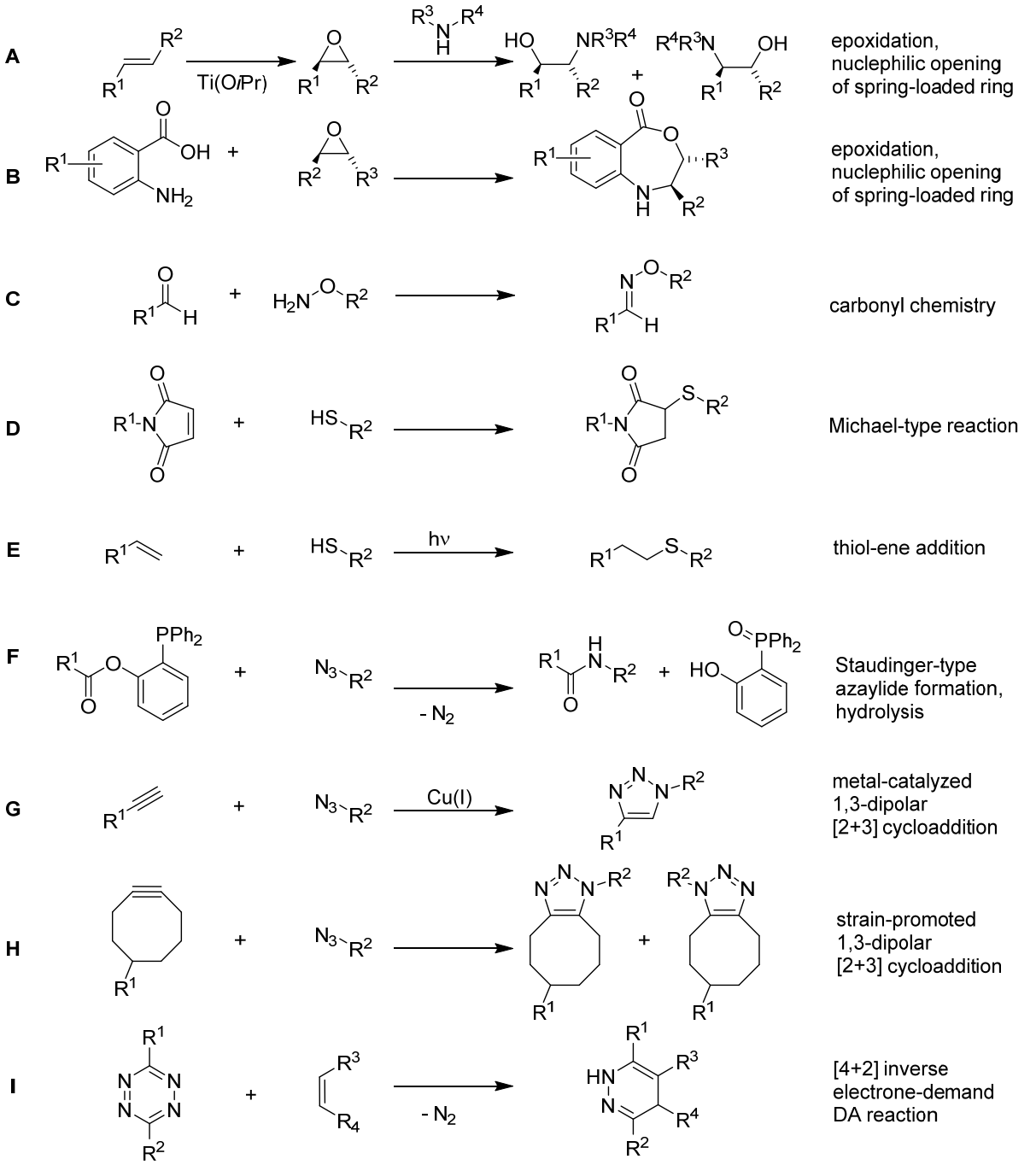

Scheme 5. Bioorthogonal conjugations referred to as “click” reactions. **A**,**B**: nucleophilic opening of epoxides; **C**: oxime ligation; **D**: sulfhydryl-maleimide conjugation; **E**: thiol-ene conjugation; **F**: traceless Staudinger ligation; **G**: CuAAC; H: SPAAC; **I**: tetrazine ligation. Most of the reaction schemes are simplified or generalized.

The benefit of these reactions is not limited to the assembly of functional fragments or the attachment of several organic or biomolecules to certain scaffolds. In some special cases, the linking motif generated during reaction can provide further functional properties itself, e.g. fluorescence, chemoluminescence, metal ion chelating functions, mimicry of protein structure elements with constrained conformations, or photo-cleavable linkage.[61]

During the last decade, some of these reactions have been found to be especially attractive for the modification of biomolecules and were applied in biochemical and biomedical research, among them oxime ligation,[62] sulfhydryl-maleimide conjugation,[63] the traceless Staudinger ligation,[64] the inverse electron-demand Diels-Alder (DA) reaction using tetrazines,[65] and several variants of 1,3-dipolar cycloaddition.

In general, the 1,3-dipolar cycloaddition between a 1,3-dipole (functional groups with four delocalized electrons in the π–system over three atoms as e.g. azides, diazoalkanes, nitrosoxides, or nitrones, **Scheme 6**) and a dipolarophile results in formation of a five-membered ring as product. The most frequently used dipolarophile in biochemical research is the alkyne group due to its high stability in biological systems and its distinct orthogonal character.[66]

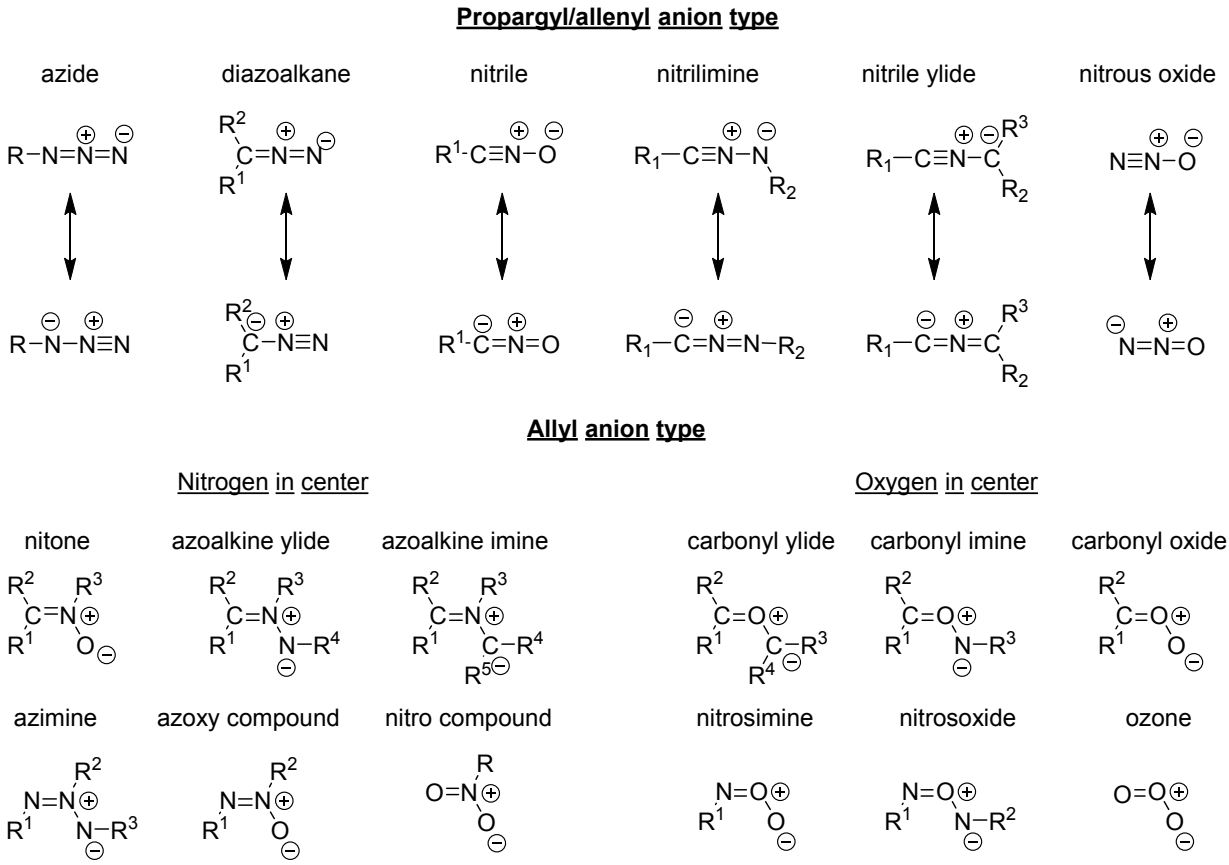

Scheme 6. Chemical structure of popular 1,3-dipoles classified depending on formal structure and central atom. For propargyl/allenyl anions both resonance structures are depicted. Scheme adapted from [67].

The diverse variants of 1,3-dipolar cycloadditions differ in the nature of the 1,3-dipoles and the way to overcome the high activation barrier (~25 kcal mol^{-1} for methyl azide and propyne) of the highly exothermic reaction.[68] As prototype of modern 1,3-dipolar cycloadditions, the alkyne-azide cycloaddition published by Huisgen et al. in 1961 can be

considered.[69] This non-catalyzed and non-regioselective reaction used thermal energy to overcome the activation barrier. Due to the harsh reaction conditions, the Huisgen cycloaddition itself was not compatible with sensitive biomolecules and had gone to oblivion for decades.

Contrary, after the discovery of the Cu(I)-catalyzed variant of this reaction, called Cu(I)-catalyzed alkyne-azide cycloaddition (CuAAC), in the beginning of 21st century (independently described by Meldal and Sharpless 2002)[70], it became one of the most valuable reactions for the covalent assembly of complex molecules in the repertoire of "click" chemistry. Even the term "click" reaction is frequently associated with it. CuAAC possesses many desirable features like high selectivity, bioorthogonality of educt functional groups and product triazole, high reliability, no need for elevated temperature; it is completely selective towards the formation of the 1,4-disubtituted regio isomer.[11, 30] Additionally to the Cu(I)-catalyzed reaction, Ag(I)-catalyzed alkyne-azide cycloaddition (AgAAC)[71] towards selective formation of 1,4-triazoles and Ru(II)-catalyzed alkyne-azide cycloaddition (RuAAC)[72] selectively forming a 1,5-disubstituted triazole, are also reported, whereby the latter one requires elevated temperature or microwave irradiation and an oxygen- and water-free condition.[73] The simplified chemical equation of 1,3-dipolar cycloaddition between terminal alkynes and an azide is shown in **Scheme 7A**.

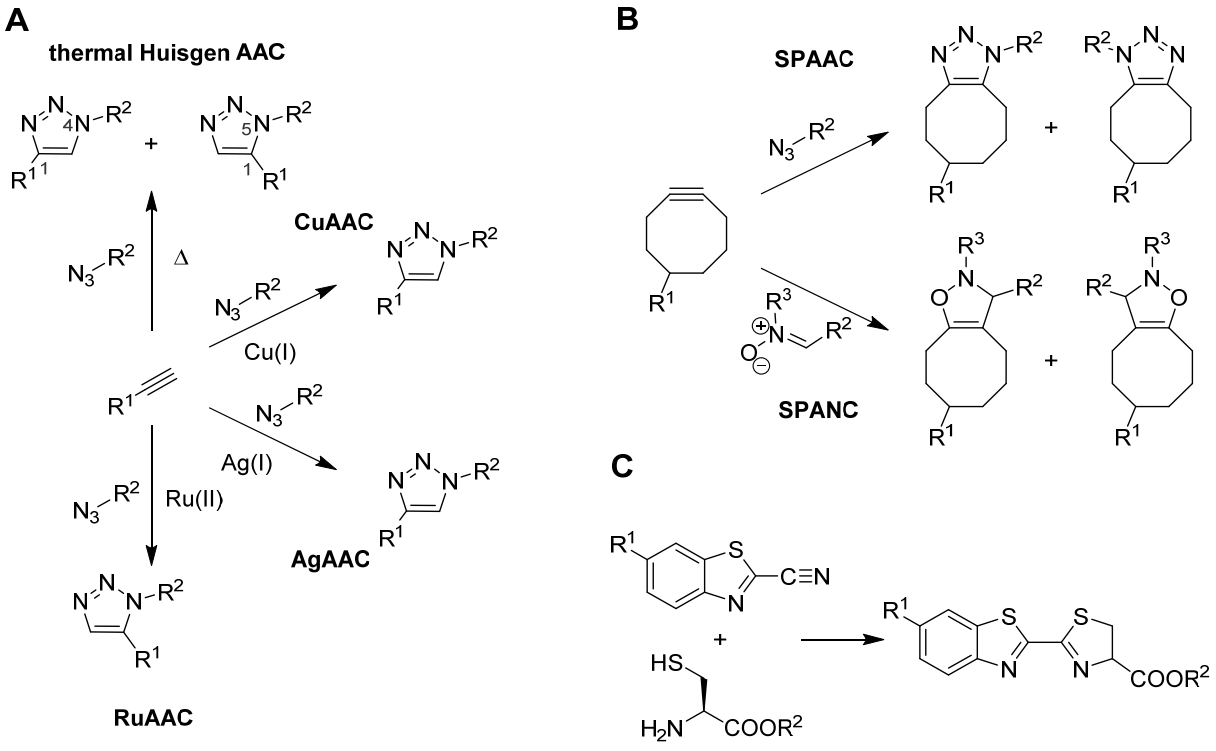

Scheme 7. 1,3-Dipolar cycloaddition between **A:** terminal alkynes and azides; **B**: strain-promoted alkynes and an azide (top) or nitrone (bottom); **C**: a cyanobenzothiazol and a thiol.

An interesting aspect of these reactions is the topologic and electronic similarity of the product, 1,2,3-triazole, with an amide bond.[30, 74] The heterocyclic linking unit can mimic peptide bonds, whereas the 1,4-disubstituted triazole can be used as conformationally constrained and hydrolytically stable surrogate for *trans*-peptides and the 1,5-disubtituted one as surrogate for a *cis*-peptides.[14a]

Nevertheless, the application of metal ion-catalyzed alkyne-azide cycloaddition in biological systems still has an unavoidable disadvantage which is caused by the metal ion itself.[75] On the one hand, the inherent cytotoxicity of transition metal ions hampers the *in vivo* application of the reactions and, on the other hand, the tendency to form stable complexes with both the reactants and products makes the isolation difficult. Thus, a metal-free click reaction was developed few years later by Bertozzi and coworkers where the alkyne dipolarophile is installed into a strained ring while using the ring tension to decrease the activation barrier (**Scheme 7B**).[75a] The reaction referred to as strain-promoted alkyne-azide cycloaddition (SPAAC) makes the 1,3-dipolar reaction possible in living cells and found application for *in vivo* labeling of several proteins.[76] But it has to be mentioned that the regioselectivity of the metal ion-catalyzed cycloaddition is lost.
An arranged variant of SPAAC using *in situ* generated nitrones as 1,3-dipoles, strain-promoted alkyne-nitrone cycloaddition (SPANC), is also reported.[77] Moreover, a thiol-based 1,3-dipolar cycloaddition using 2-cyanobenzothiazole as dipolarophile and D-cysteine derivatives as 1,3-dipole (**Scheme 7C**) was recently reported. This reaction was inspired by the natural regeneration pathway of luciferin in fireflies, and also has gathered attention, due to the inherent fluorescence or the bioluminescence emission of the resulting luciferin-like linker unit.[78]

1.4.2 Biocompatible Scaffolds for Drug Delivery and Oligomerization

An important area where bioorthogonal conjugations are frequently applied is the immobilization of functional ligands, peptides or small molecules, on solid surfaces as well as their loading to a biocompatible scaffold. Especially the latter approach has significance for the development of complex drugs with tailor-made functions and properties. As it is known from Nature, oligomerization of target-binding domains within a molecule or a molecular complex can lead to unexpected enhancements of the binding to a multimeric receptor. Thus, several natural antibodies form condensed oligomers as e.g. pentameric human IgM which is composed of five singular antibodies joined by certain peptidic linkers, or the IgG comprising a homodimer held together *via* disulfide bonds.[79] The non-linear connection between the number of paratopes and the epitope-binding ability is caused by the avidity (or functional affinity) effect and can be explained by thermodynamic and kinetic models.[80] Since the probability that multiple binding interactions simultaneously dissociate is low and the probability of re-association upon dissociation of one binding interaction is enhanced by the fixation of the second binding site, the binding constant of multivalent interaction is not a simple sum of the individual binding affinity constants K_n, but a multiple of it resulting in a cooperative effect and leading consequently to the beneficial entropic contribution to the overall free energy G.[81] In case of a polyvalent interaction with N individual receptor-ligand pairs, this can be derived from the following equation for the Gibbs free energy:

$$\Delta G = -RT\ln K_{\text{avid}} \quad (7)$$

$$\Delta G_n = -RT ln K_n \quad (8)$$

$$\Delta G = \sum_{n=0}^{N} \Delta G_n = -RT \sum_{n=0}^{N} \ln K_n \quad (9)$$

$$-RT\ln K_{\text{avid}} = -RT \sum_{n=0}^{N} \ln K_n = -RT\ln \prod_{n=0}^{N} K_n \quad (10)$$

$$\rightarrow K_{\text{avid}} = \prod_{n=0}^{N} K_n \quad (11)$$

K_{avid} is the observed affinity caused by the polyvalent interaction, G_n - the free energy of an single interaction defined by the individual binding affinity constant K_n. From the perspective of kinetics, an elevated local concentration of the components (effective molarity) is provided upon the spatial proximity of the numerous binding sites, thus decreasing the probability and reaction rate of dissociation.[80]

Analogous approaches towards the synthesis of artificial multivalent binders were investigated on various types of scaffolds, whereby the nature of the oligomerization scaffolds was also of high interest since it does not only define the number and spatial arrangement of the functional units, but also induced new properties. The range of molecules applicable for scaffold-based drug design is wide and includes inorganic materials like silsesquioxane-based nanoparticles,[82] organic materials like long-chained hydrocarbons[83] (**Figure 3A**) or dendrimers,[84] simple biomolecules like cyclic peptides or oligosaccharides,[85] and complex proteins as bovine serum albumin or monoclonal antibodies (mAbs).[86]

An interesting approach for peptide conjugation on a cube-octametric silsequioxane (COSS) scaffold was reported by Hörner and Fabritz et al. (**Figure 3B**). [87] They demonstrated the successful loading of multiple copies of various functional peptides on a single COSS particle (2-8 copies depending on the size of the payloads) using oxime ligation.[87a] On the other hand, they examined the cell-penetrating character of the amino-functionalized COSS and succeeded in the targeted delivery of a cargo peptide into living cancer cells and even to their nuclei.[87b]

As an example for peptide-based scaffold, the cyclic decapeptide developed by Mutter et al. should be mentioned.[13a] The scaffold molecule matches the concept of template assembled synthetic proteins (TASP)[13a] and the regioselectively addressable functionalized templates (RAFT).[88] Galbert et al. reported 2011 the one-pot synthesis of a highly sophisticated tetravalent and trifunctional bioconjugate based on this decapeptidic scaffold using three various bioorthogonal reactions: CuAAC, maleimide conjugation, and oxime ligation (**Figure 3C**).[89]

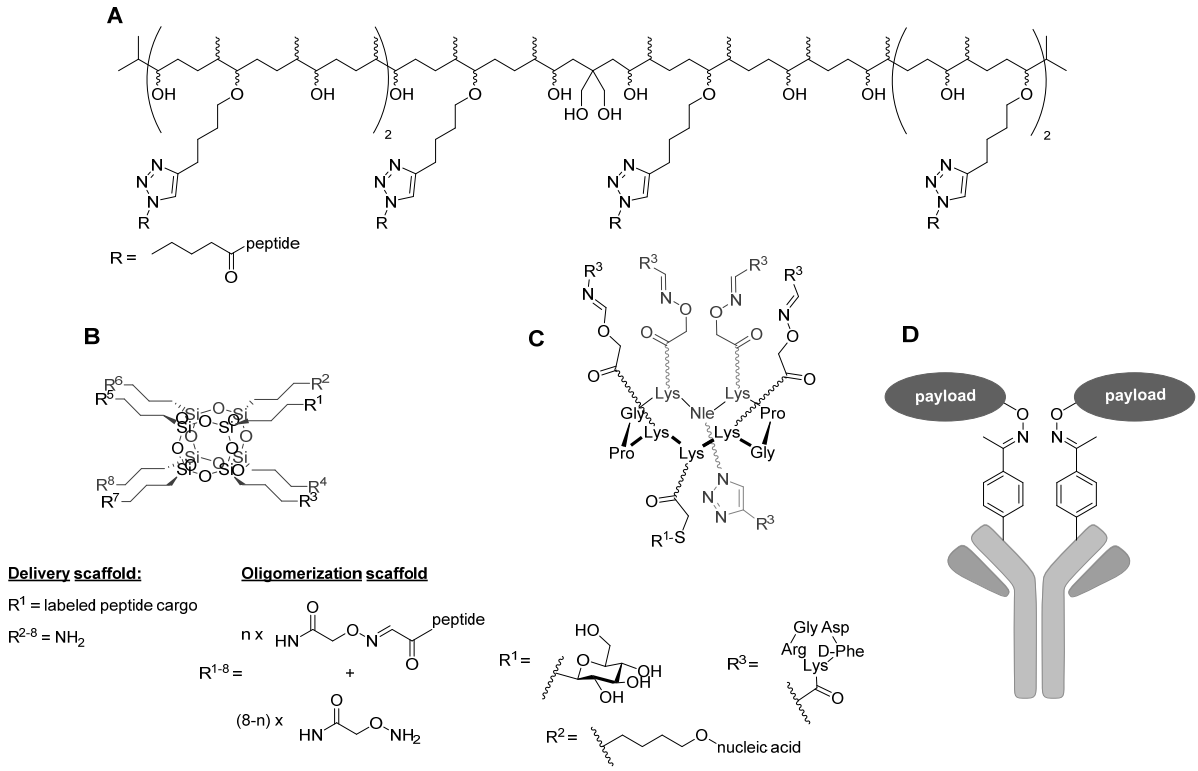

Figure 3. Exemplary chosen biocompatible scaffolds with payloads. **A**: solanesol-derived multimerization scaffold loaded with functional peptides;[83] **B**: COSS scaffold for drug delivery or oligomerization;[87] **C**: TASP- and RAFT-based cyclic decapeptide scaffolds with three orthogonally conjugated ligands;[89] **D**: schematic depiction of homodimeric ADC on IgG base with site-specifically conjugated payloads.

From the opposite perspective, the loading of small-molecule ligands onto larger biomolecular scaffolds as proteins is also a popular approach in scaffold-based drug design. Although small molecules and short peptide-based drugs often exhibit high *in vitro* bioactivity (target binding or toxicity), their application as pharmaceutical agent is strongly hampered by the inappropriate pharmacokinetical properties.[2b] Generally, the *in vivo* half-life of substances with a size below the cutoff for renal clearance (molecular weight cutoff: 48 kDa, size cutoff: 10 nm) are very short (several minutes to few hours).[90] Combined with the fact that peptide-based components can also undergo proteolytic degradation, a method to enhance their ADME properties was strongly desired. A strategy to couple the excellent bioactivity of small-molecule drugs with the pharmacokinetic profile of mAbs can be considered in a novel class of pharmaceuticals referred to as antibody-drug conjugate (ADC).[86a, 91] ADCs are mAbs or fragments of antibodies covalently linked to bioactive payloads. In the first generation of ADCs, the intrinsic target-binding properties of the Ab paratopes were combined with cytotoxic payloads linked *via* a cleavable linker, whereby non-specific conjugation techniques through native residues as side chains of Lys or Cys were applied. This resulted in the heterogeneous mixture of ADCs with diverse numbers of payloads on a single mAB making the purification and characterization very difficult and influencing the pharmacokinetics of ADCs.[86a] Thus, in the next generation of ADCs, site-selective conjugation techniques through genetically or chemically engineered sites are used resulting in the homogeneous species with a controllable drug-to-antibody ratio (DAR). For site-selective transformation, bioorthogonal transformations like oxime ligation,[92] (**Figure 3D**) SPAAC,[93] or enzymatic reactions recognizing specific amino acid sequences are appropriated.[94]

1.4.3 Affinity-Guided Reactions in Biochemistry

The concept of affinity-guided reactions rises from the field of coordination chemistry and is associated with the so-called "templated reactions". The classical templated reaction comprises two or more coordination sites of a metal ion center giving the reactive groups a certain spatial pre-orientation (**Scheme 8A**). The close proximity provided by the non-covalent binding leads to an increased local concentration of the reactive groups and, consequently, enhanced reaction rate and better selectivity.[95] As transition metal-catalyzed reactions can also be considered as non-stochiometrically templated, the majority of these reactions require the corresponding metal.[96]

In biochemistry, the scope of "templated reactions" is extended towards the admission of every non-covalent interaction between biomolecules contributing to the spatial arrangement of reactive moieties and promoting the formation of a covalent linkage. Thus, enzyme-catalyzed condensations with the reactive moieties of substrates brought in close proximity by the active site of the enzyme can also be regarded as "templated". However, template-directed chemical ligation techniques are still useful for the site-specific labeling of target molecules or for fragment-based drug discovery. Hamachi and coworkers have developed the ligand-directed tosyl (LDT) chemistry[97] and the affinity-guided DMAP (AGD) chemistry[98] for site-specific protein labeling: in both strategies, labeling probes were selectively attached to a nucleophilic residue on the protein surface, whereby the selectivity is given by the spatial approximation of the electrophilic probe conjugated to the protein-binding ligand *via* a leaving group (**Scheme 8B**)

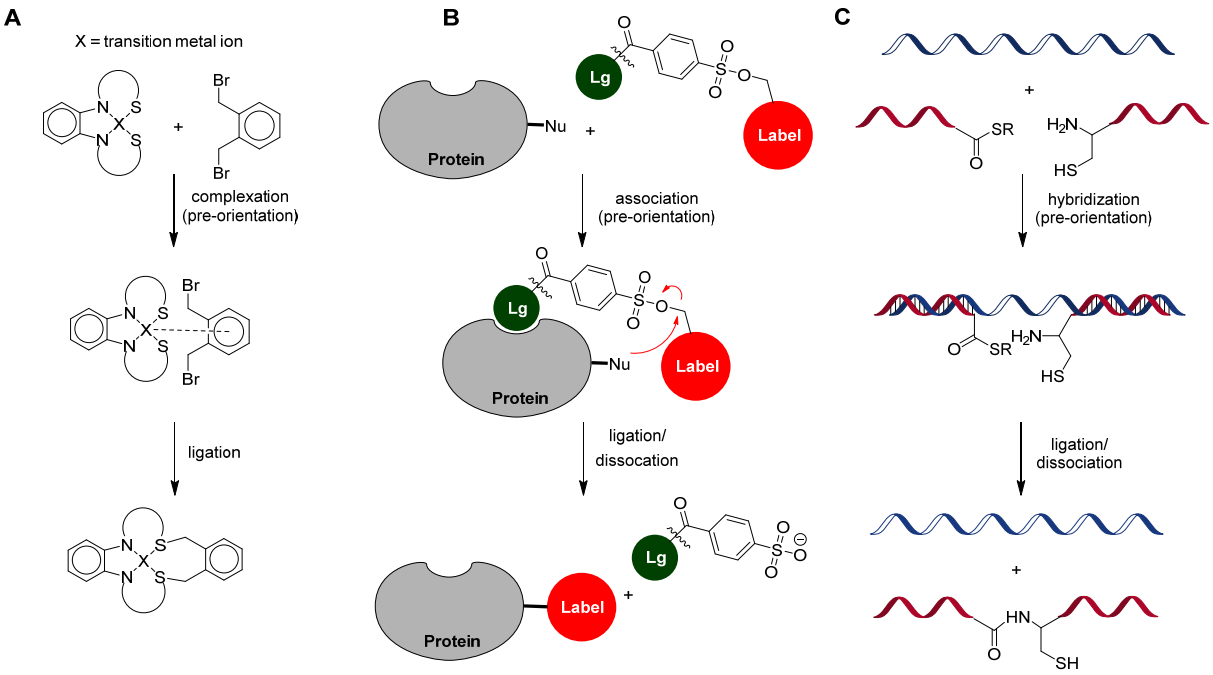

Scheme 8. Sketch of exemplary chosen affinity-guided reactions. **A:** templated reaction in coordination chemistry. **B:** protein labeling by LDT chemistry. Lg = ligand, Nu = nucleophilic residue on protein surface. **C**: DNA-templated NCL ligation of oligonucleotides. Template DNA is shown in blue. Helices shown in red are either terminally modified oligonucleotides or oligo-PNAs.

In the latter strategy, a carboxylic acid activator (AGD catalyst) is selectively attached to the nucleophile, and successive site-selective conjugation of a labeled acyl donor follows. Both approaches have found successful application for specific labeling of target cells *in vivo*.
Furthermore, a method described by Rademann et al. as dynamic, template-assisted drug discovery has found application in fragment-based drug design.[99] In this strategy, two small-molecule fragments binding two epitopes of a target protein with low affinity are covalently linked upon a fragment condensation after the non-covalent binding to their target sites has occurred. Several small-molecule enzyme inhibitors with high affinity and target specificities were identified and synthesized by this method.
In the field of biochemically templated reactions, the non-covalent interactions for reactant pre-orientation are not limited to ligand-receptor (or substrate-enzyme) binding. Non-covalent interactions between larger biomolecular subunits, among them the self-assembly of several protein subunits or the hybridization of a complementary oligonucleotide pair are of research interest as well. A large number of non-enzymatic techniques using DNA strands as a template are reported for the condensation of oligonucleotide fragments with native and non-native linkers,[100] or for the multistep synthesis of small molecules (DNA-templated organic synthesis: DTS).[101] As an interesting example, a DNA-templated fragment ligation of peptide nucleic acids (PNAs) *via* native chemical ligation (NCL) during polymerase chain reaction (**Scheme 8C**)[102] and a surface labeling of quantum dots *via* DNA-instructed amino acyl transfer reaction was recently reported by Seitz and coworkers.[103] The high combinatorial diversity of oligonucleotides and the reliability of the sequence-specific hybridization make nucleic acid-templated ligations an interesting tool for the simultaneous attachment of diverse functionalities to a scaffold molecule.

1.5 Model Compounds and Test Systems

1.5.1 Trypsin-like Proteases and Related Serine Proteases

Trypsin is an endopeptidase comprising 200 – 350 residues. Its natural function is the catalytic hydrolysis of nutritive peptides in the digestive system. Since the hydrolysis is supported by a catalytic triad within the active site possessing a serine residue which acts as a nucleophile and binds to the substrate during the reaction, it belongs to serine proteases. In **Scheme 9,** the mechanism of substrate hydrolysis by trypsin-like proteases is depicted.[104]
The catalytic triad of trypsin-like proteases is composed of three amino acids in spatial proximity. Though the most common combination is His^{57}, Asp^{102} (or Glu^{105}, respectively), and Ser^{195}, there are several other types of serine proteases with different amino acid combinations: the catalytic triads of cytomegalovirus proteases (His-His-Ser), or sedolisin (Asp-Glu-Ser).[105] Their mode of action relies on decreasing the activation energy barrier during the nucleophilic attack of the serine hydroxyl to the amide carbon of the substrate. To increase nucleophilicity of the alcohol group, a formal deprotonation *via* two further amino acids takes place. Under physiological pH, the carboxylic group of Asp^{102} (or Glu^{105}, respectively) is deprotonated (pH optimum of trypsin: ~8), thus forming a hydrogen bond with the N^{π}-proton of His^{57}. The shift of electron density leads to enhancement of the hydrogen bond from N^{τ} to the serine proton, which provides a formal deprotonation of the

serine side chain. The three-dimensional structure of the catalytic triad in bovine pancreas trypsin is depicted in **Figure 4**.

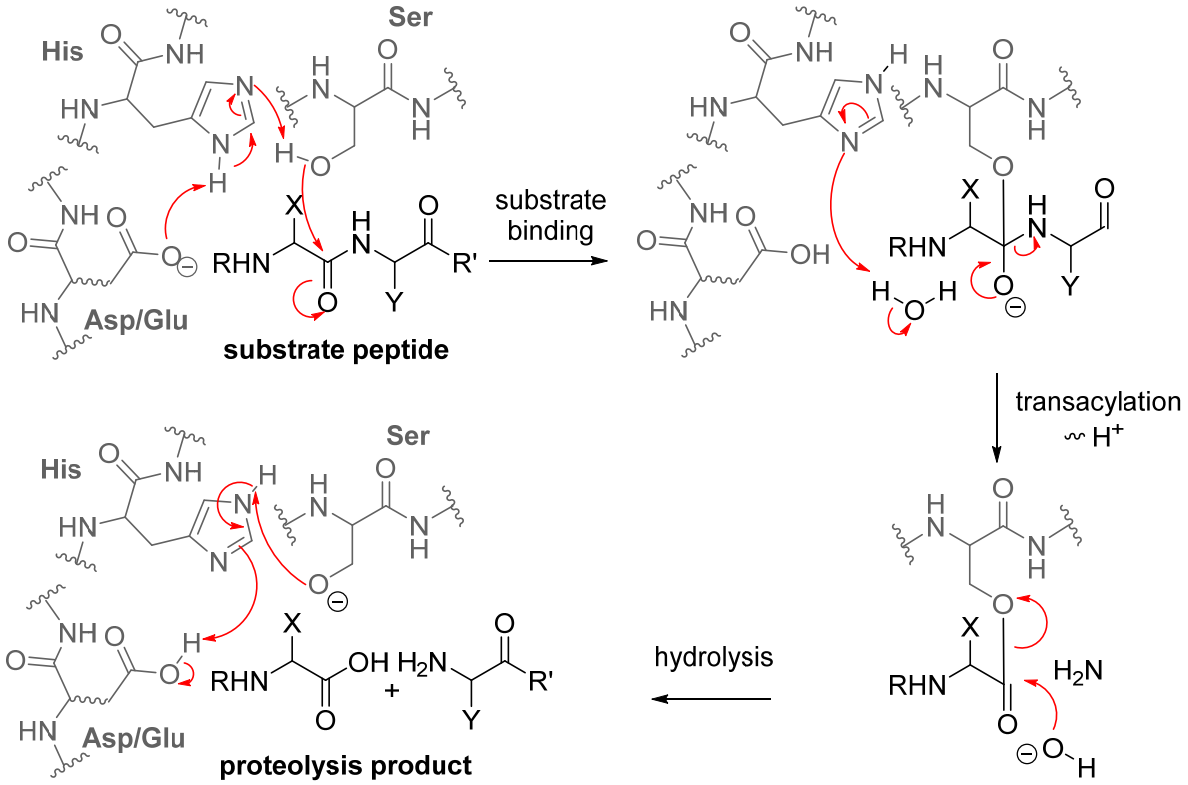

Scheme 9. Mechanism of trypsin-catalyzed proteolysis. X, Y: side chains of a substrate peptide (X = Lys/Arg). Catalytic triad residues of trypsin are shown in grey.

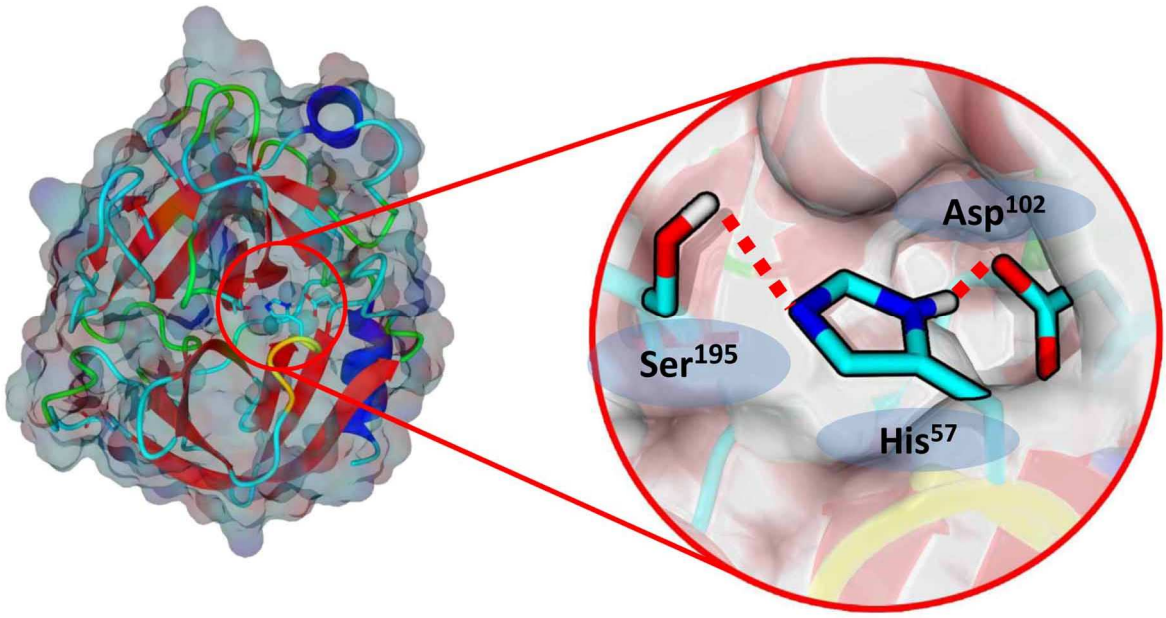

Figure 4. left: 3D computational model of trypsin in cartoon style. Residues forming the catalytic triad are shown as sticks, **right**: enlarged view of catalytic triad: red = oxygen, blue = nitrogen, cyan = carbon, grey =

hydrogen; hydrogen bonds are depicted as red, hashed lines. Model derived from crystal structure of bovine pancreas trypsin in co-complex with an inhibitor (PDB: 4ABJ).

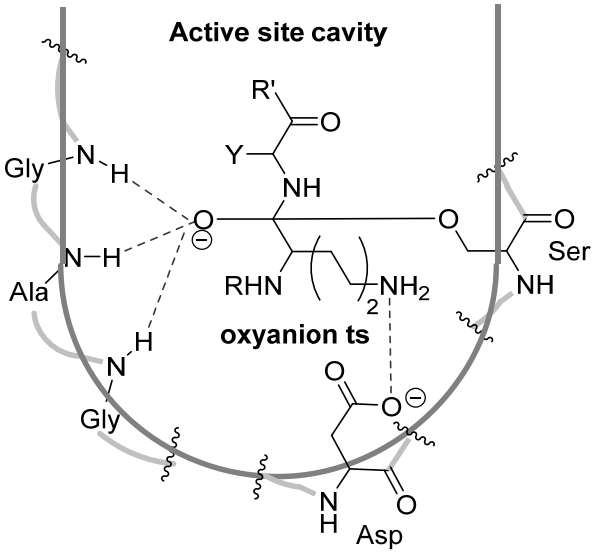

Scheme 10. Oxyanion stabilization and substrate selectivity towards positively charge amino acid in the active site of trypsin. Hydrogen bonds are depicted as dashed lines. Substrate-binding pocket of active site is shown in dark grey. Polypeptide chain of trypsin is shown in light grey.

The catalytic cycle can be separated in two single reaction steps. During the first step, a transacylation of substrate peptide *via* nucleophilic attack of the activated serine to the peptide carboxylic group takes place while leading to the generation of tetrahedral oxyanion transition state, **ts**. The transition state is additionally stabilized by hydrogen bonds with N^{α}-protons of peptide groups of surrounding amino acid residues (**Scheme 10**). This stabilizing effect induces the shift of the chemical equilibrium towards formation of **ts** and, consequently, to acceleration of substrate conversion towards product formation.[105]

The protonation of the N^{α}-group of the substrate leads to cleavage of an *N*-terminal peptide fragment while an *O*-acylated enzyme is formed. The ester bond is cleaved by alkaline ester hydrolysis and, simultaneously, the electron density flows back to Asp^{103} *via* His^{57}. Thus the initial conformation is regenerated and the protease is ready for subsequent reaction cycles.

The substrate specificity of serine proteases is mostly determined by the shape and charge of the primary specificity-site pocket inside the active site (S1 pocket). In case of trypsin, a deprotonated Asp^{189} at the bottom of the active site pocket binds to positively charged substrate residues and stipulates limited tolerance concerning substrate peptide residues. Taking into consideration the hydrophobic walls of the pocket, the residues bearing long aliphatic motifs of the side chains (Arg and Lys) are preferred as cleavage sites. Indeed, trypsin and trypsin-like proteases usually cleave non-terminal peptide bonds after these basic amino acids.

The classification of serine proteases in the subfamilies is mainly based on their specificities against diverse target substrates. Thus, chymotrypsin (**Figure 5**, middle), a digestive enzyme of the pancreatic juice, preferably catalyzes the hydrolysis of peptide bonds after amino acids with large- to medium-size hydrophobic side chains (aromatics as Phe, Tyr, or Trp) belongs to chymotrypsin-like proteases. The mode of action of the catalytic triad is as same as for trypsin, whereby chymotrypsin possesses an S1 pocket with more hydrophobic cavity. Due to their well investigated structure and mechanism, established assays for characterization of bioactivity, certain homology with therapeutically relevant proteases, and availability, trypsin and chymotrypsin are popularly used as model enzymes in the fundamental research and drug discovery.

Elastase-like proteases (**Figure 5**, right) possess a much smaller S1 pocket and preferably cleave peptide bonds after residues with small, hydrophobic side chains (Ala, Leu, or Val). The natural function of elastase is the breakup of an elastic fiber protein in the connective

tissue (elastin). Elastases are of therapeutic interest since neutrophil elastase is involved in inflammations caused by immunological response. [106]

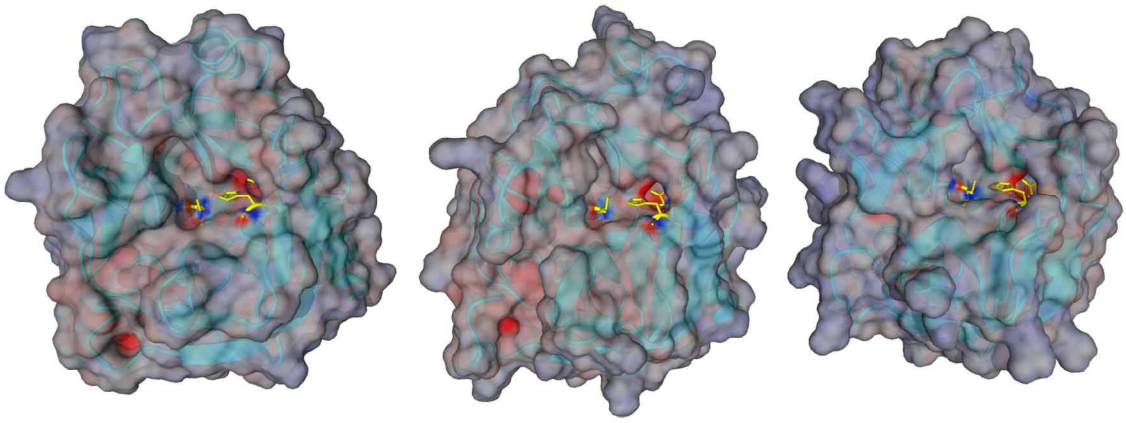

Figure 5. 3D computational models of trypsin (left), chymotrypsin (middle), and elastase (right). Residues of the catalytic triad are depicted in yellow stick model. Models are derived from the respective crystal structures (PDB 4ABJ, 1T7C, 3Q76).

Competitive inhibitors against serine proteases require two important features. First, they must possess similarity with the cleavage site of the substrate peptide to get high affinity to the active site of enzyme. Second, they must imitate the tetrahedral transition state of substrate while binding to the enzyme without subsequent cleavage of the peptide bond.[107] A vast number of natural trypsin inhibitors are found in animals (Kunitz-type inhibitors), plants (squash trypsin inhibitors, Bowman-Birk inhibitors, mustard trypsin inhibitors), and microorganisms (saccharopepsin inhibitor, *Streptomyces* metalloproteinase inhibitor).[108] Some of these inhibitors are oligopeptides of less than 100 amino acids. Due to their unique fold, these inhibitors are often extremely stable and represent interesting models for mechanistic studies.

The control of proteolytic reactions is usually achieved through a balance of protease biosynthesis (expression and zymogen activation), degradation, and its inactivation by the interaction with an inhibitor. If one of these three mechanisms is interrupted or missing, an onset or progression of several diseases can result. The control of aberrant proteolytic activities is challenging for therapeutic research, especially in the case of certain proteases which are overexpressed in cancer cells. On the one hand, a highly specific and affine drug-like agent could directly inhibit the unsolicited reaction and possibly affect tumor growth. On the other hand, the conjugation of a protease-selective inhibitor with a label would enable a development of a diagnostic method for tumor localization.[109]

Recently, trypsin has got into focus of biochemical research once again. Pan et al. demonstrated the application of an engineered trypsin variant as a tool for sequence-specific protein ligation by shifting the equilibrium of the enzyme-catalyzed hydrolysis in direction of its reverse reaction.[110]

1.5.2 Sunflower Trypsin Inhibitor 1

Despite their extremely wide diversity, many plant-derived, peptidic inhibitors possess some pinpoint similarity in structure and sequence making their categorization possible. Bowman-

Birk inhibitors (BBI) comprise one of such plant-derived inhibitor classes. The native Bowman-Birk inhibitor is a 71 amino acid peptide extracted from soybeans and comprising seven intramolecular disulfide bridges.[111] Its natural function is the growth factor regulation in several organisms; its inhibitory effect gets lost by heating or by reducing of more than four disulfide bonds. A vast number of commonly known plants as rice, wheat, beans, and peas are known to synthesize inhibitors of this class.[112] The essential characteristic BBI generally share is the constrained shape of the inhibitory loop hold together by intramolecular hydrogen bonds and a disulfide bond between two Cys residues interposing the inhibitory loop.[113] A Lys or Arg residue at the second position of the inhibitory loop ensures high affinity of Bowman-Birk inhibitors towards trypsin-like proteases.

A distinctive numbering system was introduced for the residues in the inhibitory site of BBIs. The numeration starts from the "fictive cleavage site" (scissile bond) of the enzyme-catalyzed hydrolysis, a Lys (in some species also Arg). Amino acids disposed *N*-terminally to the scissile bond are numbered with plane numbers growing up with the order of connectivity in chain: P1, P2, P3, *etc.*. Amino acids disposed in direction of *C*-terminus are numbered with dashed numbers: P1', P2', P3', *etc.* An example for this numbering is shown in **Table 3**.

Table 3. Amino acid sequence of the inhibitor loop (blue) and surroundings for BBI (SFTI-1) and the characteristic numbering of amino acid positions (lower row). The fictive cleavage site is marked as red line. *cis*-Proline is shown in bold italic.

	Sequence													
BBI	G	R	C	T	K	S	I	***P***	P	I	C	F	P	D
Numbering		P4	P3	P2	P1	P1'	P2'	***P3'***	P4'	P5'				

The smallest inhibitor from this class is the sunflower trypsin inhibitor-1 (SFTI-1) originally extracted from *Helianthus annuus*. It is a bicyclic 14 amino acid peptide comprising a typical seven amino acid inhibitory loop, a disulfide bond connecting the termini of this loop (**Figure 6**, left) and a head-to-tail cyclized backbone.

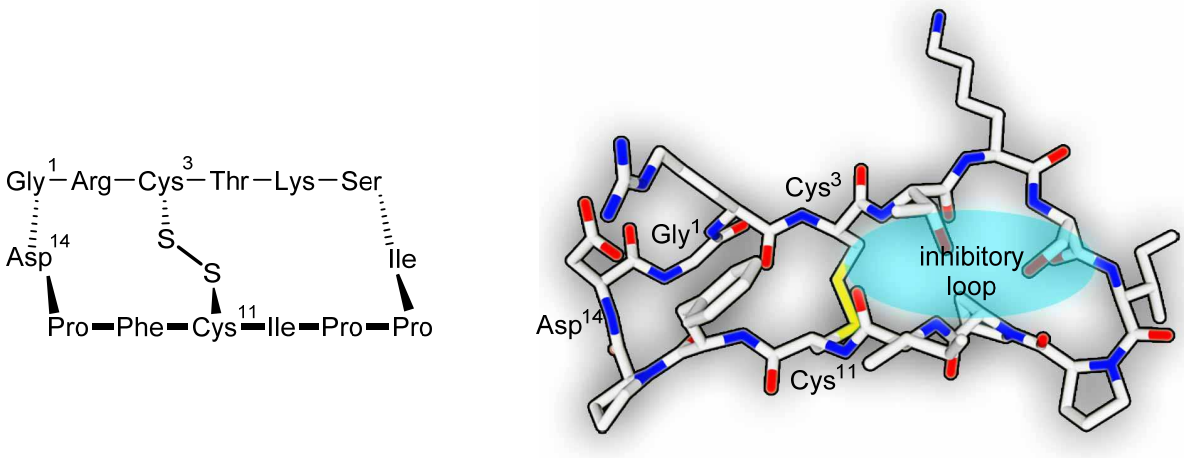

Figure 6. Amino acid sequence and connectivity (left) and 3D computational model (right) of bicyclic SFTI-1 with red = oxygen, blue = nitrogen, yellow = sulfur, white = carbon. Model derived from crystal structure of SFTI-1 in co-complex with trypsin (PDB 1SFI). Figure reprinted from own publication.[50b]

Notwithstanding its simple structure, SFTI-1 exhibits very high affinity towards trypsin with an inhibitory constant K_i at subnanomolar range (K_i = 0.1 nM).[114] The monocyclic derivative lacking backbone cyclization (open-chain SFTI-1 or SFTI-1[1,14]) is not as potent as the wild type, but still has an excellent inhibitor activity against trypsin (K_i = 0.2 nM).[73b]
The three-dimensional structure of both, SFTI-1 (**Figure 6**, right) and its monocyclic permutant, is featured by the characteristic turn induced by the proline at P3'.[115] This Pro residue is known to have a *cis*-configured peptide bond which is very rare (usual *cis/trans* isomer ratio in chemical equilibrium: 1:1000) in polypeptides and gives the inhibitory loop a constrained β-hairpin shape. The preservation of the *cis*-Pro at P3' is sufficient for the inhibitory activity of SFTI-1, as Brauer et al. demonstrated by replacement of Pro-P3' with an Ala leading to the drastic loss of inhibitory activity.[116] Contrary, Daly et al. showed that the conformation of the neighboring Pro-P4' peptide bond must be *trans* to achieve good inhibition. Thus, only the combination *cis*-Pro-P3', *trans*-Pro-P4' gives the characteristic frame of the inhibitory loop and results in high inhibitory potency.[117]
The facts that SFTI-1 comprises, in spite of its small size, several unique architectures and important structural elements, that it is simply available and modifiable *via* SPPS, and that the inhibitory activity can be examined by established assays, make the framework an excellent model scaffold for structural investigation and a template molecule for development of several therapeutics and diagnostics.

1.5.3 Heterodimeric Coiled Coils

Discovered by Crick 1953, the coiled coil is an important structural motif of peptide chains composed by two or more homo- or heteromeric α-helices.[118] In nature, it finds a wide range of applications giving a protein its superstructure or forming supermolecular protein complexes.[119] In the typical coiled-coil motif, two α-helices composed of several copies of series-connected repetitive oligopeptide units, are wrapped around each other, forming a usually left-handed supercoil (**Figure 7**).[120] The stability of this non-covalent binding motif is determined by the length of the α-helices which can vary from very long (more than 100 of repetitive triads), as it is found in collagen, to short (3-4 repetitive heptads), as in the leucine-zipper transcription factors.[121] Coiled-coil hetero- and homooligomers can be arranged in parallel or antiparallel manner depending on the amino acid sequences of the repetitive units and affecting the ultimate shape and stability of the superstructure.[122]

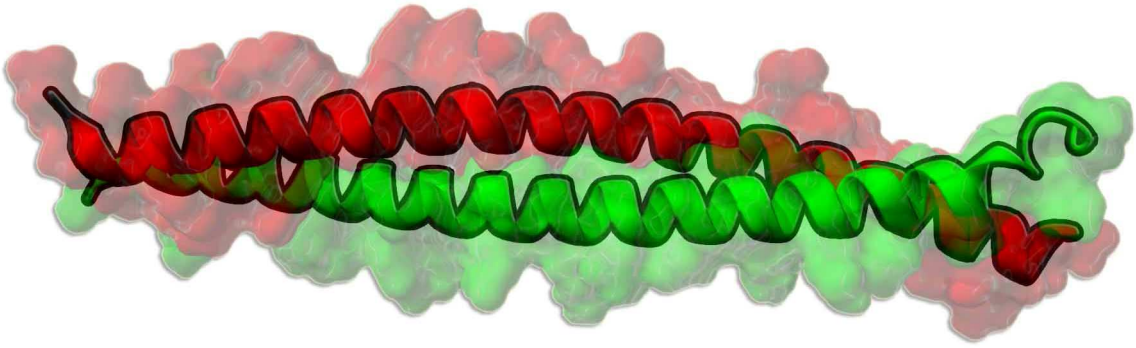

Figure 7. 3D computational model of an exemplary chosen heterodimeric coiled-coil complex shown in cartoon style. Model derived from X-ray crystal structure of Rho-binding domain of Rho-kinase (PDB: 1UXT).

The driving force of the supermolecular arrangement in coiled coils is the combination of hydrophobic and ionic interactions between the amino acid residues of the α-helices.[123] In heptad-based coiled coils, often found in short dimerization domains of proteins, an alternating order of hydrophobic residues (Ala, Leu, Ile, Val) and hydrophilic or charged residues (Ser, Lys or Arg, and Glu or Asp, respectively) are repeated in every eighth position (hence, in every second helical turn).[122] The spatial orientation of the residues of α-helices involved in a heteromeric coiled-coil can be illustrated by a helical wheel shown in **Scheme 11**. The sketch represents the spiral structure of the α-helices from top view, whereby the seven amino acid residues of the repetitive unit in heptad-based coils are positioned on the surface of the spiral in 100° angle steps and numbered with the letters **a**, **b**, **c**, **d**, **e**, **f**, and **g**. Along with the number of the repetitive units, all of the important structural information of consistently repeating heptad coiled-coils are expressed by this simple model. Generally, hydrophobic residues as Leu or Ile are placed on positions **a** and **d** forming a hydrophobic core in a dimer which can be considered as the fundamental interaction holding the helices together.[118] At positions **e**, **f**, and **g**, usually charged residues are located, whereby the residue in position **f** has the opposite charge to the residues in **e** and **g**. In case of heterodimeric coiled coils, the helices have to possess opposite charge to obtain attractive ionic interaction, thus the amino acid at these positions depends on the net charge of coil. Since the amino acid on position **f** is not facing the coiled-coil interaction site, its function is suggested to be the enhancement of water solubility and the reduction of overall charge of the coils. The most typically used ionically interacting amino acid pairs are Glu-Lys or Asp-Lys, respectively. Therefore, they are usually placed on complementary positions of each coil. Furthermore, uncharged amino acids as Ala or Ser on the remaining positions **b** and **c** provide the formation of helical structure as well as stabilization of the coils in aqueous environment.

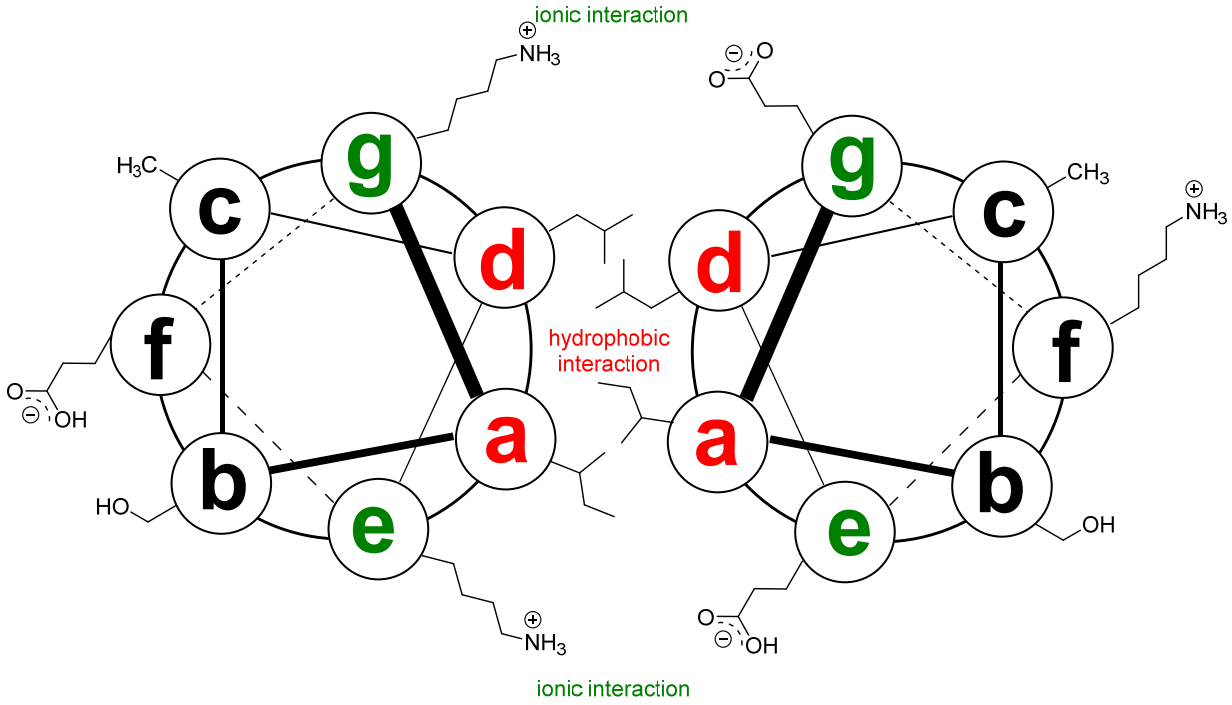

Scheme 11. Helical wheel depiction of two complementary interacting α-helices forming a heterodimeric coiled coil (E/K coil system). Residue positions contributing to hydrophobic interactions are shown in red, positions contributing to ionic interactions are shown in green. Scheme modified from [123].

K coil: *H*-(K-X-S-A-L-K-E)$_n$-*OH*

E coil: *H*-(E-X-S-A-L-E-K)$_n$-*OH*

Position in helix: g a b c d e f

X = V or I

Figure 8. Amino acid sequence of K coil and E coil with corresponding positions of the residues in the helical wheel depiction. The colors of the letters corresponds to those shown in **Scheme 11**.

A well-established model system where these fundamental structural characteristics for heterodimeric coiled coils are represented is the E/K coil system where each coil is named after its first amino acid in its original heptad sequence (**Figure 8**).[120, 122, 124]

This artificial coiled-coil system is marked by high stability, specificity, modifiability towards pinpoint mutations of single amino acids, and the well-studied effects of these amino acid replacements on the structure of a protein. That makes the system appropriate for *de novo* protein design.[124-125] Detailed studies on the influence of the primary structure, the variations in the number of repetitive heptads as well as the nature of residues within the heptad of the E/K coil system on the stability, specificity, and affinity towards the heterodimer were conducted by Litowski et al.[122] It was found that the number of repetitive units required for efficient formation of coiled-coil dimer depends on the strength of interactions in the hydrophobic core. Therefore the replacement of a Val residue by the more hydrophobic Ile resulted in the formation of a three-heptad coiled-coil heterodimer whereas the non-modified sequence needed at least four repetitive heptads. Furthermore, an interesting observation was made that some of the coils with diverse numbers of repetitive heptads tended to form homodimers or oligomers, respectively, instead of the desired heterodimers. As preferred formation of homodimers and heterotetramers was

mainly found in the four-heptad system of the Ile-bearing coils, the typically used E/K coil system is composed of three or five repetitive heptads.
These sequences characterized by Litowski et al. [122] were adapted by several researchers towards the selective conjugation of functional payloads on proteins, thus the coils are acting as recognition site for templated chemical conjugation described in chapter 1.4.3. Since the E/K coils allows the modification of single amino acid residues while retaining their specific affinity towards the complementary coil, several techniques were described for site-selective protein or cell labeling as e.g. coiled-coil guided acyl transfer[126] or the dirhodium metallopeptide-catalyzed Trp modification.[127] A general notation system for modified coiled-coil helices is shown in **Figure 9**. Combined with the sequence of the non-modified heptad, all modified positions and the most important structural information are represented in this notation.

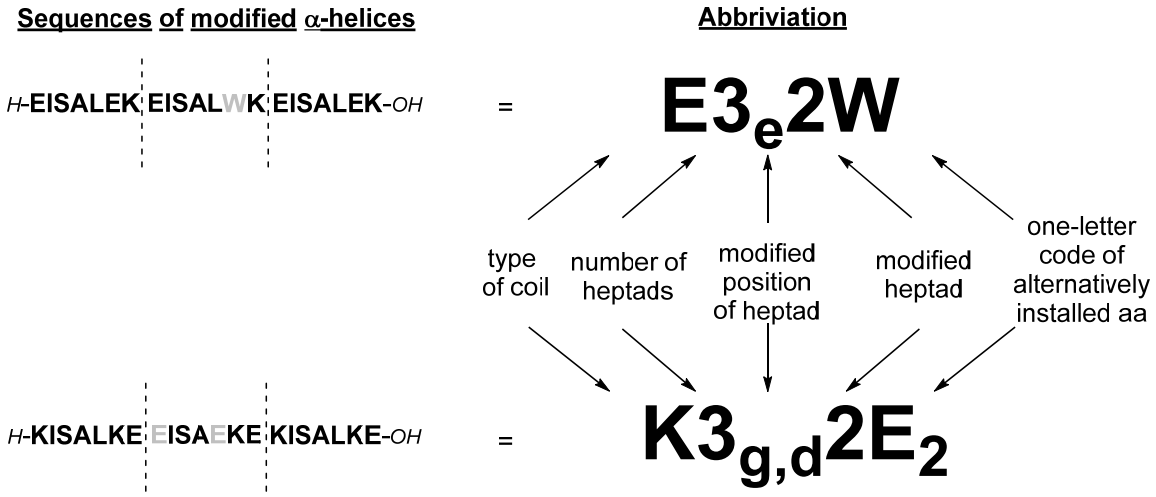

Figure 9. Amino acid sequences of E/K coils with substituted amino acids (left) and associated abbreviations. Sequence taken from modified E/K coil system for Rh_2-metallopeptide-catalyzed Trp modification.[127]

1.5.4 Peptide Nucleic Acids

The double stranded helical structure of DNA is one of the most elegant ways to assemble two or more biomacromolecules without formation of covalent linkages, which makes oligonucleotides not only attractive for storage, retrieve and translation of genetic information, but also for biomolecular engineering.[128] As mentioned in chapter 1.4.3, the non-covalent interactions between complementary oligonucleotides possess highly reliable sequence selectivity and combinatorial diversity, making them appropriate as recognition tags for site-selective conjugation of diverse biomolecules. A major barrier to apply DNA-templated chemistry to proteins is the difference in the nature of the biomolecules. Therefore, very often highly selective and orthogonal reactions that could be applied to peptides cannot be used in presence of oligonucleotides and *vice versa*. Moreover, the high charge density of the nucleic acid backbone can also affect solubility and polarity of the proteins and hamper several conventional techniques for protein analysis.
Peptide nucleic acids (PNAs) are artificial oligo- or polymers combining structural features of oligonucleotides and peptides. They consist of a pseudo-peptide backbone and nucleobase-

bearing side chains (**Figure 10A**) where all of the four purine and pyrimidine bases found in DNA are present (**Figure 10B**).[129] Although several types of PNA monomers with various backbone structures have been to date reported, the most popular one is based on *N*-(2-ethyl)glycine (aeg) forming an achiral periodic chain with alternating peptide/peptoid bonds. Contrary to conventional amino acids, the side chains of a PNA are not connected to the α-carbon, but to the amine nitrogen of glycine *via* a carboxymethylene linker.[130]

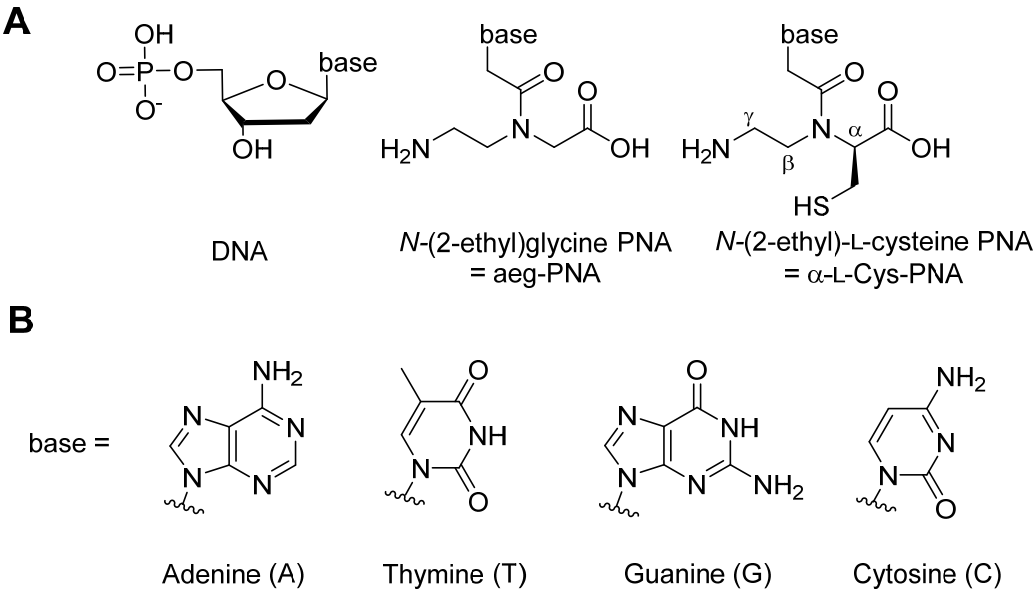

Figure 10. **A**: Backbone monomers of DNA, aeg-PNA, and a further PNA additionally bearing an amino acid side chain, **B**: nucleobases. The positions of the substitution within the amino acid side chain are shown with Greece letters.

PNAs were originally designed by Nielsen et al. in 1991 using computational models combined with chemical "common sense" to be structurally homomorphous to DNA and synthetically accessible.[129, 131] Thus, the resulting oligomers are successful structural mimics of DNA, even with the ability to undergo hybridization *via* Watson-Crick base pairing with complementary oligonucleotides and PNA strands in parallel and antiparallel manner (**Scheme 12**). Due to the lack of the charged deoxyribose phosphate backbone with repulsing electrostatic interaction, PNA-DNA and PNA-PNA duplexes have an improved thermal stability compared to the corresponding DNA-DNA duplex (ΔT_m > 30 °C in a 12-mer PNA-DNA duplex compared to the corresponding double-stranded DNA at low salt concentration).[132] Additionally, the relative rigidity of the pseudo-peptide backbone improves the sequence selectivity making PNAs convenient molecules for selective binding to DNAs whereas only a small number of residues are required for the recognition of the complementary sequence (typically 5-10 residues). Their affinity to the complementary sequence is so strong that PNAs possess the ability to invade double-stranded DNAs forming a PNA-DNA-DNA triplex.[133]

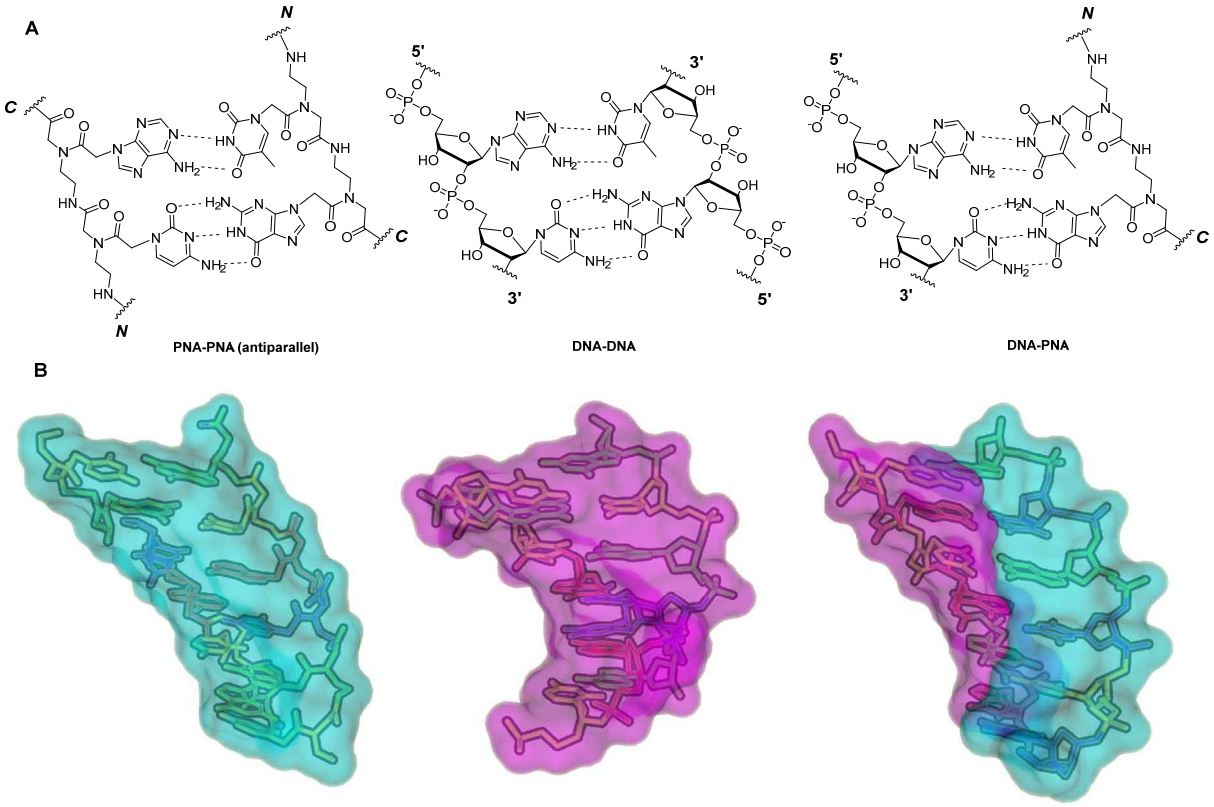

Scheme 12. **A**: Hybridization pattern of complementary PNA-PNA, DNA-DNA, and PNA-DNA *via* Watson-Crick base pairing. Hydrogen bonds within the nucleobase pairs are depicted as dashed bonds. **B**: 3D computational models of complementary PNA-PNA, DNA-DNA, and DNA-PNA heptamers. Atoms are shown as sticks and the surfaces of the strands are shown in magenta for DNA, and cyan for PNA. Models were derived from the NMR solution structures (PDB: 1PUP, 2L8Q, 3PA0).

Further beneficial features of PNAs are the resistance against proteases and nucleases, the low affinity to proteins, and the facilitated introduction of various modifications. The solid-phase synthesis of PNA oligomers is well established and relies on both Boc- and Fmoc-SPPS. Protected PNA monomers for SPPS are commercially available with an acid-labile benzhydryloxycarbonyl (Bhoc) protecting group for the orthogonal protection of the nucleobases (despite of T which needs no protection).[134] The standard procedure of Fmoc solid-phase PNA assembly is as same as for conventional peptides, but as PNAs are sensitive against elevated temperatures and also known to undergo backbiting reaction under strong basic condition, microwave-assisted SPPS should not be used. Nevertheless, an iterative synthesis of PNA-peptide fusions is possible without changing the strategy.

PNAs were mainly applied for the recognition of specific sequences in DNA duplexes. It was aimed to mimic an oligonucleotide binding to double-stranded DNA *via* Hoogsteen base pairing in the major groove.[128] The fast hybridization rate of PNAs to complementary sequences made labeled PNAs interesting as probe for diverse RNA and DNA analysis, e.g. southern or northern blotting.[128, 135] Besides target-specific labeling, PNAs are involved in assembly and immobilization of various molecules, as e.g. PNA-templated assembly of heterogeneous nanoclusters,[136] PNA-mediated immobilization of supercoiled DNAs,[137] PNA-based mimetic system of transmembrane proteins towards membrane fusion,[138] and *vice versa*, the DNA-templated fragment ligation of PNAs.[102]

Their antisense action is a further interesting feature of PNAs since they can bind to complementary mRNAs with high affinity and specificity resulting in inhibition of the

translational process. That was shown in several *in vitro* antisense experiments.[128] Unfortunately, the *in vivo* application of PNA antisense agents was hampered for quite long time as the cellular uptake of PNAs was impended by inefficient membrane penetration. The effective knock-out of a growth factor-regulating enzyme in living cells resulting in the total inhibition of cell growth was reported by Anubrata et al. They used a PNA-cell-penetrating peptide conjugate to deliver the antibacterially acting PNAs through the outer bacterial membrane.[139]

In the presented work, PNA sequences are outlined in small lettered initial of the nucleobases to distinguish them from DNA and amino acid sequences depicted in capitals. Left-hand side of the sequence corresponds to the *N*-terminus and right-hand side to the *C*-terminus of PNA oligomers.

2 Outline and Scope of Projects

2.1 Protease Inhibitor with Triazolyl Backbone Mimic

A vast number of natural enzyme inhibitors are derived from small proteins or peptides as BPP_{5a} (chapter 1.2.2) or SFTI (chapter 1.5.2) discussed above. These competitive inhibitors possess high affinity to the active site of the enzymes, which is typical for high-affine substrates. Thus, a question arises - why do these peptidic molecules act as inhibitors? Like other enzymatic processes, the catalytic proteolysis mediated by serine proteases resides at equilibrium between substrate hydrolysis and condensation. More particularly, the protease-catalyzed substrate conversion can be sketched in three equilibrium reactions: association/dissociation of substrate to enzyme, hydrolysis of substrate/re-condensation of products, and dissociation/re-association of products (**Scheme 13A**). Since a fast association is a prerequisite for both, the difference between a substrate and a peptidic inhibitor is stipulated by the position of the equilibrium in the subsequent reaction steps. In general, if the reaction rate of product dissociation is higher than the reaction rate of catalytic re-condensation, the equilibrium is on the side of hydrolysis, and thus the compound is a substrate. On the other hand, if the reaction rate of product dissociation is low, the compound remains in the active site and becomes an inhibitor (**Scheme 13B**).

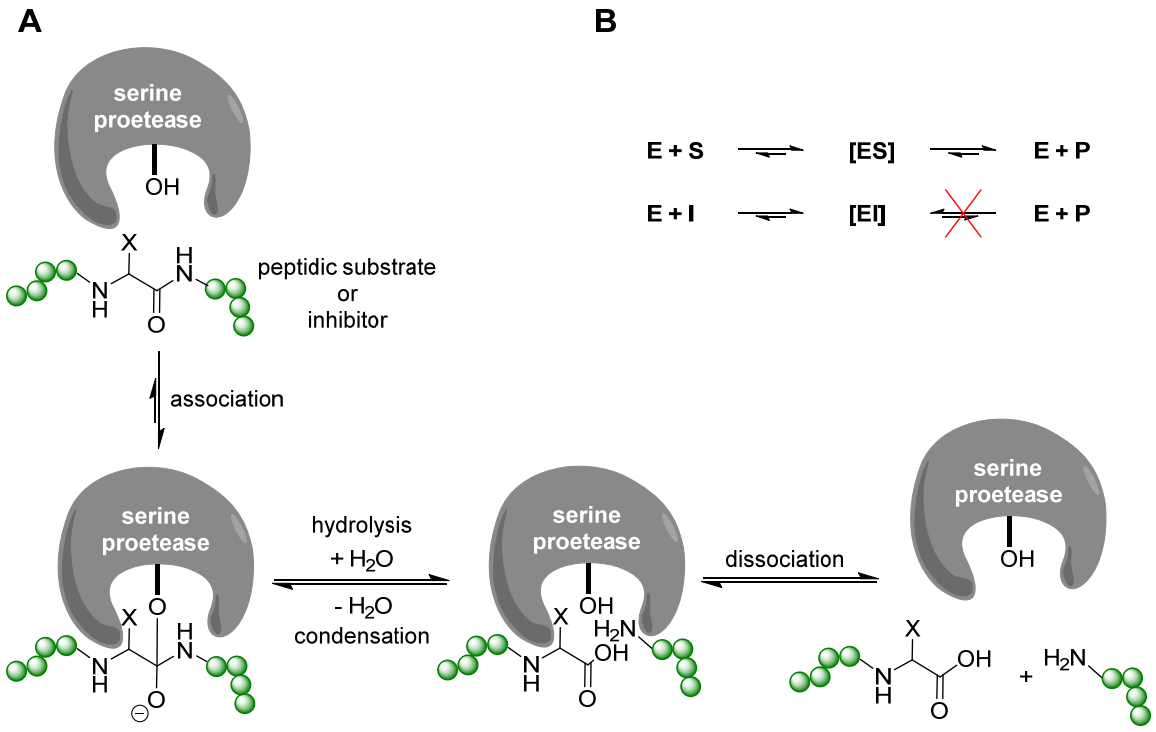

Scheme 13. A: Sketch of the reaction cascade upon proteolytic cleavage of peptidic substrates/inhibitors depicted as a series of equilibrium reactions. Peptide chain shown as green balls. **B**: Simplified chemical equation of an enzyme-mediated substrate conversion and competitive inhibition as equilibrium reaction. E = enzyme, S = substrate, I = inhibitor, P = product.

An important aspect in this simplified model is that the enzyme-bound inhibitor is permanently in an equilibrium of hydrolysis and condensation, whereby a non-negligible

probability of dissociation and release of the active site remains. As this model shows, the overall inhibition potency of a competitive inhibitor is not only affected by the association rate, but also strongly dependent on the direction of the catalytic equilibrium reaction, thus the susceptibility of the scissile bond against proteolytic cleavage became also an essential issue in the design of peptide-based inhibitors.

The inhibitory action of SFTI-1 against trypsin is given by its rigid, constrained framework hold together by intramolecular hydrogen bonds and the bicyclic architecture disabling the drifting apart of the split ex-peptide bond moieties and finally leading to an enhanced re-condensation rate. Nonetheless, Marx et al. reported 2003 that even the scissile bond in P1-P1' position of monocyclic SFTI-1 goes with a certain share through a proteolytic cleavage by trypsin, hence there is still scope for enhancement of inhibitory activity.[140]

In a previous publication, we have successfully demonstrated the introduction of 1,4- and 1,5-disubstituted 1,2,3-triazoles into the backbone of a modified open-chain permutant of SFTI-1.[14a] The triazolyl groups were found viable amide bond surrogates with locked *cis* or *trans* conformations, respectively, while only slightly affecting the bioactivity (2-10 times less active compared to parental inhibitors). In particular, the inhibitory potency of the 1,4-disubstituted triazolyl moiety mimicking an Ala residue with *trans* conformation at P4' position (**Figure 11**) was non-inferior to the parental [Ala^{9}]SFTI-1[1,14]. This fact demonstrated the usefulness of 1,4-disubstituted 1,2,3-triazole as an isosteric surrogate of *trans* amide bonds as Sharpless and Kolb have already predicted 2003.[30, 141] Its resistance to proteolytic cleavage made triazolyl backbone surrogates highly attractive for the design of proteolysis-stable inhibitors in current work.

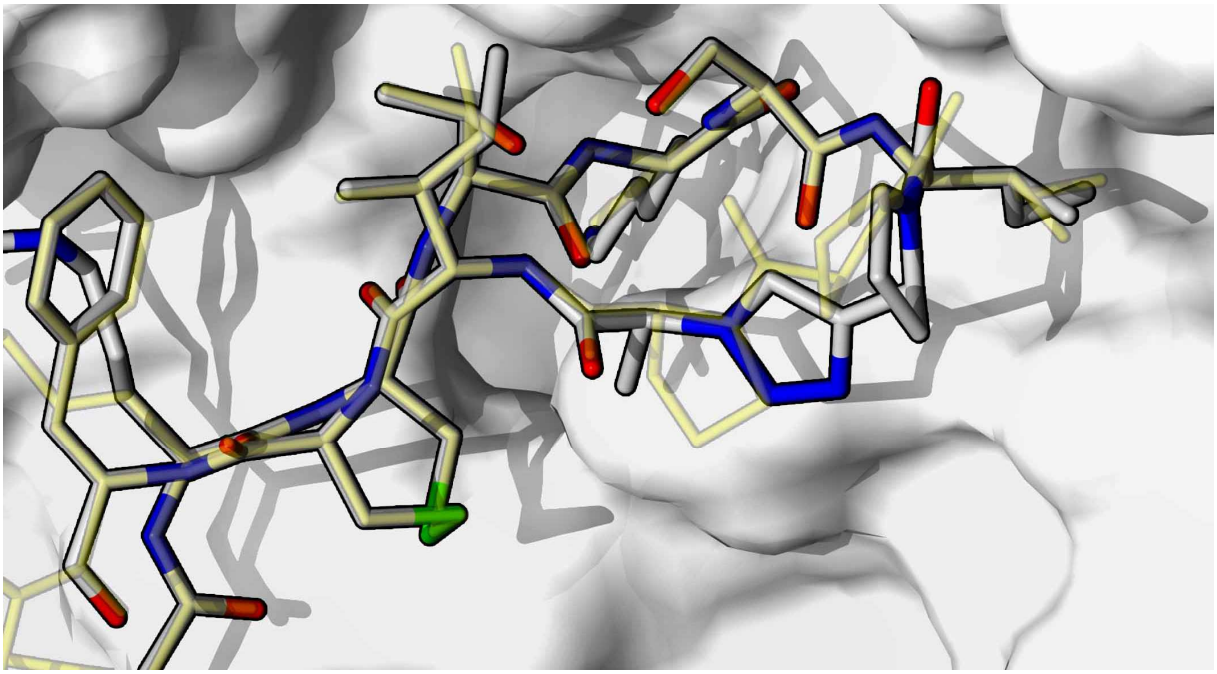

Figure 11. Structural comparison of the inhibitor loops of SFTI-1 (depicted as yellow, half-transparent sticks) and triazole-bearing peptidomimetic inhibitor $\Psi^{8,9}$ 1,4-[1,2,3]triazolyl-SFTI-1[1,14] (depicted as sticks with grey: carbon, blue: nitrogen, red: oxygen, green: sulfur) in complex with bovine pancreas trypsin. 3D computational structures modeled from corresponding X-ray crystal structures (PDB: 1SFI, 4ABI) by energy minimization and aligned at Lys5 of inhibitors.

Furthermore, Fittler and Empting reported in two consecutive publications the rational design of a potent peptidic inhibitor against matriptase, a therapeutically relevant protease, using

SFTI-1 as a starting point for molecular design.[142] Matriptase is a trypsin-like serine protease with same cleavage selectivity as trypsin (cleavage after basic amino acids at the P1 positions). Since it is overexpressed in certain type of cancer cells, a selective labeling by the peptidic inhibitor was of high therapeutic interest.

Unfortunately, the option to use matriptase or other trypsin-like serine proteases as target enzyme in the presented work was abandoned by the inconvenience in the synthetic strategy. The triazole group formed by CuAAC requires a Weinreb amide corresponding to the amino acid of the P1 position. As the synthesis of Weinreb amides of basic amino acids needs a complicated protection strategy and, furthermore, the successive reactions for generation of the alkyne moiety were also not compatible (see chapter 3.1.1), we decided to design the peptidomimetic inhibitor towards targeting a serine protease with a scissile bond selectivity after hydrophobic amino acids at P1 position. Two appropriate enzymes which came into question were chymotrypsin (selective cleavage after large, aromatic residues) and human neutrophil elastase (HNE, selective cleavage after small hydrophobic residues). As shown in **Figure 5** in chapter 1.5.1 both enzymes share remarkable structural and mechanistical similarities with trypsin despite its selectivity given by the size, shape, and associated residues of the S1 pocket (**Figure 12**).

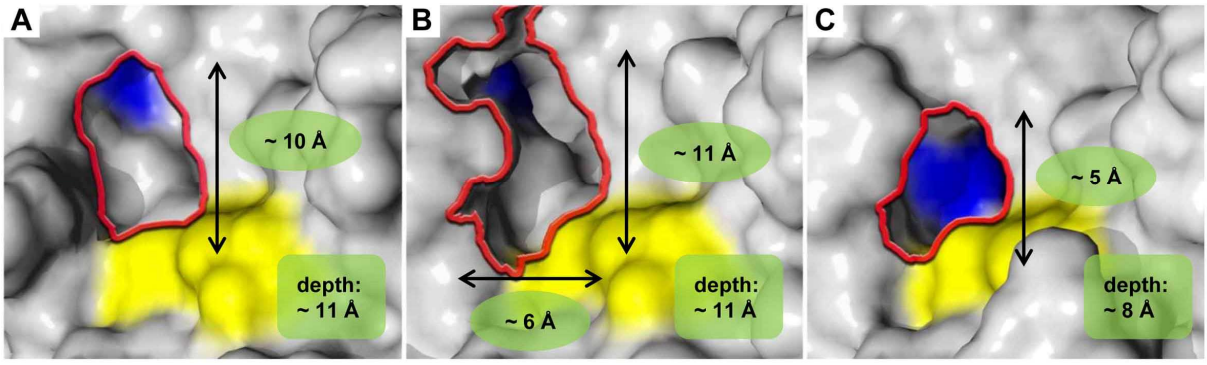

Figure 12. Structural comparison of the active sites of **A**: trypsin, **B**: chymotrypsin, and **C**: HNE. 3D computational models derived from the crystal structures of corresponding enzymes (PDB: 1SFI, 1T7C, 2Y7F). Shape of S1 pockets outlined with red lines. Molecular surfaces of the residues forming the catalytic triad are shown in yellow. Molecular surfaces of the residue inside of the S1 pocket contributing to selective substrate binding (**A**: Asp189, **B**: Val188, **C**: Val160) are shown in blue. Size and depth of the S1 pockets determined from the mean distances between corresponding atoms forming the S1 pocket.

An alignment of the X-ray crystal structure of bovine trypsin (PDB: 1SFT) and bovine chymotrypsin (PDB: 1T7C) resulted in a Root Mean Square Deviation (RMSD) value of 0.871 Å and a sequence identity of 48.7 %. Same *in silico* analysis for HNE resulted in a similarly good RMSD value of 0.997 Å and 33.7 % sequence identity emphasizing the good structural compliance of the two alternatively chosen proteases with trypsin. Furthermore, both enzymes are commercially available and (especially HNE) gathered attention as potential therapeutic target as it is involved in inflammatory response of immunological diseases and allergic symptoms as hyperresponsiveness of the airways.[143] The inhibition of catalytic activity of these enzymes by Bowman-Birk type inhibitors is already proven in several reports,[144] thus chymotrypsin and HNE are suitable model enzymes for the examination of the desired design of proteolysis-resistant BBI derivatives.

2.1.1 Aims

The ultimate goal of this subproject was the design and synthesis of a proteolytically resistant peptidomimetic inhibitor of a therapeutically relevant serine protease HNE based on the scaffold of BBIs. Bioactivity of the novel inhibitor must be evaluated using enzymatic assays.
Peptidic and peptidomimetic inhibitors **1**-**4** depicted in **Figure 13** should be chemically synthesized using monocyclic SFTI-1 as a lead structure. Design of the compounds **1**-**4** will be discussed in chapter 3.1, and their synthesis and bioactivity – in chapters 3.1.1., 3.1.2, respectively.

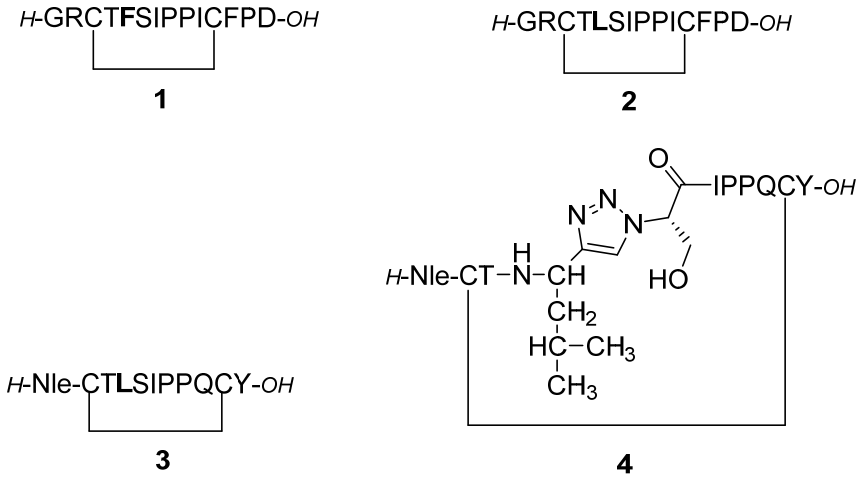

Figure 13. Chemical structures of synthesized SFTI derivatives/BBI analogs.

2.2 PHIP-Active Functional Peptides

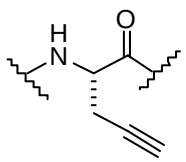

Figure 14. L-Propargylglycyl building block installed in a peptide chain.

This subproject was conducted in cooperation with the working group of Prof. Buntkowsky at the TU-Darmstadt. As described in chapter 1.3.3, the development of a viable PHIP label providing the signal enhancement upon NMR investigations of bioactive peptides and proteins was highly desired. To this end, propargylglycine (Pra, **Figure 14**) bearing a PHIP-active multiple bond was found an appropriate residue that can be installed at the arbitrary positions of a peptide chain on solid support. In our preliminary experiments, the *N*-terminally Fmoc-protected Pra exhibited strong signal amplification with an enhancement factor of more than 200.
In a previous publication,[145] we have reported a systematic study on PHIP NMR experiments using a series of tripeptides comprising an Xaa-Pra-Xaa motif (Xaa = canonical amino acid) and two cyclic decapeptides bearing four Pra residues each (chapter 1.4.2).[146] As seen from **Table 4**, the intensity of the amplified signals was influenced by the nature of the adjacent amino acids: Indeed, signal amplification varied from an SE of 26 observed for the tripeptide Tyr-Pra-Tyr to complete lack of PHIP signals for the sulfur-containing tripeptides *H*-Cys-Pra-

Cys-*OH* and *H*-Cys(Me)-Pra-Cys(Me)-*OH*. Interestingly, *H*-Met-Pra-Met-*OH* and the tetra-Pra cysteinyl decapeptide exhibited an adequate enhancement factor of 14 and 5, respectively.

Table 4. Sequences and simplified structures of the investigated PHIP-labeled peptides and their observed signal enhancement factors. Table reprinted from own publication. [145]

Sequence/Structure[a]	Signal Enhancement
Fmoc-Pra-*OH*	206
Fmoc-AllylGly-*OH*	*n.h.*
H-Gly-Pra-Gly-NH_2	8
H-Ala-Pra-Ala-NH_2	15
H-Phe-Pra-Phe-NH_2	2
H-Tyr-Pra-Tyr-NH_2	26
H-Lys-Pra-Lys-NH_2	12
H-Asp-Pra-Asp-NH_2	2
H-Ser-Pra-Ser-NH_2	10
H-Cys-Pra-Cys-NH_2	*n.h.*
H-Cys(Me)-Pra-Cys(Me)-NH_2	*n.h.*
H-Met-Pra-Met-NH_2	14
Gly-Pro-Pra-Cys-Pra-Gly-Pro-Pra-Ala-Pra	5
Gly-Pro-Pra-Lys-Pra-Gly-Pro-Pra-Ala-Pra	38

n.h.: No hydrogenation observed.

Since the PHIP procedure is based on the polarization transfer during catalytic hydrogenation, the resulting signal amplification is supposed to be mainly dependent on the efficacy of respective chemical reaction. Indeed, no signal amplification was observed for Cys- and (Me)Cys-bearing tripeptides as, according to the lack of expected chemical shifts corresponding to the desired product in the ^{1}H-NMR spectra, no catalytic hydrogenation took place.

Furthermore, Trantzschel et al reported that the PHIP-mediated signal enhancement of non-protected Pra was recorded only at pH ≈ 2.7.[147] Considering that Pra takes a zwitterionic form at neutral pH, this result might be explained by the strong donor character of the functional groups, especially of the free amines that compete for the coordination site of the transition metal catalyst, conclusively leading to its poisoning and inhibition of the hydrogenation. This suggests that the effective labeling of peptides and proteins is only feasible in absence of strong electron-donors (sulfhydryls or amines) in spatial proximity to the multiple bond, thus narrowing the scope of labeling targets.

2.2.1 Aims

The aim of this part is the introduction of PHIP-active moieties in a functional peptide while preserving the PHIP-mediated signal amplification of the label, on one hand, and bioactivity of the parental peptide, on the other hand. As the application of Pra as a PHIP label for functional peptides was strongly impeded as outlined above, we addresses this issue applying two complementary strategies. First, the strong electron-donor groups, supposed to mediate poisoning, should be substituted by suitable surrogates or disposed. Second, alternative SPPS-compatible PHIP building blocks with distinct structural and functional features (**Figure 15**) should be considered.

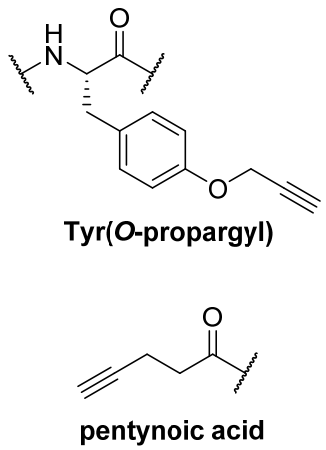

Figure 15. Chemical structures of alternative PHIP labels, L-*O*-propargyl-tyrosine and Pentynoic acid as building blocks installed in a peptidic chain.

As a model bioactive peptide, the monocyclic variant of sunflower trypsin inhibitor SFTI-1 was chosen (chapter 1.5.2 and 2.1). Thus, this subproject was divided into two parts: design and synthesis of SFTI-derived peptides and peptidomimetics bearing PHIP-active elements and the evaluation of their bioactivity and parahydrogen-mediated NMR signal enhancement.

2.3 Affinity-Guided Chemical Ligation towards Multifunctionalization of Biomolecular Scaffolds

This subproject was conducted in cooperation with the working group of Prof. Diederichsen at the University of Göttingen.

Despite the promising bioactivity, a vast number of potent therapeutics remained petty and failed to reach preclinical studies due to the lack of drug-like properties (chapter 1.4.2). However, the pharmacokinetic properties of small molecules can be easily improved upon their conjugation with certain macromolecules. To this end, development of antibody-drug conjugates (ADCs) is of particular interest as the *in vivo* half-life of small-molecular counterparts can be extended from few minutes to several days or even weeks upon covalent anchoring with IgG-based scaffolds.[92] In conventional ADCs, the target-specific binding is provided by the inherent paratope of the parental mAb located at the antigen-binding fragment (Fab). Upon engineering of an ADC aimed on delivery of a drug payload to an alternative target, an elaborated screening is inevitable. To avoid this procedure, we suggested to replace the complete Fab of the parental mAb by a small-molecular binding motif that, being used solitarily, possesses restricted drug-like properties. That means, only the Fc part of the mAb should be used as multifunctionalization and drug-delivery scaffold.

This approach allows to develop ADCs comprising synthetic small-molecule ligands, oligopeptides (especially those which are hardly recombinantly expressible), and non-peptidic biomolecules (i.a. DNA aptamers or oligosaccharides).

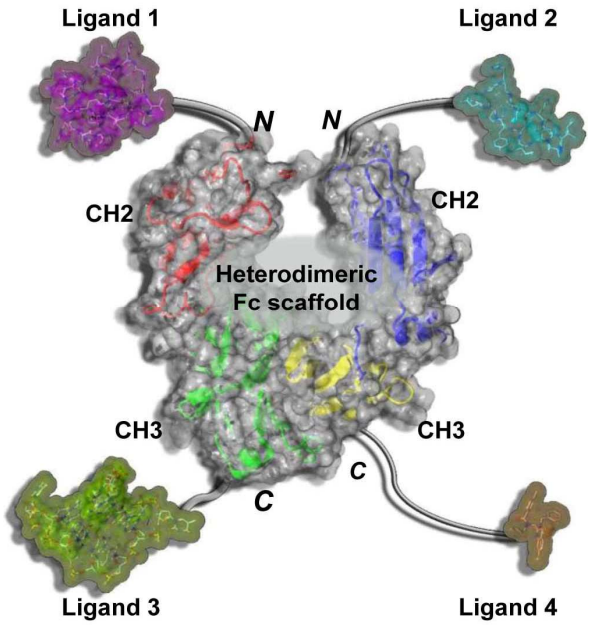

Figure 16. Schematic depiction of a contrived drug-delivery system based on a heterodimeric Fc scaffold with four diverse ligands (or payloads). 3D computational model of Fc derived from X-ray crystallographic structure (PDB: 3AVE). Ligands were exemplary chosen without special meaning: ligand 1 (purple): knottin MCoTI-II (PDB: 4GUX), ligand 2 (cyan): $\Psi^{8,9}$ 1,4-[1,2,3]triazolyl-SFTI-1[1,14] (PDB: 4ABI), ligand 3 (yellow): DNA aptamer (PDB: 4DII), ligand 4 (orange): cytotoxin ispinesib (PDB: 4A5Y). Linker unit depicted as grey tubes.

Considering the assembly of a multifunctionalized and multivalent drug-delivery system, a set of orthogonal ligations, enabling the selective attachment of various ligands, is a prerequisite. For instance, synthesis of a tetrafunctionalized, heterodimeric Fc conjugate (**Figure 16)** requires four orthogonal biocompatible chemical transformations, which is rather sophisticated, especially from the view of the molecular complexity of the reaction partners. Thus, an alternative strategy is required where site-selectivity is not compromised by the reliability of sequential couplings. *In brevi*, it is desirable to ensure orthogonality and efficacy upon simultaneous conjugation of different ligands on the desired macromolecular scaffold within a single reaction step.

On this account, we decided to apply templated bioorthogonal chemistry where the selectivity control is determined by the pre-orientation of the reactive functionalities provided upon association of biomolecular subunits.

In this approach referred to as affinity-guided ligation (**Scheme 14**), the reactive moieties for a chemoselective coupling are brought in spatial proximity *via* non-covalently interacting complementary guiding unit pairs. Only upon pre-orientation, the triggered bioorthogonal ligation is manually started by exposure to e.g. further reactants, catalysts, electromagnetic irradiation, by varying pH, or by applying other factors. Consequently, the reaction is controlled by regioselectivity rather than chemoselectivity, and the application of orthogonal guiding unit pairs would enable a one-pot ligation of multiple ligands and payloads. The installation of a selective cleavage site between guiding unit pairs and the respective ligand or scaffold would enable the separation of counterparts as soon as the covalent linkage has been formed.

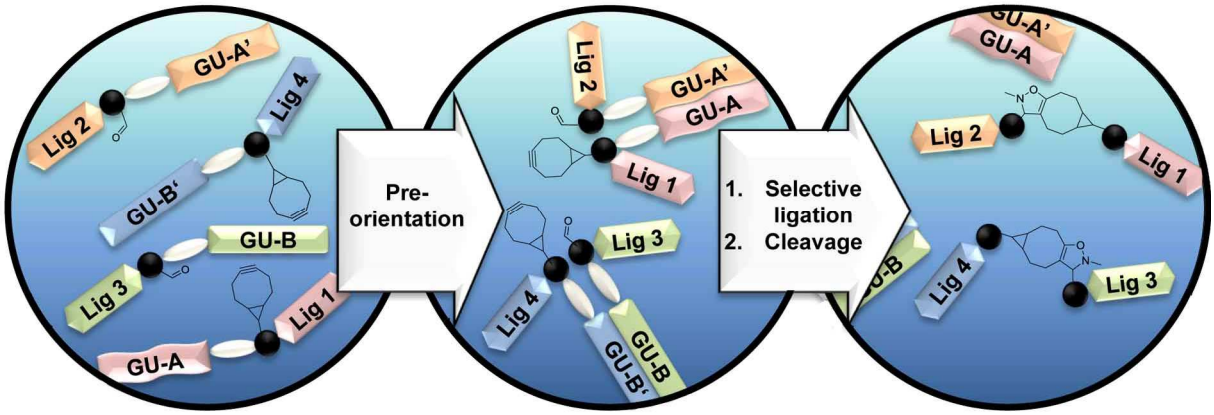

Scheme 14. The concept of the affinity-guided ligation with two complementary guiding unit pairs. The SPANC-reactive moieties are exemplarily depicted. Different colors illustrate diversity of the ligands and the guiding units. GU: guiding unit. Lig: functional ligand; white ellipsis: selective cleavage site; black balls: linker units.

2.3.1 Aims

The ultimate goal of this part is the development of a multifunctionalized drug-delivery system using an antibody Fc scaffold as a platform for modular construction of custom-made drug-ligand conjugates *via* affinity-guided ligation (**Scheme 15**).

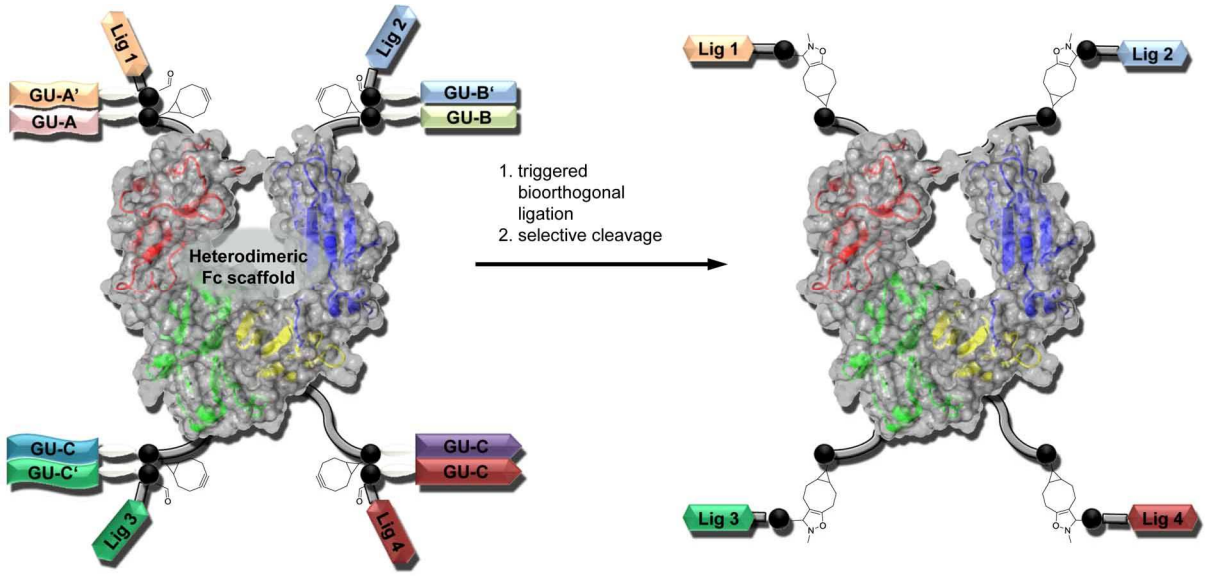

Scheme 15. Attachment of four different ligands to a heterodimeric Fc scaffold *via* affinity-guided ligation. The SPANC-reactive moieties are exemplarily depicted. Different colors illustrate diversity of the ligands and the guiding units. GU: guiding unit. Lig: functional ligand; white ellipsis: selective cleavage site; black balls: linker units.

Since this goal requires thorough interdisciplinary investigations, the experiments were mainly focused on two sub-projects, the establishment of the affinity-guided ligation technique and the attachment of a biomolecular guiding unit to a biocompatible scaffold. Affinity-guided ligation was studied using a model system which comprised a complementary

guiding unit pair equipped with the reactive moieties for a switchable, bioorthogonal ligation. We reduced the complexity of the model system to select an appropriate guiding unit pair and the suitable ligation technique in view of synthetic efficiency and feasibility. Considering the ultimate goal of the project, the prerequisites for the guiding units comprised: high site- or sequence-selectivity, good affinity, combinatorial diversity, and smart installation into the scaffold. Moreover, the guiding unit must possess a peptidic or peptide-like structure to keep the molecular properties and synthetic setup uniform.

Two candidate systems sharing the mentioned features were examined: heterodimeric coiled coils and complementary PNAs. Both non-covalently interacting architectures have intrinsic advantages and disadvantages (**Table 5**). Thus, PNAs provide combinatorial diversity originating from the high sequence-selectivity, and can be preferred for the simultaneous multiple ligations, whereas the coiled-coil system is cost-efficient and can be recombinantly expressed as fusion protein with the Fc scaffold.

Table 5. Selected characteristics of non-covalently interacting coiled-coil heteromers and complementary PNAs.

Features	Coiled-coil heteromers	Complementary PNAs
Dissociation equilibrium constant K_D	9×10^{-6} M[a]	4.4×10^{-9} M[b]
Sequence-specificity	low: pinpoint derivatization allowed	high: recognition of single-base mismatches
Oligomerization pattern	Homo/heterodimers or higher oligomers	Heterodimers only
Required size of monomers	3-5 repetitive heptads = 21-35 residues ≙ ~ 2000 – 5000 Da	5-10 residues ≙ ~ 1500 – 3000 Da
Synthesis	SPPS or recombinant expression	SPPS
Costs for SPPS	low	high

a: Value determined for three-heptad E/K coil system with sequence XISALXY at pH 7.[122]
b: Value determined for a fully-complementary PNA-PNA hybrid (12 residues) at pH 7.[135]

To be suitable for the present study, the chosen ligations require bioorthogonality, switchable reactivity, and high efficacy. The application of metal catalysts which can interfere with involved biomacromolecules or impede the purification of the resulted conjugate, must be avoided. Therefore, metal-catalyzed “click” reactions were excluded from the outset. Preliminary experiments with Rh_2-metallopeptide-catalyzed Trp modification of a coiled coil[127] and site-selective conjugation of polymeric diazonium salts to Tyr residue[148] (data not shown) demonstrated the limited operability in our model systems.

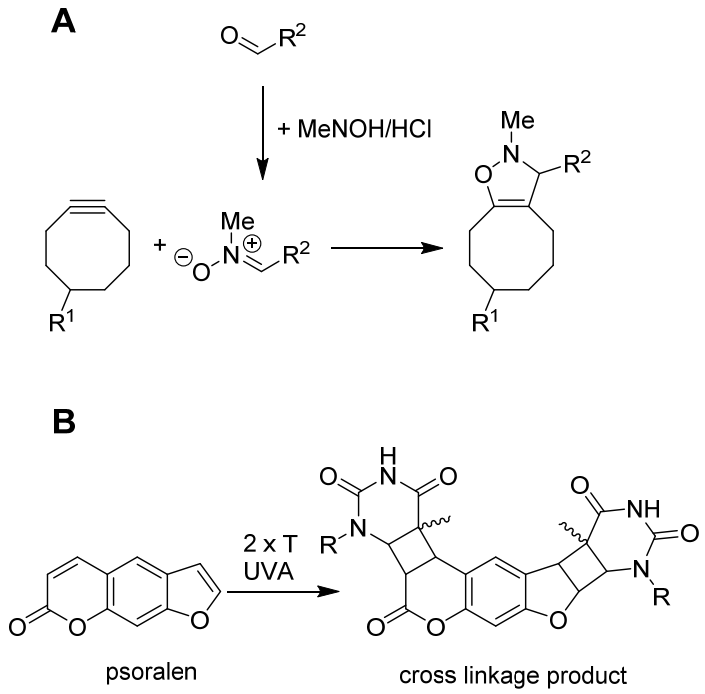

Scheme 16. **A**: SPANC mediated by the *in situ* generated nitrone. **B**: UVA-mediated addition of psoralen to two thymine bases.

Therefore, we decide to use the strain-promoted alkyne-nitrone cycloaddition (SPANC). SPANC is a [2+3] 1,3-dipolar cycloaddition where one of the reagents, the nitrone moiety, is *in situ* generated from an aldehyde. Thus, the reaction is triggered by addition of an *N*-substituted hydroxylamine (**Scheme 16A**). As an alternative conjugation method for PNA-mediated ligations, nucleobase cross-conjugation using a psoralen derivative (**Scheme 16B**) should be examined as well.

The multifunctionalization of an Fc scaffold is the second part of the project. To this end, the conjugation of a guiding unit should be examined in an enzyme-catalyzed ligation, and the applicability of the resulting conjugate as a biocompatible delivery module will be evaluated by the loading of functional ligands with subsequent bioassays. The concept of this study, utilizing a PNA-guided self-assembly with a therapeutically relevant DNA aptamer, is depicted in **Scheme 17A**.

Ideally, a cytotoxic payload should be attached to the construct *via* a cleavable linker allowing the release of the agent after internalization of the conjugate (**Scheme 17B**). The main tasks in the presented work were the design and synthesis of the PNA guiding units and their conjugation to the Fc scaffold. Further modification of the scaffold and the evaluation of the bioactivity of the system was the subject of the research of a cooperator and won't be discussed in detail.

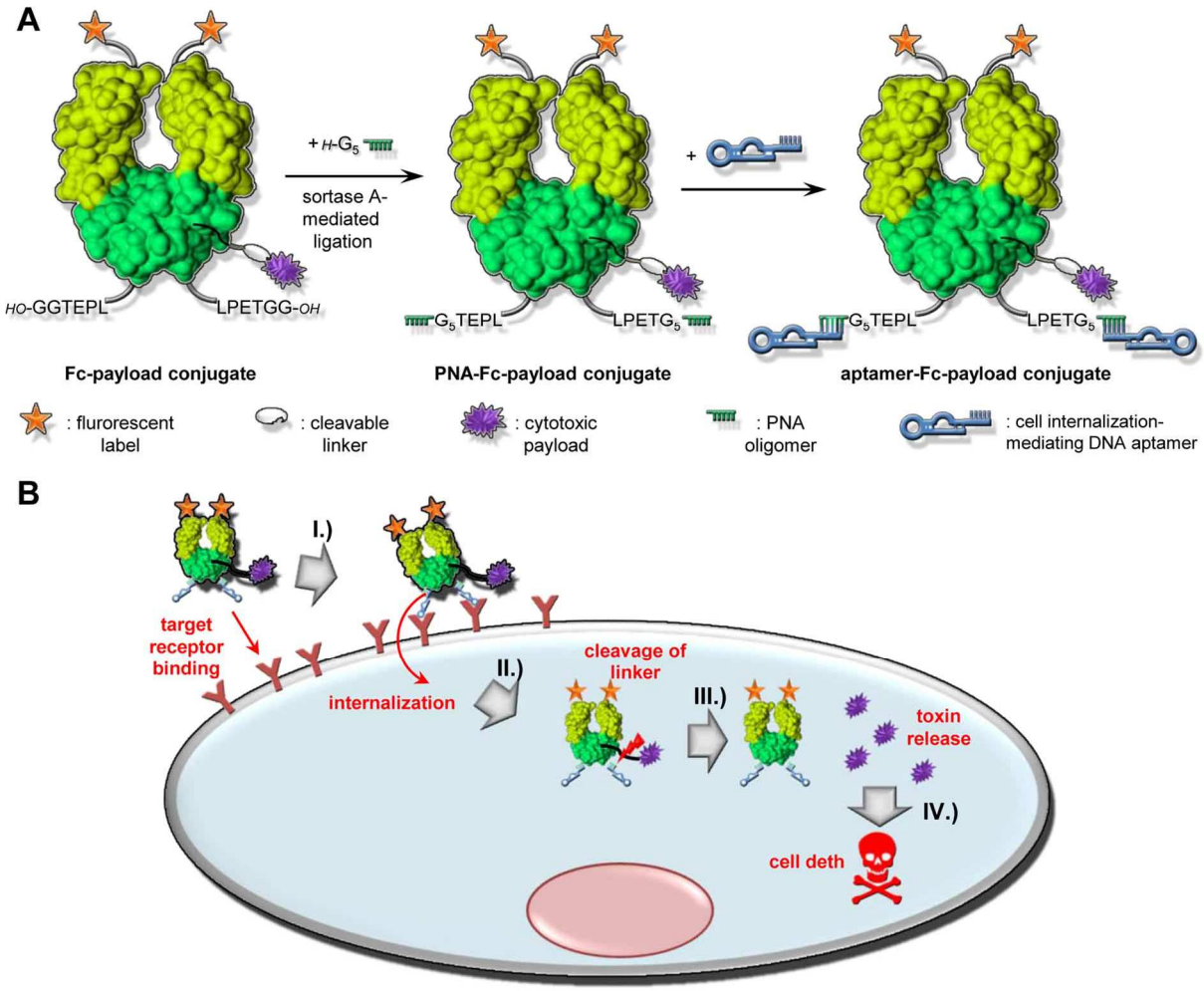

Scheme 17. A: Synthesis of the aptamer-Fc-payload conjugate equipped with further cargos *via* PNA-mediated self-assembly. **B**: Mechanism of action of the targeted aptamer-Fc-payload conjugate (structure simplified) in living cells: I.) Selective binding to target receptor; II.) Cell internalization by endocytosis; III.) Cleavage of the linker unit between toxic payload and scaffold; IV) Release of toxin in lysosome and consequential death of target cells.

3 Results and Discussion

3.1 Protease Inhibitor with Triazolyl Backbone Mimic

3.1.1 Design and Synthesis

To generate a proteolysis-resistant, peptidomimetic HNE inhibitor comprising a triazolyl backbone mimic and based on the scaffold of BBIs, the sequence and structure of the parental peptidic inhibitor had to be chosen. Therefore, a structural comparison of the electrostatic potentials of the substrate-binding sites of trypsin, chymotrypsin and HNE was performed in presence of SFTI using 3D computational modeling and simulation by YASARA software. The intention of this *in silico* study was to evaluate if the rigid scaffold of SFTI could be applied to the proteases of interest in view of electrostatic interactions impending the formation of a stable inhibitor-protease complex. First, the structures of chymotrypsin and HNE were aligned to the co-complex structure of trypsin with SFTI-1 using AMBER 03 force field. After swapping the residue within the inhibitor determining the selectivity of proteolysis (Lys5Phe for chymotrypsin and Lys5Leu for HNE, respectively), suspension of the backbone cyclization, and energy minimization of the associated inhibitor-protein complexes at pH 7.4, the electrostatic potentials of the active site surfaces were displayed. A comparison of the surface potentials of each protease in attendance of corresponding modeled inhibitors [Phe^{5}]SFTI[1,14] **1**, [Leu^{5}]SFTI[1,14] **2** and the parental monocyclic SFTI[1,14] (**Figure 17A**) resulted in nearly total compliance of the surface patterns of the associated active sites. As deriving of **1** and **2** from the parental peptide SFTI[1,14] was limited to the residue at the P1 position, the charge patterns of all the other residues were retained, thus highly preserved bioactivity towards inhibition of corresponding proteases could be expected. Furthermore, this hypothesis was supported by the display of the hydrogen bonds between proteases and corresponding inhibitors. As it is apparent from **Figure 17B**, the numbers of hydrogen bonds between **1** and chymotrypsin, and **2** and HNE, respectively, are not different from the corresponding SFTI-trypsin complex. These results from *in silico* examinations led to the decision for actual synthesis and investigation of inhibitors **1** and **2**.

Considering the expected selectivity of the synthetic inhibitors **1** and **2** towards binding to the corresponding enzymes which can be strongly restricted by significant homology with their parental peptide, an alternative BBI-derived scaffold des-Gly^{1},-Pro^{13},-Asp^{14}[Nle^{2},Leu^{5},Gln^{10},Tyr^{12}]SFTI-1[1,14] (**3**) was designed as an elastase inhibitor. The sequence of **3** is based on a BBI found *via* screening of a library of chemically synthesized and randomized peptides by McBride et al. in 1999.[144b] The original cyclic peptide exhibited an inhibition constant against HNE of 65 nM. An original Ala at the P1 was substituted by a Leu in **3**. The 3D computational model of **3** is depicted in **Figure 18** (analogously modeled and simulated as described for **1** and **2**).

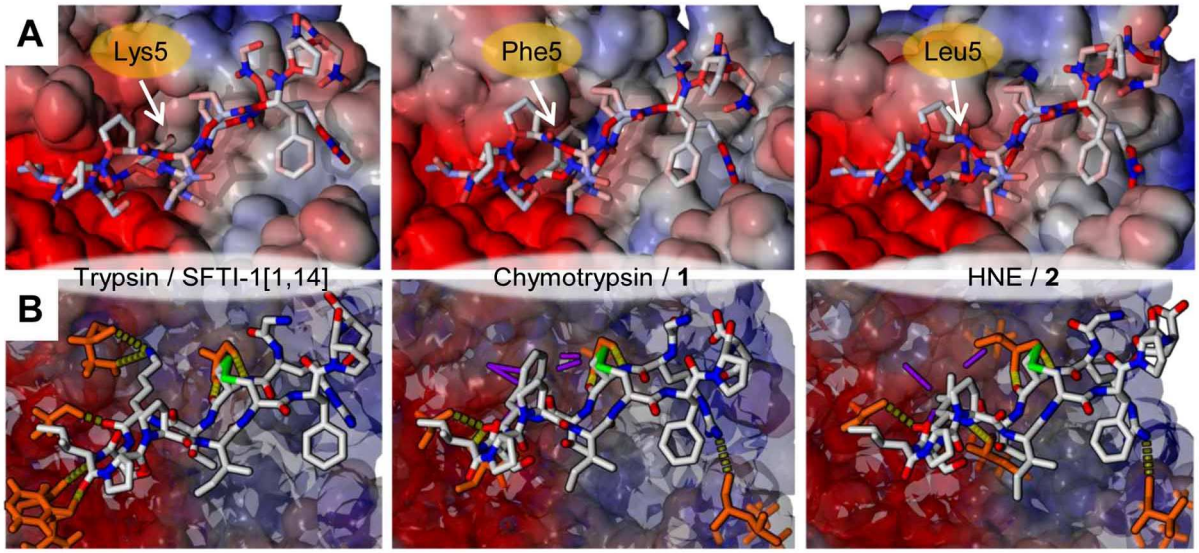

Figure 17. 3D computational models of SFTI-1[1,14] (left), **1** (center), and **2** (right) as co-complexes with corresponding proteases. Structures were produced from crystallographic data of the SFTI-1-trypsin co-complex (PDB: 1SFI) by modeling and energy minimization at aqueous environment (pH 7.4). **A**: Molecular surfaces of proteases and atoms (styled as sticks) of respective inhibitors are colored according to the electrostatic potential and charges in a gradient; red: highest electron density, negatively charged; blue: lowest electron density, positively charged. P1 residues of respective inhibitors are marked with labels. **B**: Intermolecular interactions between inhibitors and corresponding proteases are shown. Atoms of inhibitor colored by element color with grey: carbon, red: oxygen, blue: nitrogen, green: sulfur; protease residues forming intramolecular hydrogen bonds to respective inhibitors are shown in orange, hydrogen bonds are depicted as yellow, dashed bonds. Hydrophobic interactions within the S1 pocket are shown as purple columns. Molecular surfaces of proteases are shown in semi-transparent style and are colored according to their electrostatic potentials.

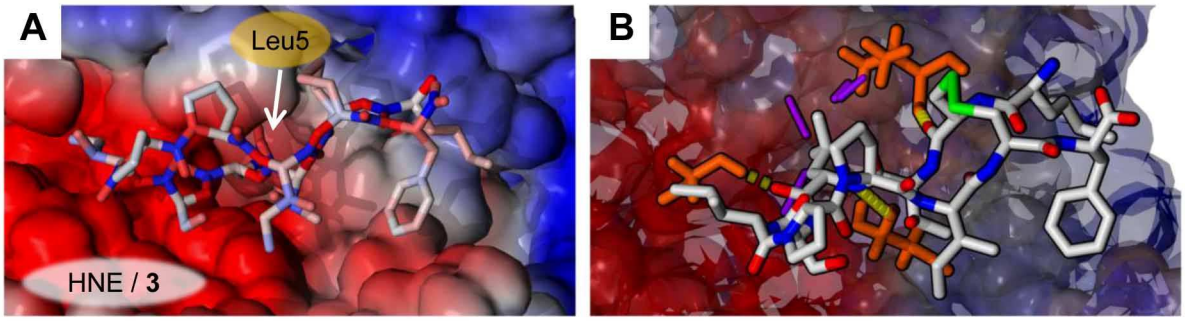

Figure 18. 3D computational models of **3** as a co-complex with HNE. Structures modeled analogously to corresponding structures in **Figure 17**. **A**: Distribution of electrostatic potentials and charges are shown. Same colors and depiction style was applied as described for **Figure 17A**. **B**: Intermolecular interactions between inhibitors and corresponding proteases are shown. Same colors and depiction style was applied as described for **Figure 17B**.

Based on the structure of **3**, the triazole-bearing peptidomimetic **4** potentially resistant against proteolytic cleavage was designed and modeled analogously to the peptides **1**-**3**. The modeled co-complex structure of HNE with **4** (**Figure 19**) exhibited similar electrostatic potential patterns and intramolecular interactions as shown for its parental peptide **3**.

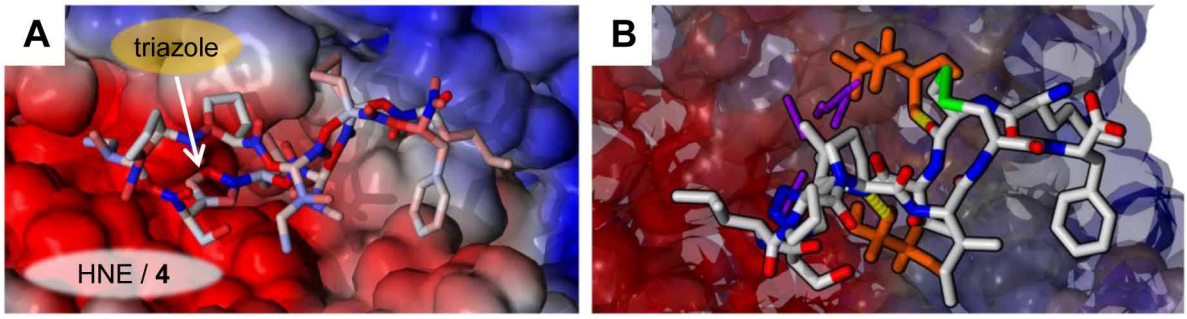

Figure 19. 3D computational models of **4** as a co-complex with HNE. Structures modeled analogously to corresponding structures in **Figure 17**. **A**: Distribution of electrostatic potentials and charges are shown. Same colors and depiction style was applied as described for **Figure 17A**. **B**: Intermolecular interactions between inhibitors and corresponding proteases are shown. Same colors and depiction style was applied as described for **Figure 17B**.

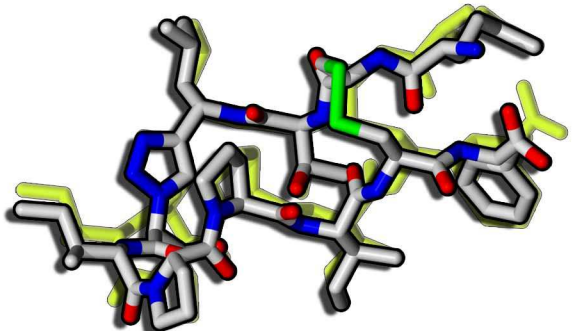

Figure 20. Overlay of computational models of **3** (yellow, semi-transparent sticks) and **4** (sticks in element colors with grey: carbon, red: oxygen, blue: nitrogen, green: sulfur) after energy minimization and structural alignment using AMBER03 force field.

Moreover, a structural alignment of **4** to **3** using AMBER 03 force field (**Figure 20**) resulted in an RMSD value of 0.7230 Å which is similar to the value calculated for the peptidomimetic $\Psi^{8,9}$1,4-[1,2,3]triazolyl-SFTI-1[1,14], synthesized in previous publication, and its parental peptide [Ala^{9}]SFTI-1[1,14] (RMSD = 0.5310).[14a] The observed inhibition constants K_i of the peptide/peptidomimetic pair from the former publication were differed by the factor of 2, thus a restriction of bioactivity in similar magnitude was expected for the peptide/peptidomimetic pair **3**/**4**.

3.1.1.1 Synthesis of peptides 1 – 3

Peptidic inhibitors **1**, **2**, and **3** were synthesized by partially-automated SPPS using standard Fmoc strategy. The associated linear precursor peptides **1'**, **2'**, and **3'** were obtained in very good to excellent yield (78.5%, 86.9%, and 83.6%; considering a reaction cascade of more than 10 successive coupling cycles, nearly quantitative yield for each cycle). **1'** and **2'** were side-chain-cyclized by oxidative folding in 0.1 M $(NH_4)_2CO_3$ buffer with 0.5 % DMSO while monitoring reaction progress by HPLC and ESI-MS, lyophilized and successively isolated by semi-preparative RP-HPLC. The chromatographic traces of **1'**/**1** and **2'**/**2** before and after folding and purification are depicted in **Figure 21**. Both cyclic peptides **1** and **2** were obtained in moderate folding and purification yields of about 35%, presumably due to the limited

recovery rate of the used HPLC system. However, the amount of isolated inhibitors was sufficient for the examination of their bioactivity and further analysis.

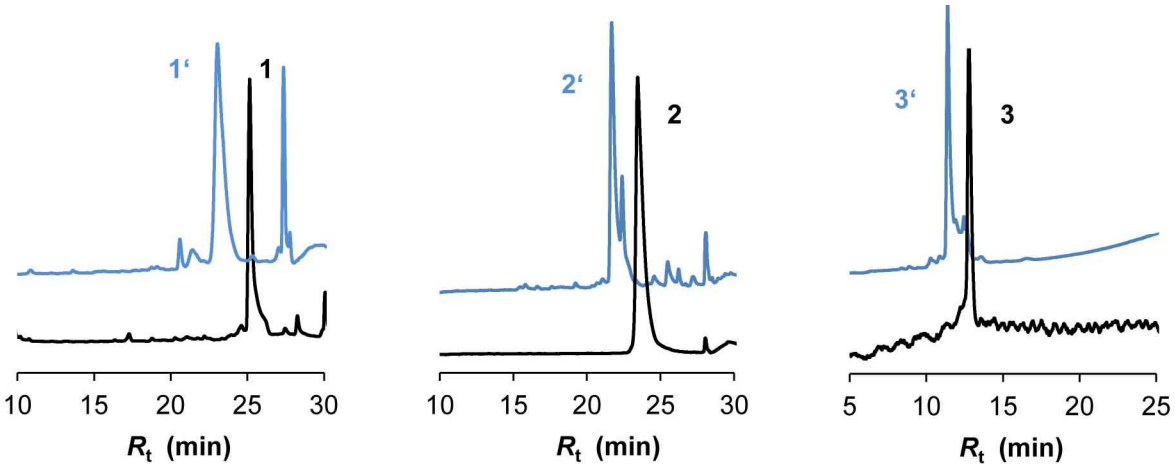

Figure 21. Chromatographic profiles of protease inhibitors **1** – **3** (black) and corresponding linear precursors (blue). UV detection at λ = 220 nm; eluent left: 18→40.5 % acetonitrile in 0.1 % aq. TFA over 20 minutes at flow rate 1 ml/min, eluent center: 18→54 % acetonitrile in 0.1 % aq. TFA over 20 minutes at flow rate 1 ml/min, eluent right: 9→90 % acetonitrile in 0.1 % aq. TFA over 20 minutes at flow rate 1 ml/min.

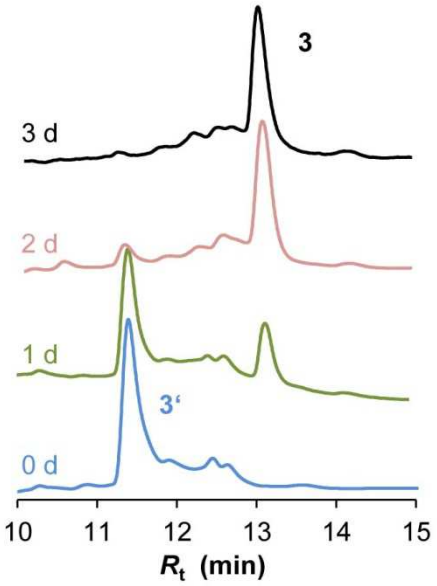

Figure 22. Chromatographic profiles of oxidative folding of **3'** to **3**. Colored numbers on left-hand side: Reaction time of corresponding samples picked from rm. UV detection at λ = 220 nm; eluent left: 9→90 % acetonitrile in 0.1 % aq. TFA over 20 minutes at flow rate 1 ml/min.

First, the oxidative folding of linear precursor peptide **3'** was conducted in the same folding buffer as **1'** and **2'**. Since after more than 10 days shaking no product formation was observed, neither in HPLC nor in ESI-MS, an alternative folding approach using a buffer system comprising DMSO/TFE in 1 M guanidium hydrochloride and 50 mM Na_2HPO_4 (pH 7) was employed. Associated HPLC traces of the monitored folding progress are depicted in **Figure 22**. Formation of a folding product could already be observed after a reaction time of less than 1 day. After three days folding, cyclic peptide **3** was isolated *via* semi-preparative RP-HPLC with 8.2 % folding and purification yield. The poor yield is presumably caused by the harsh folding conditions and the limited recovery rate of the semi-preparative HPLC system.

3.1.1.2 Synthesis of peptidomimetic 4

Towards achieving the triazolyl backbone mimic-bearing peptidomimetic inhibitor **4**, an on-support CuAAC-comprising solid-phase synthesis strategy was applied (**Scheme 18**).

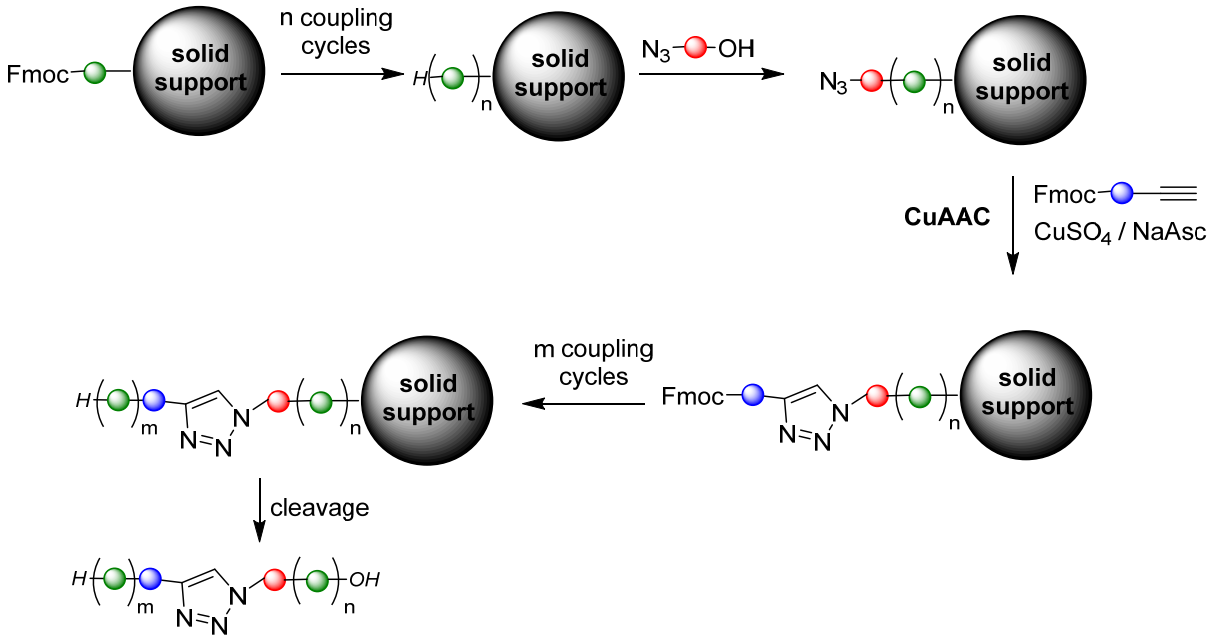

Scheme 18. General strategy to towards pseudo-peptides with triazolyl backbone mimics *via* CuAAC on solid support. Amino acids and building blocks are depicted as balls, canonical amino acids in green, α-azido acid in red, α-acetylenyl amine in blue. Solid support is depicted as grey ball.

First, an iterative chain elongation was performed by standard Fmoc-SPPS up to the position where the amide bond surrogate should be installed. In the present work, this corresponded to the scissile bond, thus chain elongation using standard coupling and deprotection techniques was accomplished up to Ile at P2'. Regarding the formation of a 1,4-disubstituted triazole isosteric to its parental peptide **3** *via* copper "click" reaction, two precursor building blocks were required: an α-azido acid on the P1' position and an α-acetylenyl amine component at the P1 position. Thus, (2*S*)-2-azido-3-*O*-*tert*-butyl-propanoic acid (**4a**) was synthesized according to a published protocol[149] from *H*-L-Ser(tBu)-*OH* by Cu(II)-catalyzed diazo transfer using triflyl azide prepared from the corresponding anhydride (**Scheme 19A**). **4a** was obtained in good yield (75 %) and analyzed by ^{1}H and ^{13}C NMR (shown in **Scheme 19B** and appendix, respectively). No distinct peaks of contaminations or reactants could be observed except small traces of residual solvents and water.

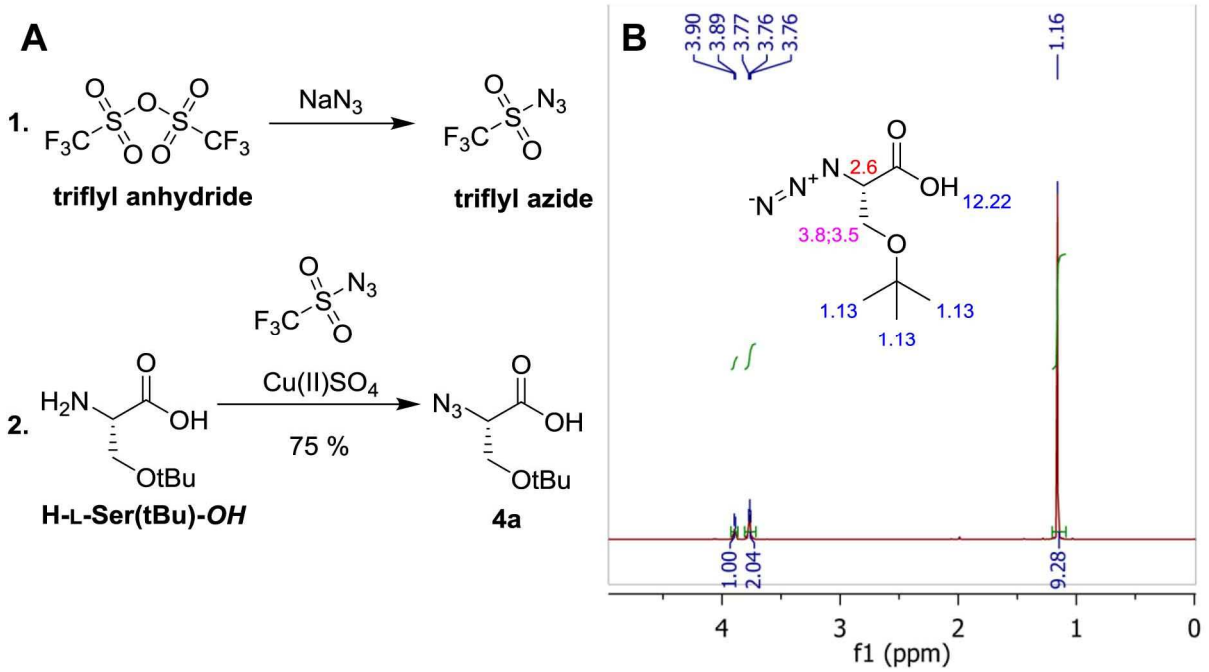

Scheme 19. A: Two-step synthesis of **4a**. **B**: ^{1}H NMR spectrum and chemical structure of **4a**. Peak integrals are shown as blue numbers below the spectrum. As reference for peak integrations duplet signal at 3.90-389 ppm was chosen. Colored numbers besides structures are predicted chemical shift values in ppm whereby estimation quality is indicated with blue: good; pink: medium; red: rough (estimation performed using NMR prediction tool of ChemBioDraw®).

The preparation of its counterpart building block (2*S*,3*S*)-*N*-Boc-1-ethynyl-3-methyl-butylamine (**4b**) was performed from Boc-protected Weinreb amide of leucine Boc-L-Leu-*N*(OMe)Me by a two-step reaction comprising the reduction of the Weinreb amide to an aldehyde and the successive Bestmann modification with the dimethyl-1-diazo-2-oxopropyl phosphonate (Ohira-Bestmann reagent).[150] Furthermore, to make alkyne-bearing building block compatible with the Fmoc-SPPS strategy, an exchange of the amino protecting group from Boc to Fmoc was accomplished yielding sufficient amount of (2*S*,3*S*)-*N*-Fmoc-1-ethynyl-3-methyl-butylamine (**4c**) for its application in on-support CuAAC (**Scheme 20**). The corresponding ^{1}H NMR spectra of **4b** and **4c** (**Figure 23**) confirmed the high purity of synthesized compounds with no contaminations except small traces of residual solvents.

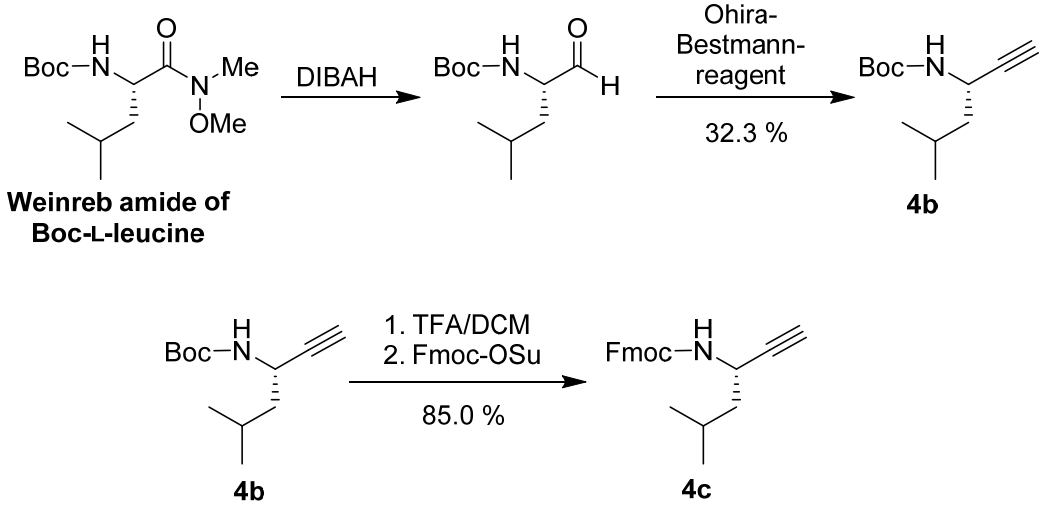

Scheme 20. Three-step synthesis of **4c** from the corresponding Weinreb amide.

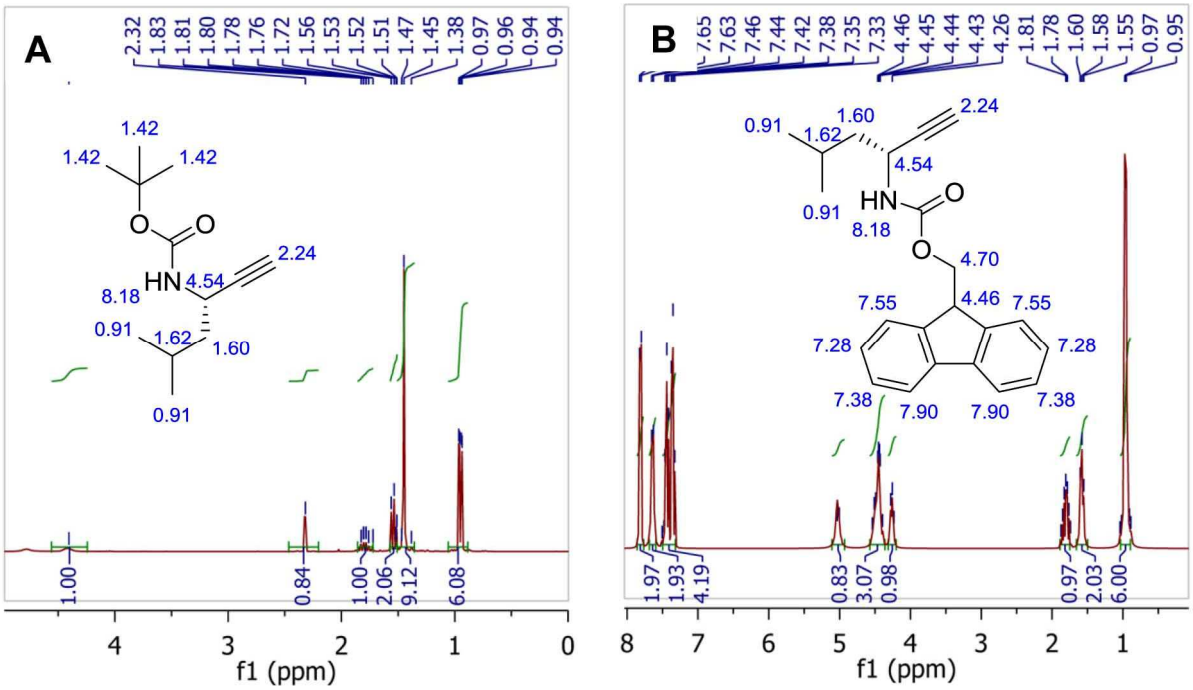

Figure 23. ^{1}H NMR spectra and chemical structure of **4b** (**A**) and **4c** (**B**). Peak integrals are shown as blue numbers below the spectrum. As reference for peak integrations multiplet signals at 1.83-1.72 ppm (**A**) and 0.97-0.95 ppm (**B**) were chosen. Colored numbers besides structures are predicted chemical shift values in ppm whereby estimation quality is indicated with blue: good; pink: medium; red: rough (estimation performed using NMR prediction tool of ChemBioDraw®).

For CuAAC on solid support, first **4a** was coupled to the free *N*-terminus of the peptide-resin. Cycloaddition was performed as described in previous publication.[14a] Conversion of the azide component during CuAAC was verified by ESI-MS and IR spectroscopy of deprotected and test-cleaved intermediates.

After manual, iterative chain elongation up to the *N*-terminal norleucine (Nle), cleavage from solid support and precipitation, the linear precursor peptidomimetic **4'** was obtained with nearly quantitative crude yield, whereby a presumably high amount of contamination by remaining Cu salts and further side products was expected. As the oxidative folding in ammonium acetate buffer failed, **4'** was cystine-cyclized and isolated by same procedure as described for **3'**. Due to the non-trivial folding condition and high amount of contaminations in the crude product, the final purification yield was poor (5.9 %) but **4** could be obtained in sufficient amount and purity for further bioactivity assays and proteolysis experiments. Yields of synthesized chymotrypsin and elastase inhibitors are summarized in **Table 6**.

Table 6. Synthesis of inhibitors **1** – **4**.

Entry	Strategy	MW	Crude yield precursor [%]	Folding/purification yield [%]	Overall yield [%]
1	Automated	+	85.9	39.5	33.9
2	Automated	+	78.5	34.8	27.3
3	Automated	+	83.6	8.2	6.8
4	Automated	+	97.1	5.9	5.8

3.1.2 Characterization and Evaluation of Activity

3.1.2.1 Bioactivity Assays

Prior to the examination of the synthesized inhibitors, the proteolytic activities of discussed proteases trypsin, chymotrypsin, and HNE were evaluated. Thus, time-dependent degradation of corresponding chromogenic substrates was studied at different concentrations. That was done to confirm activity of the proteases, establish an assay setup and determine the Michaelis-Menten constant K_M of the discussed enzyme-substrate systems. Especially the last point was of particular importance, since K_M was required for the calculation of K_i (chapter 5.4.1.3). All of the tested enzymes exhibited sufficient proteolytic activity for the application in subsequent inhibition assays. The assay setups developed by these preliminary experiments are described in chapter 5.4. K_M was graphically determined from the Hanes-Woolf plot (quotient of substrate concentration and initial reaction rate: $[S]_i/v_i$ against the substrate concentration $[S]_i$).[14a] The Hanes-Woolf plots of three HNE activity measurement series against MeO-Suc-AAPV-pNA are exemplary shown in **Figure 24**. Further Hanes-Woolf plots are shown in the appendix.

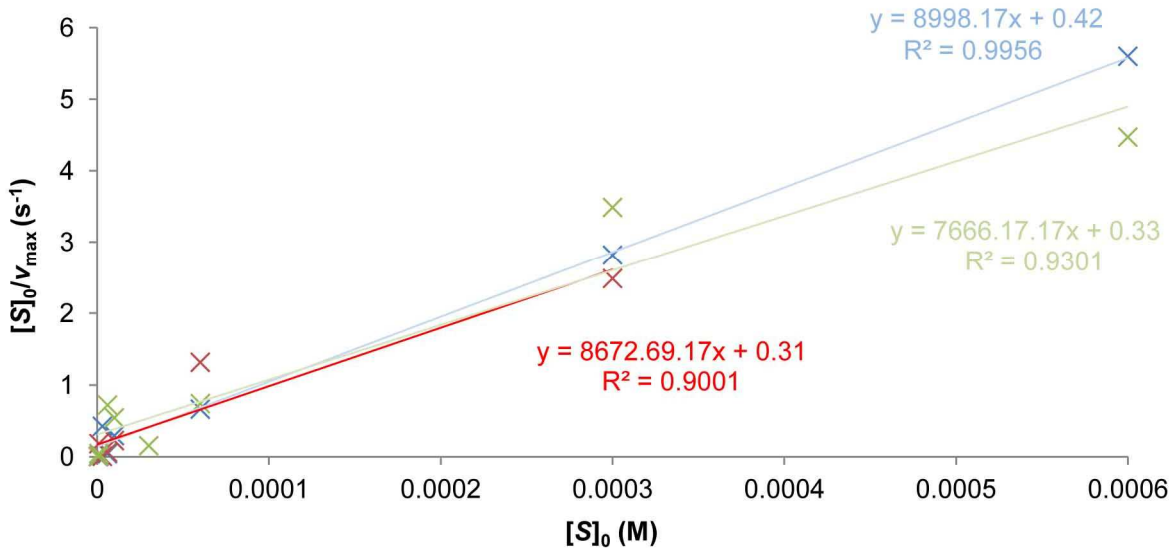

Figure 24. Hanes-Woolf plot of three HNE activity assays against MeO-Suc-AAPV-pNA. Data points, trend lines of linear regressions, linear equation of trend lines, and associated regression coefficient of each measurement series are marked in individual colors.

K_M can be calculated from the slope and point of intersection with the x-axis of the linearly regressed trend line of the measured data points using the converted Michaelis-Menten rate equation:

$$\frac{[S]_i}{v_i} = \frac{[S]_i}{v_{max}} + \frac{K_M}{v_{max}} \qquad (12)$$

The calculated K_M of the discussed enzyme-substrate pairs are shown in **Table 7**. The determination of K_M for chymotrypsin against Suc-AAPF-pNA failed because of inconsistent

measurement values presumably due to the formation of bubbles on the sample surface. Thus, a published value is listed for the K_M of chymotrypsin and used for further calculations.[151]

Table 7. Michaelis-Menten constants of discussed proteases.

Protease	Substrate	K_M determined [μM]	K_M published [μM]
Trypsin	Boc-QAR-pNA	58.9±7.3	41.7±6.2[14a]
Chymotrypsin	Suc-AAPF-pNA	-	60±7[151]
HNE	MeO-Suc-AAPV-pNA	42.0±5.2	140[152]

The obtained values of K_M for trypsin and HNE were in typical magnitude for proteolytic cleavage of affine substrates. The experimentally determined K_M of HNE against MeO-Suc-AAPV-pNA was slightly better than the published one, probably due to the difference in experimental setups *i. a.* used buffer systems and enzyme/substrate concentration range.
Based on the established setups for proteolytic activity assays, enzyme inhibition assays of the synthesized peptidic and peptidomimetic inhibitors **1** – **4** against corresponding serine proteases were performed.[14a, 73b, 153] In general, the time-dependent proteolytic degradation of chromogenic substrates at defined starting concentrations in presence of a concentration series of respective inhibitors was recorded. After preliminary tests to adjust the concentration range of the inhibitors, the measurements at optimized concentrations were performed in triplicate. Exemplary, a single measurement plot of the photometrically recorded time-dependent substrate degradation by HNE in presence of **4** is shown in **Figure 25A**.
The apparent inhibitory constants K_i^{app} were graphically determined from the Dixon plot (**Figure 25B**) of the measurement series (quotient of initial reaction rate of inhibited reaction and the reaction rate of the non-inhibited reaction = v_i/v_0 against the inhibitor concentration = $[I]_i$) by a global fitting of the data points to the Morrison equation (see chapter 5.4.1.4). Further Dixon plots of inhibition assays with global fittings are given in the appendix. The experimentally determined values of K_i^{app} and respective values for K_i of the inhibitors **1** – **4** and the linear precursors **3'** and **4'** are listed in **Table 8**.

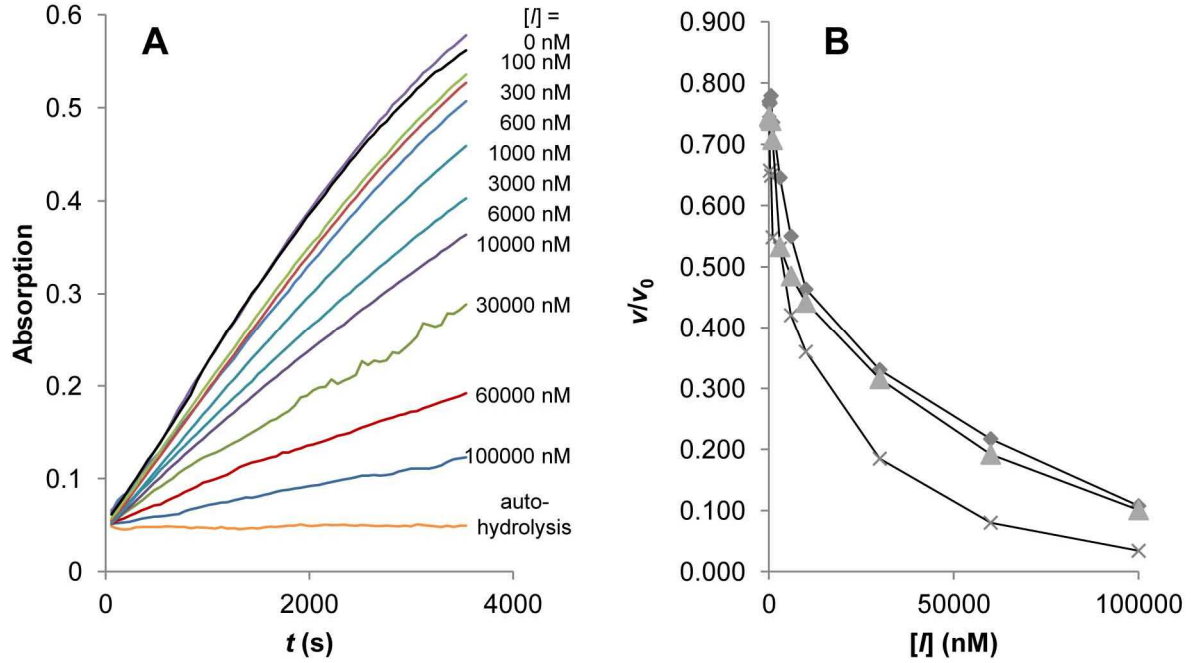

Figure 25. **A**: HNE inhibition with **4**. Relative absorption at λ = 410 nm (y-axis) is plotted against the reaction time (x-axis). **B**: Dixon plot of HNE inhibition assay using **4** as inhibitor. Experiment was performed as triplicate. Relative reaction rate (y-axis) is plotted against the inhibitor concentration (x-axis).

Table 8. Apparent inhibition constants and substrate concentration-independent inhibition constants of examined enzyme-inhibitor combinations.

Inhibitor	Protease	K_i^{app} [nM]	K_i [nM][a]
1	Chymotrypsin	0.37±0.03	0.07±0.01
1	Trypsin	N/A	-
2	HNE	623.91±45.00	99.98±12.50
2	Trypsin	N/A	-
3	HNE	901.71±161.96	144.48±29.62
4	HNE	3642.45±687.97	563.63±125.37
3'	HNE	13260.62±1020.49	2124.89±271.70
4'	HNE	N/A	-

a: Errors of K_i calculated by propagation of errors of K_i^{app} and K_M (see chapter 5.4.1.5).
N/A: No activity observed or K_i higher than 100 μM.

The obtained K_i value for **1** against chymotrypsin was in picomolar range and even better as the reported K_i of SFTI-1 against trypsin. As Zablotna et al. reported an association equilibrium constant K_a (which reciprocal is corresponding to K_i for reversible inhibitors) of 2×10^9 M^{-1} the obtained value in present work is in same range.[144c] However, due to the observation that the applied method for non-linear curve fitting reached to the limit of its

validity range and the difficulty to provide the corresponding Weinreb amide, the idea to synthesize a mimic of **1** with triazolyl surrogate at the scissile bond was finally abandoned for the present work.

The inhibitory constants of elastase inhibitors **2** and **3** were in triple-digit nanomolar range. These results could be compared to published data of similar inhibitors as [Leu^5, Trp^9]SFTI-1[1,14] is reported with a K_a of 3×10^7 M^{-1} against HNE which is comparable to the K_i of the related inhibitor **2,** found in the present work.[144c] McBride et al. reported a K_i of 130 nM for the inhibitor des-Gly^1,-Pro^{13},-Asp^{14}[Nle^2,Val^5,Gln^{10},Tyr^{12}]SFTI-1[1,14].[144b] This value is matching to the determined K_i =144 nM of its P1-mutant **3** with a Leu at the scissile bond.

Peptidomimetic inhibitor **4** exhibited a K_i^{app} in single-digit micromolar range and a K_i in triple-digit nanomolar range. The determined inhibitory constant was higher than its parental inhibitor **3** by the factor of 3–4 which is in similar range as for previously reported triazolyl amide bond surrogates.[14a] The influence of the exchange on the inhibitory potency was smaller as in the case of the *cis* amide surrogate at the P3' position (decrease by factor 10) but greater as for the *trans* amide mimic at the P4' position (decrease by factor 2), which emphasizes the importance of scissile bond conformation for the inhibitory effect. However, from the view of activity preservation, the replacement of the scissile bond by a triazole can be considered as successfully realized, since Legowska et al. reported 2011 for SFTI-derived trypsin and chymotrypsin inhibitors with scissile bond replacements by Pro or its derivatives a decrease in inhibitory activity by 2 – 4 orders of magnitude compared to their parental inhibitors.[154]

An important observation was made during the inhibition assays of the reduced variants of HNE inhibitors **3** and **4** (**3'** and **4'**). Both inhibitors underwent a drastic loss in inhibitory potency upon opening the disulfide macrocycle. This outcome can be explained by two reasons, the loss in affinity to the active site of the protease by deletion of the rigid framework and the lower probability of recondensation after cleavage of the scissile bond. Since the decrease in inhibitory activity is also significant for **4'** with a hydrolytically stable surrogate at the corresponding position, the loss in affinity is supposed playing a more important role in this case.

Furthermore, the inhibitory activity of **1** and **2** against trypsin was tested to evaluate selectivity of synthesized inhibitors. In both cases, no distinct inhibitory effect could be observed in the corresponding assays. The inhibitory activity of **3** and **4** against chymotrypsin was evaluated only qualitatively in a preliminary experiment without a photometrical assay. Comparing the degradation of a chromogenic substrate in presence and absence of an inhibitor, no significant difference was observed. Since the target selectivity of synthesized inhibitors was not the main issue in present work, no further investigations were done.

3.1.2.2 Evaluation of Proteolytic Stability

Susceptibility of synthesized inhibitors to proteolytic cleavage was examined by incubation of the linear precursors **1'** – **4'** (for minimization of the influence of recondensation) in the presence of corresponding proteases under reducing conditions. The reaction progress was monitored by HPLC and ESI-MS; samples were prepared by precipitation of the proteases from the reaction mixture in acidic milieu. Additionally, DTT was added to avoid formation of

disulfide bonds and make the characterization by respective analytic methods possible. In **Table 9**, the experimental data for the inhibitor precursors **1'** – **4'** and the cyclic HNE inhibitors **3** and **4** are listed. Detailed information on experimental setup is given in chapter 5.3.1.

Table 9. Proteolysis of the linear precursors **1'** – **4'** and the cyclic inhibitors **3** and **4**.

Entry	Enzyme	Setup	Hydrolyzed amount/hour[a]	Finally Hydrolyzed amount (h)[b]
1'	HNE	1	3.42 %	3.42 % (1 h)
1'	Chymotrypsin	2	27.90 %	69.8 % (2.5 h)
2'	HNE	1	22.68 %	56.7 % (18 h)
2'	Chymotrypsin	2	2.29 %	5.75 % (2.5 h)
3'	HNE	1	52.55 %	93.02 % (24 h)
3	HNE	3	3.35 %	16.91 % (16 h)
4'	HNE	1	5.23 %	56.24 % (24 h)
4	HNE	3	0.26 %	4.96 % (24 h)

a: Mean value of hydrolysis per hour of first 2 - 3 measurements.
b: Final conversion determined from the last measurements of corresponding reaction mixtures. Numbers in brackets are the time after reaction start when the last sample was prepared and measured.

The progress of proteolytic degradation was assessed upon integration of the HPLC traces for the hydrolysis of compounds 1' – 4'. Due to the low concentration of samples (near to the error limit of the applied HPLC system), the obtained conversion should only be considered as approximate values and do not possess quantitative accuracy. Nevertheless, a general tendency was the enhanced hydrolysis of compounds possessing at the P1 position a residue which complied with the substrate selectivity of the enzyme. Thus, linear precursor **1'** comprising the P1 Phe underwent chymotrypsin-mediated degradation but showed certain resistance against HNE-promoted hydrolysis. A similar effect was observed for **2'**.

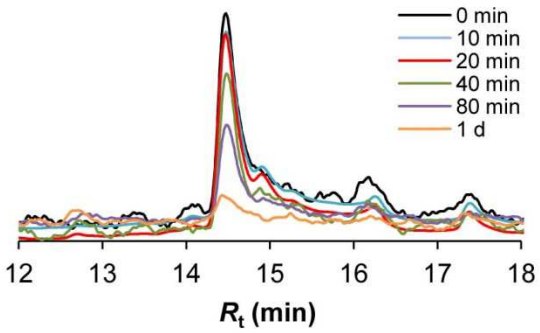

Figure 26. Chromatographic traces of HPLC-monitored proteolysis of **3'** by HNE. UV detection at λ = 220 nm; eluent: 9→54 % acetonitrile in 0.1 % aq. TFA over 20 minutes at flow rate 1 ml/min.

In **Figure 26** the HPLC monitoring of the proteolytic degradation of **3'** by HNE is exemplary shown. According to the observed tendency, nearly total degradation of the linear precursor could be observed after an incubation time of 1 d. The cleavage at the scissile bond could be confirmed by ESI-MS of the collected fraction at R_t = 12.8 min after separation of the sample mixture *via* HPLC. The corresponding

m/z signals of both of the cleaved fragments, *H*-Nle-CTL-*OH* and *H*-SIPPQCY-*OH*, were found either as positively ($[M+H]^+$ and $[M+2H]^{2+}$) or negatively charged species ($[M-H]^-$). Respective MS spectra for **3'** are shown in **Figure 27**.

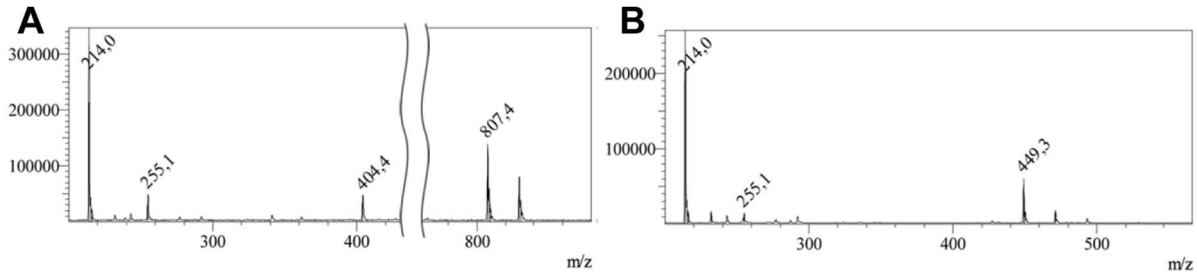

Species	Ions	m/z calc.	m/z obs.
H-SIPPQCY-*OH*	$[M+H]^+$	807.9	807.4
	$[M+2H]^{2+}$	405.0	404.4
H-Nle-CTL-*OH*	$[M-H]^-$	449.6	449.3

Figure 27. ESI mass spectra of prepared reaction mixture after proteolytic cleavage experiment of **3'** after chromatographic isolation of fraction at R_t = 12.8 min. **A**: Spectrum in positive mode. **B**: Spectrum in negative mode. Corresponding m/z signals of calculated and found fragments are listed in the table below.

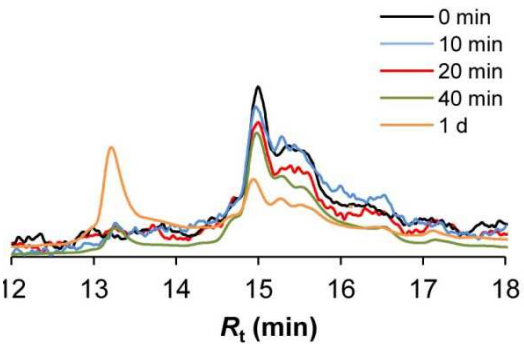

Figure 28. Chromatographic traces of HPLC-monitored proteolysis of **4'** by HNE. UV detection at λ = 220 nm; eluent: 9→54 % acetonitrile in 0.1 % aq. TFA over 20 minutes at flow rate 1 ml/min.

In contrast to **3'**, compound **4'** exhibited only slow degradation under the same reaction conditions. The chromatographic traces of proteolytic degradation of peptidomimetic **4'** are depicted in **Figure 28**.

After incubation over 1 d, about 43% of peptidomimetic **4'** still remained in the reaction mixture, whereby the MS signals found in the fraction at R_t = 13.2 min corresponded to the P2-P3 cleaved fragment *H*-T[LtS]IPPQCY-*OH* and P1-P2 cleaved fragment *H*-[LtS]IPPQCY-*OH* of **4'** (**Figure 29**). This result is in accordance with the reported data by McBride et al. concerning the affinity of a BBI-based inhibitor comprising a Thr at the P1 position with preserved affinity to HNE.[144b] The scissile bond selectivity of HNE towards cleavage after Thr is also reported by Dall'Acqua et al.[155] As no corresponding signals to the discussed cleavage pattern could be found in case of **3'**, the observed proteolysis at these positions is assumed to be done alternatively to the more affine Leu, mimicked by a hydrolysis-stable surrogate in **4'**. Nonetheless, peptidomimetic **4'** seemed to possess also higher overall stability against proteolytic degradation than its parental peptide **3'**.

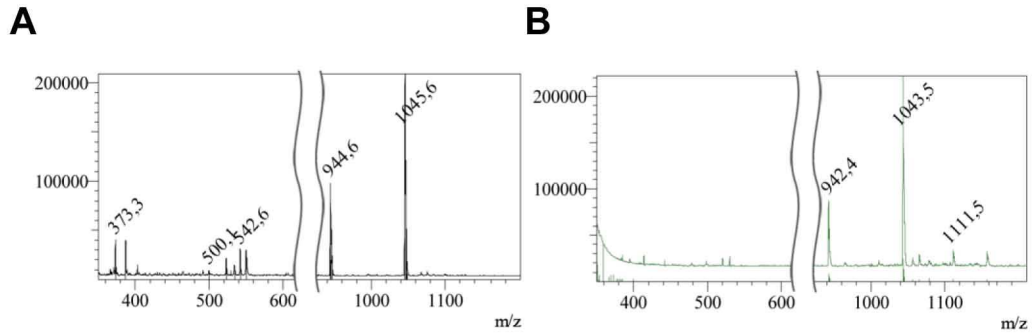

Species	Ions	m/z calc.	m/z obs.
H-T[L*t*S]IPPQCY-*OH*	$[M+H]^+$	1147.5	1145.6
	$[M-H]^-$	1145.5	1143.5
H-[L*t*S]IPPQCY-*OH*	$[M+H]^+$	945.5	944.6
	$[M-H]^-$	943.5	942.4

Figure 29. ESI mass spectra of prepared reaction mixture after proteolytic cleavage experiment of **4'** after chromatographic isolation of fraction at R_t = 13.2 min. **A**: Spectrum in positive mode. **B**: Spectrum in negative mode. Corresponding m/z signals of calculated and found fragments are listed in the table below.

The same tendency was observed for the cystine-bearing inhibitors **3** and **4**, whereby the overall conversion and reaction rate were significantly suppressed by enhanced re-condensation of hydrolyzed species. This effect gives to the peptides and peptidomimetics their actual activity as protease inhibitors. Especially in case of **4**, where the final conversion is kept in range of measurements uncertainty of the HPLC system, presented excellent stability against proteolytic cleavage (**Figure 30**). Even by direct injection of the sample after a reaction time of 24 h, only m/z signals of the non-cleaved inhibitor could be found. On the other hand, a direct MS analysis of the sample mixture of **3** with analogous reaction setup, resulted in the detection of same signals observed for **3'**, thus the hydrolysis of the scissile bond is not completely suppressed.

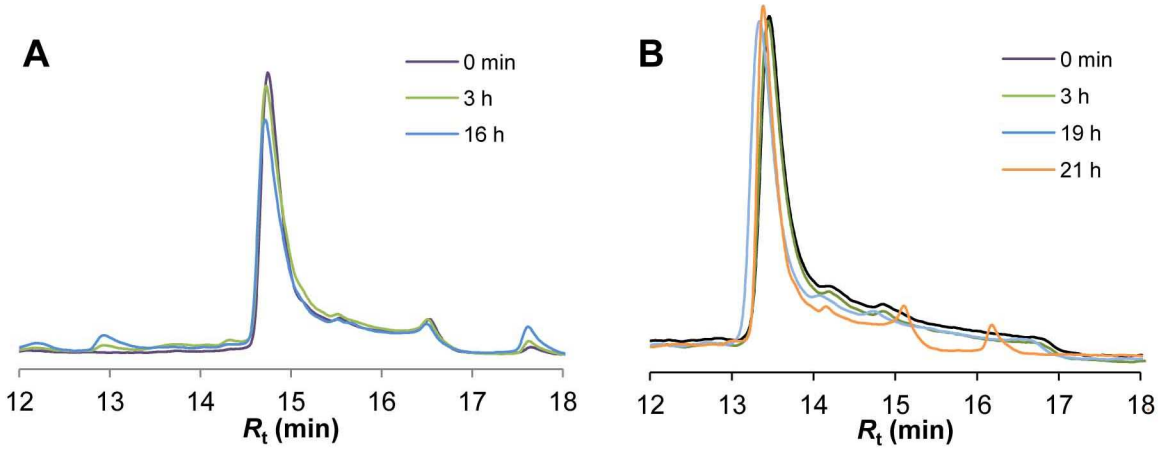

Figure 30. A: Chromatographic traces of HPLC-monitored proteolysis of **3** by HNE. UV detection at λ = 220 nm; eluent: 9→54 % acetonitrile in 0.1 % aq. TFA over 20 minutes at flow rate 1 ml/min. **B**: Chromatographic traces of HPLC-monitored proteolysis of **4** by HNE. UV detection at λ = 220 nm; eluent: 18→40.5 % acetonitrile in 0.1 % aq. TFA over 20 minutes at flow rate 1 ml/min.

The hydrolytic stability of **4** is higher by a factor of 15 (determined from the hydrolysis of **3** and **4** per hour), compared to **3**. This showed that the approach to improve proteolytic stability by replacement of the scissile bond by a triazolyl group was successfully accomplished.

3.1.3 Digest of Chapter 3.1

An HNE inhibitor with a triazolyl group as scissile bond mimic was computationally and knowledge-based designed from a BBI and successfully synthesized. Its inhibitory activity and susceptibility against proteolytic cleavage was examined and compared with the parental peptide and further BBI-derived HNE and chymotrypsin inhibitors. All synthesized peptides exhibited strong inhibitory potency and selectivity towards their target proteases (pico- to nanomolar range). The determined K_i values were all in the range of either published data of same/similar compounds, or matching to assumed values derived from *in silico* modeling. Thus, the RMSD of **4** to **3** was 0.723 Å and the loss in activity by the amide bond surrogate is marked by the factor 3.9, whereas the SFTI-derived trypsin inhibitor with a triazolyl *trans* amide mimic from previous publication was marked with an RMSD of 0.531 Å and an activity loss by the factor of 2, respectively. However, this result demonstrates the applicability of the triazole-containing unit [L*t*S] as a mimic of the associated amino acid residues at P1-P1', which provides the binding selectivity and high affinity of the inhibitors to the active site of the corresponding enzyme. At present, this finding cannot be generalized for every inhibitor-enzyme combination due to the lack of further examples.
At a first glance, the SFTI-derived chymotrypsin inhibitor **1** demonstrated the best inhibitory constant against the associated protease, but the synthesis of its triazolyl-bearing analogue was abandoned by practical reasons.
The most important issue in this project was the improvement of susceptibility against proteolytic degradation of **4** compared to its parental BBI-derived inhibitor **3** which was examined in hydrolysis experiments. Generally, all non-cyclized inhibitor precursors **1'** – **4'** and cystine-cyclized inhibitor **3** showed certain susceptibility in the scissile bond against cleavage by their associated proteases. However, **4** exhibited nearly total resistance against hydrolysis and underlined the usability of triazole groups as hydrolysis-stable scissile bond mimics with only a slight loss of bioactivity compared to the parental peptide. Furthermore, it was shown that the side-chain cyclization *via* disulfide bond formation, which provides the rigid framework of BBIs, is not only essential for the inhibitory activity but also a highly important requirement for the proteolytic stability of the scissile bond.

3.2 PHIP-Active Functional Peptides

3.2.1 Design and Synthesis

Regarding the design of a PHIP-labeled SFTI derivative, first, the position for installation of the label within the scaffold of SFTI-1[1,14] had to be discussed. Since the label should not affect the bioactivity of the inhibitor, positions should be avoided that face the binding side of the enzyme and possibly interfere with enzyme-inhibitor interactions. Furthermore, modifications within the inhibitory loop (Cys3 – Cys11) were also prevented to keep the rigid framework of the scaffold maximally constrained. According to the Ala-scan experiments by Daly et al.[117] and an *in silico* modeling of the SFTI-1[1,14]-trypsin co-complex (derived from PDB: 1SFI) the residues Gly1 and Pro13 facing apart from the active site of trypsin were found to be favorable for the substitution by a PHIP-active synthetic amino acid (**Figure 31A**). Hence, two SFTI derivatives with substitutions of corresponding residues by Pra, [Pra^{1}]SFTI-1[1,14] (**5**) and [Pra^{13}]SFTI-1[1,14] (**6**) were designed. It was clearly apparent from the modeled and energy minimized co-complex structure of **5** and **6** shown in **Figure 31B** and **31C** that in both cases the substitution does not affect the conformation of the SFTI framework and that the side-chain extension is not interfering with the binding sites.

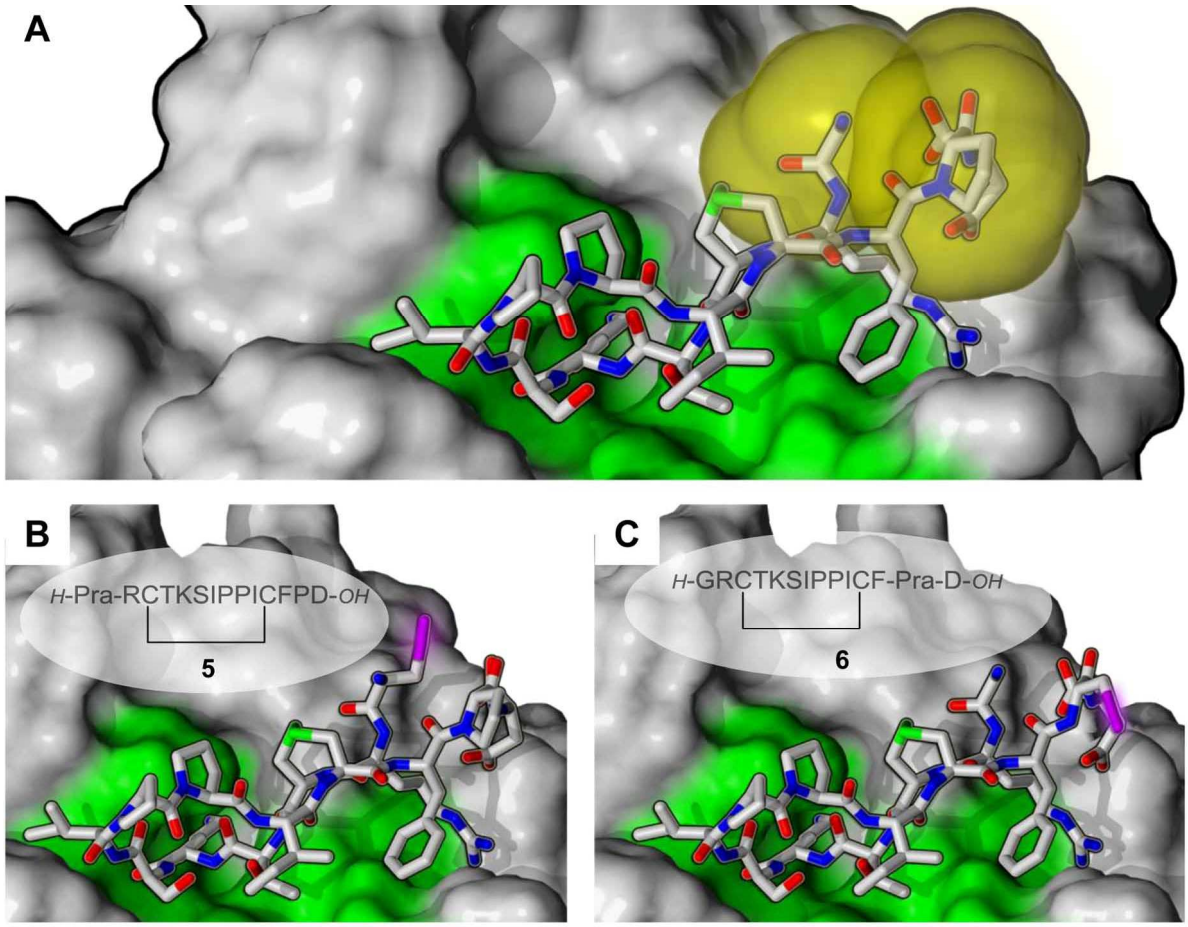

Figure 31. 3D computational models of SFTI-1[1,14], **5** and **6** as co-complexes with trypsin. Structures modeled from crystallographic data (PDB: 1SFI) by *in silico* building and energy minimization. Surface of residues forming the active site: green. Atoms of inhibitors are shown as sticks with grey: carbon, red: oxygen, blue: nitrogen, green: sulfur. **A**: Residues for planned substitution by PHIP-active labels are implied by depiction of the surface in yellow. **B&C**: Triple bonds of installed PHIP labels are highlighted in purple.

As discussed in chapter 2.2, the NMR signal enhancement by PHIP is extremely affected by the presence of strong electron-donating groups presumably poisoning the hydrogenation catalyst. Thus, we supposed that the remoteness of the alkyne functionality from those groups is an important criteria for the effective PHIP labeling. This presumption was examined by the application of two strategies in combination. First, L-Tyr(*O*-propargyl) was introduced as PHIP label with an extended distance between corresponding multiple bond and the peptide backbone by the size of a phenyl ring. Second, associated interfering moieties were substituted by respective surrogates. [Tyr(*O*-propargyl)[1]]SFTI-1[1,14] (**7**) was designed to pursue former strategy (**Figure 32A**). In view of practicability and efforts in synthesis, the installation of PHIP labels in all following SFTI derivatives was restricted to the position of Gly1.

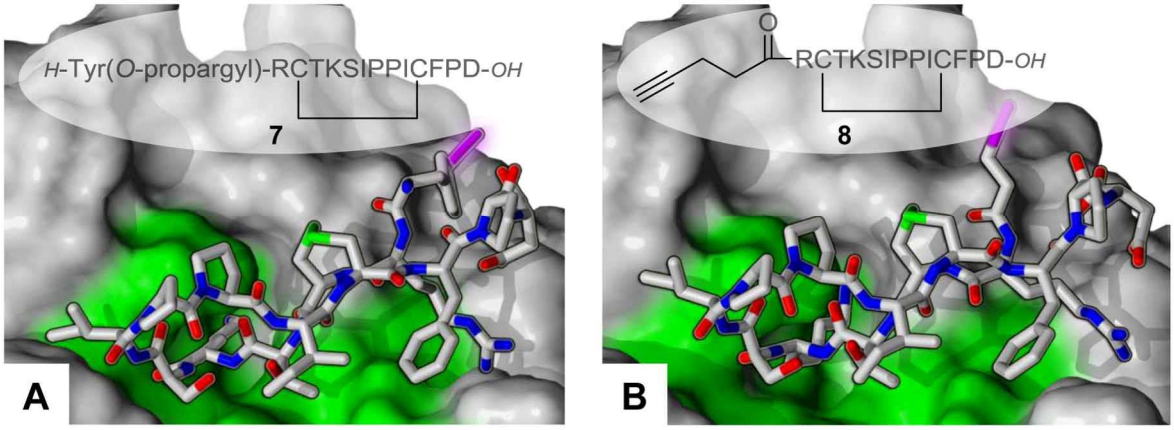

Figure 32. 3D computational models of **7** and **8** as co-complexes with trypsin. Structures modeled as described for **Figure 31**. Same depiction style and color patterns used as described for **Figure 31**.

Considering the data from the previous publication[145] and the findings by Trantzschel et al.,[147] sulfhydryle derivatives and primary amines in close proximity to the PHIP label were categorized as most drastically hydrogenation-impairing moieties and were decided to be substituted. In case of the SFTI-1 scaffold, the cystine-forming residues Cys3 and Cys11, and Lys5 as well as the α-amine were concerned. Since Lys5 is essential for the selective binding of the inhibitor to trypsin[117] and is not in direct proximity to the PHIP label, the modifications were restricted to the replacement of the *N*-terminal amine group and the disulfide bond. Regarding investigation of the influence of the free *N*-terminus, first an elimination of this moiety was undertaken. Thus, SFTI derivative **8** bearing an amine-free isoster of Pra, 4-pentynoic acid, was designed (**Figure 32B**). Furthermore, the conversion of the primary to the secondary amine by acyl capping was investigated. The modeled structure of resulting SFTI derivatives **9** and **10,** each bearing Pra and Tyr(*O*-propargyl) as PHIP labels, are depicted in **Figure 33**.

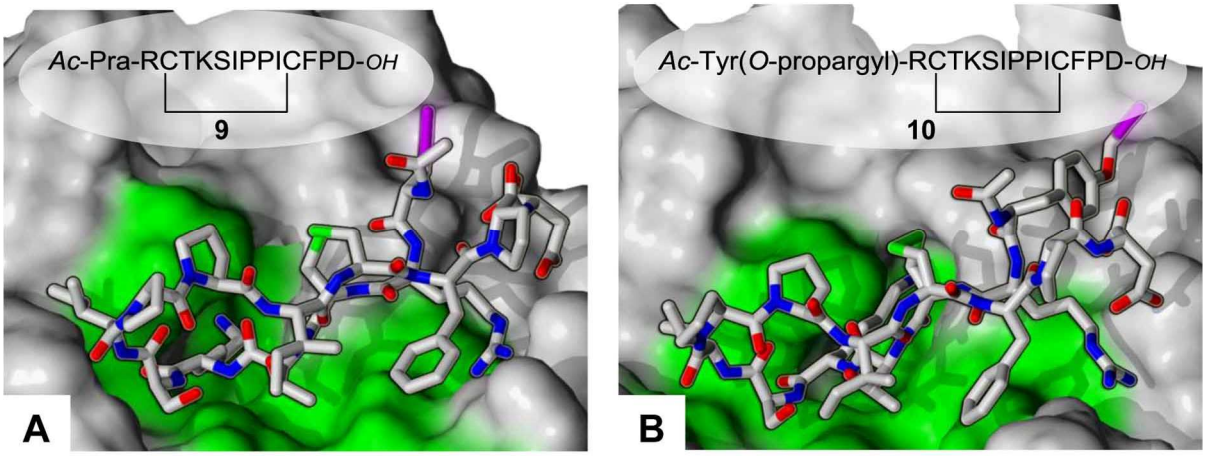

Figure 33. 3D computational models of **9** and **10** as co-complexes with trypsin. Structures modeled as described for **Figure 31**. Same depiction style and color patterns used as described for **Figure 31**.

Finally, the remaining issue was the exchange of the sulfur atoms within the cystine pattern. Appropriately, Empting et al. published 2011 the successful replacement of a disulfide bond in a monocyclic SFTI derivative by a 1,5-disubstituted 1,2,3 triazole with only minimal loss in bioactivity.[73b] This strategy was applied to inhibitors **5** and **7** resulting in the peptide analogs **11** and **12** bearing Pra and Tyr(*O*-propargyl) as PHIP labels, respectively. From the modeled structure of **11** and **12** shown in **Figure 34** no dramatic derivation from the original template scaffold of SFTI-1 can be observed, thus preserved bioactivities of corresponding peptide analogs could be expected.

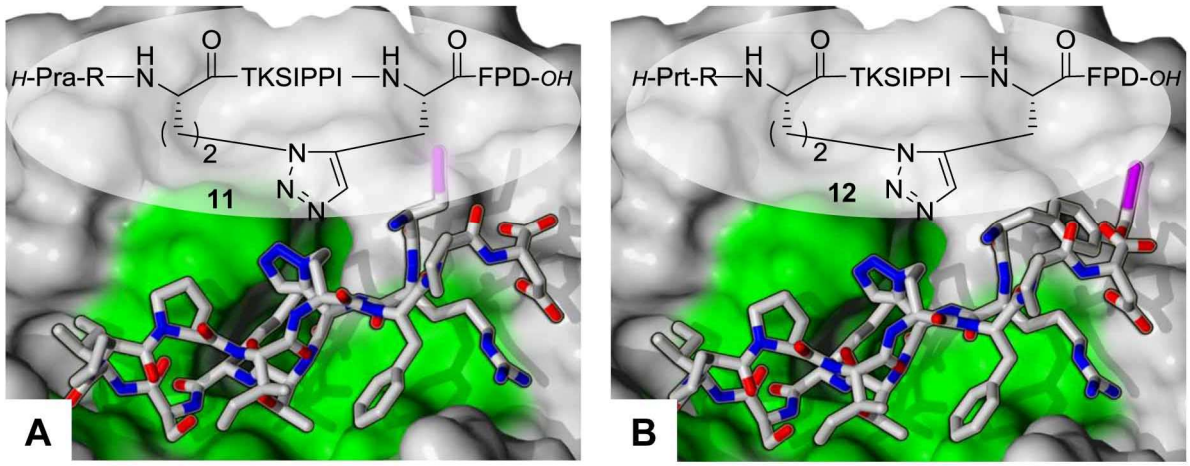

Figure 34. 3D computational models of **7** and **8** as co-complexes with trypsin. Structures modeled as described for **Figure 31**. Same depiction style and color patterns used as described for **Figure 31**..

An overlay of the modeled SFTI derivatives **5** – **12** is shown in **Figure 35**. As expected, the structural derivations were mainly concentrated within the moieties of respective amino acid substitution, while the residues directly contacting with the active site of trypsin (left-hand side of **Figure 35**) are only minimally affected. Even the disulfide bond replacement seemed to provide only minor influence on the rigid, constrained SFTI framework.

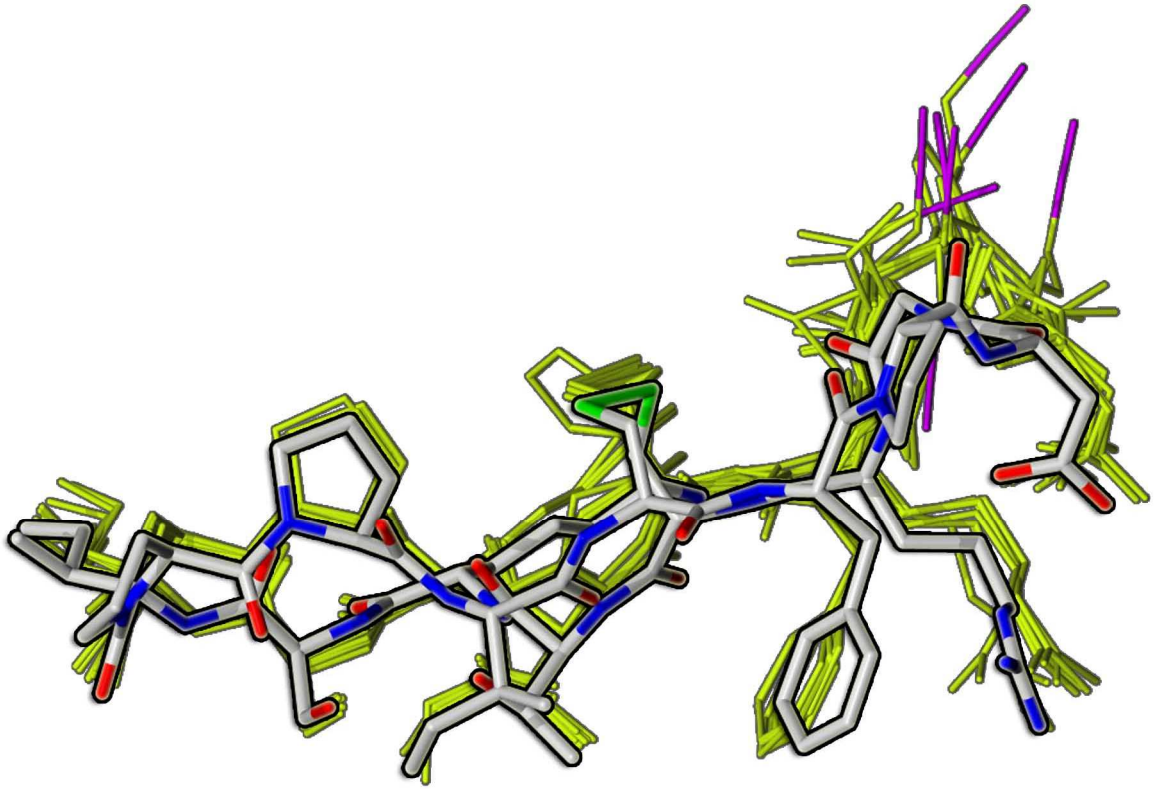

Figure 35. Overlay of computationally modeled inhibitors **5** – **12** (yellow, thin sticks) and SFTI-1[1,14] (sticks in element colors with grey: carbon, red: oxygen, blue: nitrogen, green: sulfur) after energy minimization of respective trypsin-inhibitor co-complexes and structural alignment using AMBER03 force field. Triple bond moieties are shown as purple sticks.

Table 10. Summary of geometric parameters from the *in silico* models of inhibitors **5** – **12** presumably influencing bioactivity and resulting SE during PHIP experiments. Values analyzed from model shown in **Figure 35**.

Entry	RMSD to SFTI-1[1,14] [Å]	Distance to *N*-terminus[a] [Å]	Distance to next backbone amide[b] [Å]	Distance to cystine bond[c] [Å]
5	0.3700	3.668	5.189	7.407
6	0.5021	6.767	2.881	9.976
7	0.6327	9.519	8.825	10.705
8	0.3750	-	4.656	7.288
9	0.3830	-	3.453	7.189
10	0.5449	-	9.170	10.680
11	0.6959	3.411	5.176	-
12	0.7856	9.066	8.314	-

a: Values calculated from mean distances between carbon atoms of triple bonds and nitrogen atom of terminal amine
b: Values calculated from mean distances between carbon atoms of triple bonds and nitrogen of nearest peptide bond
c: Values calculated from mean distances between carbon atoms of triple bonds and nearest sulfur atom

The *in silico*-determined geometric parameters of the modeled SFTI derivatives **5** – **12** are listed in **Table 11**. Generally, the RMSD values indicate the degree of structural similarity and the usability of **5** – **12** as mimic of the original inhibitor. According to the calculated RMSD values, the variants with low RMSD values, **5**, **8**, and **9,** were expected to possess respectively high inhibitory potency against trypsin. Analogously to the calculated RMSD values, the distances between triple bonds of the installed PHIP labels and potentially catalyst-poisoning elements, should give an indication to the efficacy of catalytic hydrogenation and, furthermore, to the resulting signal enhancement during PHIP experiments.

Finally, two further SFTI derivatives, **13** and **14,** bearing Tyr(*O*-allyl) or 4-pentenoic acid, respectively, at the positions for PHIP labeling were designed to study the T_1 relaxation times of the corresponding labels within the functional peptides. The corresponding sequences of **13** and **14** are shown in **Figure 36**. The modeled 3D structure was supposed to be similar to peptides **7** and **8**.

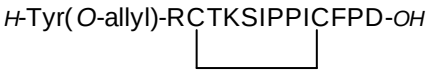

13

14

Figure 36. Inhibitors **13** and **14**.

3.2.1.1 Synthesis of peptides 5 – 10, 13, and 14

Peptidic inhibitor **5** was synthesized in the lab of Prof. Buntkowsky by manual SPPS; peptidic inhibitors **6 – 10, 13** and **14** were synthesized by partially automated SPPS, in both cases using standard Fmoc strategy. Peptides **8** – **10** were synthesized from the same starting batch, whereby the peptide-resin was splitted after chain elongation up to the last shared amino acid. The associated linear precursors were obtained in good to excellent yield (T**able 11**). All precursor peptides were side-chain-cyclized by oxidative folding in 0.1 M $(NH_4)_2CO_3$ buffer with 0.5 % DMSO (in few cases with addition of glutathione, see chapter 5.2.3) while monitoring reaction progress by HPLC and ESI-MS. The cyclized inhibitors were lyophilized and isolated by semi-preparative RP-HPLC. Chromatographic traces of peptidic inhibitors **5** – **10**, **13**, and **14** after folding and purification as well as the corresponding linear precursors are shown in F**igure 37**. In case of SFTI derivatives, the oxidative folding generally led to delayed elution of the product fraction compared to the corresponding precursors, indicating a decrease in net-polarity or drastic conformational changes within the molecules. Since the net-polarity of oxidized oligopeptides should not dramatically differ from the reduced species, the observed shift in R_t is assumed to be caused by structural constraint.

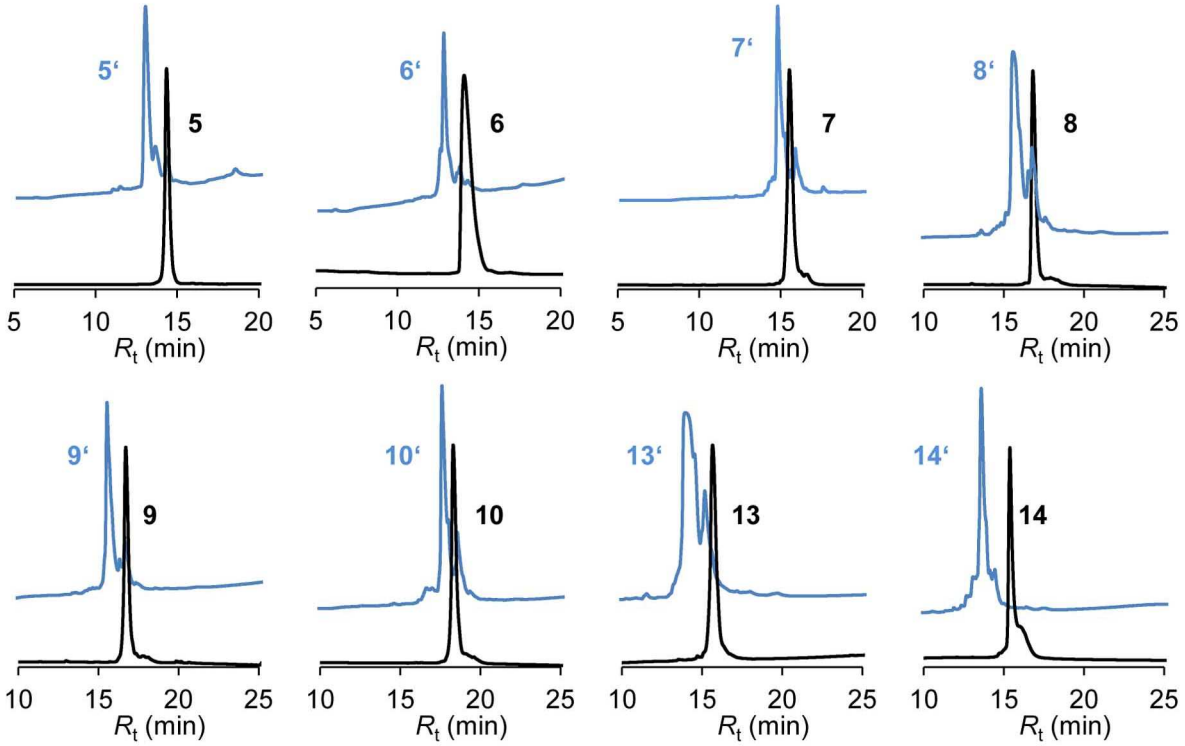

Figure 37. Chromatographic profiles of purified trypsin inhibitors **5** – **10**, **11, 12** (black) and corresponding linear precursors (blue). UV detection at λ = 220 nm; eluent **5** – **7**, **13**, **14**: 9→72 % acetonitrile in 0.1 % aq. TFA over 20 minutes at flow rate 1 ml/min, eluent **8**, **9**: 9→90 % acetonitrile in 0.1 % aq. TFA over 20 minutes at flow rate 1 ml/min.

The folding and purification yields and overall yields of the corresponding peptides are listed in **Table 11**. All crude yields were typical for SPPS. The variation in folding and purification yields resulted from the application of different oxidation conditions and batch sizes which influenced the recovery rate of chromatographic purification. The amount and purity of isolated inhibitors were sufficient for the examination of their inhibitory potential and PHIP activity.

Table 11. Synthesis of peptidic inhibitors **5** – **14**.

Entry	Strategy	MW	Crude yield precursor [%]	Folding/purification yield [%]	Overall yield [%]
5	Manual	-	55.6	18.8	10.5
6	Automated[a]	+	82.5	41.5	34.3
7	Manual	+	71.9	27.8	20.1
8	Automated[b]	+	94.6	35.8	30.8
9	Automated[b]	+	88.0	36.8	32.4
10	Automated[b]	+	81.2	40.3	32.5
13	Automated[b]	+	98.8	44.3	43.6
14	Automated[b]	+	76.6	41.7	31.7

a: Synthesized on Liberty® 12-channel peptide synthesizer platform.
b: Synthesized on Liberty® Blue peptide synthesizer platform.

3.2.1.2 Synthesis of peptide analogs 11 and 12

Peptidomimetic SFTI derivatives **11** and **12** were synthesized according to the published technique *via* manual Fmoc-SPPS and microwave-assisted on-support RuAAC.[73b] The strategy of synthesis depicted in **Scheme 21** relies on the side-chain macrocyclization by formation of the 1,5-disubstituted triazole from Pra and L-azidohomoalanine (Aha). Both surrogates were installed during iterative chain elongation using standard coupling protocols (see chapter 5.2.1) as Fmoc-protected building blocks.

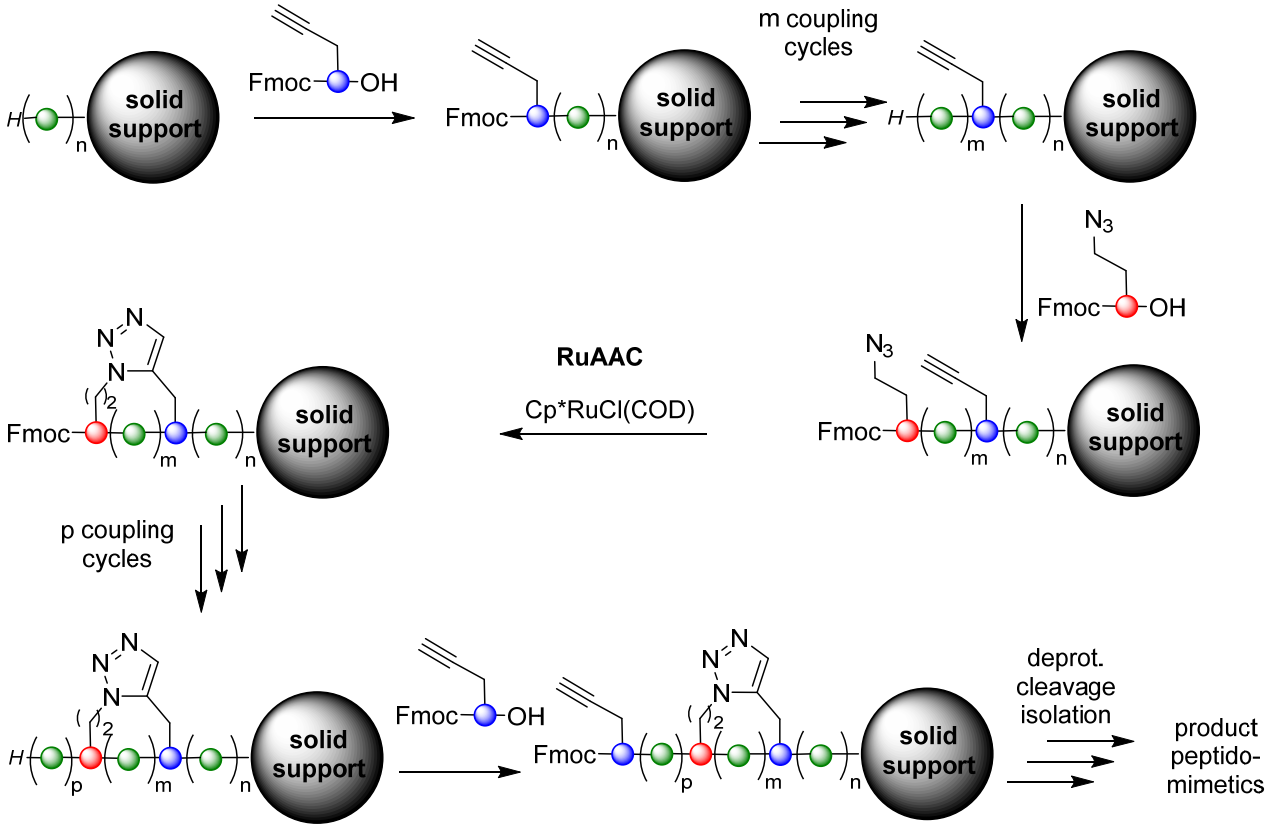

Scheme 21. Synthetic strategy towards peptides analogs with triazolyl disulfide surrogate *via* RuAAC on solid support. Amino acids and building blocks are depicted as colored balls with green: canonical amino acid; red: Aha; blue: Pra. Solid support is depicted as grey ball.

On-support macrocyclizations were accomplished after coupling of Arg2. To avoid undesired side reactions and maximize the efficacy of Ru(II) catalyst, RuAAC was performed under exclusion of humidity and atmospheric oxygen. The success of backbone macrocyclization was examined by treatment of the *N*-terminally deprotected and test-cleaved peptide analog **11a** (**Scheme 22A**) with reducing agent. If the reaction was incomplete, an m/z signal of a species with a reduced molecular weight of 26 (formation of an amine from azide by reductive cleavage of molecular nitrogen, **Scheme 22B**) should be observed in mass spectrometric analysis.

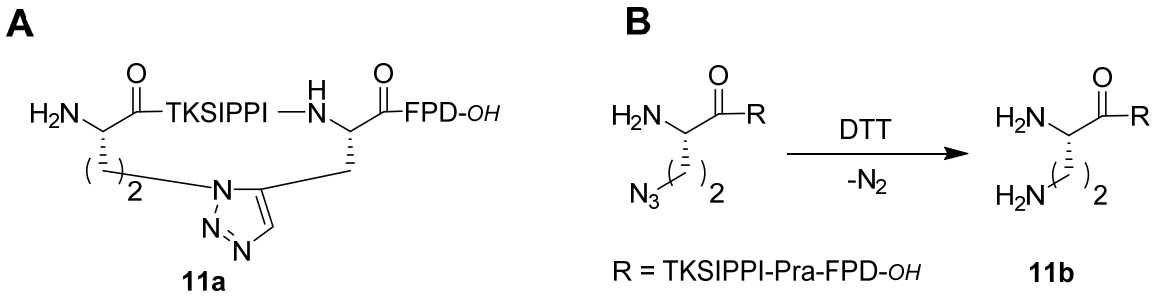

Scheme 22. A: Intermediate **11a**. **B**: Reductive denitrogenation of non-cyclized intermediate towards **11b**.

Since no corresponding mass peak was found in the ESI mass spectrum of the test-cleaved intermediate (**Figure 38**), the PHIP labels Pra or Tyr(*O*-propargyl), respectively, were attached to the deprotected resin-bound peptide.

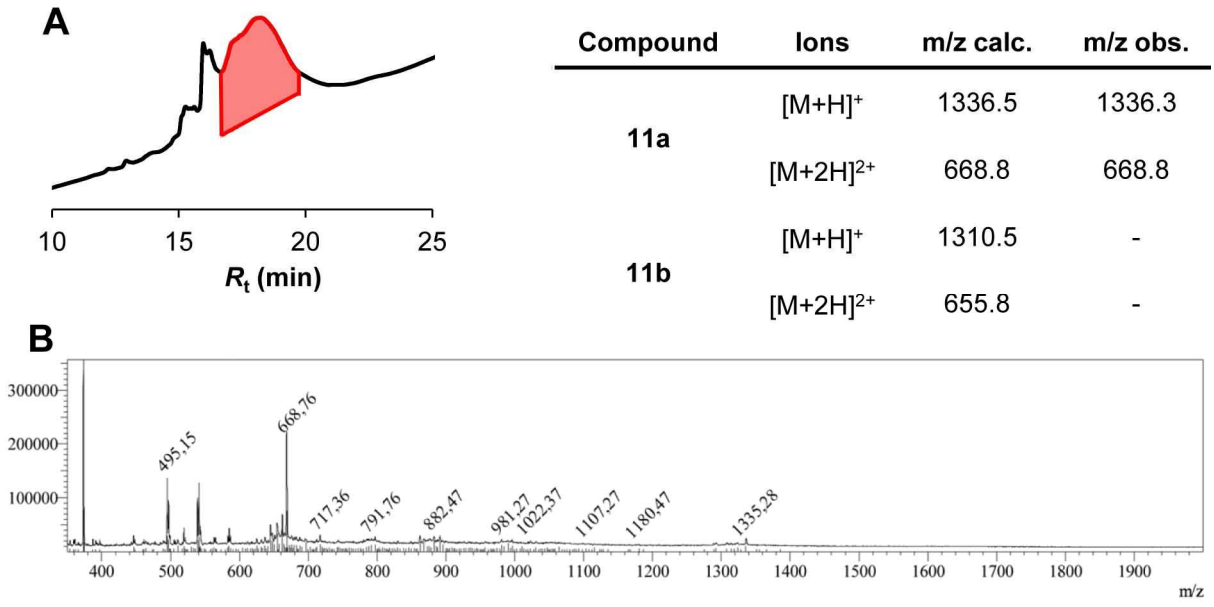

Compound	Ions	m/z calc.	m/z obs.
11a	$[M+H]^+$	1336.5	1336.3
	$[M+2H]^{2+}$	668.8	668.8
11b	$[M+H]^+$	1310.5	-
	$[M+2H]^{2+}$	655.8	-

Figure 38. A: Chromatographic trace of intermediate of **11** after RuAAC, Fmoc deprotection and test cleavage from solid support. UV detection at λ = 220 nm; eluent: 9→72 % acetonitrile in 0.1 % aq. TFA over 20 minutes at flow rate 1 ml/min. Main fraction collected for ESI-MS analysis is marked in red. **B**: ESI mass spectrum of collected fraction. Average ion counts are plotted against m/z.

After cleavage from support and purification, **11** and **12** were obtained in sufficient purity and amount for the examination of inhibitory and PHIP activity. Chromatographic traces of purified products can be found in the appendix. Corresponding yields of the peptide analogous are summarized in **Table 12**. The poor crude yield and purification yield resulted from the harsh reaction conditions during microwave-assisted RuAAC and the presence of the transition metal catalyst responsible for undesired complex formation hampering the chromatographic purification.

Table 12. Synthesis of peptidomimetic inhibitors **11** and **12.**

Entry	Strategy	MW	Crude yield [%]	Purification yield [%]	Overall yield [%]
11	Manual	+	39.1	12.0	4.7
12	Manual	+	48.1	11.6	5.6

3.2.2 Characterization and Evaluation of Activity

3.2.2.1 Bioactivity Assays

The majority of the results presented in this chapter was recently published.[50b] The inhibitory potency of the labeled SFTI derivatives **5** – **13** was studied by time-dependent protease inhibition assays analogously that described for the HNE and chymotrypsin inhibitors **1** – **4** in chapter 3.1.2. The most important issue of this investigation was to examine the influence of the installed PHIP labels in combination with certain structural modifications (disulfide mimicking motif and *N*-terminal capping) on the activity of the inhibitors. The general setup for bovine pancreas trypsin assays was similar to that described for other proteases in previous chapter, and Boc-QAR-pNA was used as a chromogenic substrate. Detailed experimental procedure is described in chapter 5.4.1. The Michaelis-Menten constant for the used enzyme-substrate system was determined as K_M = 58.9±7.8 μM (chapter 3.1.2.1). Furthermore, to evaluate if the discussed enzymatic reaction is also feasible under the conditions of NMR experiments and to assess how the activity is influenced by the solvent system, trypsin activity assays were performed in non-buffered D_2O (pD ~7.8) and distilled water (pH 6.8). Thereby, a K_M of 114.3±27.4 μM in non-buffered water and 51.3±18.3 μM in non-buffered D_2O were determined. These results did not find direct application in the present work, but they are important clues for the future development of PHIP NMR experiments with labeled inhibitors in presence of their target enzyme.

The substrate-independent inhibition constants for **5** – **13** were determined by a modified setup of an enzyme inhibition assay in trypsin activity buffer (TA buffer) composed of 50 mM Tris/HCl, 150 mM NaCl, 0.01 % Triton X-100, 0.01 % sodium azide, pH 7.6.[14a, 73b, 153] The resulted K_i and K_i^{app} values of all examined labeled SFTI derivatives are listed in **Table 13**.

All experimentally determined inhibition constants were at single-digit to subnanomolar range. Inhibitory activity of compound **6** was additionally tested in non-buffered D_2O (pD ~7.8) and distilled water (pH 6.8) for the reasons mentioned above. The obtained values for K_i were about one order of magnitude higher than those for the measurements in buffered system, but strong inhibitory potency around 10 nM was determined confirming the applicability of the inhibitory assay to non-buffered solvents.

Table 13. Inhibitory activity of inhibitors **5** – **13**.

Entry	Label (position)	Solvent	K_i^{app} (nM)	K_i (nM)[b]
5	**Pra** (1)	TA buffer	8.02±0.91	1.53±0.28
6	**Pra** (13)	TA buffer	8.12±1.46	1.55±0.32
6	**Pra** (13)	H_2O (pH 6.8)	57.25±4.44	10.91±3.27
6	**Pra** (13)	D_2O (pD 7.8)	45.76±10.04	8.73±2.91
7	**Tyr(*O*-propargyl)** (1)	TA buffer	7.37±1.18	1.41±0.27
8	**4-Pentynic acid** (1)	TA buffer	1.02±0.09	0.20±0.03
9	**Pra** (1)	TA buffer	1.12±0.15	0.21±0.04
10	**Tyr(*O*-propargyl)** (1)	TA buffer	1.09±0.10	0.21±0.03
11	**Pra** (1)	TA buffer	37.81±1.20	7.21±0.90
12	**Tyr(*O*-propargyl)** (1)	TA buffer	22.70±2.21	4.33±0.61
13	**Tyr(*O*-allyl)** (1)	TA buffer	6.68±0.81	1.27 ± 0.20

a: Error calculated by propagation of error for K_i^{app} and K_M (see chapter 5.4.1.3).

Three synthetic inhibitors (**8**, **9**, and **10**) displayed an inhibitory potential in the same range as their parental peptide (0.28 nM for monocyclic SFTI-1). This result is assumed to be caused by the lack of the free *N*-terminus in **8** – **10**. Indeed, their analogues, **5** and **7**, bearing an *N*-terminal amine, exhibited a K_i of ~ 1.5 nM. Considering the fact that the bicyclic SFTI-1 lacking an alpha-amine possesses a better K_i as its open-chain variant, the observed result corroborates the reported data on the inhibitory potency of SFTI constructs.[156] Since compounds **5** – **13** showed K_i in the range of tight-binding inhibitors, it was proven that their bioactivity was not affected by the labels, confirming the accuracy of the *in silico* modeling shown in **Figures 31 – 34** (chapter 3.2.1).

3.2.2.2 PHIP Experiments

All NMR PHIP experiments and corresponding data analysis were performed by Grit Sauer and Dr. Marco Körner from the working group of Prof. Buntkowsky at the Technische Universität Darmstadt. Prior to the PHIP experiments with the SFTI derivatives **5** – **13**, the ^1H hyperpolarization ability of individual building blocks Fmoc-L-Tyr(propargyl)-OH, 4-pentynoic acid, and the corresponding potential hydrogenation products Fmoc-L-Tyr(All)-OH and 4-pentenoic acid were examined (**Table 14**).

Table 14. SE factors and ^{1}H-T_1 values for the PHIP-active building blocks and their hydrogenation products.

	Fmoc-L-Pra-OH	Fmoc-L-Tyr(*O*-propargyl)-OH	Fmoc-L-Tyr(*O*-All)-OH	4-Pentynoic acid	4-Pentenoic acid
SE[a]	206	200	1.5	900	1.1
T_1[a]	2.2 s	3.5 s	3.1 s	5.2 s	5.0 s

a: SE and T_1 represents the average signal enhancement and relaxation time of the H_a-H_b spin system, it was not possible to distinguish between the protons.

Hydrogenation was performed with 50 % para-enriched H_2 at a pressure of 2 bar in methanol-d_4 and using Rh(dppb)(COD)BF_4 as a homogeneous catalyst. Generation of para-H_2 was realized by cooling with liquid nitrogen with activated charcoal as catalyst.[157] The samples containing a probe and a catalyst were treated with para-H_2 and vigorously shaken for a short time at terrestrial magnetic field. Subsequently, the reaction mixtures were placed immediately in the NMR spectrometer and the hyperpolarized spectra were detected by a single scan experiment using a 45° excitation pulse. After relaxation of the hyperpolarized state, the spectra of the hydrogenation products under thermal equilibrium were recorded employing multiple scans (typically 256 scans). These signals were required for the calculation of signal enhancement (SE) factor which is defined as the ratio of the integrals of the hyperpolarized signals and corresponding signals at thermal equilibrium (details in chapter 5.3.2). Besides the hyperpolarized signals of the hydrogenated probes, additional hyperpolarized signals around 5.8, 2.2, and 1.5 ppm were observed. These signals were caused by the self-hydrogenation of the cyclooctadienyl moiety of the catalyst, as reported by Aime et al. 2001.[158]

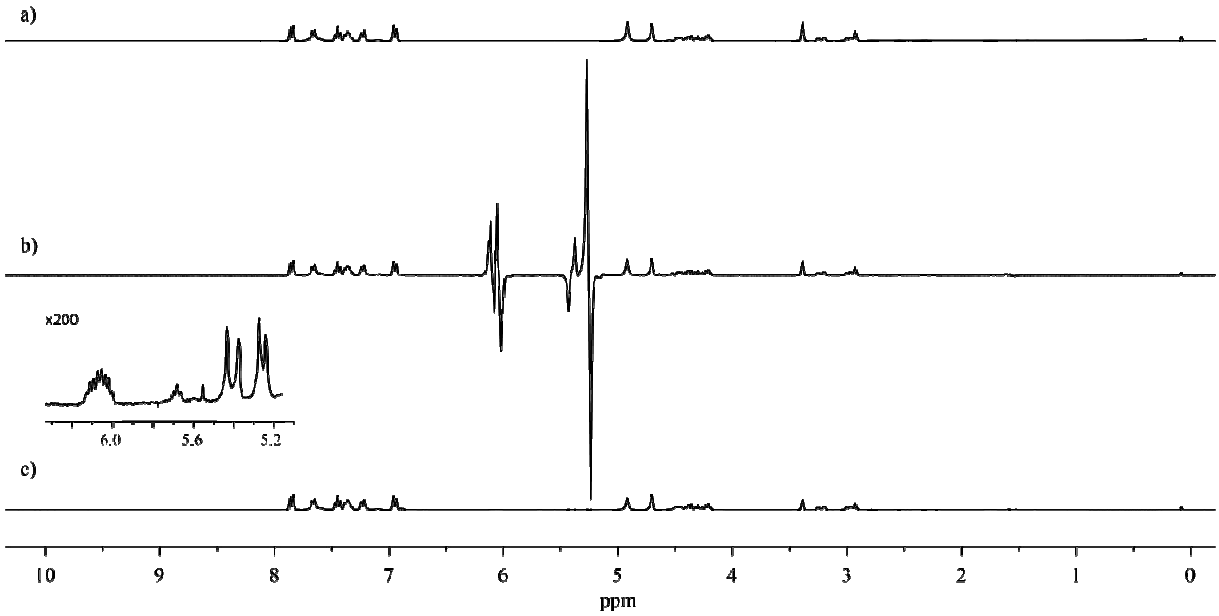

Figure 39. a) ^{1}H NMR spectrum at 300 MHz of Fmoc-Tyr(*O*-propargyl)-OH and Rh(dppb)(COD)BF_4 in methanol-d_4; b) 46 s after the hydrogenation with para-enriched hydrogen was started; c) 150 s after hydrogenation with para-enriched hydrogen. Figure applied from own publication.[50b]

The SE observed during hydrogenation of the propargyl moiety of Fmoc-L-Tyr(*O*-propargyl)-OH (**Figure 39**) with an enhancement factor of 200 were in same range as the factor we have

reported for Fmoc-L-Pra-OH in pervious publication.[159] The hyperpolarized proton signals were found at 5.2-5.5 ppm. Hydrogenation of the triple bond of 4-pentynoic acid towards respective 4-pentenoic acid exhibited an enhancement factor of 900 which was more than 4 times higher than the SE of the Fmoc-protected PHIP labels. In an examination of the longitudinal relaxation times T_1 for the newly formed CH_2 (H^a/H^b) group of the double bond within the discussed building blocks (see chapter 5.3.2.1 for details), the highest T_1 value was also observed for 4-pentynoic acid (see **Table 14**) underlining the high PHIP activity of this compound. SE for the second hydrogenation step towards fully saturated products was negligibly small or not observable. As the T_1 values of these compounds were in same range as their triple bond-bearing analogues, the efficacy of hydrogenation (and not the polarization transfer efficacy) is assumed to be the main reason for the lack in PHIP activity.
After these preliminary experiments, PHIP experiments were performed with the labeled SFTI derivatives **5** – **13** using the same reaction setup and conditions as described above. The obtained SE factors of all PHIP measurements are summarized in **Table 15**.

Table 15. SE values for SFTI-derivatives **5** - **13**, experimentally determined in ALTADENA experiments.

Entry	Label (position)	Macrocyclization	*N*-terminus	SE[a]
5	**Pra** (1)	cystine	*H-*	*n.h.*
6	**Pra** (14)	cystine	*H-*	*n.h.*
7	**Tyr(*O*-propargyl)** (1)	cystine	*H-*	70
7[b]	**Tyr(*O*-propargyl)** (1)	cystine	*H-*	74
7[c]	**Tyr(*O*-propargyl)** (1)	cystine	*H-*	66
8	**4-Pentynic acid** (1)	cystine	none	5
9	**Pra** (1)	cystine	*Ac-*	*n.h.*
9'	**Pra** (1)	-	*Ac-*	*n.a.*
10	**Tyr(*O*-propargyl)** (1)	cystine	*Ac-*	68
10'	**Tyr(*O*-propargyl)** (1)	-	*Ac-*	65
11	**Pra** (1)	triazole	*H-*	*n.a.*
12	**Tyr(*O*-propargyl)** (1)	triazole	*H-*	35
13	**Tyr(*O*-allyl)** (1)	cystine	*H-*	*n.h.*

a: Values were calculated as described in chapter 5.3.1.
b: SE was studied in a water-methanol-d_4 mixture (1:1, v/v) at 333°K
c: SE was studied in a water-ethanol-d_6 mixture (1:1, v/v) at 333°K
n.h.: No hydrogenation was observed; n.a.: not analyzable, product signals were negligibly small.

For the majority of the investigated SFTI derivatives typical antiphase signals for ALTADENA experiments were found, whereby no or only negligibly small signals of the corresponding hydrogenation products could be detected for the compounds **5**, **6**, **9**, **11**. These compounds were all labeled with Pra which exhibited stronger SE as an Fmoc-protected building block. The observation supported our suggestion (chapter 2.2) that the hydrogenation efficacy can be affected by the presence of functional groups with strong electron donor character, especially when the distance between the target triple bond moiety and the peptide backbone is not sufficient. Compound **13** labeled with a Tyr(*O*-All) group showed no PHIP activity, too. This was according to our expectation, since the Fmoc-protected building block Fmoc-L-Tyr(All)-OH exhibited only low SE of 1.5.
Contrary, the high SE factors in range of 35 – 70 were obtained for the SFTI variants labeled with Tyr(*O*-propargyl) at the position 1 (compounds **7**, **10**, and **12**). The ^{1}H NMR spectra of **7** which showed the highest PHIP activity with an SE of 70 upon ALTADENA experiment is shown in **Figure 40**. Further examples of PHIP NMR spectra can be found in the appendix or respective publication.[50b]

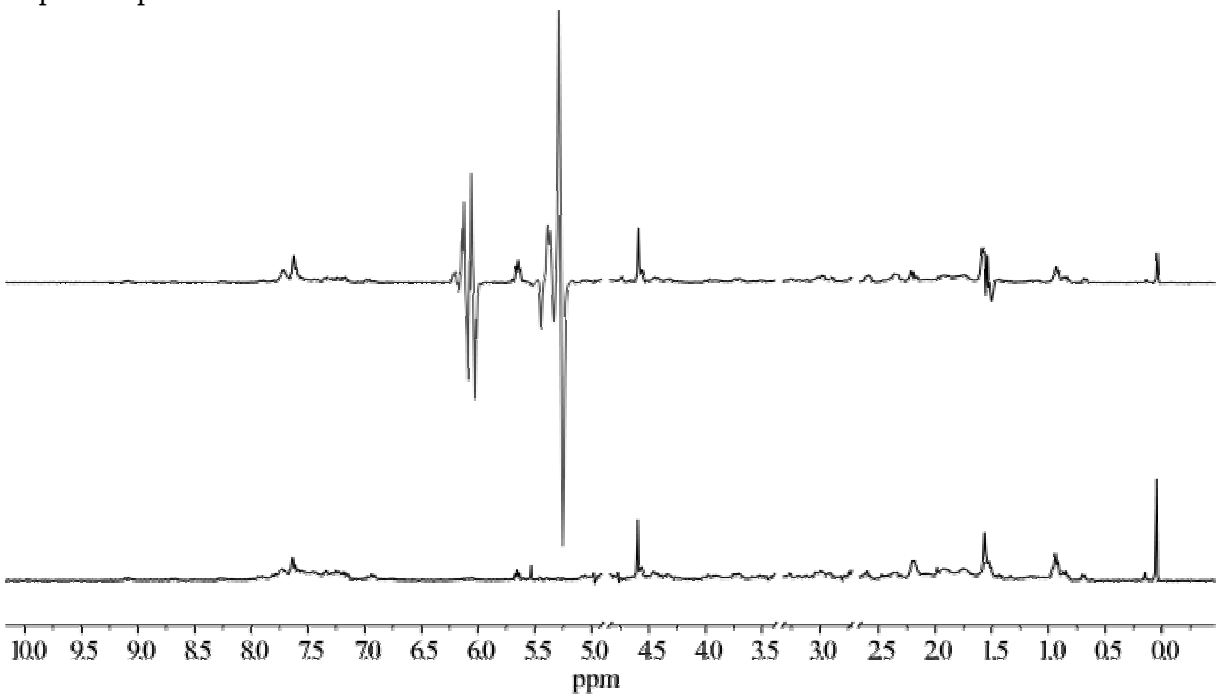

Figure 40. Top: ^{1}H-NMR spectrum of the reaction mixture comprising **7** and Rh(COD)(dppb)BF_4 in methanol-d_4, recorded ca. 34 s after hydrogenation with para-enriched hydrogen. Bottom: ^{1}H-NMR spectrum recorded after relaxation of polarized spin states. Figure applied from own publication.[50b]

The ^{1}H relaxation time of the resulting CH_2 (H^a/H^b) group in **7** was determined as T_1 = 2.8 s. This value was at the same range as the ^{1}H T_1 time determined for the CH_2 groups of **8** (T_1 = 2.5 s). However, the SE of **8** was obviously lower by the factor of more than ten (SE of about 5). As the free 4-pentynoic acid exhibited the highest SE while possessing a T_1 relaxation time at the same order of magnitude as all other compounds, this result was against our expectations and supported our assumption that the observed SE of the individual building blocks and their respective SFTI-bound derivatives are only minimally stipulated by the relaxation behavior of the spin-states. Hence, the efficacy of PHIP is supposed to be determined by the rate of Rh-catalyzed hydrogenation process, which includes the binding of para-H_2 at Rh-center yielding the dihydrido complex and coordination of the catalyst with the

respective multiple bond, as well as the migratory insertion of H-atoms at the unsaturated bonds. Thus, the kinetics of hydrogenation is influenced by diverse structural issues.

The influence of the free *N*-terminus that provides a suitable coordination site for the catalyst was further examined with the *N*-terminally acylated peptides **9** and **10**. The Pra-labeled peptide **9** displayed only very weak antiphase signals while its Tyr(*O*-propargyl)-labeled analog **10** exhibited an excellent SE of factor 68 which was at same range as SE found for the non-acylated variant **7**. This outcome and the fact that peptide **8** lacking an *N*-terminus exhibited only a moderate SE of 5, indicates that the signal enhancement cannot be enhanced by elimination of an alpha-amine.

A similar result was found for the triazolyl-cyclized peptide analogs **11** and **12**. As shown for its cystine-bridged counterpart **5**, no distinct SE could be observed for Pra-labeled **11**, whereas respective Tyr(*O*-propargyl)-bearing peptidomimetic **12** exhibited a strong SE with a factor of 35. Interestingly, this value was decreased by a factor of two compared to its cystine-cyclized parental peptide **7** and other Tyr(*O*-propargyl)-labeled peptides **9** and **9'**, which indicates that the triazolyl moiety probably affects the hydrogenation process by providing a further suitable coordination site for the Rh-catalyst.

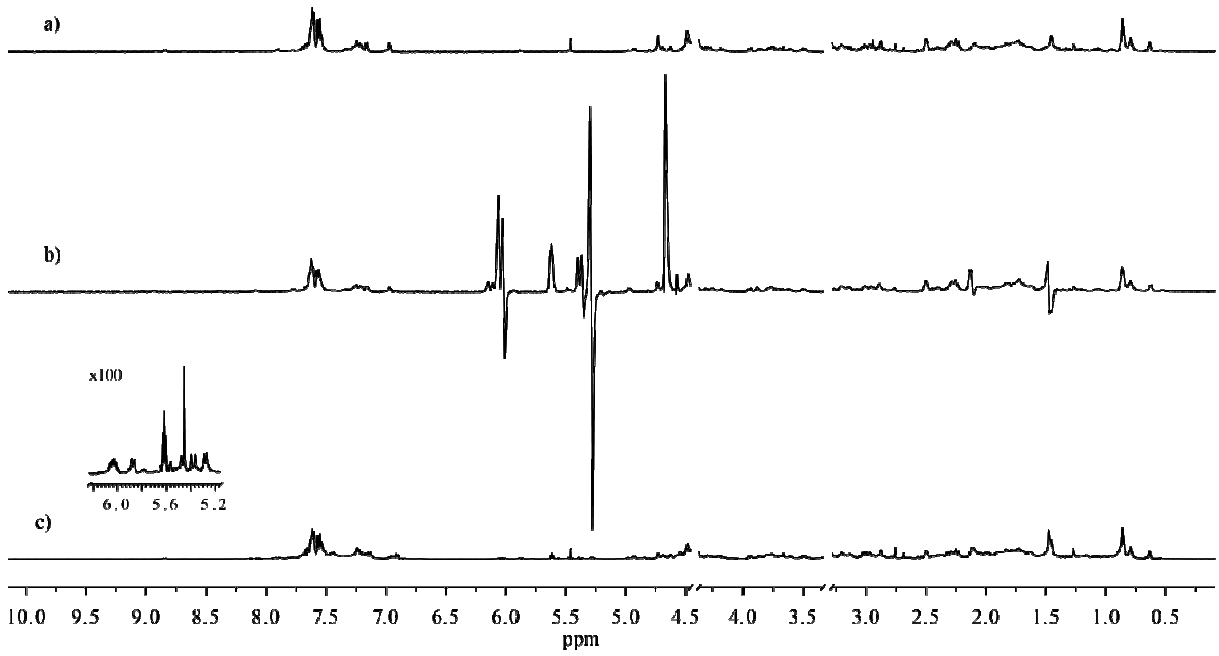

Figure 41. a) ^{1}H NMR spectrum at 500 MHz of **7** and Rh(dppb)(COD)BF_4 in D_2O-methanol-d_4 (1:1, v/v); b) 22 s after the hydrogenation with para-enriched hydrogen was started; c) 150 s after hydrogenation with para-enriched hydrogen. All Spectra were recorded at 333 K. Figure applied from own publication.[50b]

Furthermore, ALTADENA experiments with **7** were conducted in aqueous systems as D_2O-methanol (**Figure 41**) and D_2O-ethanol (1:1, *v/v*). The rationale behind it was to evaluate the applicability of PHIP experiments in more biocompatible environment, as some organic solvents can affect folding and activity of biomolecules. The experiments were performed at 333 K since the catalyst required an elevated temperature (data not shown). In both solvent systems, water-MeOH and water-EtOH, strong SE of 74 and 66, respectively, was determined for **7**. These values were similar to that in neat MeOH (SE = 70) corroborating the general

applicability of the discussed system for PHIP experiments. We also have evaluated the structural integrity and preservation of the inhibitory activity of **7** under these conditions by HPLC, ESI-MS and inhibitory assay of the hydrogenated product after incubation at 333 K for 30 min. The obtained K_i^{app} was with 7.57±0.88 nM similar to the value determined in the experiment without thermal treatment (K_i^{app} = 6.68±0.81 nM).

3.2.3 Digest of Chapter 3.2

PHIP-labeled trypsin inhibitors **5** - **14** were computationally and knowledge-based designed by using SFTI-1 as a starting point and synthesized *via* SPPS. Their PHIP activity was examined by ALTADENA experiments and the bioactivity was evaluated in trypsin inhibition assays. The majority of the synthesized peptides and peptide analogs exhibited characteristic antiphase signals at 6.5-5.0 ppm, but a distinct enhancement in NMR signals could only be observed in case of Tyr(*O*-propargyl)-labeled variants **7**, **10**, **12** and the 4-pentynoic acid-labeled **8**. Best values of SE were found for the peptide **7**, with free *N*-terminus and a cystine-bridged macrocyclization. This suggests that the effect of catalyst poisoning by competitive coordination by these moieties has only a minor influence to the SE, compared to the remoteness of the unsaturated moiety from the peptide backbone.

A comparison of the ^{1}H-T_1 relaxation time of the individual labels (or the Fmoc-protected derivatives) and the observed SE of the synthesized peptides revealed no direct correlation between ^{1}H-T_1 relaxation time and the enhancement of PHIP signals, thus underlining the hypothesis that the PHIP activity strongly depends on the hydrogenation efficacy as described in chapter 2.2. On the whole, we suppose that the degree of signal enhancement mainly depends on the hydride transfer between unsaturated bond and metal ion center and the competition with further coordination sites of the biomolecules while the T_1 relaxation represents a general prerequisite for the PHIP effect.

The outcome of PHIP experiments are in good accordance with the geometric parameters determined from the *in silico* models (chapter 3.2.1). Indeed, only the compounds where the distance between the triple bond and the nearest electron-donating moiety is larger than 5 Å exhibited strong SE. An exception could be seen in case of **8** with a distance to the next backbone amide of 4.657 Å. This can be explained by the extremely strong inherent PHIP activity of the label.

Furthermore, the compatibility of the PHIP experiments with aqueous milieu was also demonstrated using water-MeOH and water-EtOH mixtures. Under these conditions and elevated temperature, peptide **7** exhibited strong SE without loss in the enhancement factor while preserving its structural integrity and inhibitor activity.

The K_i's of **5** - **13** were all in single-digit nano to picomolar range, thus a distinct decrease in inhibitory activity was only found for the triazolyl-cyclized variants **11** and **12** with the deterioration in K_i by the factor of 3 – 5 compared to their parental peptides **5** and **7**. These values are similar to those reported by Empting et al. for the decrease in activity of SFTI-1[1,14] upon disulfide mimicking by a 1,5-disubstituted triazole (decrease by the factor of 1.6).

Interestingly, several novel inhibitors presented an inhibitory potency similar to the original SFTI-1[1,14]. These inhibitors (compounds **8** - **10**) all lack a free *N*-terminus and exhibited

enhanced inhibitory activity by the factor of ~7 compared to their related peptide **5** and **7** with an *N*-terminal amine.

On the whole, the influence of the PHIP labels on the inhibitory activity is kept within a limit, thus all examined inhibitors displayed K_i values in the range of tight-binding inhibitors. The obtained K_i's were generally in accordance with the tendency of the *in silico* determined RMSD values with the exception of the Tyr(*O*-propargyl)-labeled variants as they showed better activity than expected from the computational models. This outcome confirmed our prediction that the labeling at positions P1 and P14 only minimally affects the bioactivity of the inhibitors.

The compatibility of the assays in NMR-related solvents was also confirmed, whereby a slight decrease in inhibitor activity by a factor of about 6 – 7 was found compared to the setups in the buffered milieu.

3.3 Affinity-Guided Chemical Ligation towards Multifunctionalization of Biomolecular Scaffolds

3.3.1 Design and Synthesis

The model systems for affinity-guided ligation in the presented work comprised only a pair of reactive moieties for the bioorthogonal ligation linked to complementary guiding units for spatial pre-arrangement of associated functionalities. Fundamental experiments towards establishment of a generally applicable reaction setup for the affinity-guided SPANC were tested on a heterodimeric coiled-coil system.

The sequences of a modified synthetic, three-heptad E/K coil pair were derived from the coiled-coil heteromer originally designed for Rh-metallopeptide catalyzed Trp modification published by Popp et al.[127b] During screening for an appropriate conjugation technique applicable for the modification of protein scaffolds, the mentioned methodology was chosen as possible candidate (data not shown). However, after preliminary studies, we renounced our attempts due to several reasons, among them poor reaction rate and the narrow range of applicable diazo-modified ligands. However, the α-helical peptides synthesized during this trial, $\mathbf{K3_{g,d}2E_2}$ and $\mathbf{E3_e2W}$ were already tested for heterodimerization in the original publication and could be conveniently reused for preliminary experiments of the SPANC-based model system. All amino acid substitutions (pinpoint derivatization from E/K coil system with consistent sequence) in respective coils are orthogonal to the reactive functionalities of SPANC, hence no undesired interference to the final conjugation was expected. The installation of SPANC-reactive moieties within the Lys-rich $\mathbf{K3_{g,d}2E_2}$ coil was planned to be realized by *N*-terminal elongation of the coils by corresponding precursor residues.

Towards incorporation of a strained, cyclic alkyne group, two various strategies depending on the pre-installed linker functionalities of two commercially available (1*R*,8*S*)-bicyclo[6,1,0]non-4-yne (BCN) derivatives were proposed. First, the on-support attachment of (1*R*,8*S*,9*s*)-bicyclo[6.1.0]non-4-yn-9-ylmethyl *N*-succinimidyl carbonate (BCN-NHS) to the free *N*-terminal amine or to the deprotected side chain of Lys was considered. The second strategy was the in-solution conjugation of BCN-$(POE)_3$-NH-C(O)$(CH_2)_3$-maleimide (**15**) to the side chain of Cys *via* maleimide conjugation. Since the on-resin installation of the BCN moiety was unsuccessful in a preliminary trial (probably due to the non-compatibility of BCN to either Fmoc deprotection or strongly acidic cleavage conditions). Therefore, the in-solution strategy was chosen for conjugation of a BCN moiety to the guiding unit. Consequently, the precursor K coil peptide **16'** and its derived product **16** were designed (**Scheme 23**). As *C*-terminal functionality, an amide was chosen instead of a carboxylic acid. The chemical and physical properties, especially the affinity towards dimerization of the coils should not be influenced dramatically by this exchange.

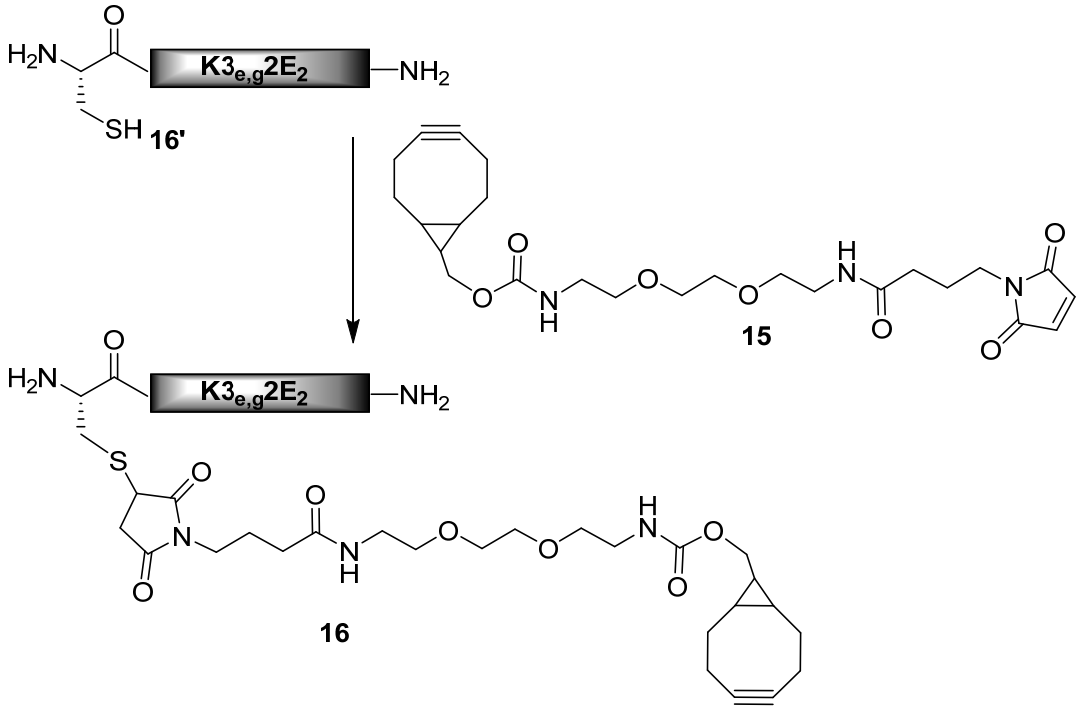

Scheme 23. Compounds **15**, **16'**, and **16** and reaction scheme towards formation of **16** by maleimide-sulfhydryl conjugation. Guiding unit part is shown as a grey bar.

As a counterpart for **16,** the acidic **E3$_e$2W** coil should be equipped with a glyoxylyl moiety at the side chain. The most popular technique to incorporate aldehydes into proteins is the oxidation of terminal vicinal diols and amino alcohols by periodate.[160] For this purpose, the modified E coil with an *N*-terminal Lys residue equipped with Ser at the side chain (**17'**) was designed as precursor peptide of respective aldehyde-bearing guiding unit **17** (**Scheme 24**).

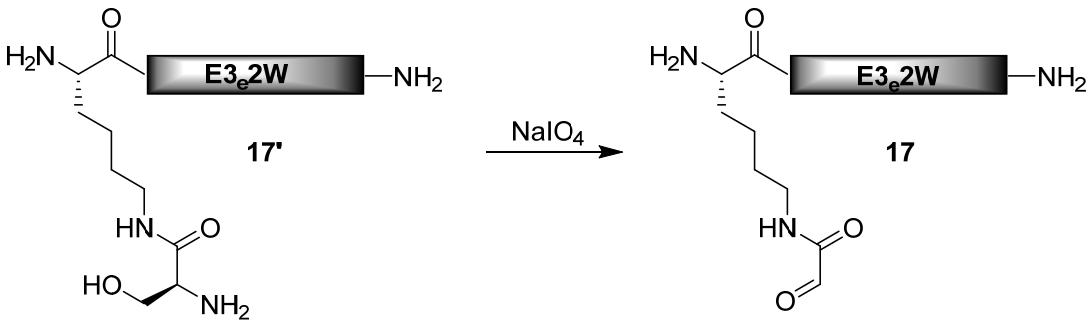

Scheme 24. Peptidomimetics **17'** and **17** and reaction scheme towards formation of **17** by periodate-mediated oxidation of a corresponding amino alcohol. Guiding unit part is shown as a grey bar.

Both of the modified coils **16** and **17** were computationally modeled from the crystal structure of a three-heptad coiled-coil heterodimer (PDB: 1U01) by residue exchanges and energy minimization (**Figure 42**). The key issue of this *in silico* study was to ensure that the collision of the reactive moieties for SPANC is not influenced by the length or strains within the linker units between reactive sites and peptide backbone.

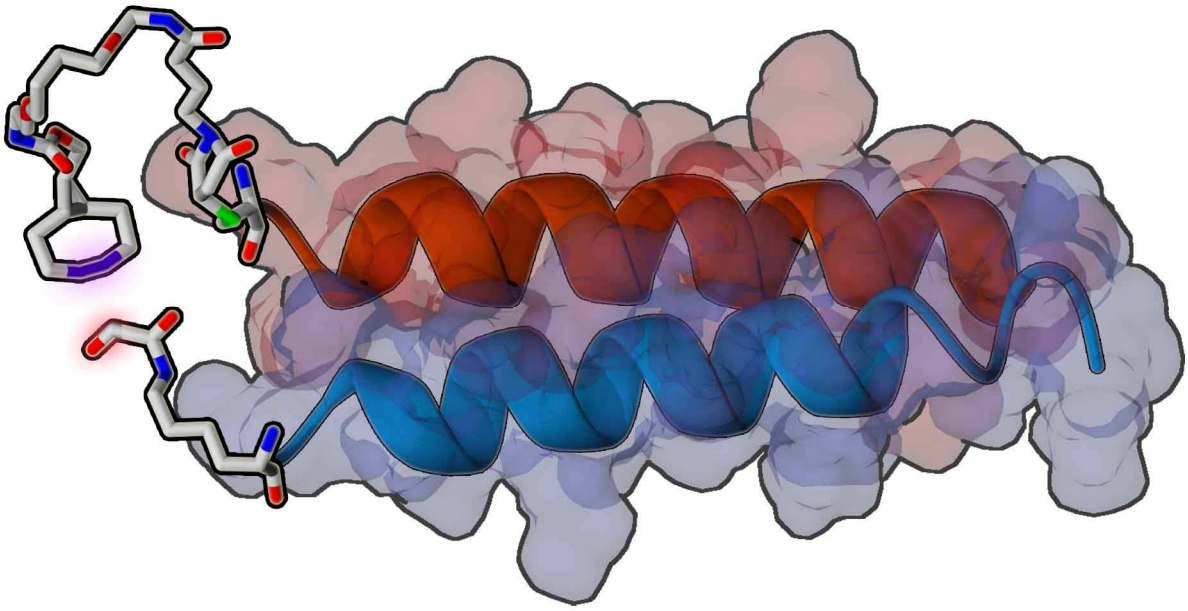

Figure 42. 3D computational model of the modified three-heptad coiled-coil system comprising **16** (orange) and **17** (blue). Structure derived from solution NMR structure of original E/K coil system[161] (PDB: 1U01) by residue substitution, *in silico* building, and energy minimization. Secondary structures of α-helices shown in cartoon style. SPANC-reactive moieties are shown as sticks with grey: carbon; red: oxygen; blue: nitrogen; green: sulfur. Strained triple bond within the BCN moiety is highlighted in purple.

A molecular dynamic simulation of the computational model demonstrated that the aliphatic hydrocarbon chains and the oligoethylene glycol unit within the linkers comprised high degree of freedom, thus ensuring sufficient flexibility for the desired collision of associated functionalities.

Furthermore, a second coiled-coil model system for affinity-guided SPANC comprising a coiled-coil heteromer with an expanded number of repetitive heptads was designed. Since the strength of coiled-coil interactions depends on the length of the complementary recognition sites, stronger affinity and, conclusively, enhanced reaction rate of the cycloaddition was expected to the new system. The coiled-coil scaffolds of the second model system are composed of five repetitive heptads with the consistent sequence of XISALXY (X = K and Y = E for K coil; X = E and Y = K for E coil). Same strategies as described for the three-heptad system were planned for the installation of the reactive moieties within the guiding units. BCN-functionalized peptide **18** and its aldehyde-bearing reaction counterpart **19** and corresponding precursor peptides **18'** and **19'** before in-solution modifications are depicted in **Figure 43**.

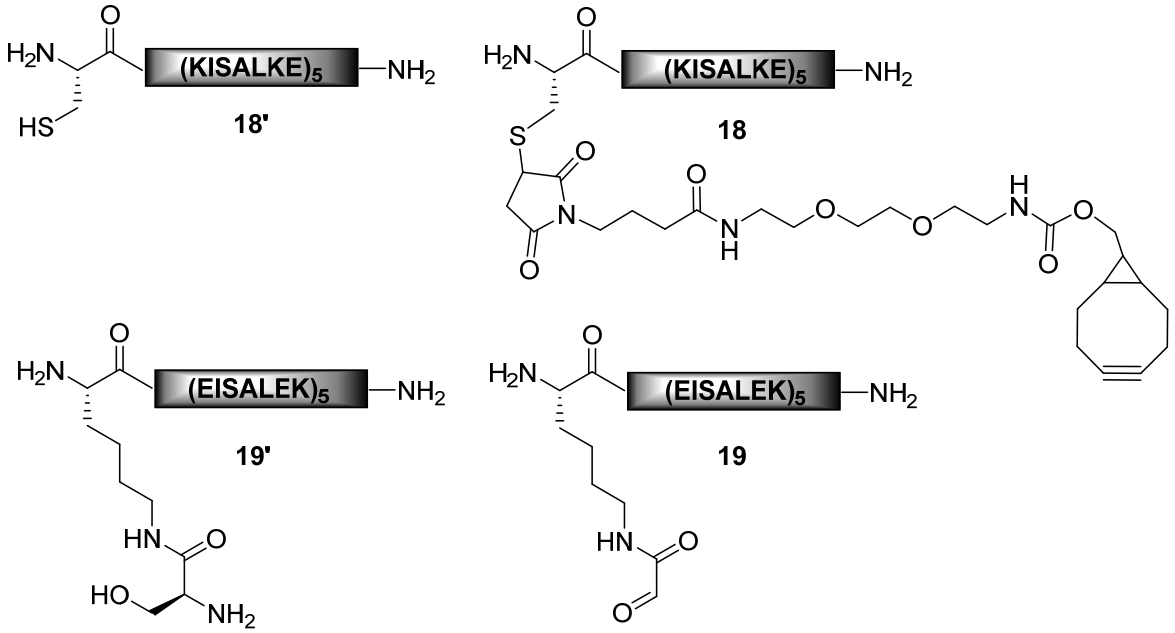

Figure 43. Peptidomimetics **18**, **19** and corresponding precursor peptides. Guiding unit parts are shown as gray bars.

Conclusively, the molecular design and synthesis strategy applied to the coiled-coil model system were transferred to a model system using a complementary PNA oligomer pair as guiding unit. The sequences of the PNA oligomers (PNA **A** and PNA **B**) were taken from a publication of Lygina et al.[138] Respective sequences and all further PNA sequences used in presented work, are listed along with the corresponding abbreviation in **Table 16**.

Table 16. Sequence and corresponding abbreviation of PNAs used in the presented work.

Sequence	Abbreviation	Comment
gtagatcact	PNA **A**	Complementary to PNA **B** (parallel).
catctagtga	PNA **B**	Complementary to PNA **A** (parallel).
agtaagctct	PNA **C**	No complementarity to PNA **A**, **B**, **D**, **E**.
tatagtagatcact	PNA **D**	PNA **A**, *N*-terminally extended for cross-conjugation
catctagtgaggag	PNA **E**	PNA **B**, *C*-terminally extended for aptamer loading

According to the melting temperature T_m of 46 °C reported in the literature for the similar constructs,[138] the hybridization affinity between this parallel interacting PNA pair was expected to be sufficiently strong for the proposed application despite its small size. Consequently, BCN-equipped PNA oligomer **20** and aldehyde-bearing PNA oligomer **21** were designed according to the strategies discussed for the former model systems. The simplified structures and sequences of respective compounds **20**, **21**, and corresponding precursors **20'**

and **21'** before in-solution modifications are depicted in **Figure 44**. As the incorporation of a basic amino acid is a common strategy to improve the solubility and cellular uptake of PNAs,[162] the *C*-terminally installed Lys residue had the same purpose and is proposed not to affect hybridization of the PNA oligomers.

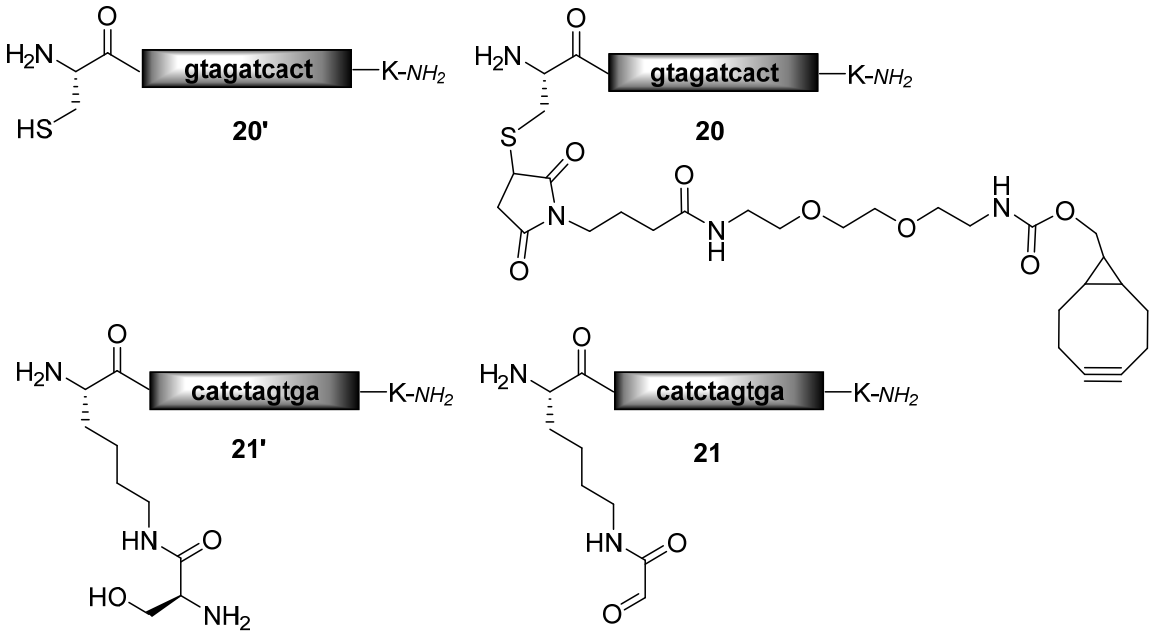

Figure 44. Conjugate **20**, **21** and corresponding precursor PNA-peptide hybrid molecules. Guiding unit parts are shown as gray bars.

However, a 3D computational modeling of **20** and **21** was not possible since no crystallographic data of PNAs with corresponding sequences has been published so far and *de novo* building of the molecules was not possible due to the lack of structural clues and exact physical properties of PNA monomers required for successful simulations. Nevertheless, as the installed reactive moieties for SPANC, including linker and conjugation units, are completely the same as the previously described coiled-coil systems, similar chemical properties were expected for the PNA-based model system.

Additionally, a further PNA-peptide hybrid **22** comprising an alternative PNA sequence (PNA **C**), neither complementary to PNA **A** nor to PNA **B**, but with the same modifications and SPANC-reactive functionalities as in **21** was designed. This hybrid molecule was aimed to act as a competitor of **21** to check the selectivity provided by the affinity-guided approach. Sequences and simplified structures of **22** and its precursor **22'** are shown in **Figure 45A**.

Based on the complementary sequences of PNA **A**

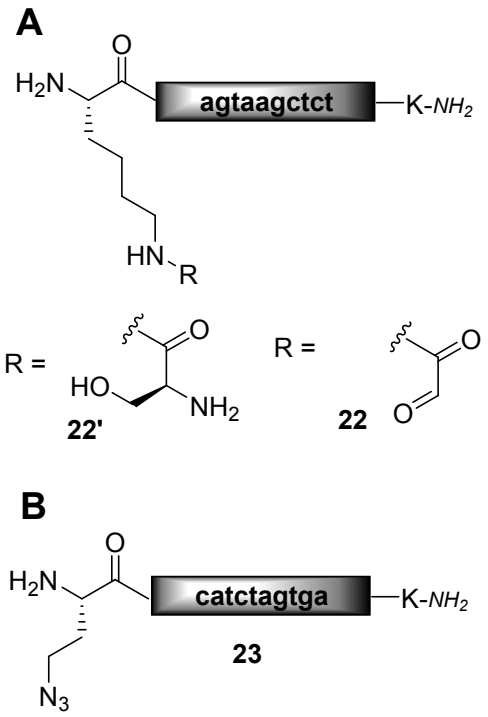

Figure 45. A: PNA-peptide hybrid molecule **22** and corresponding precursor **22'**. **B**: PNA-peptide hybrid molecule **23**. Guiding unit parts are shown as gray bars.

and PNA **B**, further model systems using PNAs as guiding units but comprising diverse bioorthogonal conjugations as an alternative to SPANC were designed. Aha-bearing PNA oligomer **23** (**Figure 45B**) possessed the same PNA scaffold as **21** and was drafted for the application of SPAAC. As this technique required a strained alkyne as a reactive counterpart, no further design of the alkyne-bearing PNA was needed. The purpose of this examination was to compare the efficacy of SPANC and a non-triggered SPAAC.

As described in chapter 2.3.1, UVA irradiation-mediated psoralen cross-conjugation was chosen as a triggered alternative to SPANC. This two-step cycloaddition (**Scheme 25A**) between psoralen, a DNA-intercalating aromatic photosensitizer, and two thymine bases of hybridized, complementary nucleic acid strands has found application for the treatment of vitiligo and psoriasis.[163] On the other hand, it is a useful tool for structural studies of nucleic acids.[164] The reaction is triggered by electromagnetic irradiation with a wavelength of λ = 320-380 nm and can also be reversed by high frequency UV irradiation of λ = 220-280 nm. The technique utilizes the spatial pre-arrangement of the corresponding reaction sites of psoralen and thymine provided by the selective intercalation of psoralen to the major groove of DNA typically formed by successively ordered nucleic acid sequences of an A-T and T-A pair (**Scheme 25B**).

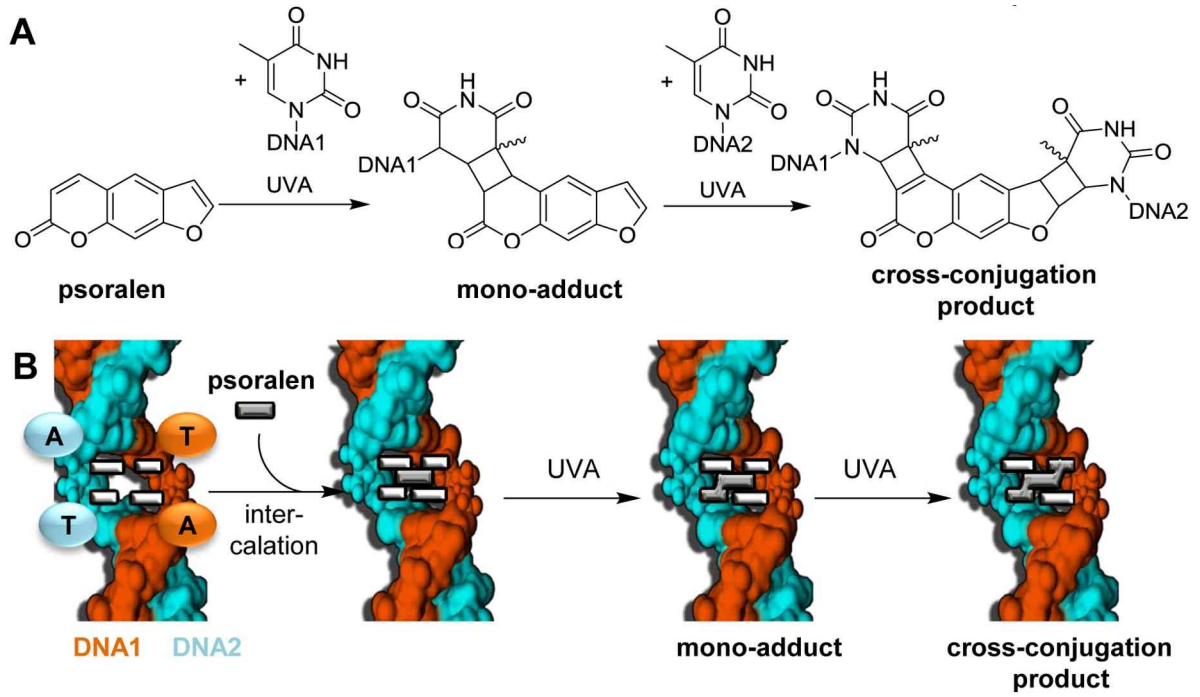

Scheme 25. A: General reaction scheme of UVA-mediated two-step cycloaddition of psoralen to two thymine bases. **B**: Schematic depiction of the psoralen-mediated cross-conjugation of complementary DNA strands from side view. Structure of DNA strands modeled and modified from NMR structure (PDB: 2V3L). Plain nucleobases are depicted as white bars. Psoralen molecule and cycloadducts are depicted as gray shapes.

However, considering the fact that the sequences of PNA1 and PNA2 contain a number of respective sequence pattern, an uncontrollable multiple addition of the psoralen molecule was expected making the direct application of **20** and **21** inappropriate as selective conjugation technique. An idea to overcome this drawback was found in the publications of Okamoto et al. 2001[165] and Kim et al. 2007,[166] who reported the synthesis and application of a psoralen derivative preinstalled into a PNA oligomer, whereby the cross linker was used for selective cross-conjugation of two complementary DNA strands *via* PNA-mediated sequence specificity.

Nevertheless, a psoralen unit covalently linked to one of the PNA oligomers would limit the possible cross-conjugation sites and was expected to provide advantage in stoichiometrical and site-selective conjugation. To this end, the sequence of PNA **B** was redesigned with an *N*-terminal extension by an SPS-compatible psoralen building block **24** and a Lys side chain-coupled triple glycine motif representing a conjugation site for loading to a protein scaffolds *via* sortase-mediated ligation, resulting in the psoralen-functionalized PNA **25**. Further modification within the peptidic part of **25** was based on the re-usage of the PNA-loaded resin and should be ignored in presented work. To afford cross-conjugation sites in reachable distance from the psoralen unit, a complementary PNA oligomer extended with an *N*-terminal tata PNA (PNA **D**) motif **26** was appropriately designed. Reaction scheme of planned affinity-guided conjugation is given in **Scheme 26**.

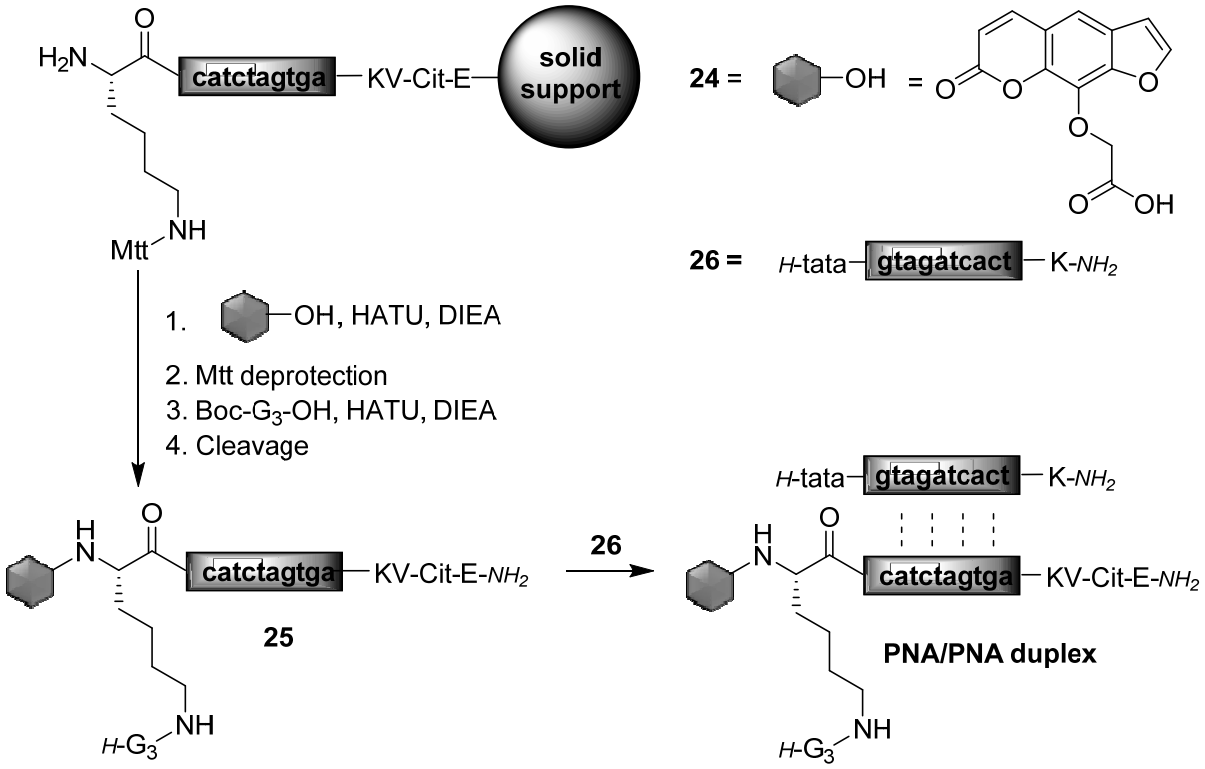

Scheme 26. Compounds **24** – **26** and reaction scheme towards formation of **25** by SPS and successive PNA duplex formation with **26**. Guiding unit parts are shown as grey bars.

Further PNA oligomers derived from the sequence of PNA **B** were designed for the conjugation of guiding units with an antibody Fc scaffold and towards subsequent application of the resulting conjugate to drug delivery (**Figure 46**). First, the plain PNA-peptide hybrid **27** comprising the PNA sequence, a *C*-terminal Lys residue to improve solubility, and an *N*-terminal pentaglycine motif as recognition tag for sortase A was constructed along with PNA-peptide hybrid **28** equipped with an additional TEV protease recognition site (ENLYFQS) and a Lys side chain-coupled Ser as an aldehyde precursor to get a further conjugation site for carbonyl-reactive payloads.

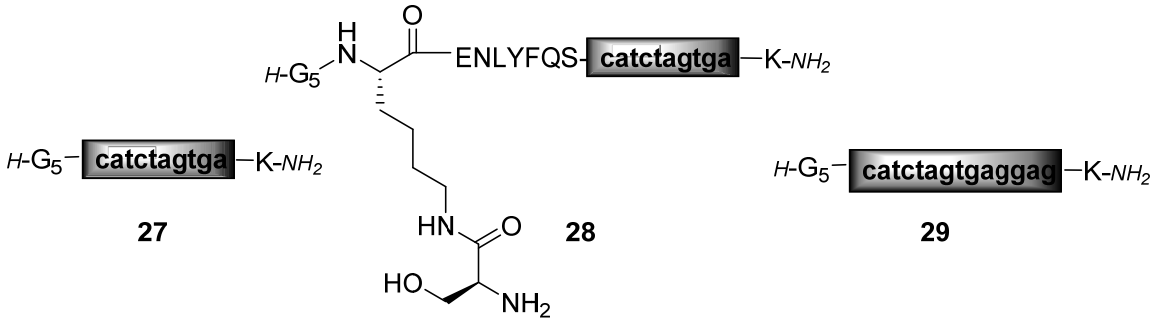

Figure 46. Conjugate **27**-**29**. Guiding unit parts are shown as grey bars.

Both hybrid molecules were applied for preliminary experiments aimed on conjugation of the guiding units to the Fc *C*-terminus as well as hybridization sites for DNA aptamer CLN0003[167] equipped with the complementary nucleobase sequence (analogous sequence as PNA **A**). The DNA sequence of the aptamer which specifically binds to the receptor tyrosine kinase hepatocyte growth factor receptor (HGF-R or c-Met receptor) was as following:

5'GGAGGGAAAAGTTATCAGGCTGGATGGTAGCTCGGTCGGGGTGGGTGGGTTGGCAAGTCTGATTAGTTTTGGAGTACTCGCTCCTCACTAGATG3'

Thereby, the complementary sequence to PNA 2 was elongated towards hybridization to the Fc-loaded **27** or **28**, respectively (red). Therefore, a further PNA guiding unit was designed. PNA-peptide hybrid **29** comprised the sequence of PNA **B** extended on the *C*-terminus with four further PNA residues (PNA **E**) complementary in anti-parallel manner to the four nucleobases on 3'-side of the PNA-hybridization tag within the DNA aptamer.
Furthermore, the PNA guiding unit was additionally equipped with a cytotoxin. The resulting hybrid might function as a hybridization site for the DNA aptamer and as a conjugation site for a toxic payload at the same time (**Scheme 27**).

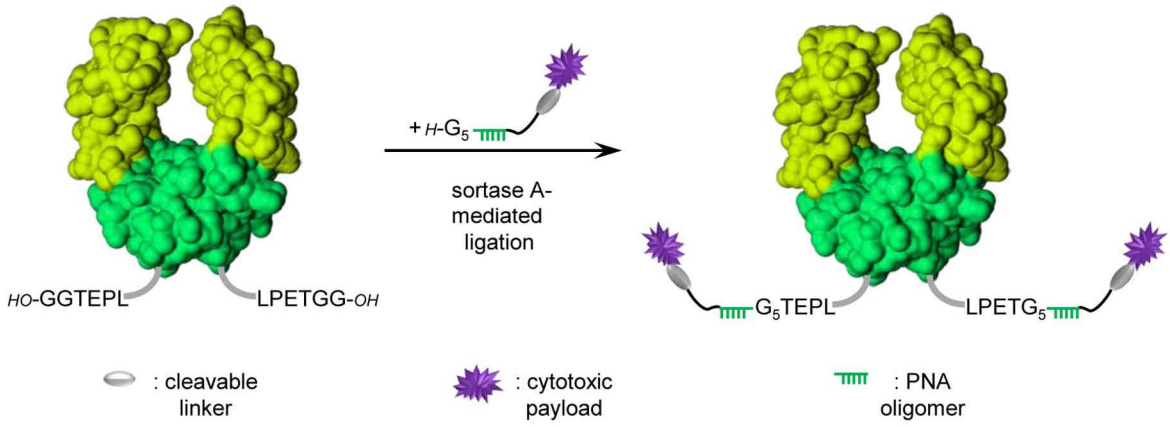

Scheme 27. Synthetic strategy towards a toxin-loaded Fc scaffold for aptamer hybridization by sortase A-mediated ligation.

Precursor molecule **30'** comprising the PNA sequence **B**, an *N*-terminal pentaglycine motif, a *C*-terminal Aha as conjugation site for the toxin, and a Val-Cit linker was designed (**Scheme**

28). SPAAC was chosen for conjugation of **30'** with cytotoxin ispinesib, a highly efficient and selective small molecule kinesin spindle protein inhibitor.[168] Therefore, ispinesib was functionalized with the complementary conjugation site for the bioorthogonal ligation resulting in building block **31** The Val-Cit linker between PNA part and conjugation site of the toxin represents a selective cleavage site for the endogenous protease cathepsin B.

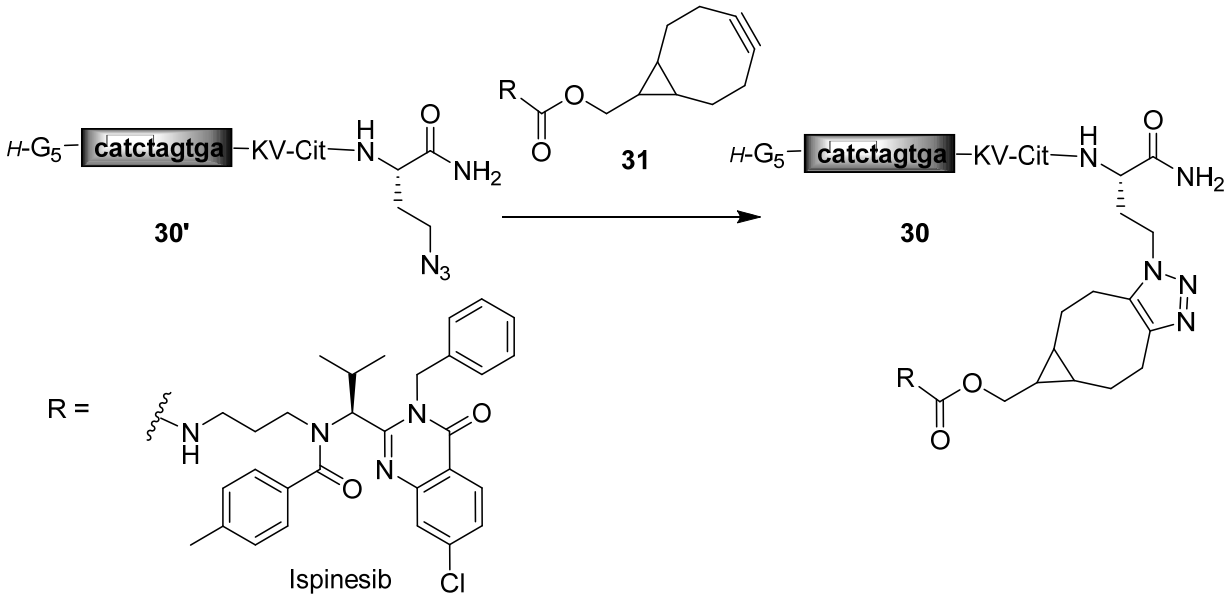

Scheme 28. Compounds **30**, **31** and respective precursor **30'** and reaction scheme towards formation of **30** *via* SPAAC. Guiding unit parts are shown as gray bars.

3.3.1.1 Synthesis of BCN-Comprising Guiding Units 16, 18, and 20

The general strategy to obtain BCN-comprising guiding units is depicted in **Scheme 29**. Maleimide-sulfhydryl conjugation was used for the covalent loading of the BCN group to the plain precursor peptides or PNAs, synthesized on solid phase.

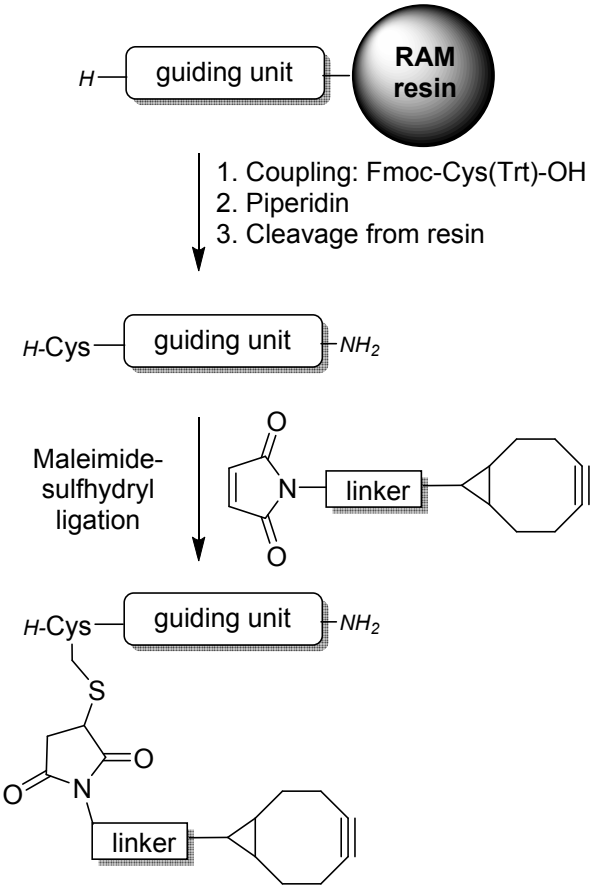

Scheme 29. Synthetic strategy towards BCN-loaded guiding units *via* maleimide-sulfhydryl conjugation.

SPPS of *N*-terminally derivatized α-helical K coils **16'** and **18'**, and PNA-peptide hybrid **20'** were performed by standard Fmoc-SPPS (see chapter 5) on a Rink amide MBHA (RAM) resin providing the formation of a *C*-terminal amide after cleavage. Microwave assistance was only applied for coupling of canonical amino acids when no PNA component was present within the resin-bound peptides. First batches of PNA-loaded resins (without *N*-terminal modifications) were synthesized by Stephen Middel and Dr. Cornelia Panse from Diederichsen group (Universität Göttingen) using the PNA chain elongation protocol I (see chapter 5.2.2). The crude yield of the cleaved and precipitated precursor peptides **16'** and **18'** (50.0 % and 84.0 %) depended on the conditions of the automated peptide synthesis. The crude yield of PNA-peptide hybrid **20'** was poorer than that for the peptidic precursors (44.1 %), demonstrating the general difficulty of solid-phase PNA synthesis.

Considering the next synthetic step, the maleimide-sulfhydryl conjugation, the precursor compounds had to be separated from dithiothreitol (DTT) which was supplemented to the loaded resin during cleavage of the precursors.

Prior to the next synthetic step, the maleimide-functionalized BCN building block **15** had to be prepared. As **15** was not suitable for long-term storage, precursor of the commercially available building block was supplied as a ready-to-mix three-component system. The reaction scheme for preparation of **15** from corresponding BCN-POE_3-NH_2 and NHS-pre-activated maleimido acid is shown in **Scheme 30**.

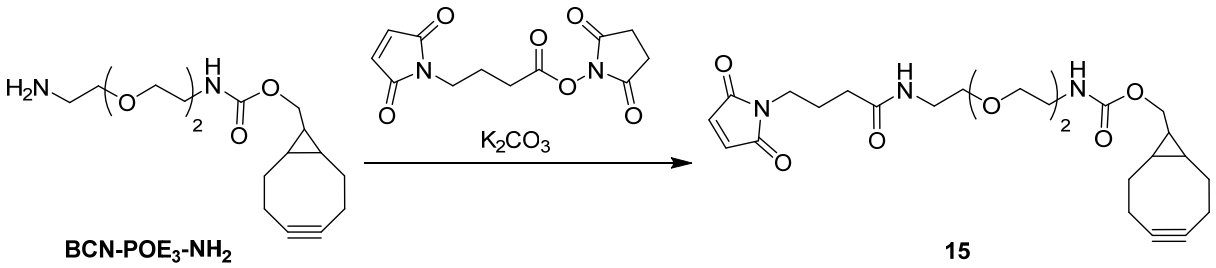

Scheme 30. Formation of **15** by in-solution coupling of NHS-pre-activated maleimide building block to BCN-POE_3-NH_2.

The reaction progress was monitored *via* ESI-MS. Full conversion of the BCN-bearing component was observed after a reaction time of about 60 min (**Figure 47**). Initial experiments to isolate **15** *via* preparative HPLC or by extraction and freeze-drying failed. Hence, the reaction mixture was stored at -80°C in small aliquots without further purification and was directly applied for maleimide conjugation after defrosting.

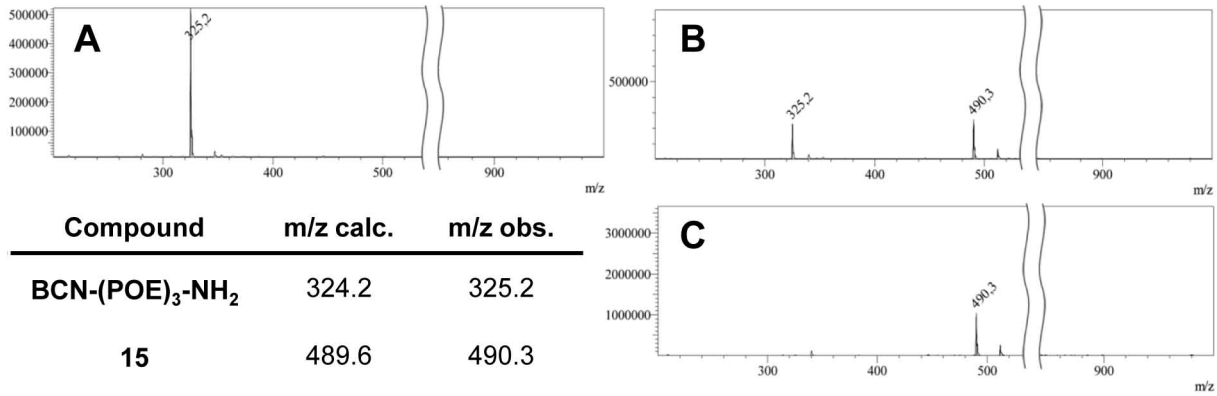

Compound	m/z calc.	m/z obs.
BCN-$(POE)_3$-NH_2	324.2	325.2
15	489.6	490.3

Figure 47. ESI mass spectra of monitored reaction mixtures towards preparation of **15** **A**: pre-reaction; **B**: 10 min; **C**: 30 min after beginning of reaction. Average ion counts of *R*t = 6.9 – 9.5 min in pre-switched LC with a gradient of 2→100 % acetonitrile in 0.1 % formic acid over 10 minutes at flow rate 0.2 ml/min are plotted against m/z.

The maleimide conjugation of precursors **16'**, **18'**, and **20'** was performed in degassed Tris-HCl or ammonium acetate buffer (pH 6.5 or 6.8, respectively). It was important to keep a slightly acidic condition to avoid side reaction by coupling of the maleimide to the amine function of Lys (nucleophilic at basic conditions) as well as to keep reaction mixture free from atmospheric oxygen to prevent spontaneous formation of disulfide bonds. The conversion of the precursors in the respective final products **16**, **18**, or **20** monitored by analytical HPLC stopped after a reaction time of about 5 h presumably by reaching the equilibrium. In case of **16'** and **18'**, a precipitation of the formed conjugates was observed. The precipitates were re-dissolved by addition of a small amount of acetonitrile before chromatographic isolation. The chromatographic traces of the isolated final products are shown in the appendix. The conversions of **18'** and **20'** were calculated from the peak integrals of corresponding chromatograms resulting in conversion values of 64.8 % and 71.5 %, respectively (**Figure 48A**). A second-order reaction kinetics (k_2 = 0.21 $M^{-1}s^{-1}$) was estimated for the bioorthogonal conjugation regarding the conversion of **18'** (**Figure 48B**). The value is at same range as reported for other maleimide conjugations.[169]

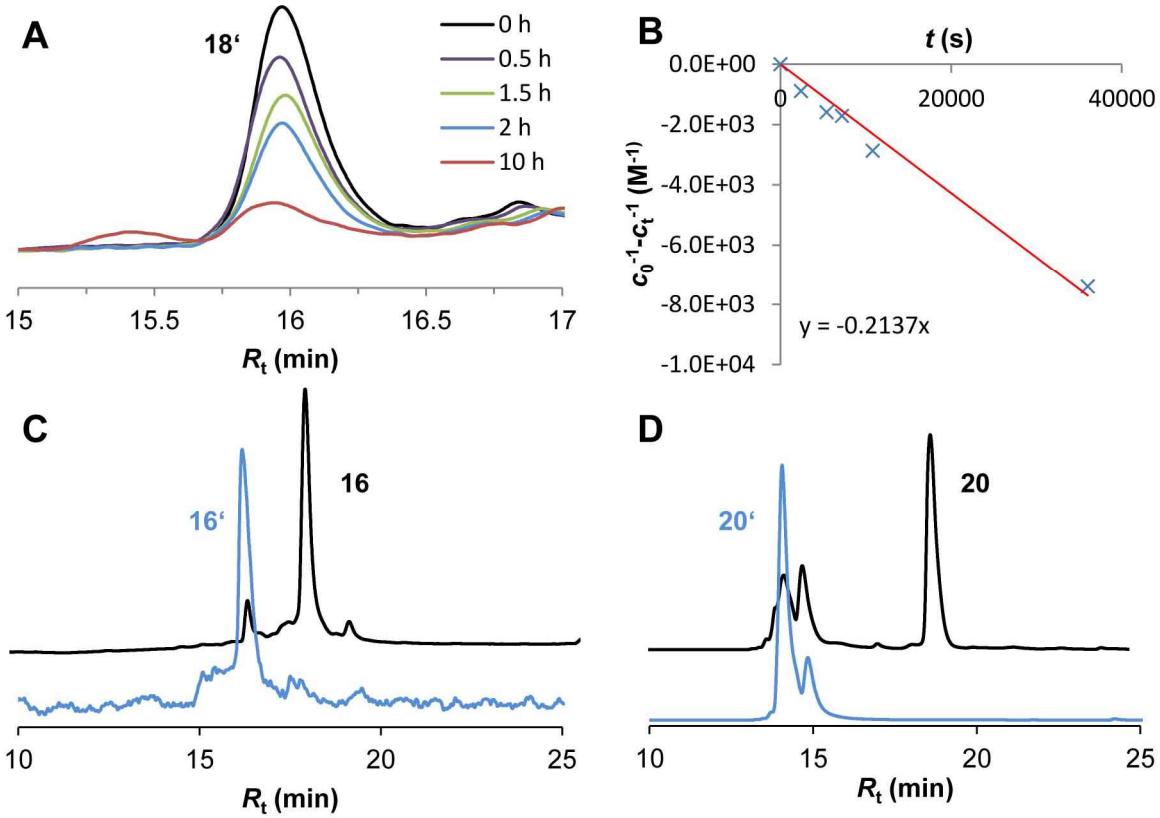

Figure 48. Chromatographic profiles of the reaction mixtures of monitored maleimide-sulfhydryl conjugations of **16'** (**A**), **18'**(**C**), and **20'**(**D**). UV detection at λ = 220 nm (**A**, **C**) or 260 nm (**D**); eluent: 18→54 % (**A**), 18→90 % (**C**), or 0→54 % (**D**) acetonitrile in 0.1 % aq. TFA over 20 minutes at flow rate 1 ml/min. **A**: Zoom-in of the corresponding peak of **18'**; diverse traces of samples analyzed after distinct reaction times are marked with corresponding colors. **B**: kinetic data plotting regarding conversion of **18'** for determination of reaction rate constant k_2 by linear regression. **C**, **D**: Profiles of respective reaction mixtures before (blue) and after 5-8 h reaction time (black).

Yields are summarized in **Table 17**. The poor overall yields resulted from the necessity of multiple chromatographic purification steps, each with restricted recovery rate (in case of compound **16**, a third chromatographic purification step had to be applied since the manual separation of the components in fractions failed at the first trial). However, the amount and purity of isolated products was sufficient for their application in subsequent affinity-guided approaches.

Table 17. Synthesis of BCN-decorated guiding units **16, 18, and 20.**

Entry	Strategy	MW	Crude yield [%]	Purification yield[a] [%]	MS-coupling[b]/ purification yield[c] [%]	Overall yield [%]
16	Automated	+	50.0	30.0	12.7	1.9
18	Automated	+	84.1	58.3	38.6	18.9
20	Manual	-[d]	44.1	43.3	22.1	4.2

a: First chromatographic purification of precursor compounds.
b: MS: maleimide-sulfhydryl.
c: Second chromatographic purification after in-solution modification.
d: First amino acid (Fmoc-L-Lys(Boc)-OH) was loaded with microwave assistance to resin.

3.3.1.2 Synthesis of Aldehyde-Bearing Guiding Units 17, 19, 21, and 22

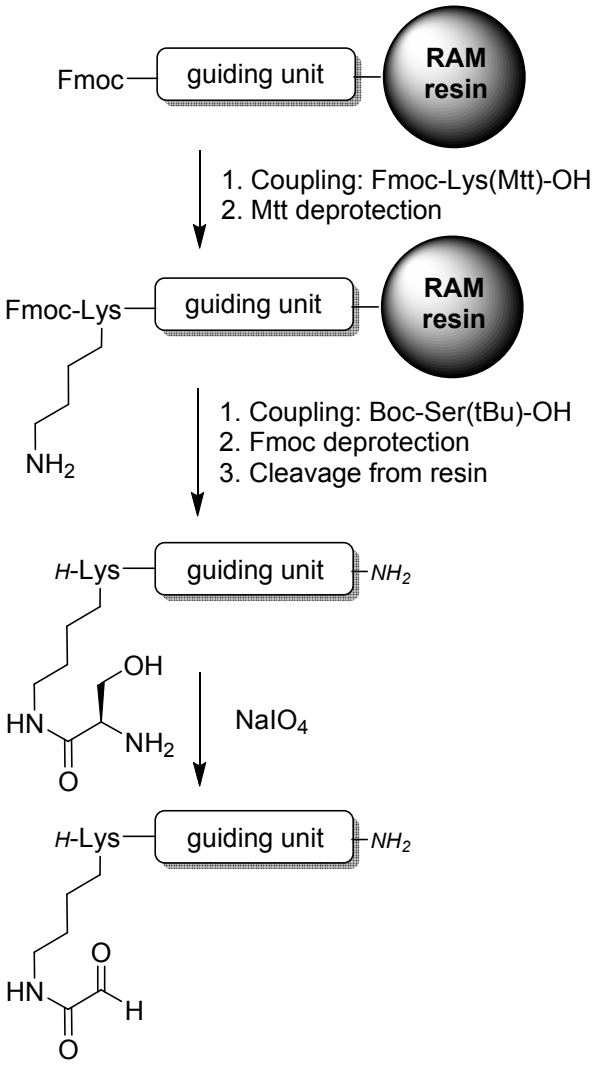

Scheme 31. Synthetic strategy towards guiding units with aldehyde functions in the side chain *via* periodate-mediated oxidation of terminal and vicinal amino alcohols.

The general strategy towards aldehyde-bearing guiding units is depicted in **Scheme 31**. Periodate-mediated oxidation of an amino alcohol yielded glyoxylyl from a Ser residue coupled to the side chain of Lys.

SPPS of *N*-terminally derivatized α-helical E coil peptides **17'** and **19'**, and PNA-peptide hybrids **21'** and **22'** was performed as described for **16'**, **18'**, and **20'** in chapter 3.1.3.1. First batches of PNA-loaded resins (without *N*-terminal modifications) were synthesized by Stephen Middel and Dr. Cornelia Panse from Diederichsen group (Universität Göttingen) using the PNA chain elongation protocol I (see chapter 5.2.2). Towards side chain modification of Lys, Fmoc-L-Lys(Mtt)-OH was coupled to the *N*-termini of corresponding resin-bound peptides/PNAs. Selective deprotection of the Mtt was achieved upon treatment of the loaded resins with 1 % TFA and triethyl silane (TES). Subsequently, Boc-L-Ser(tBu)-OH was coupled to the free amine moiety.

Oxidation of serine was performed with ten equivalents of sodium periodate at neutral pH. To minimize the risk of over-oxidation or further unfavorable side reactions, oxidation was terminated by quenching of the oxidative species with ethylene glycol or 4-methoxythiophenol. However, it was found that the most efficient method was the direct injection into preparative HPLC. The net polarity of the final products were similar to the precursor compounds resulting in a similar retention time R_t during HPLC analysis. Therefore, the conversion upon periodate-mediated oxidation was assured by disappearance of the corresponding reactant signals in ESI mass spectrum. The chromatographic profiles of respective substances before and after periodate-mediated oxidation are shown in **Figure 49**.

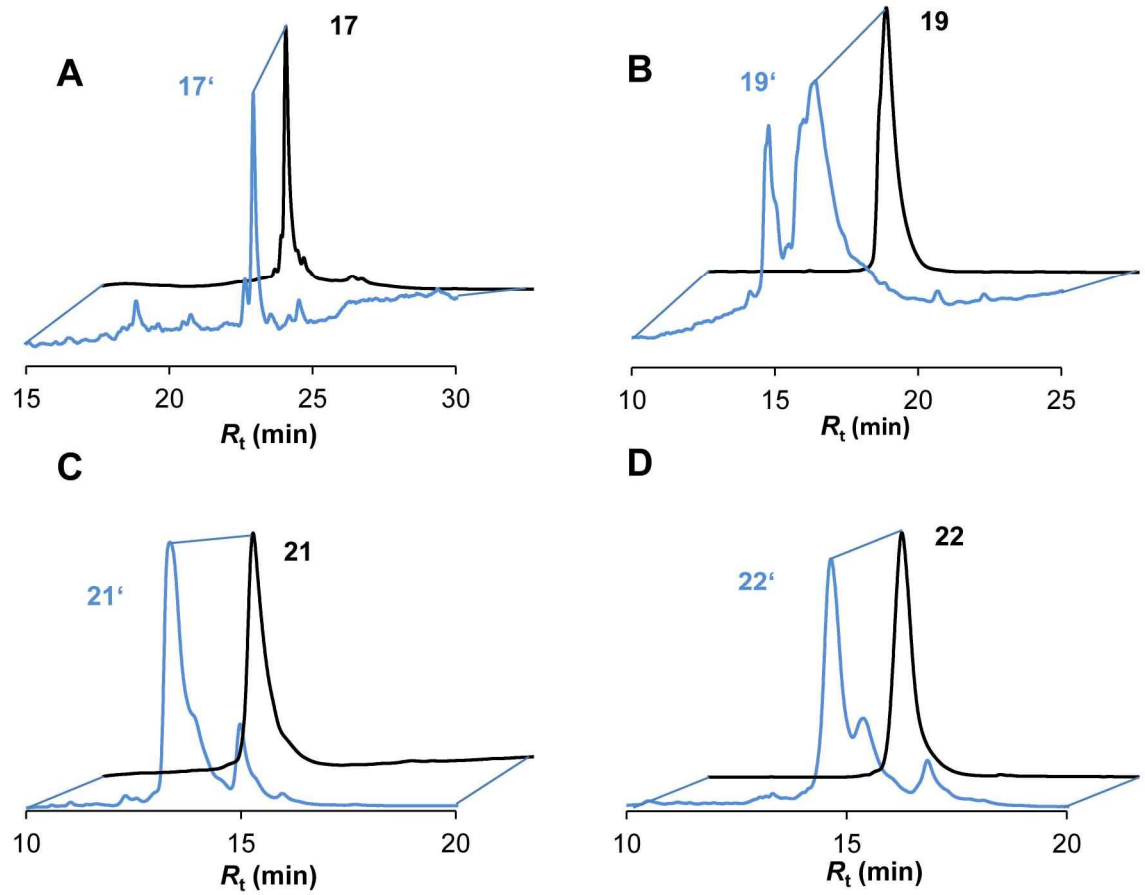

Figure 49. Chromatographic profiles of the reaction mixtures of crude precursor molecules of **17'** (**A**), **19'**(**B**), **21'** (**C**), and **22'** (**D**) and corresponding purified products after periodate-mediated oxidation. UV detection at λ = 220 nm (**A**, **B**) or 260 nm (**C**, **D**); eluent: 9→90 % (**A**), 9→72 % (**B**), 0→90 % (**C**), and 0→54 % (**D**)acetonitrile in 0.1 % aq. TFA over 20 minutes at flow rate 1 ml/min.

The cleaved and precipitated crude precursor peptides **17'** and **19'** were used in successive oxidation step without chromatographic purification, whereas the crude PNA-peptide hybrids **21'** and **22'** were purified prior to oxidation. Corresponding yields regarding SPPS of precursors and in-solution modification towards final products are summarized in **Table 18**.

Table 18. Synthesis of aldehyde-bearing guiding units **17**, **19**, **21** and **22.**

Entry	Strategy	MW	Crude yield [%]	Purification yield[a] [%]	Oxidation / purification yield[b] [%]	Overall yield [%]
17	Automated	+	27.9	-	6.4	1.8
19	Automated	+	35.9	-	12.0	4.3
21	Manual	-[c]	44.1	61.0	63.7	17.3
22	Manual	-[c]	22.5	63.7	52.3	7.5

a: First chromatographic purification of precursor compounds.
b: Second chromatographic purification after in-solution modification.
c: First amino acid (Fmoc-L-Lys(Boc)-OH) was loaded with microwave assistance to resin.

3.3.1.3 Synthesis of Psoralen-Decorated PNA Guiding Unit 25

Synthesis of hybrid molecule **25** was accomplished on solid phase according to S**cheme 32** shown in chapter 3.3.1. PNA chain elongation was performed according to the protocol II (chapter 5.2.2.3). After manual chain elongation up to Lys1 (side chain-protected by Mtt protecting group), SPPS-compatible psoralen derivative **24** was attached to the *N*-terminus. **24** was prepared from 8-hydroxy psoralen (xanthotoxol) *via* a two-step synthesis comprising the attachment of a protected acetic acid derivative by a Williamson ether synthesis towards intermediate **24'** and subsequent deprotection of the carboxylate moiety (**Scheme 32**).[166] A good overall yield (67.8 %) of **24** was obtained, though the main loss was caused by the chromatographic purification of **24'**. However, a sufficient amount of **24** was gained. Corresponding NMR spectra of **24'** and **24** demonstrating the purity of respective compounds are shown in the appendix.

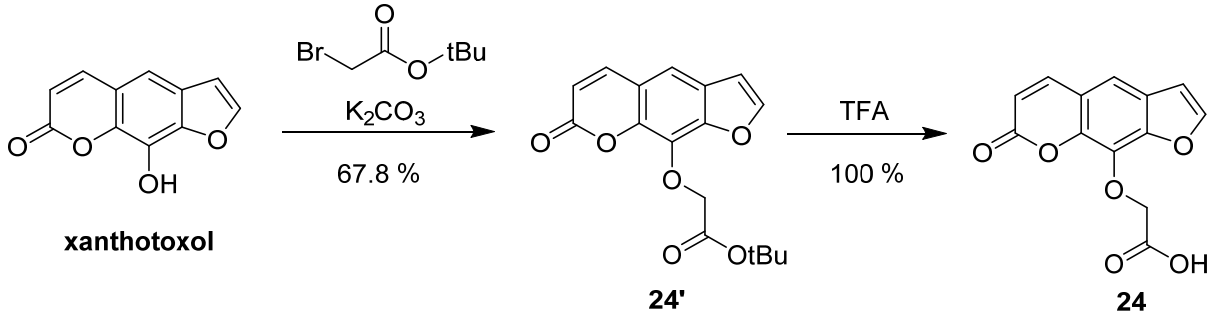

Scheme 32. The two-step synthesis of **24** from xanthotoxol.

After the aminoterminal capping of the resin-bound peptide-PNA hybrid with **24**, Boc-Gly_3-OH was coupled to the side chain of Lys1 by the on-resin side chain modification described in chapter 3.3.1.2. Final product **25** was gained in sufficient amount and purity for the successive studies towards affinity-guided PNA-DNA and PNA-PNA cross-conjugations. The overall yield of **25** (10.0 %) was similar to other PNA-based guiding units.

3.3.1.4 Synthesis of PNA guiding units 23, 26, 27, 28 and 29

PNA-peptide hybrid molecules **23** and **26** – **29** were synthesized by iterative chain elongation on solid support, cleavage from resin and chromatographic purification. Generally, two various protocols were applied for PNA chain elongation (chapter 5.2.2.2 and 5.2.2.3), whereby protocol I is featured by a larger excess of Fmoc-protected PNA monomers and coupling reagents with numerous washing steps between coupling, capping, and deprotection cycles. Chain elongation protocol II is a cost- and time-saving variant of protocol I with a smaller excess of coupling reagents, less washing steps and with application of DMF instead of NMP in some cases. The corresponding yields of respective compounds are listed in **Table 19**.

Table 19. Synthesis of PNA-peptide hybrids **23** and **26 – 29.**

Entry	Number of PNA residues	Number of overall residues	PNA chain-elongation protocol	Crude yield [%]	Purification yield [%]	Overall yield [%]
23	10	12	I	69.8	44.0	30.7
26	14	15	I+II[a]	37.6	26.6	10.0
27	10	16	II	30.9	50.4	15.6
28	10	23	I	27.0	51.5	13.9
29	14	20	II	44.2	12.6	5.6

a: Coupling up to c^5 with protocol I; coupling of last four PNAs with protocol II.

Generally, the application of protocol I resulted in slightly better yields, but a direct comparison of the batches is not possible due to different numbers of incorporated PNAs and considering the impact of further peptidic residues. However, the variance between crude yield and overall yield demonstrated that the purity of the crude product was much higher when using protocol I. In conclusion, it was found that the protocol II provides sufficient coupling efficacy for shorter PNA sequences of up to 10 residues, but for longer PNA sequences it resulted in drastic loss of purity. A generic protocol for PNA SPS could not be established during the presented work, thus the combination of the two protocols was found to be optimal as it was demonstrated for PNA-peptide hybrid **26** (compared to **29**).

3.3.1.5 Synthesis of Toxin-Loaded PNA Guiding unit 30

Synthesis of the toxin-loaded hybrid molecule **30** was realized using the strategy depicted in **Scheme 27** (chapter 3.3.1). First, precursor molecule **30'** was prepared on solid phase using the PNA chain elongation protocol I. After cleavage from solid support and precipitation, **30'** was yielded in sufficient purity (chromatographic profile shown in appendix) for successive conjugation to the toxin.

Since SPAAC was chosen as conjugation technique, a strained triple bond moiety had to be installed into the payload toxin as reaction counterpart. Therefore, the toxin ispinesib was decorated with a BCN group by in-solution coupling of a commercially available NHS-pre-activated BCN leading to molecule **31** (**Scheme 33**).

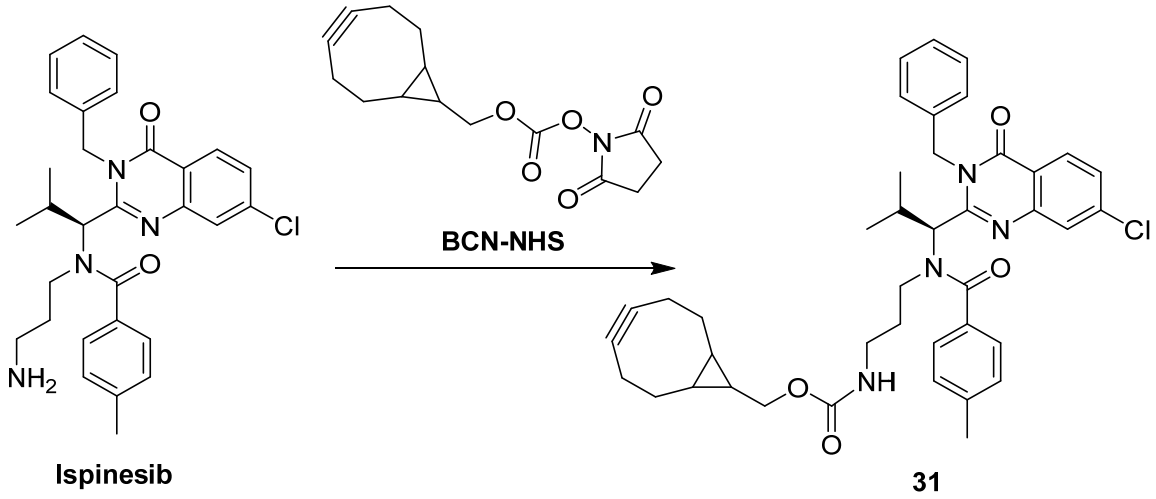

Scheme 33. Reaction scheme towards formation of **31** from ispinesib.

In preliminary experiments it was found that, although the reaction was quantitative regarding the consumption of BCN-NHS, the chromatographic isolation of **31** was not efficient due to low recovery rate and purity. Hence, a decision was made to treat **30'** directly with the respective reaction mixture after consumption of the BCN-NHS. Formation of **31** and SPAAC with **30'**, were monitored *via* HPLC and ESI-MS. The progress of cycloaddition was assessed from the integrals of respective peaks of the chromatographic traces (**Figure 50**). Thus, 79.6 and 89.1 % conversion was calculated for two different batches with the same reaction setup. The slightly greasy profile of the product peak at R_t = 19.3 min was supposed to be caused by the formation of a mixture of steroisomers (regarding to the relative configuration of C1 and C8 within the BCN moiety). A mean second-order kinetic constant of k_2 = 0.55 $M^{-1}s^{-1}$ was calculated for the two corresponding SPAAC batches which is similar to published values (0.2-0.3 $M^{-1}s^{-1}$).[170] The slightly higher values obtained in the presented work were presumably caused by the excess of the BCN component **31** (2 eq. related to **30'**).

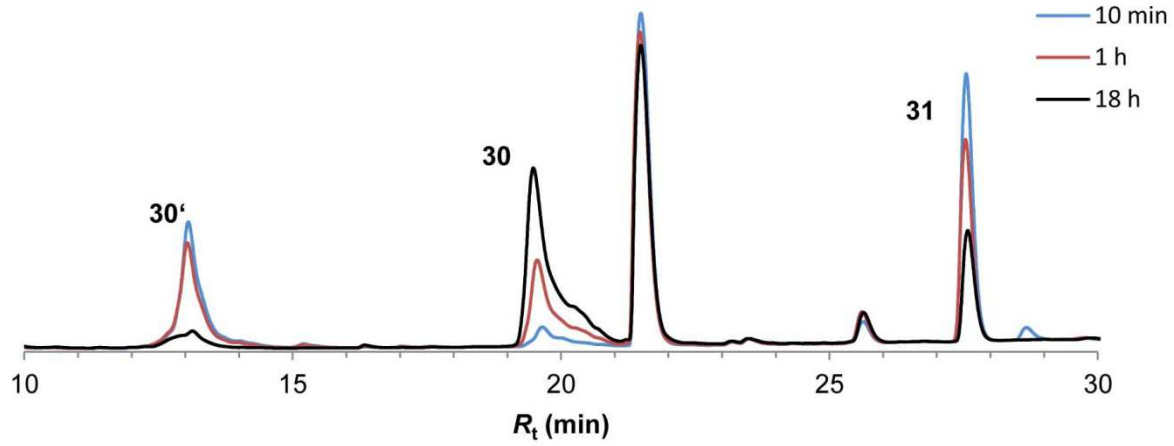

Figure 50. Chromatographic profiles of the reaction mixture of SPAAC of **30'** and **31** towards formation of **30**. UV detection at λ = 260 nm; eluent: 0→ 54% acetonitrile in 0.1 % aq. TFA over 20 minutes at flow rate 1 ml/min. Divers traces of samples analyzed after distinct reaction times are marked with corresponding colors.

Chromatographic isolation yielded **30** (66.7 %) in sufficient purity for subsequent sortase A-mediated conjugation to the Fc scaffold.

3.3.1.6 Recombinant Production of Fc scaffold

The production of homodimeric Fc scaffold, *C*-terminally decorated with the recognition site for sortase A-mediated ligation (LPETG), was performed by Stephan Dickgießer from Kolmar group. Recombinant expression was realized in suspension-adapted human embryonic kidney (HEK293-6E) cells transiently transfected with Fc fragment-encoding plasmid pEXPR-IBA42 and the produced protein was purified using protein A chromatography. Since this part of project was not a subject of presented work, further experimental data and protocols are presented in a respective publication.[171]

3.3.2 Characterization and Evaluation of Activity

3.3.2.1 SPANC of Guiding Unit Pairs

Alkyne-nitrone cycloaddition of synthetic guiding unit pairs **16** and **17**, **18** and **19**, and **20** and **21** were examined in a series of test-reactions comprising respective model compounds, an *N*-hydroxylamine component and a catalyst for the nitrone-formation. The reaction setup was based on the protocol reported by Temming et al. in 2013,[172] whereby the stoichiometry, temperature, or incubation time were varied. In **Scheme 34** the alkyne-nitrone cycloaddition between the five-heptad E/K coiled coil **18** and **19** is shown as an example of the affinity-guided SPANC.

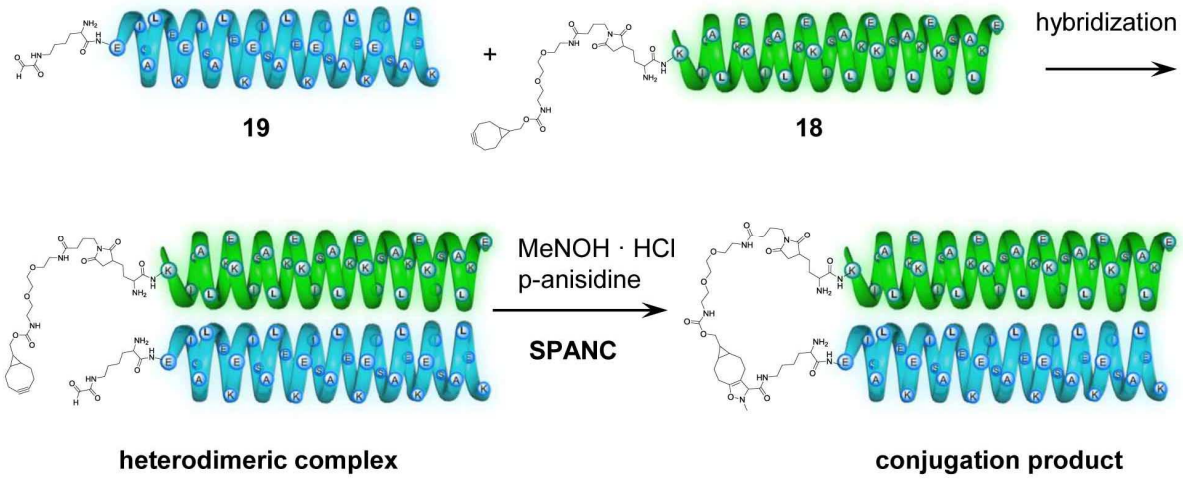

Scheme 34. Reaction scheme of the affinity-guided SPANC of **18** and **19** towards a covalently linked heterodimer. Coils are depicted as green (Kcoil) and blue (Ecoil) cartoon, whereby the shapes were chosen only for graphic representation and do not reflect the real geometric data of the molecules. An enlarged image of the scheme is given in the appendix.

In a general approach, an aldehyde-bearing molecule and its alkyne counterpart were incubated in neutral to slightly acidic buffered solution for 1 h. Subsequently, *p*-anisidine and an *N*-hydroxylamine derivative of choice were added and the reaction mixture was shaken at

ambient temperature or under cooling on ice. The reaction progress was monitored by HPLC and ESI-MS; in few experiments the samples were diluted afterwards with acetonitrile since precipitation was observed. The isolation of the cycloaddition product was not possible due to the small batch sizes of the test reactions and formation of a side-product with similar R_t (explained in the next chapter). Hence, the efficacy of the reaction was assessed from the consumption of the aldehyde components along with reaction progress using HPLC analysis.

In view of its application to the site-selective one-pot ligation of multiple components the affinity-guided coupling had to be optimized regarding conversion, reaction rate and specificity. An important issue was to minimize excess of the alkyne component to enhance selectivity. Indeed, in the majority of the reported protocols concerning SPANC of biomolecules, the alkyne component was used in 5-10 eq. excess to accelerate the reaction.[172-173] As we assume that pre-orientation of the reactive moieties boosts their local concentration *per se*, the guiding unit pairs were applied in the present work almost equimolarly.

Therefore, the next parameters were varied: batch size (200-1500 μl), final concentration of reactants (max. 200 μM, concentration adjusted to minimally required for analysis), stoichiometry of guiding units, concentration of hydroxylamine derivatives (1 – 20 eq.) and *p*-anisidine (5 – 50 eq.), coupling and incubation conditions (prior to reaction initiation and during SPANC, respectively), buffer solutions, and order and timing of reactant/catalyst addition. Moreover, few approaches employing *in situ* generated aldehydes were also tested. Detailed information on the setup for SPANC test reactions are given in chapter 5.3.2 (coiled-coil) and 5.3.3 (PNA), respectively.

Coiled-Coil Guiding Units

Initial affinity-guided SPANC experiments were conducted with the three-heptad and five-heptad coiled-coil peptides; respective data are given in **Table 20**. In these experiments, the formation of a covalently conjugated product was confirmed by ESI-MS. Detailed information is given in chapter 5.3.2.

Table 20. Setups and conversion of preliminary affinity-guided SPANC experiments using three-heptad and five-heptad coiled coils.

Setup	A[a]	B[b]	Eq. A:B	[A] (μM)	[MeNOH] (μM)	Analysis	Conversion[c] (%)
1	**16**	**17**	1:1	125	150	HPLC, ESI-MS	74.1±5.2[e]
2	**18**	**19**	1:1	50	60	ESI-MS	*n. c.*
3	**18**	**19**	1:1	50	240	ESI-MS	*n. c.*
4	**18**	**19**	1:1	50	240	HPLC, ESI-MS	69.8
5[d]	**18**	**19**	1:1	50	240	HPLC, ESI-MS	61.2

a: BCN-decorated guiding unit.
b: Aldehyde-bearing guiding unit.
c: Conversion calculated from decrease in HPLC traces of aldehyde-bearing guiding unit.
d: Reaction performed in water pH 7.0.
e: Mean value of conversions of two reaction batches using same setup.
n.c.: Conversion not calculated.

In all setups, guiding units were used equimolarly and their conversion into the conjugations products **cp1** and **cp2** (list of conjugation products given in appendix) was determined as 60 – 75 %. In case of setup 1 using the three-heptad coiled coils **16** and **17**, precipitation of the ligation product **cp1** was observed after 1 h. This precipitate was dissolved by addition of acetonitrile and analyzed by HPLC. The chromatographic profiles of the monitored reaction are shown in **Figure 51A**.

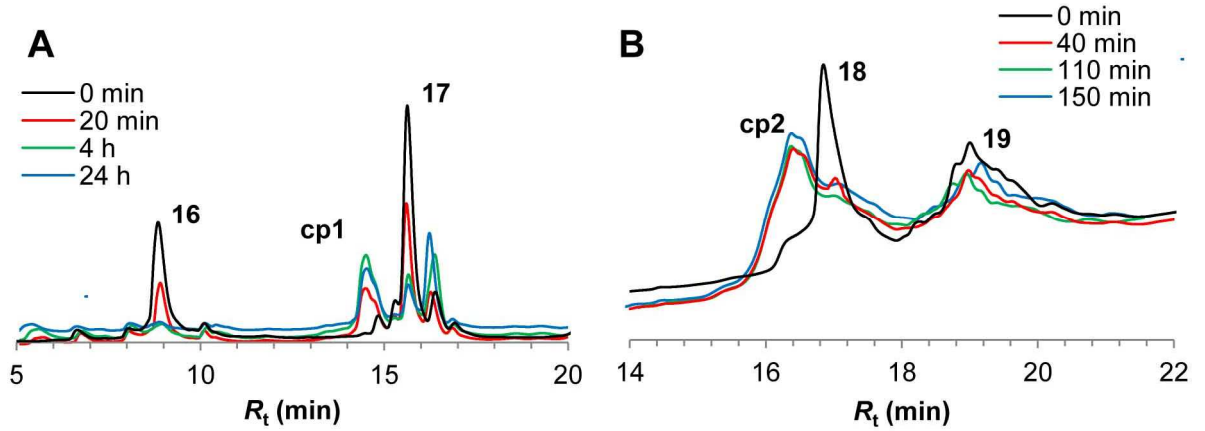

Figure 51. Chromatographic profiles of the reaction mixture of **A**: SPANC between **16** and **17** (setup 1) and **B**: SPANC between **18** and **19** (setup 4) towards formation of the heterodimeric conjugation product. UV detection at λ = 220 nm; eluent: 9→90 % acetonitrile in 0.1 % aq. TFA over 20 minutes at flow rate 1 ml/min. Divers traces of samples analyzed after distinct reaction times are marked with corresponding colors.

A conversion of 74.1% regarding **17** was calculated, while the absorption profile of **16** showed its consume during the reaction. The reaction with the five-heptad guiding units **18** and **19** (setup 4) had similar conversion rate (chromatographic profile shown in **Figure 51B**). A mean second-order kinetic constant of k_2 = 1.88 $M^{-1}s^{-1}$ was calculated for setup 1 while a higher k_2 of 4.61 $M^{-1}s^{-1}$ was determined for setup 4 indicating a faster reaction for the five-heptad coiled-coil system. This outcome is presumably caused by the fact that the used three-heptad coiled coils can form homo- and hetero oligomers, as shown by size exclusion chromatographic analysis (SEC, see appendix) in a preliminary study. Thus, the five-heptad coiled-coil system appeared more advantageous for affinity-guided conjugation and for successive HPLC analysis, thus, further SPANC experiments were performed using this model system.

The formation of **cp2** was confirmed by ESI-MS and HPLC analysis. The mass spectrum of the conjugation product (setup 4, after HPLC isolation) is exemplarily shown in **Figure 52A**.

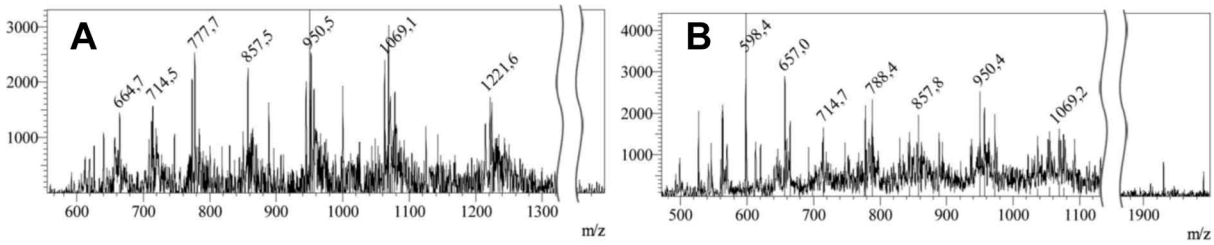

Species	Ions	m/z calc.	m/z obs.
cp2 (M = 8542.99 g/mol)	$[M+7H]^{7+}$	1221.4	1221.6
	$[M+8H]^{8+}$	1068.9	1069.1
	$[M+9H]^{9+}$	950.2	950.5
	$[M+10H]^{10+}$	855.3	857.5
	$[M+11H]^{11+}$	777.6	777.7
	$[M+12H]^{12+}$	712.9	714.5
	$[M+13H]^{13+}$	658.1	657.0

Figure 52. ESI mass spectra of the main product fraction of test reactions **A**: using setup 4 and **B**: using setup 8 upon chromatographic purification of the reaction mixture after a reaction time of 150 min (R_t = 16.1 min). Spectra are in positive mode. Corresponding m/z signals of calculated and found species are listed in the table below.

The reaction was performed in ammonium acetate buffer to assure its direct analysis by LC-MS. Indeed, under these conditions the E/K coils could easily become multiply charged upon ionization. Thus, a number of positively charged species with a complex ionization pattern was observed due to the formation of ammonium, sodium, or potassium (traces found in dist. water used for preparation of buffers and HPLC eluent) salts. This leads to the strong background signals and made the evaluation of the spectrum difficult. Nevertheless, the m/z of the desired conjugation product were found as 7 – 13 times charged cations.

Furthermore, a SPANC experiment employing the five-heptad coiled coils was performed in non-buffered aqueous milieu at pH 7.0 (setup 5). A conversion of 61.2 % (regarding **19**) was determined and a second-order kinetic constant of k_2 = 3.55 $M^{-1}s^{-1}$was calculated. Both values were slightly worse than those for setup 4, which indicated that the non-buffered reaction was less efficient for SPANC, presumably due to the change in pH by addition of MeNOH·HCl as reaction initiator.

To check the selectivity provided by the affinity-guided approach, further SPANC setups were developed in the presence of benzaldehyde as competitor of **19** (setup 6 – 9). The reaction efficacy and selectivity was evaluated by alteration in conversion of **19** and by investigation of all relevant HPLC fractions by ESI-MS towards corresponding signals of the benzaldehyde-conjugation product **cp3**. Information and data of the setups are summarized in **Table 21**.

Table 21. Setups and conversion of affinity-guided SPANC using five-heptad coiled coils in presence of benzaldehyde as a competitive reactant.

Setup	A[a]	B[b]	C[c]	Eq. A:B:C	[A] [μM]	Analysis	Conversion[d] [%]
6	**18**	**19**	benzaldehyde	1:1:1	50	HPLC, ESI-MS	80.0
7	**18**	**19**	benzaldehyde	2:3:2	100	HPLC, ESI-MS	71.5
8	**18**	**19**	benzaldehyde	1:1:1	150	HPLC, ESI-MS	79.3
9[e]	**18**	-	benzaldehyde	1:0:10	100	HPLC, ESI-MS	50.1

a: BCN-decorated guiding unit.
b: Aldehyde-bearing guiding unit.
c: Competitive aldehyde component.
d: Conversion calculated from decrease in HPLC trace of aldehyde-bearing guiding unit after termination of reaction (when no further consumption of **B** was observed).
e: Control experiment using **18** and benzaldehyde. Conversion calculated from consumption of **18**.

All conversions regarding **19** were in similar range (70 – 80%) as found for setup 4 without competitive aldehyde component. All reactions were performed in ammonium acetate buffer pH 6.5 with an excess of MeNOH (2.5-5 eq.). The slightly poorer conversion found for setup 7 was caused by the small excess of **19** (1.3 eq.) for this setup. During reaction monitoring (**Figure 53A**), all relevant HPLC fractions were collected and analyzed by ESI-MS, but in none of the fractions the corresponding signals of **cp3** were found (**Figure 52B**).

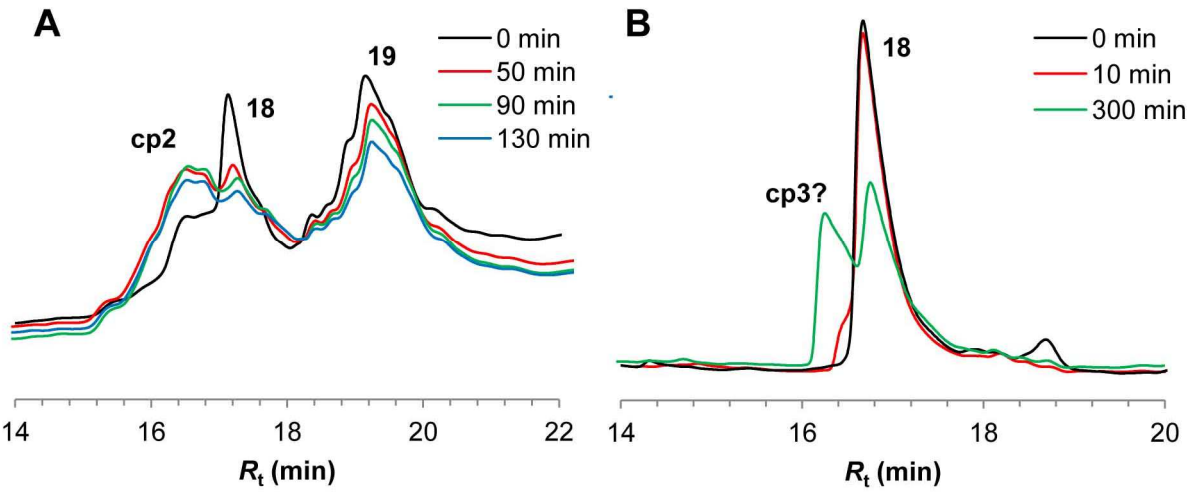

Figure 53. Chromatographic profiles of the reaction mixture of **A**: SPANC between **18** and **19** (setup 8) and **B**: SPANC between **18** and benzaldehyde (setup 9) towards formation of conjugation products. UV detection at λ = 220 nm; eluent: 9→90 % acetonitrile in 0.1 % aq. TFA over 20 minutes at flow rate 1 ml/min. Diverse traces of samples analyzed after distinct reaction times are marked with corresponding colors.

To evaluate the SPANC reactivity of **18** against benzaldehyde, a control reaction was performed (setup 9). The HPLC profile of the monitored reaction (**Figure 53B**) indicated the consumption of **18** along with reaction progress, but in the MS spectrum of the newly formed fraction (R_t = 16.1 min) the signals corresponding to the **cp3** were found only in traces (spectrum given in appendix).

At this point, we recognized that in none of the test reactions the aldehyde-bearing guiding units were fully consumed, whereas the signals of their reaction counterparts disappeared after a certain reaction time. Hence, we hypothesized that the BCN-comprising component underwent a competitive side reaction. To evaluate this assumption, a control experiment employing only guiding unit **18** and MeNOH was performed (setup 10). The reaction was conducted in ammonium acetate buffer at pH 6.5 and a 20-fold excess of MeNOH was applied. No distinct changes were found in the HPLC traces during reaction progress. However, ESI-MS analysis showed the signals of the conjugation product between MeNOH and **18** (**cp4**, **Scheme 35**) along with those corresponding to unmodified **18** (**Figure 54**).

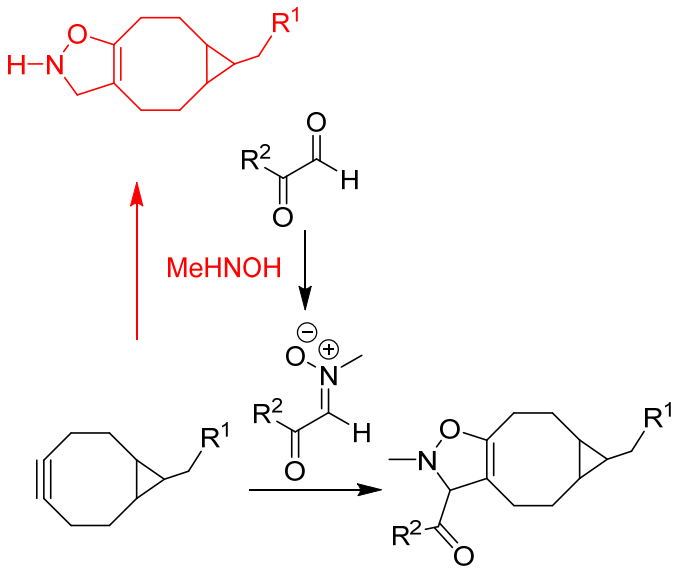

Scheme 35. General SPANC with BCN and a nitrone, *in situ* formed from an aldehyde (black) and suspected side reaction towards formation of a conjugation product between BCN and MeNOH (red).

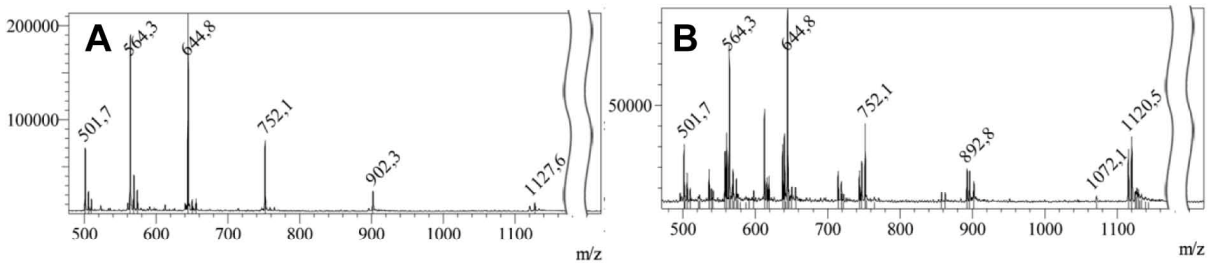

Species	Ions	m/z calc.	m/z obs.
18 (M = 4458.37 g/mol)	$[M+3H+Na]^{4+}$	1121.1	1120.5
	$[M+5H]^{5+}$	892.7	892.8
	$[M+4H]^{4+}$	1127.5	1127.6
cp4 (M = 4506.21 g/mol)	$[M+5H]^{5+}$	902.2	902.3
	$[M+6H]^{6+}$	752.0	752.1
	$[M+7H]^{7+}$	644.3	644.8
	$[M+8H]^{8+}$	564.3	564.3

Figure 54. ESI mass spectra of the reaction mixture of the control reaction with only **18** and MeNOH (setup 10) after a reaction time of 24 h. **A**: averaged ionization signals at 9.0 – 9.5 min. **B**: averaged ionization signals at 9.5 – 9.8 min. Spectra are in positive mode. Corresponding m/z signals of calculated and found species are listed in the table below.

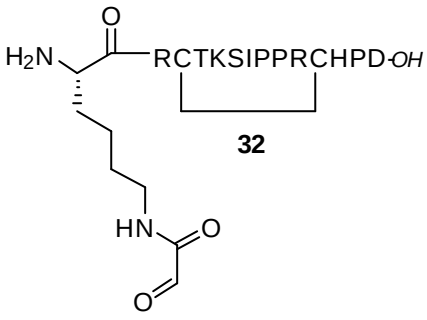

Figure 55. Competitive aldehyde-bearing peptide **32**.

This product **cp4** exhibited a similar retention time as the unmodified **18**, thus the HPLC traces were indistinguishable. Therefore the determination of conversion and reaction rate for this side reaction was not possible. But as the MS signals corresponding to **18** still remained after a reaction time of 1 day despite the excess of MeNOH, this undesired side-reaction was supposed to be generally slower than SPANC. Interestingly, this observation has not been reported in previous publications dealing with alkyne-nitrone cycloaddition of biomolecules,[77, 172-173] presumably due to the fact that in all cases the BCN component was employed in excess (5 – 10 eq., equimolar to MeNOH). Nevertheless, the stoichiometry of the reactants was further kept nearly equimolar in the present work.

Further test reactions with an alternative aldehyde-bearing competitive peptide **32** (**Figure 55**) were performed (setup 11 and 12). Peptide **32** is an SFTI-derived matriptase inhibitor with an aldehyde installed *via* the Lys side-chain as a conjugation site. It was synthesized by Heiko Fittler[142b] using a similar procedure as described for the aldehyde-bearing peptides **17** and **19**. The advantage of **32** over benzaldehyde was that the consumption of the peptide can be monitored by RP-HPLC, whereas benzaldehyde was eluted without interaction with the column material. Information and data of the setups are summarized in **Table 22**.

Table 22. Setups and conversion of affinity-guided SPANC using five-heptad coiled coils in presence of peptide **32** as a competitive reactant.

Setup	A[a]	B[b]	C[c]	Eq. A:B:C	[A] [μM]	Analysis	Conversion[d] [%]
11	**18**	**19**	**32**	1:1:1	100	HPLC, ESI-MS	89.2
12[e]	**18**	-	**32**	1:0:1	100	HPLC, ESI-MS	60.2

a: BCN-decorated guiding unit.
b: Aldehyde-bearing guiding unit.
c: Competitive aldehyde component.
d: Conversion calculated from decrease in HPLC trace of aldehyde-bearing guiding unit after termination of reaction (when no further consumption of **B** was observed).
e: Control experiment using **18** and **32**. Conversion calculated from consumption of **32**.

The test reaction employing setup 11 exhibited an excellent conversion of about 90 % regarding **19** after a reaction time of 5 h. The HPLC profiles of the reaction progress are shown in **Figure 56A**.

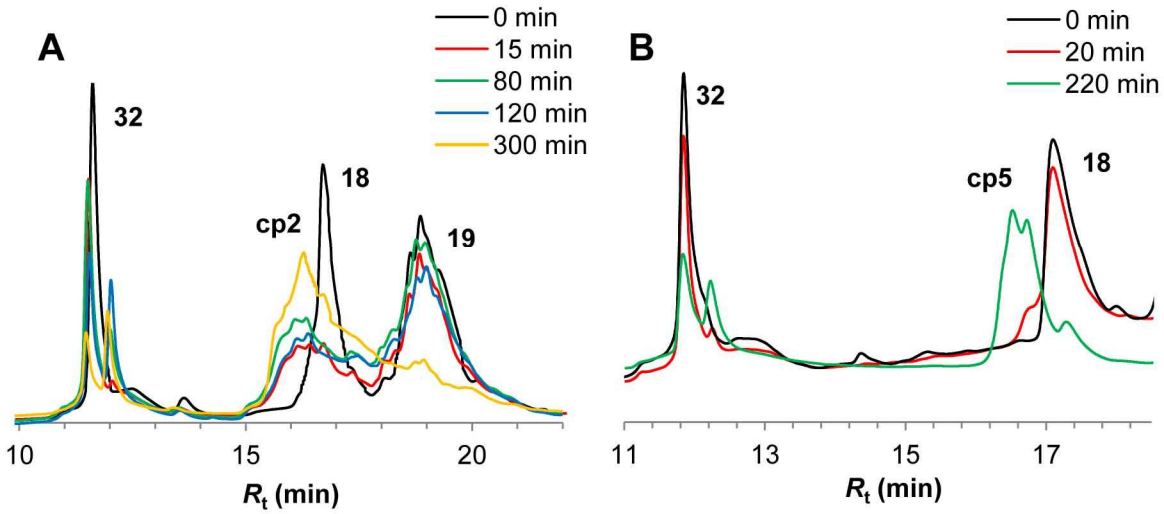

Figure 56. Chromatographic profiles of the reaction mixture of **A**: SPANC between **18** and **19** in presence of **32** (setup 11) and **B**: SPANC between **18** and **32** (setup 12) towards formation of conjugation products. UV detection at λ = 220 nm; eluent: 9→90 % acetonitrile in 0.1 % aq. TFA over 20 minutes at flow rate 1 ml/min. Divers traces of samples analyzed after distinct reaction times are marked with corresponding colors.

In none of the relevant HPLC fractions the corresponding signals of conjugation product between **32** and **18** (**cp5**) were found. A fraction with R_t = 12.0 min was also collected and analyzed by ESI-MS but only the m/z corresponding to **32** were observed. In all SPANC experiments the nitrone intermediate could not be detected by MS analysis, presumably due to the reverse reaction to the corresponding aldehydes during ionization or by the acidic HPLC and LC-MS eluent.[173b] The analyzed fraction is presumed to belong to the nitrone intermediate of **32**. Analogously to the setups using benzaldehyde, the general SPANC reactivity of **32** was evaluated in a test reaction lacking guiding unit **19** (setup 12, **Figure 56B**). The formation of **cp5** was confirmed by MS analysis and 60.2% conversion of **32** was determined. A second-order kinetic constant of k_2 = 0.39 $M^{-1}s^{-1}$ was calculated for this non-templated reaction, whereas the affinity-guided reaction (setup 11) exhibited a significantly enhanced reaction rate with k_2 = 3.57 $M^{-1}s^{-1}$, hence the benefits of the affinity guided approach towards reaction rate and selectivity was proven by these experiments.

Furthermore, an additional reaction setup where the aldehyde component was formed *in situ* (without chromatographic purification) prior to SPANC was developed and tested (setup 13). The oxidation of **19'** was quenched by addition of 4-methoxythiophenol (MeOPhSH) and further procedure was similar to those described for the SPANC setups 2 – 5. The completion of oxidation was confirmed by MS analysis of the reaction mixture as no signals of the precursor **19'** were found in the spectrum. A conversion of 72.2 % was calculated for **19** from the HPLC traces of the monitored reaction (figure given in appendix), which was similar to the values of all other test reactions using this guiding unit pair. But in contrast to the reaction using the solitaire aldehyde, the reaction rate was significantly lower (k_2 = 0.66 $M^{-1}s^{-1}$) and only traces of **cp2** were found in MS analysis. Possible reasons for this outcome were, for instance, the interruption of the conjugation process by quenching agents or the decrease in complexation efficacy of the guiding units by the application of a more complicated solvent system with several additional compounds. However, it was shown that

the approach comprising an *in situ* oxidation of the amino alcohol component is also applicable for the affinity-guided SPANC, whereby further optimization must be done.
All conversions and kinetic data of the test reactions of coiled coil-guided SPANC and control reactions are summarized in **Table 23**.

Table 23. Conversion and kinetic data of affinity-guided SPANC experiments using coiled-coil guiding units.

Setup	A[a]	B[b]	C[c]	Eq. A:B:C	Conversion[d] [%]	k_2 [$M^{-1}s^{-1}$]	R^2 [e]	Data points[f]
1	**16**	**17**	-	1:1	74.1	1.88	0.931	6
4	**18**	**19**	-	1:1	69.8	4.16	0.981	3
5	**18**	**19**	-	1:1	61.2	3.56	0.991	3
6	**18**	**19**	benzaldh.	1:1:1	80.0	7.24	0.825	5
7	**18**	**19**	benzaldh.	2:3:2	71.5	2.34	0.596	3
8	**18**	**19**	benzaldh.	1:1:1	79.3	7.82	0.783	4
9	**18**	-	benzaldh.	1:0:10	50.1	1.42	0.476	3
11	**18**	**19**	**32**	1:1:1	89.2	3.57	0.707	5
12	**18**	-	**32**	1:0:1	60.2	0.39	0.681	3
13	**18**	**19'**	-	1:1	72.2	0.66	0.757	3

a: BCN-decorated guiding unit.
b: Aldehyde-bearing guiding unit.
c: Competitive aldehyde component.
d: Conversion calculated from decrease in HPLC trace of aldehyde-bearing guiding unit after termination of reaction (when no further consumption of **B** was observed).
e: Regression coefficient of trend line determined for calculation of k_2.
f: Number of data points used for the liner regression.

As an excess of MeNOH was used in each reaction, a simplified kinetic model of a two-component system could be applied (plots for determination of k_2 given in appendix). Due to the low number of recorded data points few trend lines of the linear regressions were of low quality ($R^2 < 0.8$). Hence, these values should only be considered as approximate values. But on the whole, it became obvious that a significantly higher reaction rate was found for affinity-guided SPANC approaches. A summary of all affinity-guided SPANC setups with coiled coil guiding units is given in the appendix.

PNA Guiding Units

The basic setup for the test reactions of PNA-guided SPANC experiments was similar to those for coiled coil-mediated test reactions, whereby two analytical approaches were examined to confirm product formation. In preliminary experiments, a limited applicability of PNAs to ESI-MS analysis was observed, presumably caused by the high charge density and the ability to

form a vast number of multiply charged species, leading to a complex ionization pattern. Therefore, two denaturing polyacrylamide gel electrophoresis (PAGE) techniques were used as an alternative method to detect conjugate formation. First, an SDS-PAGE with a highly concentrated polyacrylamide gel was performed (details given in chapter 5.3.4). As the resulted bands were not distinct and sharp, only tendency to form dimers was seen. An SDS-PAGE gel of the PNA guiding units **20**, **21** and the reaction mixtures of SPANC, SPAAC, and psoralen cross-linkage, stained with coomassie brilliant blue, is shown in **Figure 57**.

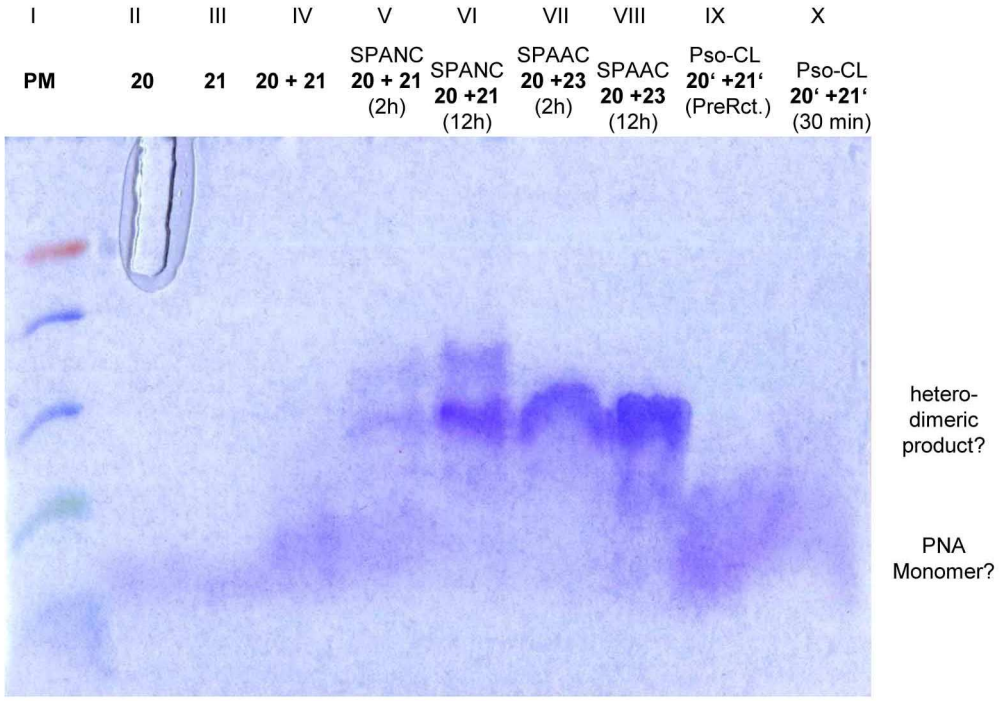

Figure 57. SDS-PAGE gel to monitor diverse PNA-guided conjugation reactions and solitary guiding units **20** and **21**. PM = protein molecular mass marker (low range). Since the electrophoresis behavior of PM and PNAs was not comparable, the protein sizes of the marker bands are not given.

As the protein marker (PM) loaded along with the samples exhibited a different electrophoresis behavior as the PNA probes, the marker bands could not be used as references and size determination and quantification of the product was not possible. As a second electrophoresis technique an urea-PAGE with a highly concentrated and highly cross-linked urea-polyacrylamide gel (26% w/v in polyacrylamide and 8 M urea at pH 3) modified from a reported protocol for PNA analysis was tested.[174] The experiment was performed more than 10 times under slightly altered conditions (e.g. voltage of electrophoresis, electrophoresis time, and sample preparation) but in none a distinct separation of the bands could be observed (gel pictures not shown). As both PAGE techniques were found to be inappropriate for reaction monitoring and an optimization was expected to be too cost- and time-consuming, finally, the conventional strategy using chromatographic isolation and successive MS analysis of the collected fractions was chosen. UV detection of HPLC probes was performed at 260 nm to minimize the background signals and for facilitated tracking of the PNA-containing fractions.

After preliminary experiments to adjust the concentration range and the gradient of HPLC eluents, three standard setups employing BCN-decorated guiding unit **20** and aldehyde-bearing guiding unit **21** with small variation in reactant stoichiometry were developed (**Table**

24). All reactions were performed in ammonium acetate buffer at pH 6.5 and ambient temperature.

Table 24. Setups and conversion of affinity-guided SPANC using PNA guiding units.

Setup	A[a]	B[b]	Eq. A:B	[A[a]] (μM)	[MeNOH] (μM)	[p-anisidine] (μM)	t_{comp} (min)	Conversion[c] (%)
1	**20**	**21**	1:1	200	333	333	60	51.0
2	**20**	**21**	4:3	130	667	0	60	52.0
3	**20**	**21**	4:3	130	667	333	60	57.1

a: BCN-decorated guiding unit.
b: Aldehyde-bearing guiding unit.
c: Conversion calculated from decrease in HPLC trace of aldehyde-bearing guiding unit after termination of reaction (when no further consumption of **B** was observed).

Similarly as observed for the coiled coil-based test reactions, the BCN component was consumed within 6 – 7 h, whereby the conversion of the aldehyde-component **21** was about 50-60 % and generally worse than found for the coiled-coil setups. A further important result from these reactions was that the final conversion of the reactant was not distinctly influenced by the presence of *p*-anisidine as the reaction lacking this additive (setup 2) exhibited a similar conversion of **21** as the other setups. Chromatographic profiles and the MS spectrum of the collected product fraction of the test reaction using setup 3 is shown in **Figure 58** and **Table 25**. As expected, the product **cp6** was poorly ionizable and possessed the high diversity in ionization patterns resulting in a complex spectrum with strong background signals. But the m/z corresponding to **cp6** were actually found.

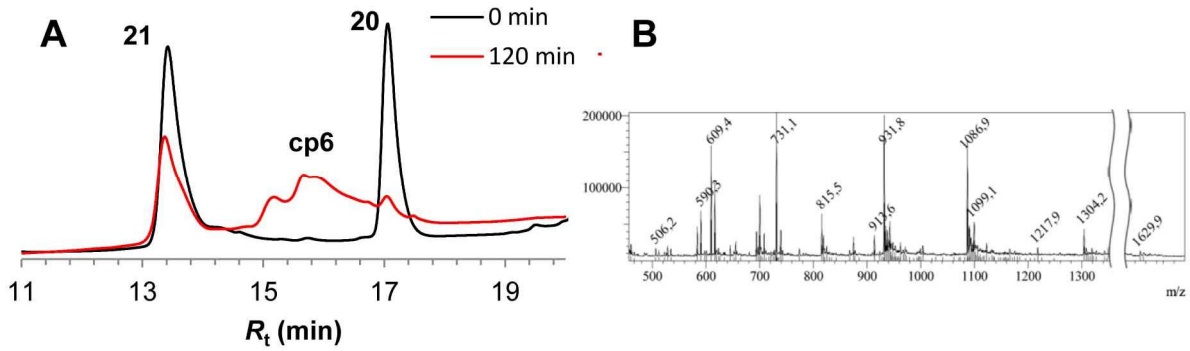

Figure 58. A: Chromatographic profiles of the reaction mixture of SPANC between **20** and **21** (setup 3) after 120 min towards formation of a covalently bond heterodimer. UV detection at λ = 260 nm; eluent: 0→72 % acetonitrile in 0.1 % aq. TFA over 20 minutes at flow rate 1 ml/min. **B**: ESI mass spectrum of the main product fraction of the test reaction using setup 3 after chromatographic purification of the reaction mixture (R_t = 16.3 min). Spectra are in positive mode.

Table 25. List of m/z signals corresponding to **cp6** found in the ms spectrum given in **Figure 58B**.

Species	Ions	m/z calc.	m/z obs.
cp6 (M = 6515.60 g/mol)	$[M+4H]^{4+}$	1628.9	1629.9
	$[M+5H]^{5+}$	1303.3	1304.2
	$[M+6H]^{6+}$	1086.3	1086.9
	$[M+7H]^{7+}$	931.3	931.8
	$[M+8H]^{8+}$	815.0	815.5
	$[M+11H]^{11+}$	591.1	590.3

Addressing the optimization of reaction conditions, test-reactions were performed using the general conditions of setups 1-3 and varying buffer system, reaction temperature, and complexation time (setup 4-10, 13; **Table 26**).

Table 26. Setups and conversion of affinity-guided SPANC experiments using PNA guiding units.

Setup	A[a]	B[b]	Eq. A:B	[A[a]] (μM)	Main solvent (pH)	t_{comp} (min)	T_{rct}	Conversion[c] (%)
4	**20**	**21**	4:3	130	$HEPES_{aq}$ (6.0)	60	rt	66.1
5	**20**	**21**	1:1	67	NH_4OAc_{aq} (6.0)	60	rt	75.1
6	**20**	**21**	1:1	67	NH_4OAc_{aq} (6.0)	60	4°C	75.9
7	**20**	**21**	1:1	67	$NaOAc_{aq}$ (5.0)	60	4°C	55.6
8	**20**	**21**	1:1	67	PBS_{aq} (7.4)	60	4°C	39.3
9	**20**	**21**	6:5	80	$HEPES_{aq}$ (6.0)	60	4°C	73.2
10	**20**	**21**	1:1	220	$HEPES_{aq}$ (6.0)	0	4°C	61.3
13	**20**	**21**	1:1	200	NH_4OAc_{aq} (6.0)	60	rt	73.1

a: BCN-decorated guiding unit.
b: Aldehyde-bearing guiding unit.
c: Conversion calculated from decrease in HPLC trace of aldehyde-bearing guiding unit after termination of reaction (when no further consumption of **B** was observed).

An improvement in conversion was realized by changing the buffer system, whereby the best results were observed in ammonium acetate and HEPES buffer systems at pH 6.0 (10-15 % improvement in conversion of **21**). Chromatographic profiles and the MS spectrum of the collected product fraction in setup 4 is shown exemplary in **Figure 59**.

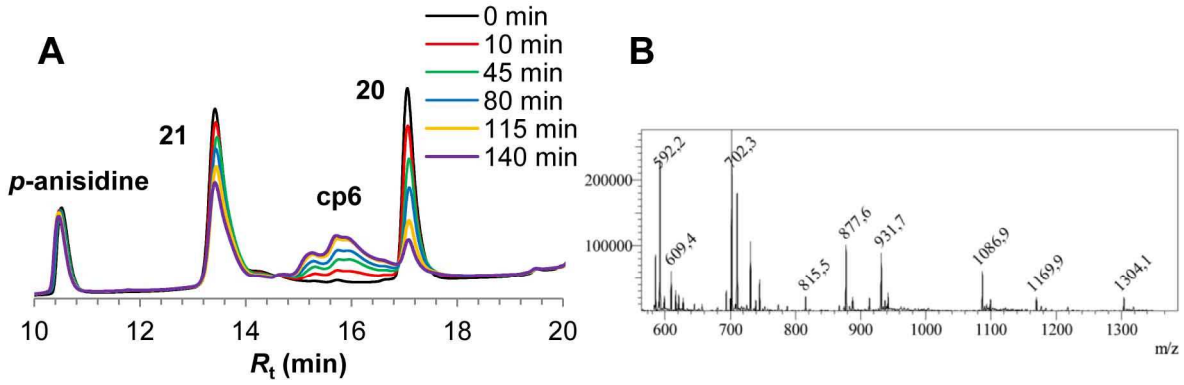

Species	Ions	m/z calc.	m/z obs.
cp6 (M = 6515.60 g/mol)	$[M+5H]^{5+}$	1303.3	1304.2
	$[M+2HEPES+Na+7H]^{6+}$	1169.71	1169.9
	$[M+6H]^{7+}$	1086.3	1086.9
	$[M+7H]^{7+}$	931.3	931.8
	$[M+2HEPES+Na+9H]^{8+}$	877.5	877.6
	$[M+8H]^{8+}$	815.0	815.5
	$[M+2HEPES+Na+11H]^{10+}$	702.2	702.3
	$[M+11H]^{11+}$	591.1	592.2

Figure 59. A: Chromatographic profiles of the reaction mixture of SPANC between **20** and **21** (setup 4) towards formation of a covalently bond heterodimer. UV detection at λ = 260 nm; eluent: 0→72 % acetonitrile in 0.1 % aq. TFA over 20 minutes at flow rate 1 ml/min. **B**: ESI mass spectrum of the main product fraction of the test reaction using setup 4 upon chromatographic purification of the reaction mixture after a reaction time of 140 min (R_t = 15.8 min). Spectra are in positive mode. Corresponding m/z signals of calculated and found species are listed in the table below.

As a reaction in sodium acetate buffer (pH 5.0, setup 7) exhibited similar conversion as in ammonium acetate buffer pH 6.5 (setup 3) and, contrary, a drastic loss in conversion was observed in PBS at pH 7.4, the optimal pH for PNA-guided SPANC was assumed to be slightly acidic (pH 6.0). The reactions in HEPES buffer resulted in formation of complex PNA-HEPES salts found in MS-spectrum and making the signal mapping extremely complicated. Hence, ammonium acetate (pH 6.0) was chosen as the most appropriate buffer for SPANC experiments in the present work. Chromatographic profiles and the MS spectrum of the collected product fraction of the test reaction using setup 13 is shown exemplary in **Figure 60**.

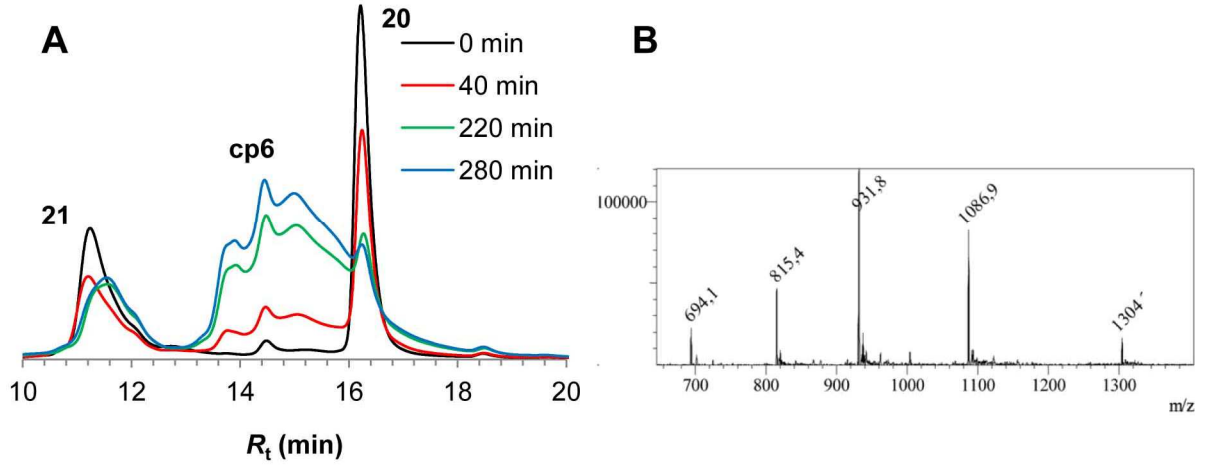

Figure 60. A: Chromatographic profiles of the reaction mixture of SPANC between **20** and **21** (setup 13) towards formation of a covalently bond heterodimer. UV detection at λ = 260 nm; eluent: 9→63 % acetonitrile in 0.1 % aq. TFA over 20 minutes at flow rate 1 ml/min. **B**: ESI mass spectrum of the main product fraction of the test reaction using setup 13 upon chromatographic purification of the reaction mixture after a reaction time of 280 min (R_t = 14.6 min). Spectra are in positive mode. Corresponding m/z signals of calculated and found species are as same as given in **Table 26**.

A variation of reaction temperature (ambient temperature or on-ice) resulted in no remarkable differences in reaction efficacy, contrary to our expectations that the decrease in temperature could eventually suppress the previously discussed side reaction (direct addition of MeNOH to BCN group).

However, in setup 10, the order of reactant addition was altered. Thus, *p*-anisidine and MeNOH was added first to the aldehyde component **21** and the reaction counterpart **20** was given later to the mixture (complexation time = 0 min). This experiment resulted in decrease of conversion of about 10 %. Further experiments with no pre-complexation of guiding units are described later for the SPAAC of PNA guiding units.

Furthermore, reaction setups using phenyl hydroxylamine (PhNOH) instead of MeNOH as nitrone-forming agent were also tested (**Table 27**) as McKay et al. reported an enhanced reaction efficacy for nitrones formed by this alternative hydroxylamine.[77]

Table 27. Setups and conversion of affinity-guided SPANC using PNA guiding units in combination with phenyl hydroxylamine as nitrone-forming agent.

Setup	A[a]	B[b]	Eq. A:B	[A[a]] (μM)	Main solvent (pH)	t_{comp} (min)	T_{rct}	Conversion[c] (%)
11	**20**	**21**	6:5	240	NH_4OAc_{aq} (6.5)	60	4°C	50.9
12	**20**	**21**	4:1	320	NH_4OAc_{aq} (6.5)	60	4°C	68.5

a: BCN-decorated guiding unit.
b: Aldehyde-bearing guiding unit.
c: Conversion calculated from decrease in HPLC trace of aldehyde-bearing guiding unit after termination of reaction (when no further consumption of **B** was observed).

Contrary to our expectations, no obvious enhancement in conversion of **21** was observed. As the signals of the conjugation product between PhNOH and **20** (**cp9**) were found in MS analysis, the presence of the undesired side reaction was confirmed also for these setups.

Thus, it was shown that the strongest rate- and efficacy-limiting issue in SPANC was this unavoidable side reaction. This fact was also confirmed by the improvement of conversion of **21** by about 20 % using a four-fold excess of the BCN compound (setup 12) whereby full conversion of an aldehyde was still not possible.

Selectivity of the PNA-guided SPANC was examined in a test reaction comprising **20** and **21** in the presence of the competitive aldehyde-bearing PNA-peptide hybrid **22** bearing a non-complementary PNA sequence. All of the three components were mixed equimolarly in ammonium acetate buffer pH 6.0 and incubated for 1 h (setup 14). The reaction was initiated by addition of MeNOH (5 eq.). The HPLC profiles of the monitored reaction progress are given in **Figure 61**.

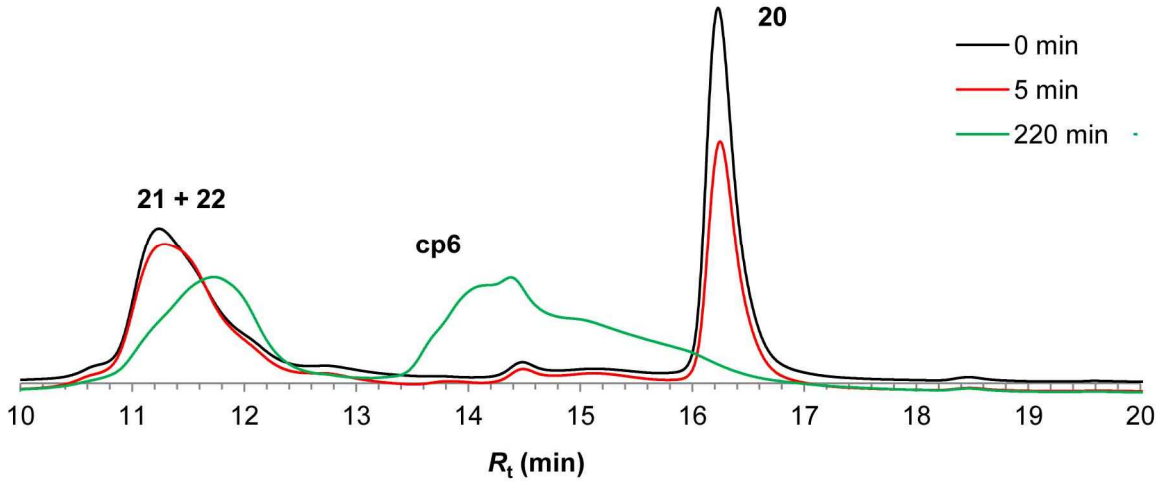

Figure 61. Chromatographic profiles of the reaction mixture of SPANC between **20** and **21** in presence of **22** (setup 14) towards formation of a covalently bond heterodimer. UV detection at λ = 260 nm; eluent: 9→63 % acetonitrile in 0.1 % aq. TFA over 20 minutes at flow rate 1 ml/min.

The retention times of both aldehyde-bearing guiding units, **21** and **22**, were completely the same (R_t = 11.3 min), thus a distinction in HPLC was not possible. Hence, the selectivity was evaluated by the presence of the MS signals corresponding to the conjugation product between **22** and **20** (**cp7**) in the spectrum of all relevant fractions. As no traces of a SPANC conjugate **cp7** was detected, the selectivity of the PNA-guided SPANC was confirmed. This outcome was additionally supported by Matrix Assisted Laser Desorption/Ionization mass spectrometry (MALDI-MS) of the collected main fractions (**Figure 62**).

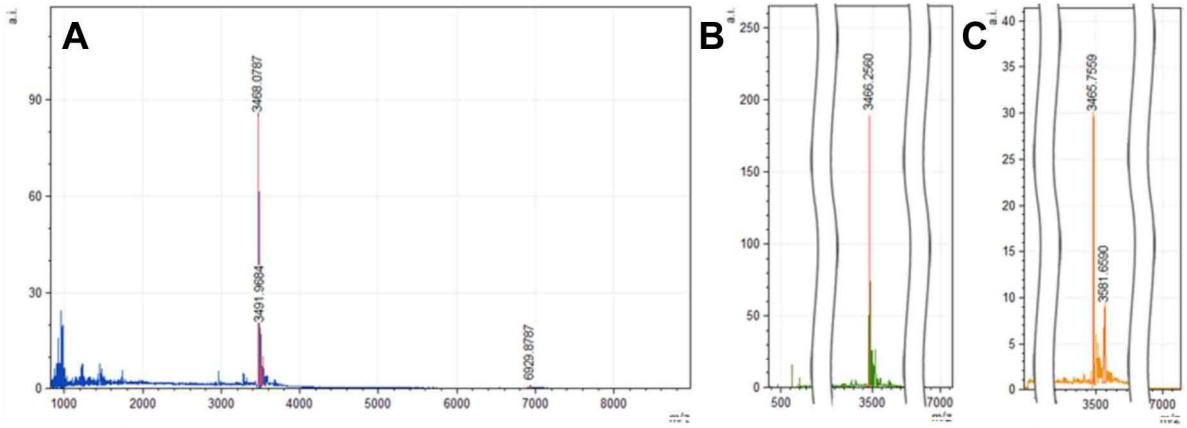

Species	Ions	m/z calc.	m/z obs.
cp6 (M = 6515.60 g/mol)	[M+2sinapic acid+H]$^{+}$	6928.7	6929.9
	n. r.	-	3491.9
		3464.9	3468.1
	[M+2sinapic acid+2H]$^{2+}$	3464.9	3466.8
		3464.9	3466.3

Figure 62. MALDI mass spectra of the collected fractions of test reactions using setup 3 after chromatographic purification of the reaction mixture (**A**: R_t = 14.3 – 14.8 min, **B**: R_t = 13.3 – 14.3 min, **C**: R_t = 14.8 – 15.8 min). Spectra are in positive mode. Corresponding m/z signals of calculated and found species are listed in the table below. Spectra recorded by Dr. Alesia Tietze (Prof. Thiele group, TU Darmstadt).

The found m/z of 6929.9 was in good agreement with that calculated for **cp6** (m/z = 6515.6) whereby two sinapic acid molecules from the matrix surface were added upon measurement (additional m/z of + 412.05), which is a frequently reported observation for MALDI-MS.[175] The same effect was also found in the doubly charged species with m/z = 3466.3 - 3468.1 (calculated m/z = 3258.8). In none of the fractions the signals of the side products, neither of **cp7**, nor of **cp8**, were found. As the retention time in HPLC of the aldehyde-bearing compounds **21** and **22** was indistinguishable, only the sum of conversion of these compounds could be determined (50.4 %). Since no formation of the **cp7** was confirmed, it was supposed that after 220 min the remaining signals (R_t = 11.8 min) mainly corresponded to **22**. That means, **21** was converted into **cp6** nearly quantitatively. This assumption was confirmed by ESI-MS of the respective fraction where only corresponding m/z signals of **22** were found (**Figure 63**).

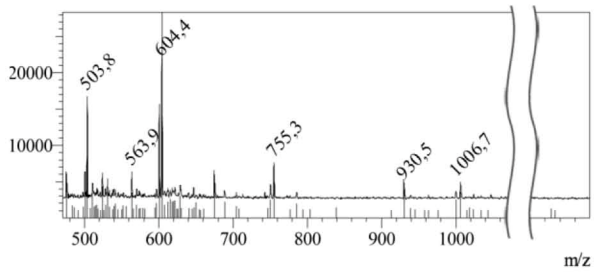

Species	Ions	m/z calc.	m/z obs.
22 + H_2O^a	[M+3H]$^{3+}$	1006.7	1006.7
	[M+4H]$^{4+}$	755.2	755.3
	[M+5H]$^{5+}$	604.4	604.4
	[M+6H]$^{6+}$	503.8	503.8

Figure 63. ESI mass spectrum of the HPLC-separated reaction mixture of SPANC using setup 14. Fraction at R_t = 11.8 min (**Figure 61**) Spectrum in positive mode. Corresponding m/z signals of calculated and found species are as same as given in the table on right. *a*: Found mass mainly corresponded to monohydrate of **22** (hemiacetale) with M = 3016.95 g/mol.

The SPANC reactivity of **22** was evaluated by a test reaction with **20** using a similar setup as for the coiled-coil modes system (setup 5, SPANC between **18** and **32**). As the m/z corresponding to **cp8** was found in the ESI-MS spectrum of the reaction mixture after 4 h, the general reactivity of **22** was confirmed (MS-spectrum given in appendix).
Finally, four reaction setups based on the *in situ* generation of the aldehyde were tested (**Table 28**). All test reactions were performed at ambient temperature after one hour incubation of equimolar ratio of the PNA guiding units.

Table 28. Summary of reaction setups and conversion of affinity-guided SPANC experiments using PNA guiding units with *in situ* oxidation of **21'**.

Setup	A[a]	B[b]	[A[a]] (μM)	Main solvent (pH)	Quenching agent	Conversion[c] (%)
15	**20**	**21'**	100	NH_4OAc_{aq} (6.5)	4-MeOPhSH	51.0
16	**20**	**21'**	200	NH_4OAc_{aq} (6.5)	4-MeOPhSH	51.9
17	**20**	**21'**	200	NH_4OAc/THF[d]	4-MeOPhSH	49.5
18[e]	**20**	**21'**	200	NH_4OAc/THF[d]	Ethylene glycol	76.6

a: BCN-decorated guiding unit.
b: Aldehyde-bearing guiding unit.
c: Conversion calculated from decrease in HPLC trace of aldehyde-bearing guiding unit after termination of reaction (when no further consumption of **B** was observed).
d: 7:5, v/v mixture of NH_4OAc buffer pH 6.0 and THF.
e: PhNOH used instead of MeNOH as nitrone-forming agent.

The test reactions showed similar conversion as determined for the setups comprising the isolated compound **21**. In setup 18, employing PhNOH as nitrone-forming agent and ethylene glycol as a quenching additive, a good conversion of more than 75 % was found. As described for the coiled-coil system, only traces of the corresponding m/z signals of **cp6** were found.
In general, all determined conversions of the aldehyde components in the PNA-guided approach were slightly worse compared to those obtained for the coiled coil-guided approach (10 – 15 % lower conversion). Similar tendency was observed for the reaction rate in each model systems, with the second order kinetic constant k_2 being generally smaller by the factor of 2-5 in the PNA-guided setups (**Table 29**).

Table 29. Conversion and kinetic data of affinity-guided SPANC experiments using PNA guiding units.

Setup	A[a]	B[b]	C[c]	Eq. A:B:C	Conversion[d] [%]	k_2 [$M^{-1}s^{-1}$]	R^2 [e]	Data points[f]
4	**20**	**21**	-	4:3	66.1	3.03	0.924	5
6	**20**	**21**	-	1:1	75.9	0.97	0.412	4
7	**20**	**21**	-	1:1	55.6	0.61	0.991	6
8	**20**	**21**	-	1:1	39.3	0.12	0.789	5
9	**20**	**21**	-	6:5	73.2	1.86	0.946	5
10	**20**	**21**	-	1:1	61.3	0.74	0.529	3
11	**20**	**21**	-	6:5	50.9	0.34	0.516	4
12	**20**	**21**	-	4:1	68.5	1.40	0.965	5
13	**20**	**21**	-	1:1	73.1	0.80	0.963	3
14	**20**	**21**	**22**	1:1:1	50.4[g]	0.90	0.971	3
16[h]	**20**	**21**	-	1:1	51.9	0.71	0.566	4
17[h]	**20**	**21**	-	1:1	49.5	0.14	0.339	5
18[h]	**20**	**21**	-	1:1	76.6	0.69	0.686	6

a: BCN-decorated guiding unit.
b: Aldehyde-bearing guiding unit.
c: Competitive aldehyde component.
d: Conversion calculated from decrease in HPLC trace of aldehyde-bearing guiding unit after termination of reaction (when no further consumption of **B** was observed).
e: Regression coefficient of trend line determined for calculation of k_2.
f: Number of data points used for the liner regression.
g: Sum of decreased ratio of the HPLC signals of **21** and **22**.
h: *In situ* formation of aldehyde without isolation of **21**.

As the number of used data points to determine the kinetic constants were limited, the calculated values should only be given as approximate values, especially for those with low R^2 for the linear regression (plots given in appendix). However, the obtained k_2 values were still in distinctly higher range than the reported ones. Indeed, MacKenzy et al. reported a second order kinetic constant k_2 of 0.05 $M^{-1}s^{-1}$ for a non-guided SPANC of BCN with a cyclic nitrone and McKay et al. a k_2 of 0.09 $M^{-1}s^{-1}$ for the reaction between dibenzo cyclooctyne (DIBO) and benzaldehyde.[77, 173b] A linear relation between the overall conversion of the aldehyde component and the kinetic constant was not observed, presumably, due to the fact that the reaction progress and efficacy were mainly limited by the unexpected consumption of the BCN component by the side-reaction discussed above. Since the direct addition of hydroxylamine seemed not to be dramatically fast, the simple incensement in reaction rate would be the best

way to suppress this reaction. To this end, the application of biarylazacyclooctynone (BARAC) as strained alkyne component with a up to 800 fold higher reported kinetic constant compared to BCN could become a viable alternative.[173b]
A general problem in the isolation of the conjugation product by HPLC was its broad elution profile, presumably caused by the formation of stereoisomeric SPANC product, and the fact that by-products have similar HPLC retention. Thus, for future approaches a more appropriate separation method should be used as e.g. SEC.

SPAAC of PNA Guiding Units

To underline the benefits of the affinity-guided SPANC approaches, SPAAC test reactions employing the BCN-decorated PNA guiding unit **20** and the azide-functionalized PNA guiding unit **23** were performed. The general setup of the test reaction (**Table 30**) was similar to the SPANC approaches but since the reaction was non-triggered, the guiding unit pair was not pre-incubated.

Table 30. Setups, conversion, and kinetic data of SPAAC using PNA guiding units **20** and **23**.

Setup	A[a]	B[b]	Eq. (A:B)	[A[a]] (μM)	Main solvent (pH)	Conversion[c] (%)	k_2 [$M^{-1}s^{-1}$]
1	**20**	**23**	3:4	130	NH_4OAc_{aq} (6.5)	54.4	0.54
2	**20**	**23**	1:1	330	NH_4OAc_{aq} (6.5)	33.7[d]	0.82

a: BCN-decorated guiding unit.
b: Aldehyde-bearing guiding unit.
c: Conversion calculated from decrease in HPLC trace of aldehyde-bearing guiding unit after termination of reaction (when no further consumption of **B** was observed).
d: Reaction monitored only for 5 h. Reaction progress presumably not terminated.

Compared to the SPANC approaches, the conversions regarding the azide component **23** within same reaction time were slightly worse. The calculated k_2 values were in similar range as found for the affinity-guided SPANC approaches but also slightly worse. As a second-order constant of $k_2 = 0.55\ M^{-1}s^{-1}$ was calculated for a non-templated SPAAC approach (see chapter 3.3.1.5) no significant improvement in reaction rate could be observed by application of the guiding units. This outcome emphasized the importance of the complexation step before initiation of the reaction. The HPLC profiles of the monitored test reaction are given in **Figure 64**. The formation of a conjugation product (**cp10**) was confirmed by ESI-MS.

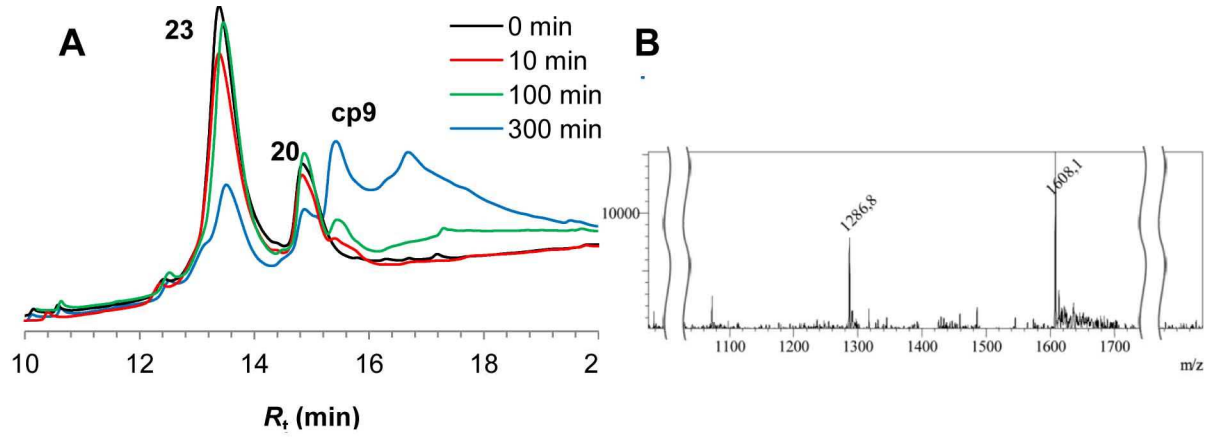

Species	Ions	m/z calc.	m/z obs.
SPAAC product **20** + **23** (M = 6428.40 g/mol)	$[M+4H]^{4+}$	1608.1	1608.1
	$[M+5H]^{5+}$	1268.7	1268.8
	$[M+6H]^{6+}$	1072.4	1072.5

Figure 64. A: Chromatographic profiles of the reaction mixture of SPAAC between **20** and **23** (setup 1) towards formation of a covalently bond heterodimer. UV detection at λ = 220 nm; eluent: 0→72 % acetonitrile in 0.1 % aq. TFA over 20 minutes at flow rate 1 ml/min. **B**: ESI mass spectrum of the main product fraction of the SPAAC using setup 1 after chromatographic purification of the reaction mixture (R_t = 15.8 min). Spectra are in positive mode. Corresponding m/z signals of calculated and found species are listed in the table below.

3.3.2.2 Psoralen Cross-Linkage of PNA Guiding Units

As an alternative conjugation technique, the UVA-mediated nucleobase cross-linkage by psoralen was chosen. Preliminary experiments using solitaire psoralen and the precursor PNA guiding units **20'** and **21'** (lacking SPANC-reactive groups) were performed. After incubation of the guiding units in PBS at pH 7.0 for hybridization, an excess of psoralen was given to the mixture. The mixture was exposed to UVA irradiation with λ = 366 nm. Detailed reaction setup is given in chapter 5.3.4.1.

In full agreement with our expectation (see chapter 3.3.1), a non-controllable addition of multiple psoralen molecules to the PNA guiding units occurred, which was indicated by precipitation during UVA irradiation and the emerge of multiple peaks in the HPLC traces at R_t > 20 min (strongly nonpolar area, **Figure 65**).

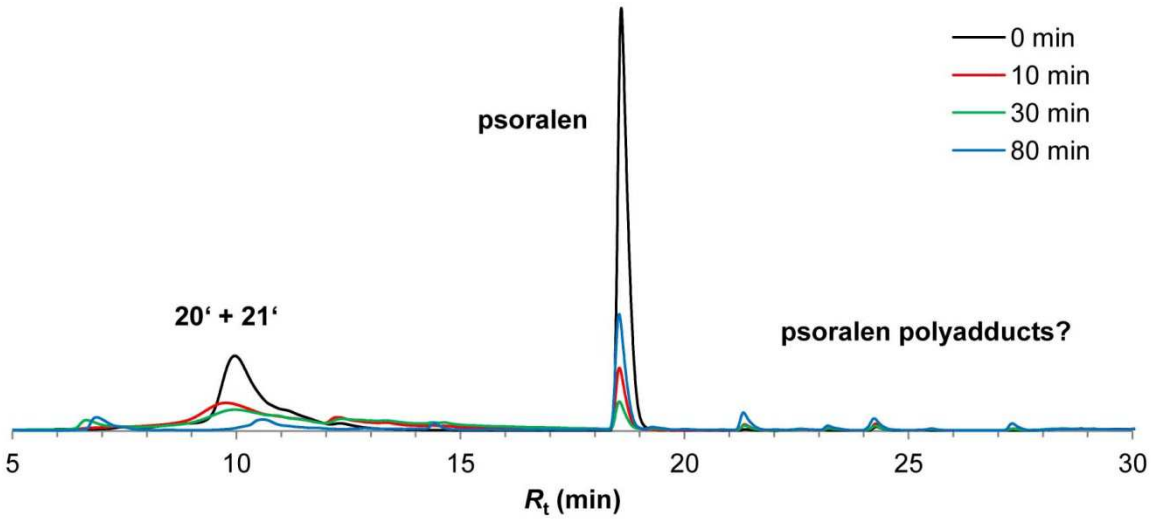

Figure 65. Chromatographic profiles of the reaction mixture of UVA-mediated cross-linking between **20'** and **21'** with free psoralen molecules. UV detection at λ = 260 nm; eluent: 9→54 % acetonitrile in 0.1 % aq. TFA over 20 minutes at flow rate 1 ml/min.

ESI-MS analysis of the collected fractions showed a vast number of non-assignable signals emphasizing the formation of a non-defined mixture of conjugates. Also in SDS-PAGE of the test reaction (chapter 3.3.2.1, **Figure 57**) no distinct bands of conjugation products or traces of covalently linked dimers were observed.

Therefore, a cross-linking strategy using the PNA guiding unit **25** with *N*-terminally pre-installed psoralen moiety was pursued. The complementary guiding unit **26** with an *N*-terminal extension by a tata motif (for PNA-PNA cross-linkage) and its DNA analogue **33** with the sequence $^{5'}$TATAGTAGATCACT$^{3'}$ (for PNA-DNA cross-linkage) were applied.

Preliminary experiments were performed in Tris-HCl buffer at pH 7.5, ammonium acetate buffer at pH 6.5, and sodium acetate buffer at pH 5.0, whereby only in Tris-HCl buffer a distinct reaction progress was observed by HPLC analysis. The general reaction setup was similar to the reaction with psoralen itself (see chapter 5.3.4.2). The chromatographic profiles of the HPLC-monitored reactions of PNA-DNA cross-conjugation and PNA-PNA cross conjugations are shown in **Figure 66**.

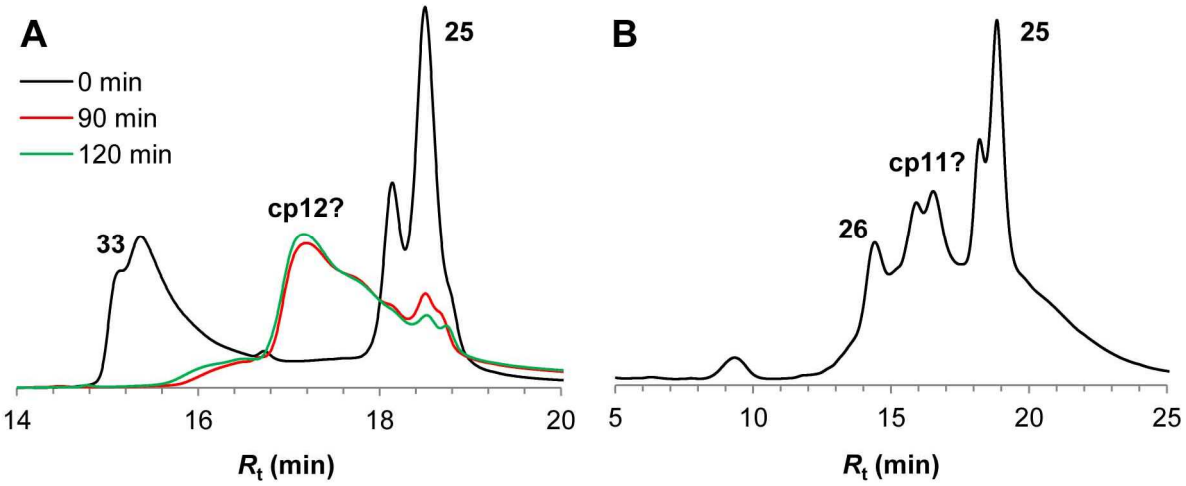

Figure 66. Chromatographic profiles of the reaction mixture of UVA-mediated cross-linking using PNA-bound psoralen **25** and **A**: complementary DNA **33**; **B**: complementary PNA **26**. UV detection at λ = 260 nm; eluent: 0→36 % acetonitrile in 0.1 % aq. TFA over 20 minutes at flow rate 1 ml/min.

In general, a distinct reaction progress was only observed after a prolong UVA irradiation (about 90 min). In both approaches, the emerging of a novel HPLC peak could be observed, whereby no further progress was found after an irradiation time of about 2 h in case of the PNA-PNA conjugation, despite both of the reactants remained in reaction mixture. A distinct calculation of reactant consumption was not possible as the retention of the reactants and the newly formed compound was similar. A proof for formation of the desired heterodimeric conjugate (**cp12**) was also not given as in MS analysis only traces of signals contingently matching to the calculated m/z of products were found (MS spectra given in appendix).
Contrary, the test reaction of PNA-DNA cross-conjugation resulted in nearly full consumption (99 % for **25**) of both the guiding units while emerging of a novel product peak at 17.8 min. But since only traces of highly charged and complexly ionized signals of the potential product were found in MS, a proof for formation of desired product conjugate **cp13** was not given for this approach, too. Thus, the results of the preliminary studies given in this subchapter should be interpreted with wariness and further detailed investigation is needed. Especially, a more effective method for qualification of the PNA-DNA conjugate must be developed as the DNA molecule **33** was not detected in ESI-MS, even as pure compound (data not shown).
Furthermore, it was observed that a too long and intensive irradiation caused precipitation and formation of strongly nonpolar compounds, similar to the reaction using free psoralen. This indicated that uncontrolled addition of psoralen was not suppressed as this molecule possesses two cycloaddition sites.

3.3.2.3 Functionalization of Protein Scaffolds with PNA Guiding Units

The synthesis of a multivalent ADC by affinity-guided simultaneous conjugation of several ligands on a protein scaffold is an ultimate goal of this project. Therefore, the attachment of PNA guiding units **27** – **30** to an antibody Fc fragment was examined. Enzymatic ligation by Sortase A from *Staphylococcus aureus* (eSrtA) was chosen for coupling of the peptide-PNA-hybrids to the Fc scaffold.[176] Both counterparts were functionalized with the specific recognition sequence required for the Sortase A catalysis. This transpeptidase specifically cleaves a peptide bond between Thr and Gly of the sequence LPXTG forming a thioacyl intermediate with further attachment of an activated carbonyl to an *N*-terminal oligo-Gly motif.[177]
In initial sortase-catalyzed condensations, the Fc fragment reacted with compound **28** comprising a TEV protease cleavage sequence and a Lys(ε-Ser) unit between the *N*-terminal pentaglycine and the PNA guiding unit. Conjugation took place in sortase reaction buffer (50 mM Tris, 150 mM NaCl, 5 mM $CaCl_2$, pH 7.5). The success of ligation was examined by reducing SDS-PAGE (**Figure 67**) of the reaction mixture after 30 min incubation at 22 °C.

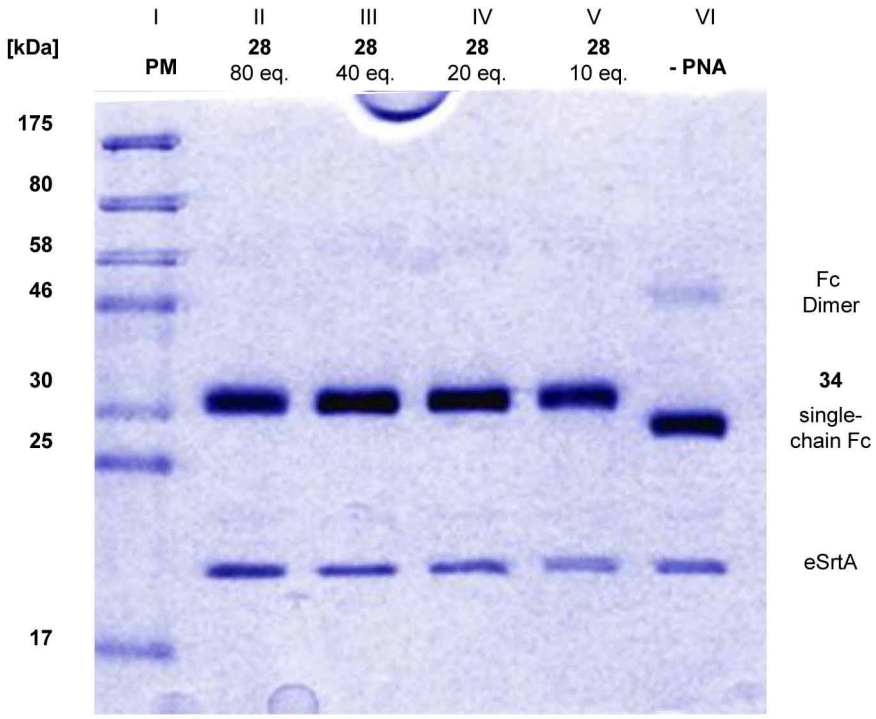

Figure 67. Reducing SDS-PAGE gel to monitor eSrtA-catalyzed ligation between **Fc** and **28** towards 3**4**. Expected molecular masses of reduced **Fc** and 3**4** are 29 kDa and 33 kDa, respectively. PM: protein molecular mass marker.

28 was used at different concentrations (10 – 80 eq. to the Fc fragment). The protein bands between 17 kDa and 25 kDa corresponded to eSrtA with a molecular mass of about 18 kDa. A distinct shift of the band corresponding to the Fc fragment (~ 29 kDa) towards increased molecular mass was observed in all reaction mixtures comprising the PNA ligand, compared to the control reaction lacking **28**. This small shift was in good agreement with our expectations, as the molecular mass of the desired Fc-PNA conjugate **34** was calculated as 33043 g/mol. Interestingly, a frequently reported side reaction of sortase A-mediated ligation, the recognition of ε-amino groups of Lys as substrate for sortase leading to an unproductive polypeptide cross-linking,[178] was not observed for the discussed setup. In contrast, a faint band was recognizable in lane VI in the range of 50 – 60 kDa, which matches the dimeric Fc fragment despite the application of a reducing PAGE. However, the full conversion of the Fc fragment to the PNA conjugate within a short reaction time was demonstrated verifying the applicability of the method to the decoration of proteins with PNA ligands.

Further, the resulted construct **34** was used in cargo delivery and cell internalization studies (by Stephan Dickgießer). The outline and aims of this study using a cMet receptor-addressing DNA aptamer was already explained in **Scheme 17** (chapter 2.3.1) and chapter 3.3.1. Thereby, the attachment of a toxic payload to the protein scaffold was abandoned due to low solubility of resulting conjugates. Instead, the Fc fragment was *N*-terminally labeled with a fluorescent TAMRA derivative *via* formylglycine-generating enzyme (FGE)-mediated oxime ligation (Fc'). However, Dickgießer succeeded in the functionalization of the respective Fc scaffold with the DNA aptamer by self-assembly of complementary PNA/DNA pair: between the Fc-conjugated PNA sequence and the extended sequence on 3' end of the aptamer. The hybridization of the aptamer to **34'** was monitored by SEC and the stability of the DNA-PNA complex was evaluated by SEC upon incubation of the Fc-PNA/DNA complex **35** for several

days. Both experiments confirmed the high stability and hybridization efficacy of the resulted aptamer/PNA-Fc construct. Furthermore, a melting curve analysis of the respective DNA/PNA duplex was performed. Thereby, a melting temperature (T_m) of 51.2±0.2 °C was determined which is slightly higher as the value reported for the PNA A/PNA B duplex (T_m = 46 °C) demonstrating the high stability of the resulted hybridized complex. More detailed information and resulted data are given in respective publication.[171]

The applicability of the complex molecule **35** as drug delivery scaffold and for cell internalization was evaluated in a set of receptor-binding assays and experiments employing cMet-overexpressing cancer cells, i. a. biolayer interferometry (BLI) experiments of the Fc'-**28** conjugate **35b** with recombinantly expressed cMet receptors, affinity titration and several flow cytometry studies of binding of **35b** to cMet-positive cells and cMet-negative cells.

An equilibrium dissociation constant K_D of 12.9 nM was determined for **35b** with cMet receptor by BLI experiments, whereas the aptamer solely exhibited a value in the same range (K_D = 7.8 nM). The dissociation constant of **35b** (cMet-positive cells) were determined to 24.5 nM from the titration experiments. Binding specificity and selective internalization of the construct by target cells was evaluated by flow cytometry and, conclusively, by fluorescence microscopy.

On the whole, the investigation towards synthesis and characterization (including evaluation of bioactivity) of an Fc-based delivery scaffold with a high flexibility for target receptors was accomplished within this follow-up study mainly elaborated by Stephan Dickgießer. As this part of the project was not essential for the present work, more detailed information is not given; it can be found in the respective publication.[171]

Moreover, the eSrtA-mediated conjugation of PNA guiding unit **27** to Fc was also demonstrated. Corresponding SDS-PAGE of the ligation is given in **Figure 70**, lanes V, VIII, XV, and XVIII.

The ligation was characterized by a similar band pattern as shown for the conjugation of **28** (see **Figure 68**), but the reaction efficacy seemed to be slightly worse than the former experiment as full conversion of the labeled Fc was not achieved. Moreover, the Fc fragment seemed to undergo the side reaction discussed above, which was considerable from the formation of a third band corresponding to a covalently linked dimeric Fc.

Conclusively, the eSrtA-mediated ligation comprising **29** bearing a pentaglycine-elongated PNA sequence, the toxin-loaded PNA **30** and the LPETG-modified Fc fragment was performed. The same experimental setup was employed as described for the ligation of **28**. The stained gels after SDS-PAGE of the test reactions are depicted in **Figure 70**, lanes VII, X, XVII, and XX.

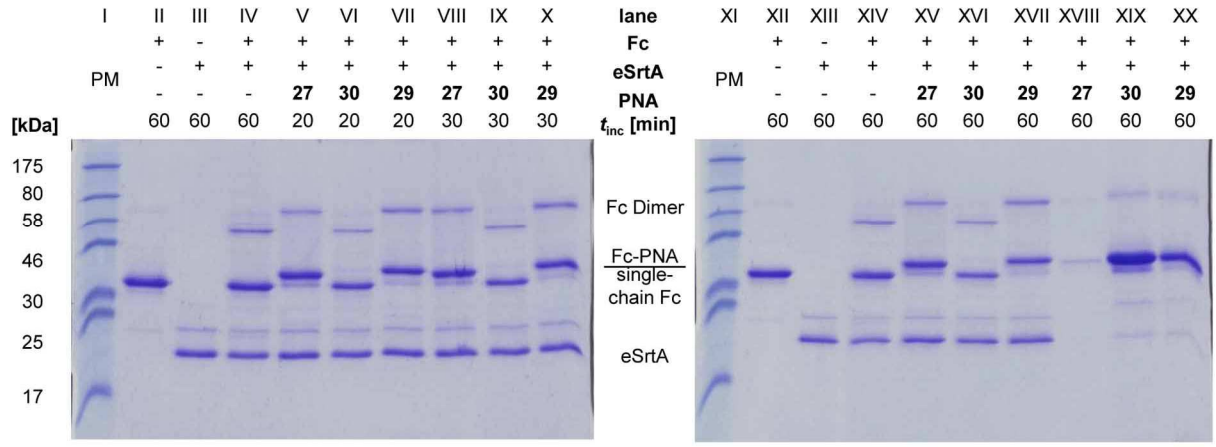

Figure 68. Reducing SDS-PAGE gel of monitored conjugation of **27**, **29**, and **30** to Fc *via* eSrtA-mediated ligation and control experiments with various incubation times**.** PM: protein molecular mass marker. PNA: PNA guiding unit **27**, **29**, and **30**. t_{inc}: incubation time. Lane VIII – X: Supernatant of reaction mixture after centrifugation of precipitate. Lane XVIII – XX: Pellet after centrifugation, resolved in SDS-PAGE loading buffer (250 mM Tris/HCl pH 8.0, 7.5 % SDS, 25 % glycerol, 0.25 mg/mL bromophenol blue, 12.5 % 2-mercaptoethanol) and heated at 90 °C. Gels were stained with coomassie-brilliant blue. PAGE experiments performed and evaluated by Stephan Dickgießer.

The conjugation of **29** was characterized by a similar separation pattern in SDS-PAGE as seen for the analogous reaction of **27.** No full conversion of the Fc scaffold was observed and the side reaction towards Fc dimerization occurred. Furthermore, small precipitation of the conjugation product was found.

eSrtA-mediated ligation of **30** using the strategy shown in **Scheme 17B** (chapter 2.3.1) and **Scheme 27** (chapter 3.3.1) with the Fc scaffold failed due to low solubility of the resulting conjugate. The shift between the protein band in the supernatant and in the centrifuged and redissolved pellet (**Figure 70**, lane IX and XIX) showed that the ligation was successful. But due to the poor solubility of the conjugation product in water, further investigation of this construct was not possible. As the observed precipitation was assumed to be caused by a hydrophobic toxin ispinesib loaded on the guiding unit, an alternative toxin should be considered.

It was demonstrated that the eSrtA-mediated ligation is an appropriate technique to load tagged PNA guiding units onto protein scaffolds. All ligation experiments, with the exception of the preliminary study using PNA guiding unit **28,** were performed by Stephan Dickgießer.

3.3.3 Digest of Chapter 3.3

A number of peptidic and peptidomimetic guiding unit molecules and corresponding building blocks comprising conjugation sites for bioorthogonal ligation (compounds **15** - **31**) were synthesized on solid support and by conventional solution-phase chemistry. Their general applicability for affinity-guided ligation was studied. All compounds were obtained in appropriate yield and purity depending on the strategy.

The efficacy of the bioorthogonal conjugations was evaluated by the conversion of the reactants and by determination of the kinetic constants of test reactions. SPANC was chosen as a ligation technique, and a series of test reactions with varied parameters were conducted.

Generally, the reactions comprising the coiled-coil guiding units demonstrated a slightly better conversion (50-90 %) compared to those comprising PNA guiding units (40-80 %). Interestingly, the reported K_D values for coiled-coil interactions are significantly higher than the values for PNA-PNA interactions.[122, 135] An explanation for this outcome was not found. However, it was found that the major conversion-limiting factor was the undesired addition of the hydroxylamine to the BCN moiety. Thus, the affinity between the guiding units was assumed to be not of prime importance for the discussed approach. Nevertheless, the affinity-guided ligation needs further investigation (e.g. application of more reactive strained alkynes as BARAC or cyclic nitrones) to suppress the discussed side reaction and reach full conversion of the reactants.

Nonetheless, the advantage of the affinity-guided approach over the non-guided ones was demonstrated by comparison of the second-order kinetic constants. Thus, all k_2 values determined for the affinity-guided SPANC with appropriate reaction conditions (0.8 - 3 $M^{-1}s^{-1}$ for PNA-guided reactions, 2 – 7 $M^{-1}s^{-1}$ for coiled coil-guided reactions) were significantly higher than those determined for the non-guided approach (0.39 $M^{-1}s^{-1}$) or the reported reactions under similar conditions (k_2 < 0.1 $M^{-1}s^{-1}$). **Table 32** shows a summary of reported or experimentally determined k_2 values of bioorthogonal conjugations used in the present work.

Table 31. Summary of experimentally determined reactant conversions and k_2 of all bioorthogonal ligations used in the present work with few reported k_2 values of similar reactions as reference.

Reaction	Templated	Trigger	Conversion [%]	k_2 (determ.) [$M^{-1}s^{-1}$]	k_2 (ref.)[a] [$M^{-1}s^{-1}$]
SPANC	+ (coils)	hydroxylamine	50 – 90	2 – 7	-
SPANC	+ (PNAs)	hydroxylamine	40 – 80	0.8 –3	-
SPANC	-	hydroxylamine	60	0.39	0.05[173b]
SPAAC	+ (PNAs)	none	54	0.54	-
SPAAC	-	none	90	0.55	0.2 – 0.3[170]
MS-coupling[b]	-	none	72	0.21	0.15[169]
Psoralen CL[c]	+ (PNAs)	UVA	99[d]	-	-

a: Reported k_2 values of reactions with similar reactants or conditions.
b: Maleimide-sulfhydryl conjugation.
c: UVA-mediated cross-linkage of PNA-bound psoralen to complementary DNA.
d: Formation of desired product not confirmed.

The experimentally determined data shown in this table should be considered as approximated values due to the analytical inaccuracy and insufficient number of data points used for the calculations. However, it is obvious that the affinity-guided approach provided a significant improvement of reaction rate, especially when the reaction start was triggered, ensuring pre-orientation of the guiding units.

Furthermore, the selectivity of the affinity-guided approach was demonstrated with the coiled coil-guided SPANC, whereby no cycloaddition of a non-guided nitrone component to the BCN compounds was observed in a competitive assay. The selectivity of the PNA-guided approach was also investigated and yielded the same outcome. However, for the application in simultaneous protein multiple labeling, this model system needs further investigation in view of sequence selectivity.

According to the expectations, the UVA-mediated psoralen cross-linkage of PNAs employing solitaire psoralen resulted in its uncontrollable addition and non-selective intra- and intermolecular cross-linking. Cross-conjugation experiments using PNA-bound psoralen were attempted but the formation of the desired product was not confirmed due to the lack of appropriate analytical methods.

Conclusively, the eSrtA-mediated ligation of PNA guiding units with a protein scaffold was studied. Conjugation of PNA-peptide hybrids **27** and **28** to an antibody Fc fragment was efficient and fast. The binding properties and bioactivity of the resulted construct **34** and its derivative **35** loaded with a cMet receptor-binding aptamer were evaluated in a follow-up study by Stephan Dickgießer.

The synthesis of a toxin-loaded ADC using the ispinesib-preloaded PNA construct **30** by eSrtA-mediated ligation failed due to poor solubility.

4 Conclusion and Outlook

4.1 Protease Inhibitor with Triazolyl Backbone Mimic

Application of a triazole structural motif to engineering of peptide-based protease inhibitors was studied. Using sunflower trypsin inhibitor (SFTI-1) as a scaffold, an inhibitor of human neutrophil elastase comprising a *trans*-amide surrogate at the P1-P1' position was rationally designed. For the first time a 1,4-disubstituted triazole was used as a non-cleavable replacement for the scissile bond in a BBI-derived protease inhibitor. It was demonstrated that the triazole-bearing peptide possessed enhanced proteolytic stability *in vitro*. Indeed, upon incubation of synthetic inhibitor **4** with its target enzyme no cleavage at the P1-P1' position was observed within 24 h, while 17 % of the parent peptide **3** was degraded under this conditions. Interestingly, introduction of a triazolyl moiety enhanced the general resistance of **4** against proteolysis. However, with the K_i of 563.63 nM, its inhibitory potency was decreased compared to **3** (K_i of 144.48 nM). Nevertheless, **4** appeared significantly more potent than similar SFTI derivatives comprising prolyl-based backbone mimics at the respective position.[154] Therefore, triazole surrogates can become a valuable tool for the engineering of intrinsically potent but proteolysis-prone inhibitors.

Comparing different SFTI-derived peptides and peptide mimetics, we found that enhancement of proteolytic stability was more pronounced for the linear precursors, presumably due to the fact that the cyclic backbone supports substrate re-condensation at the active site of an enzyme (Scheme 14). Therefore, we assume that mimicking a scissile bond by triazolyl motif can appear beneficial for peptidic inhibitors comprising linear backbone and possessing poor intrinsic stability against proteolysis, or can be used to convert highly affine substrates to potential inhibitors. However, this issue requires further investigation.

4.2 PHIP-Active Functional Peptides

For the first time para-hydrogen induced polarization (PHIP), a promising method to enhance NMR signals while analyzing biological macromolecules, was studied in a series of specifically labeled protease inhibitors in the working group of Prof. Gerd Buntkowsky. The results of this systematic study have been recently reported.[50b]

A triple bond as a target for catalytic hydrogenation with para-enriched hydrogen was installed at the desired position within the backbone of an SFTI-based trypsin inhibitor yielding constructs **5** – **12**. Propargylglycine (Pra), pentynoic acid and *O*-propargyltyrosine (Tyr(*O*-propargyl)) were examined as labels in PHIP experiments. The aminoterminus was designated as the optimal labeling site.

We hypothesized that electron-donating groups in spatial proximity to the unsaturated bond affect hydrogenation efficacy, hence, PHIP effect. Indeed, none of the peptides **5**, **6**, **9**, and **11** labeled with Pra and comprising a single carbon atom between the triple bond and the peptide backbone, exhibited significant signal enhancement. Similarly, high intrinsic PHIP

activity of 4-pentynoic acid was also attenuated by this effect when installed within peptide **8**. However, strong signal enhancement of about 70 was detected upon PHIP experiments in aqueous media using Tyr(*O*-propargyl)-labeled constructs **7**, **10**, and **12** possessing the spatially isolated label. In general, the remoteness of hydrogenation target from a peptide backbone was found to be the crucial requirement for efficient PHIP.

Poisoning of a hydrogenation catalyst was another factor found to influence the PHIP activity. However, the substitution of catalyst-poisoning groups (disulfide, terminal amine) did not result in significant signal enhancement. Therefore, we assumed that the poisoning of a catalyst is caused by a complex of factors rather than by a distinct functional group.

Generally, the investigated PHIP labels possessed short relaxation time T_1 despite their SE was sufficiently high. Therefore, further studies aimed on extension of T_1 are required. To this end, polarization transfer to neighboring ^{13}C or NMR-active heteroatoms[179] as well as transfer of the hyperpolarized nuclear spin order to long-lived nuclear singlet state[180] should be considered.

Additionally, we showed that PHIP-labeled compounds preserved their bioactivity. Indeed, constructs **5** – **13** inhibited trypsin in the range of tight-binding inhibitors. This issue is of profound importance for further investigations regarding PHIP studies of enzyme-inhibitor systems. Indeed, as trypsin-like proteases retain their activity in water-methanol mixtures[181] used in our NMR experiments, PHIP-based investigations can be extended to enzyme-ligand interactions and to the proteases of therapeutic relevance.

4.3 Affinity-Guided Chemical Ligation towards Multifunctionalization of Biomolecular Scaffolds

Application of affinity-guided ligation strategy to the synthesis of biomolecular conjugates was studied on oligopeptides and on a multifunctional protein scaffold derived from the Fc fragment of an antibody. As guiding counterparts, coiled coil systems and complementary PNA strands were used.

For SPANC-based ligations, reactive BCN with *in situ* generated nitrone were installed at the aminotermini of, respectively, 3 and 5 heptad coiled coils and complementary PNA oligomers. In our hands, affinity-guided SPANC on these constructs provided advantages over non-guided/non-triggered reactions of oligopeptides/PNAs in view of reaction kinetics and selectivity. Interestingly, compared to the PNA guiding pair, coiled coil-guided SPANC was characterized by better conversion and faster reaction rate, suggesting that strength of interaction between guiding units plays a minor role.

An unexpected side-reaction was observed during SPANC in the case of equimolar ratio of reaction counterparts; this transformation which disabled the full consumption of starting reagents has not been reported in the literature so far. Further investigations should be focused on the suppression of this reaction as application of SPANC for simultaneous multi-

labeling of proteins is not possible until full conversion of reactants is ensured. An alternative purification method should be considered as well. Additionally, further investigations aimed on enhanced selectivity of PNA guiding units are required.

Applicability of sortase-mediated ligation for the attachment of PNA-comprising ligands to an Fc scaffold was studied. The resulted Fc-PNA conjugate was used as a modular platform for the generation of multifunctionalized cellular delivery module comprising non-peptidic binders of therapeutically relevant targets, a fluorescent label, and vehicles for cellular delivery (Stephan Dickgießer). Further studies should be aimed on improvement of stability of the conjugate upon covalent linkage between Fc-PNA and aptamer ligand. Affinity-guided approach should be applied to this system and a toxic payload should be covalently attached resulting in an antibody-drug conjugate.

4.4 Closing Remarks

The present thesis summarizes three research projects addressing fundamental studies aimed on application of non-natural elements to design and synthesis of bioactive peptide mimetics, bioconjugates, and hybrid macromolecules. The study comprised computational and knowledge-based design, total synthesis, and evaluation of biologic activity as well as application to NMR-based structural analysis.
Results summarized in the present work were reported in two scientific publications[50b, 171] and should be considered as milestones for further investigations aimed on application of the discussed concepts to biomedical studies.

5 Experimental Part

5.1 General

5.1.1 Reagents and Solvents

All reagents were from highest or semi-highest grade and used without further purification. Commonly available chemicals and solvents were purchased from *Iris Biotech* (Marktredwitz, Germany), *Acros Organics* (Geel, Belgium), *Novabiochem* (Bad Solden, Germany), *Merck* (Darmstadt, Germany), *Sigma-Aldrich* (St. Louis, USA), *Rapp Polymere* (Tübingen, Germany), *Karl Roth* (Karlsruhe, Germany), *Carbolution Chemicals* (Saarbrücken, Germany), *Fischer Scientific* (Schwerte, Germany), or *Bachem* (Bubendor, Swiss). Azide- and alkyne-bearing building blocks Fmoc-L-propargylglycine (Fmoc-L-Pra-OH) and Fmoc-L-azidohomoalanine (Fmoc-L-Aha-OH) were obtained from *Iris Biotech*. Fmoc-PNA monomers were purchased from *PNA Bio* (Thousand Oaks, USA). BCN-bearing building blocks BCN-NHS and BCN-$(POE)_3$-NH-C(O)-$(CH_2)_3$-maleimide precursor mixture were acquired from *Synaffix* (Molenstraat, Netherlands). The building blocks Fmoc-L-propargyltyrosine (Fmoc-L-Tyr(O-propargyl)-OH) and Fmoc-L-Tyr(All)-OH were purchased from *PolyPetide Laboratory* (Wolfenbüttel, Germany), 4-Pentynoic acid, the Bestmann-Ohira reagent and chloro(pentamethylcyclopentadienyl)(cyclooctadiene)-ruthenium(II) (Cp*RuCl(COD)) from *Sigma-Aldrich*. Xanthotoxol were purchased by *Carbosynth* (Compton, UK). Human neutrophil elastase was purchased from *Serva Electrophoresis* (Heidelberg, Germany). Ispinesib was purchased from *ShangHai Biochempartner* (Shang-Hai, China). Boc-Leu-*N*(OMe)Me was purchased from *Chem-Implex International Inc*. (Illinois, USA). The catalyst Rh(dppb)(COD)BF_4 was purchased from *Strem Chemicals Inc.* (Boston, USA).
For special purposes dry and degassed solvents were prepared. DMF was heated along with molecular sieve 3 Å under reduced pressure and finally flushed with dry argon. DCM was pre-dried over calcium hydride, then distilled over calcium hydride and finally flushed with dry argon. Diethyl ether was pre-dried over molecular sieve 3 Å, then distilled from sodium benzophenone ketyl and flushed with dry argon.

5.1.2 Analytical and Preparative Instruments

Chromatographic analysis of purchased or synthesized compounds using HPLC was conducted with a *Varian* 920-LC® system equipped with a *Phenomenex* Hypersil® 5u BDS C18 LC column (150×4.6 mm, 5 μm, 130 Å) or *Agilent* 1260 Infinity® HPLC system equipped with the same column. Semi-preparative RP-HPLC was performed on a *Varian* modular system comprising a PrepStar® 218 Solvent Delivery Module, a ProStar® 410 HPLC autosampler and a ProStar® 325 Dual Wavelength UV-Vis HPLC Detector using a *YMC* J'sphere® ODS-H80 C-18 LC column (250×20 mm, 4 μm, 8 nm)). The eluent system for all HPLC systems comprised eluent A (0.1 % aq. TFA) and eluent B (90 % aq. MeCN containing 0.1 % TFA). For both of the eluents, deionized and degassed water with *Milli-Q*®-grade water was used. The

recorded data was processed and analyzed using the *Varian* Galaxy© software or *Agilent* HPLC Chemstation© software.
ESI mass spectra were recorded with a *Shimadzu* LCMS-2020 equipped with a *Phenomenex* Jupiter® 5u C4 LC column (50×1 mm, 5 μm, 300 Å) or *Phenomenex* Hypersil® 5u BDS C18 LC column (150×4.6 mm, 5 μm, 130 Å) and a *Bruker-Franzen* Esquire® LC mass spectrometer. The eluent system consisted of eluent A (0.1 % aq. formic acid, LC-MS grade) and eluent B (100 % MeCN containing 0.1 % formic acid, LC-MS grade). The recorded data was processed and analyzed using the *Shimadzu* Labsolution© software.
MALDI mass spectra were recorded with *Shimadzu* AXIMA$_{TM}$ TOF2 by Dr. Alesia Tietze (Prof. Thiele group) at the Frauenhofer LBF (Darmstadt).
IR spectra were measured on *PerkinElmer* FT IR spectrometer 1000PC. Freeze-dried samples were homogeneously mixed and pressed to potassium bromide pellets.
Loading determination of SPPS resins was performed *via* UV/VIS absorption spectrometry using an UV/VIS spectrometer *Shimadzu* UV-1650PC.
Enzyme kinetics assays were measured with a *Tecan* GENios® microplate reader using the Xfluor 4TM system for recording the measured absorption kinetics.
Standard NMR studies were conducted on a *Bruker* Advance® II 300 instrument (300 MHz). All samples were dissolved in chloroform-d_1, methanol-d_4, DMSO-d_6, or D_2O and measured using a symmetrical NMR microtube. Resulting spectra were processed and analyzed using the *Mestrelab Research* MestReNova© software.
Libration of dry substances was realized by evaporation of volatile organic solvents using a rotary evaporator *Buchi* Rotavapor® R-ZZZ. H_2O/MeCN mixtures and residues of other organic solvents were removed by freeze-drying with a *Martin Christ Gefriertrockungsanalgen* Alpha-2-4-LSC® at -85 °C combined with an *Ilmvac GmbH* high vacuum pump type 109012.

5.1.3 Storage

All Fmoc-protected amino acids, PNA monomers, resins, purified and dry peptides and peptidomimetics, heat-sensitive building blocks, coupling reagents, enzymes, and catalysts were stored at -20 °C. BCN-bearing building blocks, purified PNA-containing peptides and stock solution of inhibitors and enzymes were kept at -80 °C. During solid-phase synthesis, the loaded resins were dried by multiple rinsing with DCM and diethyl ether and preserved in a desiccator under reduced pressure at ambient temperature. For short-time storage the peptide-loaded resin were stored in DMF or NMP at 4 °C.

5.2 Synthesis

5.2.1 General Procedure of Solid-Phase Peptide Synthesis

All peptides and peptidomimetics were synthesized by manual or partially-automated Fmoc-SPPS. For microwave-assisted synthesis, a *CEM* Discover® SPS microwave peptide synthesizer platform was used.

5.2.1.1 Loading of First Fmoc-Amino Acid on Solid Support

Loading onto AmphiSpheres® 40 RAM resin

The resin was pre-swollen in DCM (60 min) and DMF (30 min) and thoroughly washed with DMF. To remove the Fmoc protecting group on the linker, the resin was treated with 2×2 – 5 ml 20 % piperidine in DMF for 5 min at ambient temperature. (30 W over 3 min at 50 °C when using microwave irradiation). After thorough washing with 3×DMF and 2×DCM, the pre-activated amino acid (4 eq. Fmoc-amino acid, 3.9 eq. 2-(1H-benzotriazol-1-yl)-1,1,3,3-tetramethyluronoium hexafluorophosphate (HBTU), 8 eq. *N*,*N*-diisopropylethylamine (DIEA)) was added and the reaction mixture was shaken for 30 min at ambient temperature (30 W over 15 min at 50 °C when using microwave irradiation).

Loading onto 2-Cl-Trt resin

The resin was pre-swollen in DCM for 60 min. 1 eq. of the first Fmoc-Amino acid and 4 eq. of DIEA were dissolved in 2 – 5 ml DCM and added to the resin. The coupling mixture was shaken for 2.5 h continuously at ambient temperature. After removal of the coupling solution *via* filtration, the loaded resin was treated with 3×6 mL DCM/MeOH/DIEA (17:2:1, v:v:v) for 3 min and finally washed with 3×5 mL DCM and 2×5 mL DMF.

Preloaded Rapp Polymere TentaGel® resins

TentaGel® resins were already preloaded with the corresponding Fmoc- and side chain protected amino acids. The preloaded resins were swollen in DCM (60 min) and DMF (30 min).

5.2.1.2 Manual Chain Elongation

Canonical amino acids were attached by double coupling employing 4 eq. of the corresponding Fmoc-protected amino acid, 3.9 eq. of HBTU and 8 eq. of DIEA or, in case of cysteine, 6 eq. of 2,4,6-trimethylpyridine (collidine). For coupling of Fmoc-Arg, Fmoc-Cys, and Fmoc-His, triple coupling was applied. Attachment of non-canonical amino acids and amino acids with non-common side chain protecting groups were performed as triple coupling employing 3 eq. of Fmoc-Pra, 2.9 eq. of 2-(1H-7-azabenzotriazol-1-yl)-1,1,3,3-tetramethyl uronium hexafluorophosphate (HATU) and 6 eq. of DIEA for the first coupling and 2 eq. Fmoc-Pra, 1.9 eq. HATU and 4 eq. DIEA for the further two coupling steps. For Cys, Arg and non-canonical amino acids, a microwave irradiation of 30 W was used over 30 min at 50 °C, and for other canonical amino acids - 30 W over 15 min at 50 °C. Fmoc deprotection was accomplished in two steps using 20 % piperidine in DMF: initial deprotection at 50 °C, 30 W over 0.5 min followed by a second deprotection at 50 °C, 30 W over 5 min. In case of non-microwave-assisted synthesis, each reaction time, for coupling and deprotection, were elongated by twice and the reaction vessel was shaken at ambient temperature.

After each double/triple coupling/deprotection step, the peptide-resin were washed with DMF 3×5 ml and 2×5 ml DCM. Among each single coupling and deprotection steps, the peptide-resin was washed with 3×5 ml DMF.

5.2.1.3 Automated Chain Elongation

Automated chain elongation was performed in a *CEM* Liberty® 12-channel peptide synthesizer or Liberty Blue® peptide synthesizer on a Discover SPS microwave peptide synthesizer platform. The pre-swollen (peptide-) resin was set into a 30 ml PTFE reaction chamber.

Upon using the Liberty® system, all canonical amino acids were attached by double or triple coupling employing 4 eq. of the corresponding Fmoc-amino acid, 4. eq. HBTU and 8 eq. of DIEA, or in case of Cys 4 eq. of collidine. Arg and Cys were coupled using a two-step microwave program: 1.) RT, 0 W, 25 min; 2.) 75 °C, 25 W, 0.5 min (Arg) and 1. RT, 0 W, 2 min; 2.) 50 °C, 25 W, 4 min (Cys), respectively. All other canonical amino acids were coupled using a standard microwave program: 75 °C, 21 W, 5 min. Fmoc deprotection was realized in two steps by treating with 20 % piperidine in DMF at 75 °C, 42 W for 0.5 min (initial deprotection) followed by a second deprotection step with 20% piperidine in DMF at 75 °C, 42 W for 3 min.

Upon usage of the Liberty Blue® system, all canonical amino acids despite Arg and Cys were attached using a single coupling method. Each coupling was performed with 5 eq. corresponding Fmoc-amino acid, 5 eq. DIC, and 5 eq. cyano(hydroxyimino)acetic acid ethyl ester (Oxyma). Each single coupling cycle comprises a two-step microwave method: 1.) 75°C, 170 W, 15 s; 2.) 90 °C, 30 W, 110 s. For Arg and Cys a double coupling method was applied. The two-step coupling method for Arg and Cys comprises: 1.) 25 °C, 0 W, 25 min; 2.) 75 °C, 30 W, 2 min (Arg) and 1.) 25°C, 0 W, 2 min; 2.) 50°C, 35 W, 4 min, respectively. Fmoc deprotection was performed with 20 % piperidine v/v 0.1 M Oxyma in DMF using a two-step microwave method at 75 °C, 155 W for 15 s, followed by 90 °C, 30 W for 50 s.

5.2.1.4 Cleavage and Isolation

Cleavage of peptides from the solid support and removal of side chain protecting groups were achieved *via* acidolysis of the dry peptide-resin using a cleavage cocktail consisting of TFA/H_2O/anisole/triethylsilane (TES) (47:1:1:1, v:v:v:v). In case of Cys-containing peptides an amount of 1,4-dithiothreitol (DTT) was added. The cleavage mixture was shaken for 3 h at ambient temperature followed by precipitation and subsequent washing (3×) using diethyl ether or methyl *tert*-butyl ether (MTBE) to yield crude unprotected peptides.

5.2.2 General Procedure of Solid-Phase Synthesis of PNA-Peptide Hybrids

All PNA-peptide hybrids were synthesized completely manually. Microwave-assisted coupling and deprotection was only performed before coupling of the first Fmoc-PNA to the peptide-resin.

5.2.2.1 Loading of First Fmoc-Amino Acid on Solid Support

Loading onto AmphiSpheres® 40 RAM resin

Loading of the first amino acid onto RAM resin was performed as described in chapter 5.2.1.1.

5.2.2.2 PNA Chain Elongation Protocol I

One coupling cycle for the chain elongation of PNAs comprised a double coupling, a double capping, and a double deprotection step separated by several washing steps. For coupling 5 eq. of the corresponding Fmoc-PNA monomer, 4.9 eq. HATU, 5 eq. 1-hydroxybenzotriazole (HOBt), 10 eq. DIEA, and 10 eq. 2,6-lutidine were dissolved in NMP. The final concentration of the Fmoc-PNA monomer in the coupling mixture was set to 0.25 M. After pre-activation of the coupling mixture for 10 min, the solution was given to an *N*-terminally deprotected peptide-resin. The reaction mixture was continuously shaken for 60 min at ambient temperature. After removal of the coupling mixture by filtration, the resin was thoroughly washed with 5×2 ml NMP, 5×2 ml DCM, and 5×2 ml NMP and the coupling step was repeated. After second coupling the peptide-loaded resin was washed thoroughly with 5×2 ml 5 % DIEA in NMP, 5×2 ml DCM, and 5×2 ml NMP. Quenching of the non-reacted free *N*-termini was carried out by treating of the peptide-resin with a capping mixture consisting of Ac_2O, 2,6-lutidine, NMP (1:2:7, v:v:v) for 5 min at ambient temperature. After second capping step, the peptide-resin was washed with 5×2 ml 5 % DIEA in NMP, 5×2 ml DCM, and 5×2 ml NMP. For *N*-terminal Fmoc deprotection, the peptide-resin was shaken in 2 ml of 20 % piperidine in NMP for 4 min at ambient temperature. After second deprotection step, the peptide-resin was thoroughly washed with 5×2 ml NMP, 5×2 ml DCM, and 5×2 ml NMP. Coupling cycles of canonical amino acids after the PNA sequence were performed as described in 5.2.1.2, but in all steps, NMP was used as solvent instead of DMF.

5.2.2.3 PNA Chain Elongation Protocol II

One coupling cycle for the chain elongation of PNAs comprised a double coupling, a double capping, and a double deprotection step. 2 eq. of the corresponding Fmoc-PNA monomer, 1.9 eq. HATU, and 4 eq. DIEA were dissolved in 0.5 ml NMP. The coupling solution was pre-activated for 10 min and the solution was given to the *N*-terminally deprotected peptide-resin. The reaction mixture was continuously shaken for 60 min at ambient temperature. After removal of the coupling mixture by filtration, the resin was thoroughly washed with 3×2 ml

DMF, 2×2 ml DCM, 1×2 ml DMF, and 2×2 ml NMP and the coupling step was repeated. After second coupling, the peptide-loaded resin was washed thoroughly with 5×2 ml 5 % DIEA in DMF, 5×2 ml DCM, 3×2 ml DMF, and 2×2 ml NMP. Capping was performed by shaking of the peptide-resin in a capping mixture (same composition as in 5.2.2.2) for 5 min at ambient temperature. After second capping step, the peptide-resin was washed with 5×2 ml 5 % DIEA in DMF, 5×2 ml DCM, 3×2 ml DMF, and 2×2 ml NMP. Fmoc deprotection was achieved by shaking of the peptide-resin in 2 ml of 20 % piperidine in NMP for 4 min at ambient temperature. Subsequently, the peptide-resin was thoroughly washed with 5×2 ml DMF, 5×2 ml DCM, 3×2 ml DMF, and 2×2 ml NMP.
Coupling cycles of canonical amino acids after the PNA sequence were performed as described in 5.2.1.2, but in all reaction steps, NMP was used as solvent instead of DMF. Additionally, a capping step was introduced between the coupling and deprotection steps using a capping mixture consisting of Ac_2O, DIEA, NMP (1:1:18, v:v:v) for 5 min.

5.2.2.4 Cleavage and Isolation

Cleavage and isolation of the PNA-peptide hybrids was achieved as same as described in chapter 5.2.1.4.

5.2.3 Synthesis of Protease Inhibitors

5.2.3.1 [Phe^5]SFTI-1[1,14] (1)

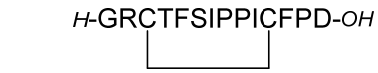

Chemical Formula: $C_{70}H_{103}N_{17}O_{19}S_2$
Exact Mass: 1549.71
Molecular Weight: 1550.81

1 was synthesized partially automated on the Liberty® 12-channel peptide synthesizer system. As a solid support, 500 mg of Fmoc-Asp(tBu)-preloaded TentaGel® S AC resin with 0.22 mmol/g loading capacity was chosen (batch size: 0.1 mmol). Iterative chain elongation was achieved following the mentioned general protocol described in 5.2.1.3.
Cleavage of the linear peptide precursor **1'** from solid support and removal of the side chain protecting groups was achieved by acidolysis using 5 ml of the standard cleavage cocktail as described in 5.2.1.4. After precipitation and washing with diethyl ether, 133.3 mg of dried crude unprotected precursor peptide **1'** (0.086 mmol, 85.9 %) was yielded. RP-HPLC: R_t = 21.7 min, 18 % MeCN over 2 min followed by 18 %→40.5 % MeCN over 20 min in 0.1 % aq. TFA at flow rate 1 ml/min. ESI-MS: m/z: $[M+H]^+$ obsd. = 1552.9 (calc = 1553.1), $[M+2H]^{2+}$ obsd. = 777.3 (calc = 777.0), $[M-H]^-$ obsd. = 1550.8 (calc = 1551.1).
20 mg (0.013 mmol) precursor **1'** was dissolved in 10 ml folding buffer (0.1 M $(NH_4)_2CO_3$ aq. with 0.5 % DMSO) and the reaction mixture was stirred for three days while monitoring with RP-HPLC and ESI-MS of the collected fractions. The solvent was removed by lyophilization

followed by purification *via* semi-preparative RP-HPLC to yield 7.9 mg of oxidatively folded peptide **1** (0.005 mmol, 39.5 % purification yield, 33.9 % overall yield). RP-HPLC: R_t = 24.5 min, 18 % MeCN over 2 min followed by 18 %→40.5 % MeCN over 20 min in 0.1 % aq. TFA at flow rate 1 ml/min. ESI-MS: m/z: $[M+H]^+$ obsd. = 1550.9 (calc = 1551.1), $[M+2H]^{2+}$ obsd. = 776.3 (calc = 776.0), $[M-H]^-$ obsd. = 1548.8 (calc = 1549.1).

5.2.3.2 [Leu^5]SFTI-1[1,14] (2)

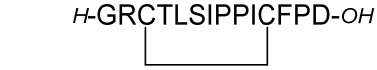

Chemical Formula: $C_{67}H_{105}N_{17}O_{19}S_2$
Exact Mass: 1515.72
Molecular Weight: 1516.80

2 was synthesized partially automated on the Liberty® 12-channel peptide synthesizer system. The choice of solid support, the iterative chain elongation, cleavage from solid support, and isolation of the linear precursor peptide was performed completely as same as described for **1** in 5.2.3.1. 119.2 mg of dried crude precursor peptide **2'** (0.079 mmol, 78.5 %) was yielded. RP-HPLC: R_t = 18.9 min, 18 % MeCN over 2 min followed by 18 %→40.5 % MeCN over 20 min in 0.1 % aq. TFA at flow rate 1 ml/min. ESI-MS: m/z: $[M+H]^+$ obsd. = 1519.0 (calc = 1519.8), $[M+2H]^{2+}$ obsd. = 760.4 (calc = 760.4), $[M-H]^-$ obsd. = 1517.5 (calc = 1517.8), $[M-2H]^{2-}$ obsd. = 758.8 (calc = 758.4).
20 mg (0.013 mmol) precursor **2'** was oxidatively folded and purified *via* semipreparative HPLC as described for **1**. 7.1 mg of oxidatively folded peptide **2** (0.005 mmol, 34.8 % purification yield, 27.3 % overall yield) was obtained. RP-HPLC: R_t = 20.4 min, 18 % MeCN over 2 min followed by 18 %→40.5 % MeCN over 20 min in 0.1 % aq. TFA at flow rate 1 ml/min. ESI-MS: m/z: $[M+H]^+$ obsd. = 1518.0 (calc = 1517.8), $[M+2H]^{2+}$ obsd. = 759.4 (calc = 759.4), $[M-H]^-$ obsd. = 1514.9 (calc = 1515.8).

5.2.3.3 des-Gly^1,-Pro^{13},-Asp^{14}[Nle^2,Leu^5,Gln^{10},Tyr^{12}]SFTI-1[1,14] (3)

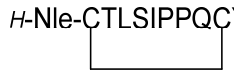

Chemical Formula: $C_{55}H_{86}N_{12}O_{16}S_2$
Exact Mass: 1234,57
Molecular Weight: 1235,47

3 was synthesized manually with microwave assistance. As a solid support, 500 mg of Fmoc-Tyr(tBu)-preloaded TentaGel® S AC resin with 0.22 mmol/g loading capacity was chosen (batch size: 0.1 mmol). Iterative chain elongation was achieved following the mentioned general protocol described in 5.2.1.2. Cleavage and isolation of the crude linear precursor peptide was as same as described for **1** (5.2.3.1). 103.5 mg of dried crude precursor peptide **3'** (0.083 mmol, 83.6 %) was yielded. RP-HPLC: R_t = 11.6 min, 9 % MeCN over 2 min followed by 9 %→90 % MeCN over 20 min in 0.1 % aq. TFA at flow rate 1 ml/min. ESI-MS: m/z: $[M+H]^+$ obsd. = 1237.8 (calc = 1238.5), $[M+2H]^{2+}$ obsd. = 619.6 (calc = 619.7), $[M-H]^-$ obsd. = 1235.5 (calc = 1236.5), $[M-2H]^{2-}$ obsd. = 617.6 (calc = 617.7).

10 mg (0.008 mmol) linear precursor peptide **3'** was eluted in 400 µl acetonitrile, followed by 3 ml redox-buffer (1 M guanidiumhydrochlorid, 50 mM Na_2HPO_4, pH 7 with 400 µl DMSO, and 400 µl trifluoroethanol (TFE)). The folding mixture was shaken at ambient temperature for 3 days while monitoring *via* RP-HPLC and ESI-MS. The reaction mixture was directly injected into the semipreparative RP-HPLC and after lyophilization of the collected product fractions, 0.8 mg of oxidatively folded peptide **3** (0.65 μmol, 8.2 % purification yield, 6.8 % overall yield) was obtained. RP-HPLC: R_t = 13.6 min, 9 % MeCN over 2 min followed by 9 %→90 % MeCN over 20 min in 0.1 % aq. TFA at flow rate 1 ml/min. ESI-MS: m/z: $[M+H]^+$ obsd. = 1235.8 (calc = 1236.5), $[M+2H]^{2+}$ obsd. = 618.8 (calc = 618.7), $[M-H]^-$ obsd. = 1233.5 (calc = 1234.5).

5.2.3.4 (2S)-2-Azido-3-*O*-*tert*-butyl-propanoic acid (4a)

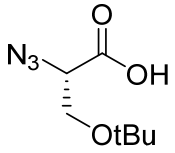

Chemical Formula: $C_7H_{13}N_3O_3$
Exact Mass: 187.10
Molecular Weight: 187.20

The synthesis of **4a** was performed according to a reported protocol.[149] A solution of sodium azide (5 g, 76.9 mmol) was dissolved in distilled H_2O (13 ml) with DCM (22 ml) and cooled on an ice bath. Triflyl anhydride (2.5 ml, 14.9 mmol) was added slowly over 5 min with a syringe and stirred continuously for 2 h while cooling. The organic phase of the reaction mixture was separated using a separatory funnel. The aqueous layer was extracted with 2×20 ml DCM and the organic fractions containing the triflyl azide were collected and washed once with saturated Na_2CO_3 and used without further purification for the next reaction step.

1.29 g H-L-Ser(tBu)-OH (8.0 mmol), 1.63 g K_2CO_3 (11.8 mmol), 26 mg $Cu(II)SO_4 \cdot 5H_2O$ (0.104 mmol) were dissolved in a mixture of 25 ml H_2O and 50 ml MeOH. The solution of triflyl azide in DCM previously prepared was added to the mixture and stirred over night at ambient temperature. After removal of the organic solvents under reduced pressure the remained suspension was dissolved in 150 ml H_2O. The pH of the aqueous solution was adjusted to 6 with conc. HCl and 150 ml of PBS (0.25 M, pH 6.2) was added. The aqueous layer was washed with 4×100 ml EtOAc to remove sulfonamide by product, acidified with conc. HCl to pH 2, and finally the product was isolated by extraction with 3×100 ml EtOAc. The combined EtOAc fractions were dried over anhydrous $MgSO_4$ and the organic solvent was removed under reduced pressure yielding 1.12 g of **4a** as pale oil (6.0 mmol, 75 %). No further purification was needed. ^{1}H NMR (300 MHz, CD_2Cl_2) δ = 9.94 (OH, 1 H), 3.90 (t, 1 H, J= 3 Hz), 3.77 (dd, J= 3 Hz, 2 H), 1.16 (s, 9 H). ^{13}C NMR (75 MHz, CD_2Cl_2) δ = 174.1, 74.4, 62.7, 61.4, 27.2.

5.2.3.5 (2*S*,3*S*)-*N*-(*tert*-butyloxycarbonyl)-1-ethynyl-3-methyl-butylamine (4b)

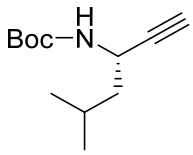

Chemical Formula: $C_{12}H_{21}NO_2$
Exact Mass: 211.16
Molecular Weight: 211.31

2.56 g of Boc-protected Weinreb amide Boc-L-Leu-*N*(OMe)Me (9.3 mmol) were weighted in a two-necked flask and flushed with dry argon. 75 ml of dry DCM was added while argon back flush from bottom and the resulting solution was cooled to -78 °C in an acetone/dry ice bath. 12 ml of Diisobutylaluminum hydride (DIBAH, 1 M in DCM, 12 mmol) was added drop-wise with an argon-flushed syringe to the solution and the reaction mixture was stirred for 40 min at -78 °C. The reaction was quenched by addition of 20 ml anhydrous MeOH.
The quenched mixture was allowed to warm to 0 °C with an ice/water bath and 2.76 g K_2CO_3 (20 mmol) was carefully added. Subsequently, 2.15 mg of dimethyl-(1-diazo-2-oxopropyl)phosphonate (Ohira-Bestmann reagent, 2.15 g, 11.2 mmol) was added drop-wise to the suspension. The resulted reaction mixture was stirred for 18 h at ambient temperature. The organic solvents were removed under reduced pressure and the resulted solid was eluted in 200 ml EtOAc/H_2O (1:1, v/v). After separation of the layers, the organic phase was washed with 3×50 ml H_2O and dried over anhydrous $MgSO_4$ and finally, the organic solvent was removed under reduced pressure. The resulted pale oil was purified by column chromatography (silica gel 600,040-0,063 mm, 230 – 300 mesh, eluent $CHCl_3$ /CH_3OH, 100:1, v/v) and after removal of the solvents 623.6 mg of **4b** (3.0 mmol, 32.3 %) was obtained. ^{1}H NMR (300 MHz, $CDCl_3$) δ = 4.80 (s, 1 H), 4.41 (dd, J= 6 Hz, 1 H), 2.32 (d, J = 3 Hz, 1 H), 1.86 – 1.71 (m, J = 6 Hz, 1 H), 1.54 (t, J= 6 Hz, 2 H), 1.45 (s, 9 H), 0.95 (dd, J = 6 Hz, 6 H). ^{13}C NMR (75 MHz, $CDCl_3$) δ = 155.1, 84.6, 79.8, 70.7, 45.5, 41.5, 28.6, 25.3, 22.7, 22.1.

5.2.3.6 (2*S*,3*S*)-*N*-(9-Fluorenylmethyloxycarbony)-1-ethynyl-3-methyl-butylamine (4c)

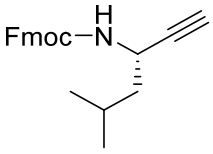

Chemical Formula: $C_{22}H_{23}NO_2$
Exact Mass: 333.17
Molecular Weight: 333.43

623.6 mg of **4b** (3.0 mmol) was dissolved in 6 ml TFA/DCM (1:1, v/v) and the resulting mixture was stirred for 1 h at ambient temperature. After removal of the solvents under reduced pressure, the resulted pale oil was dissolved in 10 ml acetone/H_2O (1:1, v/v). 322 mg of Na_2CO_3 (3.0 mmol) was added and the pH was adjusted to 9 – 10 by addition of Na_2CO_3 (aq., 1 M). 1.03 g Fmoc-OSu (3.0 mmol) was carefully added while the pH was kept at 9-10 by addition of further Na_2CO_3 (aq., 1 M). After stirring overnight, 12 ml EtOAc was added to

the suspension and the mixture was acidified by treatment with HCl (6 M) to pH 2 – 3. The organic layer was separated, washed with 4×5 ml H_2O, and dried over anhydrous $MgSO_4$. The organic solvent was removed under reduced pressure and the oily crude residue was cooled to 4 °C. Finally, the resulting crystalline product was washed with hexane yielding 836.1 mg of **4c** (2.5 mmol, 85.0 %). ^{1}H NMR (300 MHz, $CDCl_3$) δ = 7.81 (d, J = 8 Hz, 2H), 7.64 (d, J = 8 Hz, 2 H), 7.44 (t, J = 6 Hz, 2 H), 7.35 (t, J = 6 Hz, 2 H),5.04 (s, 1 H), 4.54-4.39 (m, 3 H), 4.26 (t, J = 7 Hz, 1 H), 1.81 (m, J = 6 Hz, 1 H), 1.58 (t, 8 Hz, 2 H), 0.96 (d, J = 6 Hz, 6 H). ^{13}C NMR (75 MHz, $CDCl_3$) δ = 155.8, 144.5, 141.9, 128.1, 127.4, 125.4, 120.3, 83.9, 71.2, 67.2, 47.7, 45.4, 42.2, 25.3, 22.7, 22.1.

5.2.3.7 des-Gly[1],-Pro[13],-Asp[14],Ψ[5,6] 1,4-[1,2,3]triazolyl-[Nle[2], Gln[10],Tyr[12]]SFTI-1[1,14] (4)

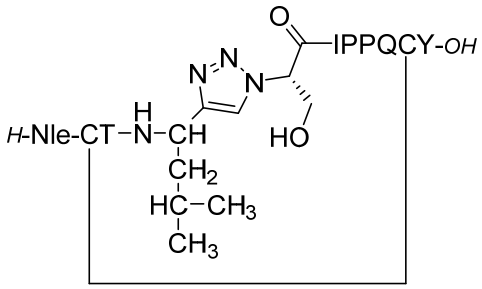

Chemical Formula: $C_{56}H_{86}N_{14}O_{15}S_2$
Exact Mass: 1258,58
Molecular Weight: 1259,50

4 was synthesized manually with microwave assistance. As a solid support, 500 mg of Fmoc-Tyr(tBu)-preloaded TentaGel® S AC resin with 0.22 mmol/g loading capacity was chosen (batch size: 0.1 mmol). Iterative chain elongation was achieved following the mentioned general protocol described in 5.2.1.2. After coupling of azido acid **4a** (procedure following the protocol described in 5.2.1.2), amino alkyne **4c** was attached *via* CuAAC: 67.2 mg of **4c** (0.2 mmol), 5.0 mg Cu(II)SO_4·$5H_2O$ (0.02 mmol, 20 % of batch size), 7.0 mg NaAsc (0.04 mmol), and 121 μl DIEA (0.08 mmol) was eluted in 2 ml dry and degassed DMF. After 2 min pre-activation, the suspension was added to the well-rinsed peptide-resin. The reaction mixture was shaken at ambient temperature over night. After removal of the solution *via* filtration, the peptide-resin was washed with 3×10 ml MeOH, 3×10 ml 0.5 % sodium diethyldithiocarbamate in DMF (w/v), 3×10 ml DMF, and 3×10 ml DCM. The iterative chain elongation was continued up to the coupling and Fmoc deprotection of the final amino acid Nle[2]. Cleavage and isolation of the crude, linear precursor peptide was as same as described for **1** (5.2.3.1). 122.4 mg of dried crude precursor peptidomimetic **4'** (0.097 mmol, 97.1 %) was yielded. RP-HPLC: R_t = 10.8 min, 9 % MeCN over 2 min followed by 9 %→90 % MeCN over 20 min in 0.1 % aq. TFA at flow rate 1 ml/min. ESI-MS: m/z: $[M+H]^+$ obsd. = 1262.8 (calc = 1262.5), $[M+2H]^{2+}$ obsd. = 631.8 (calc = 631.8), $[M-H]^-$ obsd. = 1262.8 (calc = 1260.5).

10 mg (0.008 mmol) linear precursor **4'** was oxidatively folded and purified as described for **3** (5.2.3.3). 0.6 mg of purified, oxidatively folded pseudo-peptide **4** (0.48 μmol, 5.9 % purification yield, 5.8 % overall yield) was obtained. RP-HPLC: R_t = 14.2 min, 9 % MeCN

over 2 min followed by 9 %→90 % MeCN over 20 min in 0.1 % aq. TFA at flow rate 1 ml/min. ESI-MS: m/z: $[M+H]^+$ obsd. = 1259.8 (calc = 1260.5), $[M+2H]^{2+}$ obsd. = 630.7 (calc = 630.8), $[M-H]^-$ obsd. = 1257.5 (calc = 1258.5).

5.2.3.8 [Pra[1]]SFTI-1[1,14] (5)

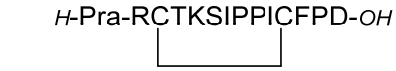

Chemical Formula: $C_{70}H_{108}N_{18}O_{19}S_2$
Exact Mass: 1568.75
Molecular Weight: 1569.86

5 was synthesized by manual Fmoc-SPPS without microwave assistance. As a solid support, 0.5 g of 2-chlorotrityl chloride resin was chosen. The resin was loaded as described in 5.2.1.1 with 0.1 mmol Fmoc-L-Asp using a loading mixture consisting of 1 eq Fmoc-L-Asp-OH, 4 eq DIEA dissolved in 5 ml DCM. Iterative chain elongation was achieved following the mentioned general protocol described in 5.2.1.2.

Cleavage of the linear peptide precursor **5'** from solid support and removal of the side chain protecting groups was achieved by acidolysis using 5 ml of the standard cleavage cocktail as described in 5.2.1.4. The resulting reaction mixture was shaken for 3 h at ambient temperature and the product was isolated by precipitation in 45 ml methyl *tert.*-butyl ether (MTBE) followed by washing with 3×15 ml MTBE. 218.5 mg of dried crude precursor peptide **5'** (0.139 mmol, 55.6 %) was yielded. RP-HPLC: R_t = 12.6 min, 18 % MeCN over 2 min followed by 9 %→90 % MeCN over 20 min in 0.1 % aq. TFA at flow rate 1 ml/min.

50 mg (0.032 mmol) precursor **5'** was dissolved in 10 ml folding buffer (100 mM $(NH_4)_2CO_3$ aq. with 0.5% DMSO) and the reaction mixture was stirred for three days with RP-HPLC monitoring and ESI-MS of the collected fractions. The solvent was removed by freeze-drying followed by purification *via* semi-preparative HPLC to yield 9.0 mg of oxidatively folded peptide **6** (0.006 mmol, 18.8 % folding yield, 10.5 % overall yield). RP-HPLC: R_t = 14.4 min, 18 % MeCN over 2 min followed by 9 %→90 % MeCN over 20 min in 0.1 % aq. TFA at flow rate 1 ml/min. ESI-MS: m/z: $[M+H]^+$ obsd. = 1570.8 (calc = 1570.9), $[M+2H]^{2+}$ obsd. = 786.0 (calc = 785.9), $[M+3H]^{3+}$ obsd. = 524.3 (calc = 524.3), $[M-H]^-$ obsd. = 1568.8 (calc = 1568.8).

5.2.3.9 [Pra[13]]SFTI-1[1,14] (6)

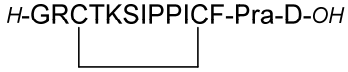

Chemical Formula: $C_{67}H_{104}N_{18}O_{19}S_2$
Exact Mass: 1528.72
Molecular Weight: 1529.80

6 was synthesized partially automated on the Liberty® peptide synthesizer system. As a solid support 1.05 g of Fmoc-Asp(tBu)-preloaded TentaGel® S AC resin with 0.22 mmol/g loading capacity was chosen (batch size 0.23 mmol). After manual, MW-assisted coupling of Fmoc-L-Pra-OH, all following amino acid were coupled by automated coupling cycles.

Cleavage of the linear peptide precursor **6'** from solid support and removal of the side chain protecting groups was achieved by acidolysis using 5 ml of the standard cleavage cocktail as described in 5.2.1.4. After a reaction time of 4 h and precipitation and washing with diethyl ether, 290.1 mg of dried crude precursor peptide **6'** (0.190 mmol, 82.5 %) was yielded. RP-HPLC: R_t = 12.6 min, 9 % MeCN over 2 min followed by 9 %→90 % MeCN over 20 min in 0.1 % aq. TFA at flow rate 1 ml/min. ESI-MS: m/z: $[M+H]^+$ obsd. = 1533.2 (calc = 1532.8), $[M+2H]^{2+}$ obsd. = 767.2 (calc = 766.4), $[M-2H]^{2-}$ obsd. = 765.1 (calc = 764.4).
20 mg (0.013 mmol) precursor **6'** was oxidatively folded and purified analogously to **5** yielding 8.3 mg of final product **6** (0.005 mmol, 41.5 % folding yield, 34.3 % overall yield). RP-HPLC: R_t = 14.1 min, 9 % MeCN over 2 min followed by 9 %→90 % MeCN over 20 min in 0.1 % aq. TFA at flow rate 1 ml/min. ESI-MS: m/z: $[M+H]^+$ obsd. = 1530.1 (calc = 1530.8), $[M+2H]^{2+}$ obsd. = 765.5 (calc = 765.9).

5.2.3.10 [Tyr(*O*-propargyl)^1]SFTI-1[1,14] (7)

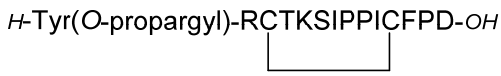

Chemical Formula: $C_{77}H_{114}N_{18}O_{20}S_2$
Exact Mass: 1674.79
Molecular Weight: 1675.99

7 was synthesized manually with microwave assistance. As a solid support, 1.14 g of Fmoc-Asp(tBu)-preloaded TentaGel® S AC resin with 0.22 mmol/g loading capacity was chosen (batch size 0.25 mmol). Further chain elongation was achieved following the mentioned general protocol described in 5.2.1.2.
Cleavage of the linear peptide precursor **7'** from solid support and removal of the side chain protecting groups was achieved by acidolysis using 5 ml of the standard cleavage cocktail as described in 5.2.1.4. After a reaction time of 4 h and precipitation and washing, 120.5 mg of dried crude precursor peptide **7'** (0.072 mmol, 71.9 %) was yielded. RP-HPLC: R_t = 14.6 min, 9 % MeCN over 2 min followed by 9 %→90 % MeCN over 20 min in 0.1 % aq. TFA at flow rate 1 ml/min. ESI-MS: m/z: $[M+H]^+$ obsd. = 1677.9 (calc = 1679.0), $[M+2H]^{2+}$ obsd. = 839.9 (calc = 840.0), $[M+3H]^{3+}$ obsd. = 560.2 (calc = 560.3), $[M-H]^-$ obsd. = 1676.8 (calc = 1677.0).
30 mg (0.018 mmol) precursor **7'** was oxidatively folded and purified analogously to **5** yielding 8.6 mg of peptide **7** (0.005 mmol, 27.8 % folding yield, 20.1 % overall yield). RP-HPLC: R_t = 15.9 min, 9 % MeCN over 2 min followed by 9 %→90 % MeCN over 20 min in 0.1 % aq. TFA at flow rate 1 ml/min. ESI-MS: m/z: $[M+H]^+$ obsd. = 1676.8 (calc = 1676.9), $[M+2H]^{2+}$ obsd. = 838.9 (calc = 839), $[M-H]^-$ obsd. = 1674,8 (calc = 1675.0).

5.2.3.11 [4-Pentynoic acid[1]]SFTI-1[1,14] (8)

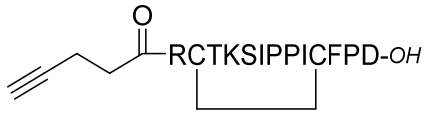

Chemical Formula: $C_{70}H_{107}N_{17}O_{19}S_2$
Exact Mass: 1553.74
Molecular Weight: 1554.85

8 was synthesized partially automated on the Liberty Blue® peptide synthesizer system. As a solid support, 1.36 g of *Fmoc*-Asp(*t*Bu)-preloaded TentaGel® S AC resin with 0.22 mmol/g loading capacity was chosen (batch size 0.3 mmol). Iterative chain elongation up to Arg[2] was achieved following the protocol for automated Fmoc-SPPS described in 5.2.1.3. After coupling of Fmoc-Arg, the peptide-resin was removed from the reaction chamber of the synthesizer and washed and dried. 500 mg of the split peptide-resin (25 wt%, 0.075 mmol) was used for attachment of *N*-terminal 4-pentynoic acid. Coupling was performed as manual double coupling with same conditions as the canonical amino acids.

Cleavage of the linear peptide precursor **8'** from solid support and removal of the side chain protecting groups was achieved by acidolysis using 5 ml of the standard cleavage cocktail as described in 5.2.1.4. After a reaction time of 4 h and precipitation and washing with diethyl ether 110.5 mg of dried crude precursor peptide **8'** (0.071 mmol, 94.6 %) was yielded. RP-HPLC: R_t = 15.2 min, 9 % MeCN over 2 min followed by 9 %→72 % MeCN over 20 min in 0.1 % aq. TFA at flow rate 1 ml/min. ESI-MS: m/z: $[M+H]^+$ obsd. = 1558.2 (calc = 1557.8), $[M+2H]^{2+}$ obsd. = 779.4 (calc = 779.4), $[M-H]^-$ obsd. = 1554.87 (calc = 1558.5).

30 mg (0.019 mmol) precursor **8'** was dissolved in 30 ml folding buffer (100 mM $(NH_4)_2CO_3$ aq. with 0.5% DMSO and ox. glutathione) and the reaction mixture was stirred for three days with RP-HPLC monitoring (9 % MeCN over 2 min followed by 9 %→90 % MeCN over 20 min in 0.1 % aq. TFA at flow rate 1 ml/min) and ESI-MS of the collected fractions. The solvent was removed by freeze-drying followed by semi-preparative purification *via* RP-HPLC and after freeze-drying of the product fraction 11.6 mg of final product peptide **8** was yielded (0.007 mmol, 35.8 % folding yield, 30.8 % overall yield). RP-HPLC: R_t = 16.3 min, 9 % MeCN over 2 min followed by 9 %→72 % MeCN over 20 min in 0.1 % aq. TFA at flow rate 1 ml/min. ESI-MS: m/z: $[M+H]^+$ obsd. = 1555.8 (calc = 1555.8), $[M+2H]^{2+}$ obsd. = 778.4 (calc = 778.4), $[M-H]^-$ obsd. = 1552.9 (calc = 1553.8), $[M-H]^-$ obsd. = 776.2 (calc = 776.4).

5.2.3.12 [*Ac*-Pra[1]]SFTI-1[1,14] (9)

Chemical Formula: $C_{72}H_{110}N_{18}O_{20}S_2$
Exact Mass: 1610.76
Molecular Weight: 1611.90

9 was synthesized partially automated on the Liberty Blue® peptide synthesizer system. 500 mg of the peptide-loaded resin (25 wt%, 0.075 mmol) synthesized and split previously for **8** was used. After coupling of Fmoc-L-Pra-OH and Fmoc deprotection, *N*-terminal acylation

was performed as double capping using acetic anhydride (Ac_2O) and DIEA (1:1, v/v) in 9 ml DMF within 60 min each.

Cleavage of the linear peptide precursor **9'** from solid support and removal of the side chain protecting groups was achieved by acidolysis using 5 ml of the standard cleavage cocktail as described in 5.2.1.4. 105.9 mg of dried crude unprotected precursor peptide **9'** (0.066 mmol, 88.0 %) was yielded. RP-HPLC: R_t = 15.5 min, 9 % MeCN over 2 min followed by 9 %→72 % MeCN over 20 min in 0.1 % aq. TFA at flow rate 1 ml/min. ESI-MS: m/z: $[M+H]^+$ obsd. = 1615.2 (calc = 1614.9), $[M+2H]^{2+}$ obsd. = 807.9 (calc = 808.0), $[M-H]^-$ obsd. = 1611.88 (calc = 1612.9).

30 mg (0.017 mmol) precursor **9'** was oxidatively folded and purified analogously to **5** yielding 11.8 mg of final product **9** (0.007 mmol, 36.8 % folding yield, 32.9 % overall yield). RP-HPLC: R_t = 16.4 min, 9 % MeCN over 2 min followed by 9 %→72 % MeCN over 20 min in 0.1 % aq. TFA at flow rate 1 ml/min. ESI-MS: m/z: $[M+H]^+$ obsd. = 1612.8 (calc = 1612.8), $[M+2H]^{2+}$ obsd. = 806.9 (calc = 806.9), $[M-H]^-$ obsd. = 1610.9 (calc = 1610.9), $[M-2H]^{2-}$ obsd. = 804.9 (calc =804.9).

5.2.3.13 [*Ac*-Tyr(propargyl)^1]SFTI-1[1,14] (10)

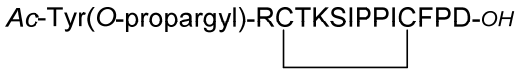

Chemical Formula: $C_{79}H_{116}N_{18}O_{21}S_2$
Exact Mass: 1716.80
Molecular Weight: 1718.02

10 was synthesized partially automated on the Liberty Blue® peptide synthesizer system. 500 mg of the peptide-loaded resin (25 wt%, 0.075 mmol) synthesized and split previously for **8** was used. After coupling of Fmoc-L-Tyr(*O*-propargyl)-OH and Fmoc deprotection, *N*-terminal acylation was performed as double capping using a acetic anhydride (Ac_2O) and DIEA (1:1, v:v) in 9 ml DMF within 60 min each.

Cleavage of the linear peptide precursor **10'** from solid support and removal of the side chain protecting groups was achieved by acidolysis using 5 ml of the standard cleavage cocktail as described in 5.2.1.4. 104.6 mg of dried crude unprotected precursor peptide **10'** (0.061 mmol, 81.2 %) was yielded. RP-HPLC: R_t = 16.7 min, 9 % MeCN over 2 min followed by 9 %→72 % MeCN over 20 min in 0.1 % aq. TFA at flow rate 1 ml/min. ESI-MS: m/z: $[M+H]^+$ obsd. = 1720.6 (calc = 1721.0), $[M+2H]^{2+}$ obsd. = 861.0 (calc = 861.0), $[M-H]^-$ obsd. = 1718.0 (calc = 1719.0).

30 mg (0.017 mmol) precursor **10'** was oxidatively folded and purified analogously to **8** yielding 11.8 mg of final product **10** (0.007 mmol, 40.3 % folding yield, 32.5 % overall yield). RP-HPLC: R_t = 18.5 min, 9 % MeCN over 2 min followed by 9 %→72 % MeCN over 20 min in 0.1 % aq. TFA at flow rate 1 ml/min. ESI-MS: m/z: $[M+H]^+$ obsd. = 1718.9 (calc = 1719.0), $[M+2H]^{2+}$ obsd. = 859.9 (calc = 860.0), $[M-H]^-$ obsd. = 1716.9 (calc = 1717.0).

5.2.3.14 [Pra[1],Ala[3](&[1]),Ala[11](&[2])]SFTI-1[1,14][(&[1]-CH[2]-1,5-[1,2,3]triazolyl-&[2])] (11)

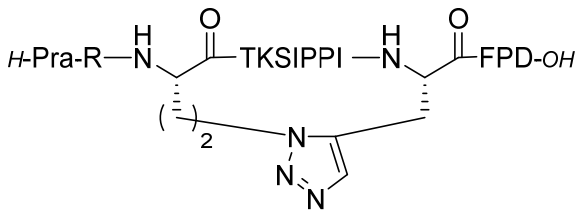

Chemical Formula: $C_{73}H_{111}N_{21}O_{19}$
Exact Mass: 1585,84
Molecular Weight: 1586,79

11 was synthesized manually on a Discover® SPS microwave synthesis platform using the Fmoc strategy. As a solid support, 0.43 g of Fmoc-L-Asp(*t*Bu) preloaded TentaGel® S AC resin with 0.22 mmol/g loading capacity was chosen (batch size 0.1 mmol). Chain elongation up to Arg^2 was achieved following the protocol for microwave assisted SPPS (5.2.1.2).

After attachment of Fmoc-Arg(Pbf)-OH to the *N*-terminus of the resin-bound precursor peptide, the ruthenium(II)-catalyzed macrocyclization on solid support was performed as previously described.[182] The well-rinsed and dried peptide-resin was put into a 20 ml open-end polypropylene syringe equipped with a frit and connected to the argon line. After addition of 5 ml dry and degassed DMF from the top, argon was bubbled through the mixture over 20 min. Subsequently, 7.6 mg (20 mol% of the initial loading of resin) Cp*RuCl(COD) was added from top while argon flush from the outlet nozzle. The mixture was flushed with argon for further 10 min. Then, the syringe was carefully sealed and placed into the microwave chamber of the Discover system. For temperature control, a second, open reference tube filled with DMF was placed into the chamber, thus the fiber-optic of the Discover SPS was able to measure the temperature inside. A microwave program with 60 °C, 30 W was used, whereby in the first heating period, the microwave irradiation was applied gradually in 10 °C steps until reaching the appointed temperature. After a reaction time of 5 h the peptide-resin was washed with 3×10 ml MeOH , 3×15 ml 0.5 % sodium diethyldithiocarbamate in DMF and 3×10 ml DMF. The success of macrocyclization was proven by a test cleavage in the presence of DTT as reducing agent.[183] 30 mg of the peptide-resin was treated with 1 ml solution of 1 M DTT and 2 M DIEA in DMF for 2 h at rt. Following the cleavage of the peptidomimetics with 1 ml of the standard cleavage cocktail and subsequent isolation by the described method (5.2.1.4) an MS analysis was performed. In case of a failed macrocyclization, the remaining azide residue of the peptide would be reduced by the DTT and a loss of 26 u would be detectable in the resulting spectrum. Since this was not the case, Pra^1 was coupled and the final Fmoc deprotection was performed according to the manual, microwave-assisted chain elongation protocol described in 5.2.1.2.

Cleavage of the macrocyclic peptidomimetic **11** from solid support and removal of the side chain protecting groups was achieved by the mentioned procedure using 5 ml of the standard cleavage cocktail as described in 5.2.1.4. Isolation of the peptide was achieved in 45 ml MTBE and washing by 4×15 ml MTBE. 62.1 mg of dried crude **11** (0.039 mmol, 39.1 %) was obtained. The crude peptidomimetic was purified *via* semipreparative RP-HPLC and after freeze-drying of the collected product fractions 7.4 mg of purified **11** (0.005 mmol, 4.7 % overall yield) was yielded. RP-HPLC: R_t = 14.4 min, 9 % MeCN over 2 min followed by 9 %→90 % MeCN over 20 min in 0.1 % aq. TFA at flow rate 1 ml/min. ESI-MS: m/z:

$[M+H]^+$ obsd. = 1587.6 (calc = 1587.8), $[M+2H]^{2+}$ obsd. = 794.4 (calc = 794.4), $[M+3H]^{3+}$ obsd. = 529.9 (calc = 529.9), $[M-H]^-$ obsd. = 1584.9 (calc = 1585.8).

5.2.3.15 [Tyr(propargyl)^1,Ala^3(&^{1}),Ala^{11}(&^{2})]SFTI-1[1,14][(&^{1}-CH^2-1,5-[1,2,3]triazolyl-&^{2})] (12)

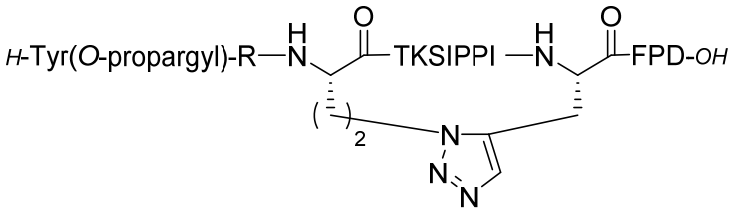

Chemical Formula: $C_{80}H_{117}N_{21}O_{20}$
Exact Mass: 1691,88
Molecular Weight: 1692,91

SPPS of peptidomimetics **12** was performed by manual Fmoc-SPPS on a Discover® SPS microwave synthesis platform. As a solid support, 0.43 g of Fmoc-L-Asp(*t*Bu) preloaded TentaGel® S AC resin with 0.22 mmol/g loading capacity was chosen (batch size 0.1 mmol). Chain elongation up to Arg^2, on-resin cyclization *via* RuAAC and the reduction test after macrocyclization was performed analogously as described for **11.** After evidence of successful macrocyclization, Fmoc-L-Tyr(*O*-propargyl) was coupled to the peptidomimetic and finally the *N*-terminal Fmoc was removed following the described procedure.

12 was cleaved and isolated as described for **11** yielding 81.5 mg of the crude peptidomimetic (0.048 mmol, 48.1 %). The crude **12** was purified *via* semipreparative RP-HPLC and after freeze-drying of the collected product fractions 9.5 mg of purified **12** (0.006 mmol, 5.6 % overall yield) was achieved. RP-HPLC: R_t = 15.3 min, 9 % MeCN over 2 min followed by 9 %→90 % MeCN over 20 min in 0.1 % aq. TFA at flow rate 1 ml/min. ESI-MS: m/z: $[M+H]^+$ obsd. = 1693.8 (calc = 1693.9), $[M+2H]^{2+}$ obsd. = 847.4 (calc = 847.5), $[M+3H]^{3+}$ obsd. = 565.3 (calc = 563.5), $[M-H]^-$ obsd. = 1692.0 (calc = 1691.9).

5.2.3.16 [Tyr(allyl)^1]SFTI-1[1,14] (13)

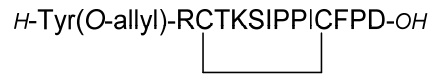

Chemical Formula: $C_{77}H_{116}N_{18}O_{20}S_2$
Exact Mass: 1676.81
Molecular Weight: 1678.00

13 was synthesized partially automated on the Liberty Blue® peptide synthesizer system. As a solid support, 0.46 g of Fmoc-L-Asp(*t*Bu) preloaded TentaGel® S AC resin with 0.22 mmol/g loading capacity was chosen (batch size 0.1 mmol). Chain elongation was achieved following protocol described in 5.2.1.3.

Cleavage of the linear peptide precursor **13'** from solid support and removal of the side chain protecting groups was achieved by acidolysis using 5 ml of the standard cleavage as described in 5.2.1.4. 159.2 mg of dried crude precursor peptide **13'** (0.098 mmol, 98.8 %) was yielded. RP-HPLC: R_t = 14.6 min, 9 % MeCN over 2 min followed by 9 %→90 % MeCN over 20 min in 0.1 % aq. TFA at flow rate 1 ml/min. ESI-MS: m/z: $[M+H]^+$ obsd. = 1677.9 (calc = 1679.0),

$[M+2H]^{2+}$ obsd. = 839.9 (calc = 840.0), $[M+3H]^{3+}$ obsd. = 560.2 (calc = 560.3), $[M-H]^{-}$ obsd. = 1676.8 (calc = 1677.0).

40 mg (0.024 mmol) precursor **13'** was oxidatively folded and purified analogously to **7** yielding 17.9 mg of peptide **13** (0.011 mmol, 44.3 % folding yield, 43.6 % overall yield). RP-HPLC: R_t = 15.7 min, 9 % MeCN over 2 min followed by 9 %→90 % MeCN over 20 min in 0.1 % aq. TFA at flow rate 1 ml/min. ESI-MS: m/z: $[M+H]^{+}$ obsd. = 1676.8 (calc = 1676.9), $[M+2H]^{2+}$ obsd. = 838.9 (calc = 839), $[M-H]^{-}$ obsd. = 1674,8 (calc = 1675.0).

5.2.3.17 [4-Pentenoic acid[1]]SFTI-1[1,14] (14)

Chemical Formula: $C_{70}H_{107}N_{17}O_{19}S_2$
Exact Mass: 1553.74
Molecular Weight: 1554.85

14 was synthesized partially automated on the Liberty Blue® peptide synthesizer system. As a solid support, 0.23 g of Fmoc-L-Asp(*t*Bu)-preloaded TentaGel® S AC resin with 0.22 mmol/g loading capacity was chosen (batch size 0.05 mmol). Chain elongation was achieved following protocol described in 5.2.1.3.

Cleavage of the linear peptide precursor **14'** from solid support and removal of the side chain protecting groups was achieved by acidolysis using 5 ml of the standard cleavage cocktail as described in 5.2.1.4. 60.4 mg of dried crude unprotected precursor peptide **14'** (0.038 mmol, 76.6 %) was yielded. RP-HPLC: R_t = 14.4 min, 9 % MeCN over 2 min followed by 9 %→90 % MeCN over 20 min in 0.1 % aq. TFA at flow rate 1 ml/min. ESI-MS: m/z: $[M+H]^{+}$ obsd. = 1558.9 (calc = 1559.9), $[M+2H]^{2+}$ obsd. = 780.4 (calc = 780.4), $[M+3H]^{3+}$ obsd. = 520.6 (calc = 520.6), $[M-H]^{-}$ obsd. = 1556.9 (calc = 1557.9).

50 mg (0.024 mmol) precursor **14'** was oxidatively folded and purified analogously to **8** yielding 15.4 mg of peptide **14** (0.010 mmol, 41.7 % folding yield, 31.7 % overall yield). RP-HPLC: R_t = 15.3 min, 9 % MeCN over 2 min followed by 9 %→90 % MeCN over 20 min in 0.1 % aq. TFA at flow rate 1 ml/min. ESI-MS: m/z: $[M+H]^{+}$ obsd. = 1558.1 (calc = 1557.9), $[M+2H]^{2+}$ obsd. = 779.4 (calc = 779.4), $[M-H]^{-}$ obsd. = 1555,8 (calc = 1555.8).

5.2.4 Synthesis of Modified Coiled Coil Guiding Units

5.2.4.1 BCN-(POE)$_3$-NH-C(O)(CH$_2$)$_3$-maleimide (15)

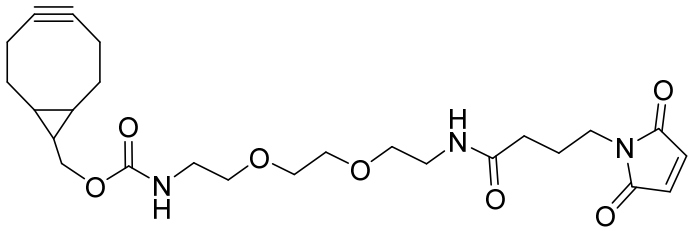

Chemical Formula: $C_{25}H_{35}N_3O_7$
Exact Mass: 489.25
Molecular Weight: 489.57

Preparation of **15** was performed following the instruction included in commercially available three-component kit (*Synaffix*). 250 μl of BCN-POE$_3$-NH$_2$ solution in DMSO (0.35 M, 87.5 μmol) was given to 33.5 mg of solid mixture of *N*-[γ-maleimidobutyryloxy]succinimide ester and K_2CO_2 (45:22, w/w). The resulted mixture was stirred at ambient temperature while the reaction progress was monitored by ESI-MS. After complete conversion of BCN-POE$_3$-NH$_2$ was verified, the solid phase was decanted and the solution was separated in 30 μl aliquots and stored at -80 °C. **15** was applied as mixture for further synthetic steps. RP-HPLC: R_t = 14.0 min, 9 % MeCN over 2 min followed by 9 %→90 % MeCN over 20 min in 0.1 % aq. TFA at flow rate 1 ml/min. ESI-MS: m/z: $[M+Na]^+$ obsd. = 512.2 (calc = 512.6), $[M+H]^+$ obsd. = 490.2 (calc = 490.6).

5.2.4.2 Cys-K3$_{g,d}$2E$_2$ Coil (16')

H-CKISALKQEISAEKQKISALKE-*NH$_2$*

Chemical Formula: $C_{106}H_{190}N_{30}O_{33}S$
Exact Mass: 2443.38
Molecular Weight: 2444.92

16 was synthesized partially automated with the Liberty® 12-channel peptide synthesizer system using the protocol described in 5.2.1.3. 480 mg AmphiSpheres® 40 RAM resin with 0.27 mmol/g loading capacity (total batch size: 0.130 mmol) were chosen as solid support and prepared as described in 5.2.1.1. After automated chain elongation up to Lys^2, the peptide-resin was dried and 200 mg (25 wt%, 0.033 mmol) was split for further microwave-assisted attachment with Fmoc-Cys(Trt)-OH according to the protocol described in 5.2.1.2. After final deprotection, cleavage, and precipitation (5.2.1.4), 44.1 mg of crude **16'** was obtained (0.017 mmol, 50.0 %). 20.0 mg of the crude peptide was purified *via* semipreparative RP-HPLC and after freeze-drying of the collected product fractions 6.0 mg of purified **16'** was achieved (0.002 mmol, 30.0 % purification yield, 15.0 % overall yield). RP-HPLC: R_t = 16.7 min, 9 % MeCN over 2 min followed by 9 %→72 % MeCN over 20 min in 0.1 % aq. TFA at flow rate 1 ml/min. ESI-MS: m/z: $[M+2H]^{2+}$ obsd. = 1223.5 (calc = 1223.46), $[M+3H]^{3+}$ obsd. = 816.0 (calc = 816.0), $[M+4H]^{4+}$ obsd. = 612.7 (calc = 612.2), $[M-H]^-$ obsd. = 1221.4 (calc = 1221.5).

5.2.4.3 [$S^{\beta1}$-(3-succinimido-$(CH_2)_3$-C(O)-NH-$(POE)_3$-BCN)]Cys-K3$_{g,d}$2E_2 Coil (16)

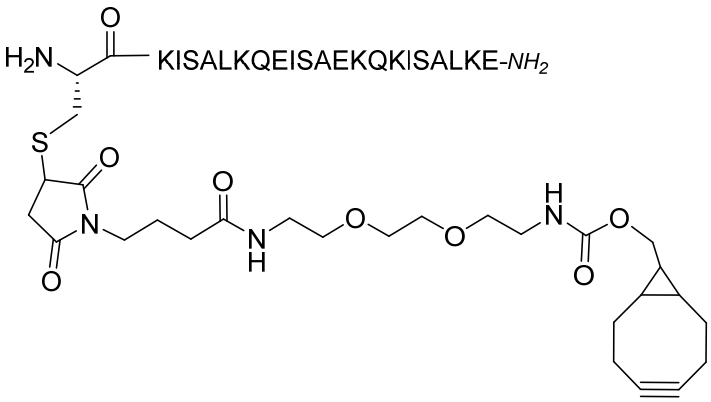

Chemical Formula: $C_{131}H_{225}N_{33}O_{40}S$
Exact Mass: 2932.63
Molecular Weight: 2934.49

Maleimide coupling of helical peptide **16'** with the maleimido-BCN building block **15** was performed according to a modified protocol.[184] 6.0 mg of **16'** (2.5 μmol) was dissolved in 2 ml Tris-HCl buffer (100 mM, pH 6.8) and 14 μl of **15** in DMSO prepared in 5.2.4.2 (0.35 M, 5 μmol) was added. The resulted mixture was stirred at ambient temperature. The reaction progress was monitored by analytical RP-HPLC. After the equilibrium of the reaction was reached, the mixture was diluted with 2 ml H_2O and purified *via* two semipreparative RP-HPLC runs. 1.0 mg of the purified BCN-loaded coil **16** (0.32 μmol, 12.7 %) was yielded. RP-HPLC: R_t = 20.3 min, 9 % MeCN over 2 min followed by 9 %→90 % MeCN over 20 min in 0.1 % aq. TFA at flow rate 1 ml/min. ESI-MS: m/z: $[M+2H]^{2+}$ obsd. = 1468.2 (calc = 1468.3), $[M+3H]^{3+}$ obsd. = 979.1 (calc = 979.2), $[M+4H]^{4+}$ obsd. = 734.4 (calc = 734.6), $[M-H]^-$ obsd. = 1466.2 (calc = 1466.3).

5.2.4.4 [$N^{\varepsilon1}$-Ser]Lys-E3$_e$2W Coil (17')

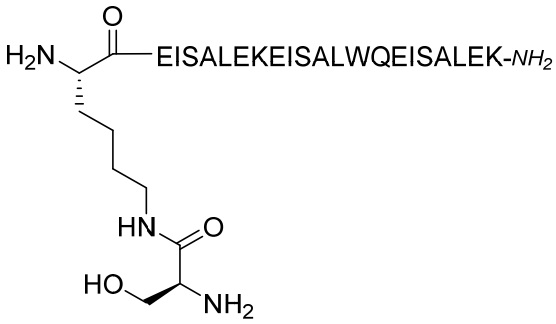

Chemical Formula: $C_{116}H_{193}N_{29}O_{38}$
Exact Mass: 2600.41
Molecular Weight: 2601.99

17' was synthesized partially automated with the Liberty® 12-channel peptide synthesizer system using the protocol described in 5.2.1.3. 479 mg AmphiSpheres® 40 RAM resin with 0.27 mmol/g loading capacity (total batch size: 0.130 mmol) was used as solid support and prepared as described in 5.2.1.1. After automated chain elongation up to Glu^2, the peptide-

resin was dried and 200 mg (25 wt%, 0.033 mmol) was split for further microwave-assisted attachment with Fmoc-Lys(Mtt)-OH according to the protocol described in 5.2.1.2. The on-resin cleavage of the Mtt protecting group was carried out *via* acidolysis under mild condition. Therefore, the peptide-resin was rinsed with 5×5 ml DCM and treated with 3 ml 1 % TFA in DCM. The cleavage mixture was shaken for 10 min at ambient temperature. Subsequently, 20 μl of TES was added and the mixture was shaken for another 5 min. After rinsing the peptide-resin with DCM, further 1 % TFA was given and the cycle was repeated as far as no yellow coloring of the liquid phase could be observed before TES was given to the mixture (5 – 10 times). Subsequently, Boc-Ser(tBu)-OH was coupled to the Lys side chain using the standard amino acid coupling protocol. After deprotection of the *N*-terminus, cleavage, and precipitation (see 5.2.1.4), 24.1 mg of crude **17'** was obtained (0.009 mmol, 27.3 %). The crude peptide was used without further purification for the next synthetic step. RP-HPLC: R_t = 22.4 min, 9 % MeCN over 2 min followed by 9 %→72 % MeCN over 20 min in 0.1 % aq. TFA at flow rate 1 ml/min. ESI-MS: m/z: $[M+2H]^{2+}$ obsd. = 1301.9 (calc = 1302.0), $[M+3H]^{3+}$ obsd. = 867.9 (calc = 868.3), $[M+4H]^{4+}$ obsd. = 651.0 (calc = 651.5), $[M-H]^-$ obsd. = 1299.9 (calc = 1300.0).

5.2.4.5 [$N^{\varepsilon 1}$-glyoxylyl]Lys-E3$_e$2W Coil (17)

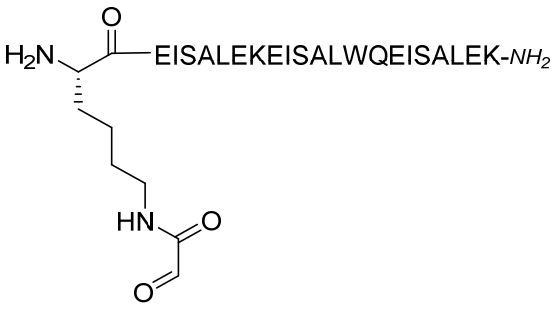

Chemical Formula: $C_{115}H_{188}N_{28}O_{38}$
Exact Mass: 2569.36
Molecular Weight: 2570.93

15.5 mg of crude **17'** (5.95 μmol) was dissolved in 3 ml PBS (1×, pH 7.4)-MeCN mixture (2:1, v/v). 12.9 mg sodium (meta)periodate (59.52 μmol) was dissolved in 1 ml PBS and added to the peptide solution. Following shaking for 10 min at ambient temperature, the reaction mixture was injected directly into the semipreparative RP-HPLC. After freeze-drying of the collected product fractions, 0.9 mg of purified **17** was achieved (0.35 μmol, 6.4 %). RP-HPLC: R_t = 22.4 min, 18 % MeCN over 2 min followed by 18 %→90 % MeCN over 20 min in 0.1 % aq. TFA at flow rate 1 ml/min. ESI-MS: m/z: $[M+H_2O+2H]^{2+}$ obsd. = 1295.4 (calc = 1295.5), $[M+H_2O-H]^-$ obsd. = 1293.4 (calc = 1293.5).

5.2.4.6 Cys-K5 Coil (18')

H-CKISALKEKISALKEKISALKEKISALKEKISALKE-NH_2

Chemical Formula: $C_{178}H_{322}N_{47}O_{51}S$
Exact Mass: 3966,38
Molecular Weight: 3968,81

18' was synthesized partially automated with the Liberty® 12-channel peptide synthesizer system using the protocol described in 5.2.1.3. 380 mg AmphiSpheres® 40 RAM resin with 0.27 mmol/g loading capacity (total batch size: 0.100 mmol) was used as solid support and prepared as described in 5.2.1.1. After automated chain elongation up to Lys^2, the peptide-resin was dried and 220 mg (25 wt%, 0.025 mmol) was split for further microwave-assisted attachment with Fmoc-Cys(Trt)-OH according to the protocol described in 5.2.1.2. After final deprotection, cleavage, and precipitation (see 5.2.1.4), 84.0 mg of crude **18'** was obtained (0.021 mmol, 84.0 %). 30.0 mg of the crude peptide was purified *via* semipreparative RP-HPLC and after freeze-drying of the collected product fractions 17.5 mg of purified **18'** was achieved (0.004 mmol, 58.3 % purification yield, 49.0 % overall yield). RP-HPLC: R_t = 19.2 min, 9 % MeCN over 2 min followed by 9 %→54 % MeCN over 20 min in 0.1 % aq. TFA at flow rate 1 ml/min. ESI-MS: m/z: $[M+4H]^{4+}$ obsd. = 993.4 (calc = 993.0), $[M+5H]^{5+}$ obsd. = 795.0 (calc = 794.6), $[M+6H]^{6+}$ obsd. = 662.7 (calc = 662.3), $[M+7H]^{7+}$ obsd. = 568.1 (calc = 567.8), $[M+8H]^{8+}$ obsd. = 497.2 (calc = 497.0).

5.2.4.7 [$S^{\beta1}$-(3-succinimido-$(CH_2)_3$-C(O)-NH-$(POE)_3$-BCN)]Cys-K5 Coil (18)

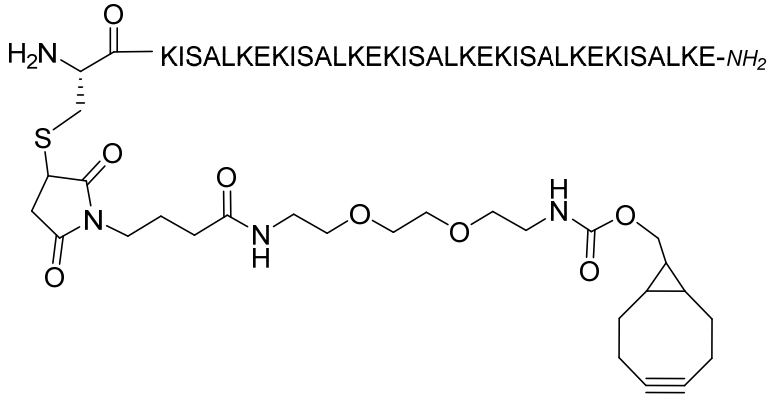

Chemical Formula: $C_{203}H_{357}N_{50}O_{58}S$
Exact Mass: 4455,62
Molecular Weight: 4458,37

4.0 mg of **18'** (1.0 μmol) was dissolved in 4 ml degassed Tris-HCl buffer (100 mM, pH 6.8) and 4.2 μl of **15** in DMSO prepared in 5.2.5.1 (0.35 M, 1.5 μmol) was added. The resulted mixture was stirred at ambient temperature. The reaction progress was monitored by analytical RP-HPLC. After the equilibrium of the reaction was reached, the mixture was purified *via* semipreparative RP-HPLC. 1.7 mg of the purified **18** (0.39 μmol, 38.6 %) was yielded. RP-HPLC: R_t = 18.8 min, 18 % MeCN over 2 min followed by 18 %→54 % MeCN over 20 min in 0.1 % aq. TFA at flow rate 1 ml/min. ESI-MS: m/z: $[M+4H]^{4+}$ obsd. = 1115.8 (calc = 1115.6), $[M+5H]^{5+}$ obsd. = 892.8 (calc = 892.7), $[M+6H]^{6+}$ obsd. = 744.2

(calc = 744.1), $[M+7H]^{7+}$ obsd. = 638.0 (calc = 637.9), $[M+9H]^{8+}$ obsd. = 558.4 (calc = 558.3).

5.2.4.8 [$N^{\varepsilon 1}$-Ser]Lys-E5 Coil (19')

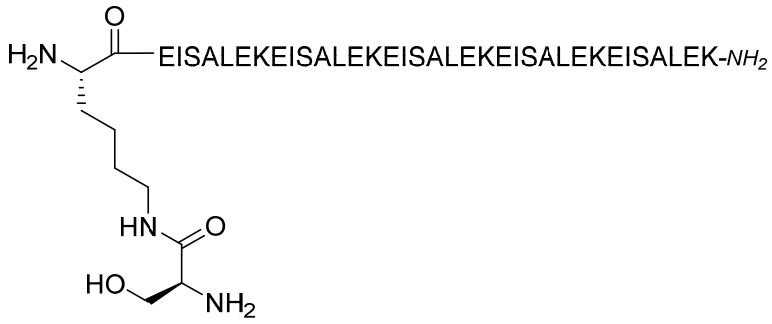

Chemical Formula: $C_{179}H_{310}N_{44}O_{63}$
Exact Mass: 4084,24
Molecular Weight: 4086,63

19' was synthesized manually using the protocol for microwave-assisted Fmoc-SPPS (5.2.1.3). 380 mg AmphiSpheres® 40 RAM resin with 0.27 mmol/g loading capacity (total batch size: 0.100 mmol) was used as solid support and prepared as described in 5.2.1.1. After manual chain elongation up to Glu^2, the peptide-resin was dried and 200 mg (25 wt%, 0.025 mmol) was split for further microwave-assisted attachment with Fmoc-Lys(Mtt)-OH according to the protocol described in 5.2.1.2. The on-resin cleavage of the Mtt protecting group and side chain modification was carried out as described in 5.2.5.4. After final deprotection of the *N*-terminus, cleavage, and precipitation (see 5.2.1.4), 36.7 mg of crude **19'** was obtained (0.009 mmol, 35.9 %). The crude peptide was used without further purification for the next synthetic step. RP-HPLC: R_t = 19.6 min, 9 % MeCN over 2 min followed by 9 %→72 % MeCN over 20 min in 0.1 % aq. TFA at flow rate 1 ml/min. ESI-MS: m/z: $[M+3H]^{3+}$ obsd. = 1363.2 (calc = 1326.2), $[M+4H]^{4+}$ obsd. = 1022.7 (calc = 1022.7), $[M+5H]^{5+}$ obsd. = 818.3 (calc = 818.3), $[M+6H]^{6+}$ obsd. = 682.1 (calc = 682.1), $[M+2Na+5H]^{7+}$ obsd. = 590.0 (calc = 591.1).

5.2.4.9 [$N^{\varepsilon 1}$-glyoxylyl]Lys-E5 Coil (19)

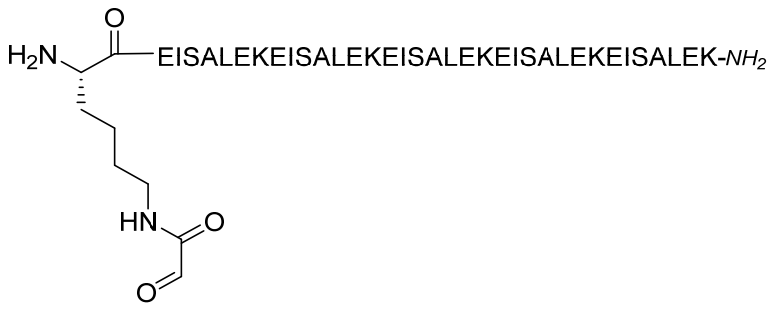

Chemical Formula: $C_{178}H_{305}N_{43}O_{63}$
Exact Mass: 4053,20
Molecular Weight: 4055,58

16.0 mg of crude **19'** (3.92 μmol) was dissolved in 2.5 ml PBS (1×, pH 7.4)-MeCN mixture (4:3, v/v). 8.4 mg sodium (meta)periodate (39.16 μmol) was dissolved in 1 ml PBS and added to the peptide solution. Following shaking for 10 min at ambient temperature, the reaction mixture was injected directly into the semipreparative RP-HPLC. After freeze-drying of the collected product fractions, 1.9 mg of purified **19** was achieved (0.47 μmol, 12.0 %). RP-HPLC: R_t = 19.1 min, 9 % MeCN over 2 min followed by 9 %→90 % MeCN over 20 min in 0.1 % aq. TFA at flow rate 1 ml/min ESI-MS: m/z: $[M+H_2O+3H]^{3+}$ obsd. = 1359.2 (calc = 1058.9), $[M+H_2O+4H]^{4+}$ obsd. = 1019.6 (calc = 1019.5), $[M+H_2O+5H]^{5+}$ obsd. = 815.8 (calc = 815.8), $[M+H_2O+6H]^{6+}$ obsd. = 679.9 (calc = 680.0).

5.2.5 Synthesis of Modified PNA Guiding Units

5.2.5.1 Cys-PNA A-Lys (20')

H-CgtagatcactK-NH_2

Chemical Formula: $C_{117}H_{153}N_{61}O_{32}S$
Exact Mass: 2956,19
Molecular Weight: 2957,92

20' was synthesized by manual Fmoc-SPPS. 185.0 mg of AmphiSpheres® 40 RAM resin with 0.27 mmol/g loading capacity (total batch size: 0.050 mmol) was used as solid support and prepared as described in 5.2.1.1. Loading of first amino acid Fmoc-Lys(Boc)-OH was performed with microwave-assistance. For the chain elongation of the PNA sequence, the protocol described in 5.2.2.2 was used. After chain elongation up to g^2, the PNA-resin was dried and 127.6 mg (50 wt%, 0.025 mmol) was spilt for further synthesis. After manual coupling of Fmoc-Cys(Trt)-OH, *N*-terminal deprotection, cleavage, and isolation 32.1 mg of the crude PNA-peptide hybrid **20'** was obtained (0.011 mmol, 44.1 %). 22 mg crude **20'** (7.57 μmol) was purified *via* semipreparative RP-HPLC and after isolation and freeze-drying of the collected product fractions, 9.7 mg of purified **20'** was achieved (3.28 μmol, 43.3 % purification yield, 19.1 % overall yield). RP-HPLC: R_t = 18.1 min, 0 % MeCN over 2 min followed by 0 %→27 % MeCN over 20 min in 0.1 % aq. TFA at flow rate 1 ml/min ESI-MS:

m/z: $[M+3H]^{3+}$ obsd. = 987.2 (calc = 986.9), $[M+4H]^{4+}$ obsd. = 740.5 (calc = 740.5), $[M+5H]^{5+}$ obsd. = 593.1 (calc = 592.6), $[M+6H]^{6+}$ obsd. = 494.2 (calc = 494.0).

5.2.5.2 [$S^{\beta 1}$-(3-succinimido-$(CH_2)_3$-C(O)-NH-$(POE)_3$-BCN)]Cys-PNA A-Lys (20)

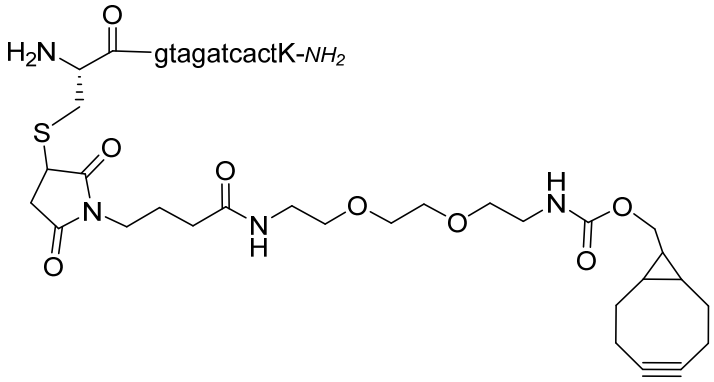

Chemical Formula: $C_{142}H_{188}N_{64}O_{39}S$
Exact Mass: 3445,44
Molecular Weight: 3447,48

4.7 mg of purified **20'** (1.59 μmol) was dissolved in 4 ml degassed NH_4OAc buffer (0.1 M, pH 6.5). 7 μl of **15** in DMSO prepared in 5.2.5.1 (0.35 M, 2.45 μmol) was added. The resulted mixture was stirred at ambient temperature. The reaction progress was monitored by analytical RP-HPLC. After the equilibrium of the reaction was reached, 500 μl MeCN was added to the mixture. The solid compounds in the mixture were separated by centrifugation and the liquid phase was purified *via* semipreparative RP-HPLC. 1.2 mg of the purified **20** (0.35 μmol, 22.1 %) was yielded. RP-HPLC: R_t = 17.3 min, 0 % MeCN over 2 min followed by 0 %→72 % MeCN over 20 min in 0.1 % aq. TFA at flow rate 1 ml/min. ESI-MS: m/z: $[M+2H]^{2+}$ obsd. = 1724.7 (calc = 1724.8), $[M+3H]^{3+}$ obsd. = 1150.2 (calc = 1150.2), $[M+4H]^{4+}$ obsd. = 862.7 (calc = 862.8), $[M+5H]^{5+}$ obsd. = 690.5 (calc = 690.4), $[M+6H]^{6+}$ obsd. = 575.6 (calc = 575.6).

5.2.5.3 [$N^{\varepsilon 1}$-Ser]Lys-PNA B-Lys (21')

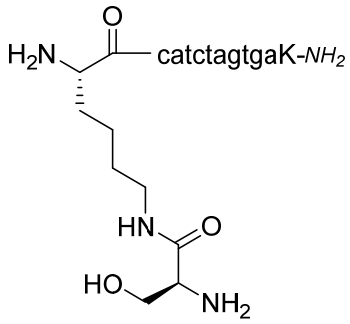

Chemical Formula: $C_{123}H_{165}N_{63}O_{34}$
Exact Mass: 3068,31
Molecular Weight: 3070,03

21' was synthesized by manual Fmoc-SPPS. 185.0 mg of AmphiSpheres® 40 RAM resin with 0.27 mmol/g loading capacity (total batch size: 0.050 mmol) was used as solid support and prepared as described in 5.2.1.1. Loading and chain elongation was performed as described for **20'** (5.2.6.1). After chain elongation up to c^2, the peptide-resin was dried and 150.1 mg (50 wt%, 0.025 mmol) was spilt for further synthesis. After manual coupling of Fmoc-Lys(Mtt)-OH, the Mtt protecting group was cleaved and Boc-Ser(tBu)-OH was coupled to the Lys side chain as described for **17'** (5.2.5.4). After *N*-terminal deprotection, cleavage, and isolation, 35.3 mg of the crude PNA-peptide hybrid **21'** was obtained (0.011 mmol, 44.1 %). 10 mg crude **21'** (3.26 μmol) was purified *via* semipreparative RP-HPLC and after isolation and freeze-drying of the collected product fractions, 6.1 mg of purified **21'** was achieved (1.99 μmol, 61.0 % purification yield, 26.9 % overall yield). RP-HPLC: R_t = 18.1 min, 0 % MeCN over 2 min followed by 0 %→27 % MeCN over 20 min in 0.1 % aq. TFA at flow rate 1 ml/min. ESI-MS: m/z: $[M+3H]^{3+}$ obsd. = 1024.4 (calc = 1024.3), $[M+4H]^{4+}$ obsd. = 768.2 (calc = 768.5), $[M+5H]^{5+}$ obsd. = 615.1 (calc = 615.0).

5.2.5.4 [$N^{\varepsilon 1}$-glyoxylyl]Lys-PNA B-Lys (21)

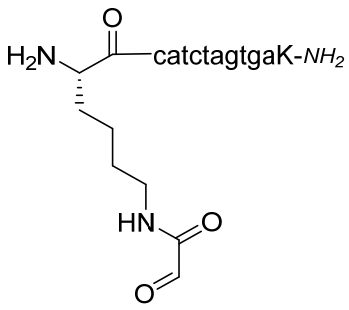

Chemical Formula: $C_{122}H_{160}N_{62}O_{34}$
Exact Mass: 3037,27
Molecular Weight: 3038,97

6.1 mg of crude **21'** (1.99 μmol) was dissolved in 3 ml PBS (1×, pH 7.4). 4.2 mg sodium (meta)periodate (19.8 μmol) was dissolved in 1 ml PBS and added to the PNA solution. Following shaking for 10 min at ambient temperature, the reaction mixture was injected directly into the semipreparative RP-HPLC. After freeze-drying of the collected product fractions, 2.2 mg of purified **21** was achieved (0.72 μmol, 36.2 %). RP-HPLC: R_t = 13.4 min, 0 % MeCN over 2 min followed by 0 %→72 % MeCN over 20 min in 0.1 % aq. TFA at flow rate 1 ml/min. ESI-MS: m/z: $[M+H_2O+2H]^{2+}$ obsd. = 1529.4 (calc = 1529.5), $[M+3H]^{3+}$ obsd. = 1014.0 (calc = 1014.0), $[M+4H]^{4+}$ obsd. = 760.7 (calc = 760.7), $[M+H_2O+5H]^{5+}$ obsd. = 612.4 (calc = 612.4), $[M+H_2O+6H]^{6+}$ obsd. = 510.5 (calc = 510.5).

5.2.5.5 [$N^{\varepsilon 1}$-Ser]Lys-PNA C-Lys (22')

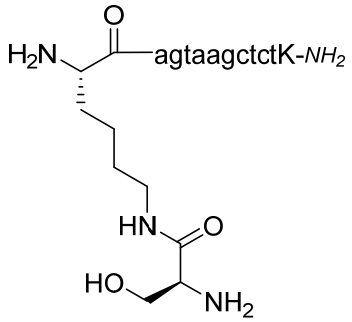

Chemical Formula: $C_{122}H_{165}N_{61}O_{34}$
Exact Mass: 3028,31
Molecular Weight: 3030,00

22' was synthesized by manual Fmoc-SPPS. 185.0 mg of AmphiSpheres® 40 RAM resin with 0.27 mmol/g loading capacity (total batch size: 0.050 mmol) was used as solid support and prepared as described in 5.2.1.1. Loading and chain elongation was performed as described for **20'** (5.2.6.1). After chain elongation up to a^2, the peptide-resin was dried and 113.3 mg (50 wt%, 0.025 mmol) was spilt for further synthesis. After coupling of Fmoc-Lys(Mtt)-OH, the Mtt protecting group was cleaved and Boc-Ser(tBu)-OH was coupled to the side chain as described for **17'** (5.2.5.4). Following the cleavage and isolation protocol discussed in 5.2.1.4, 17.4 mg of the PNA-peptide hybrid **22'** was obtained (0.006 mmol, 22.5 %). 42 mg crude **22'** (9.79 μmol) was purified *via* semipreparative RP-HPLC and after isolation and freeze-drying of the collected product fractions, 10.8 mg of purified **22'** was achieved (0.004 mmol, 63.7 % purification yield, 14.3 % overall yield). RP-HPLC: R_t = 14.2 min, 0 % MeCN over 2 min followed by 0 %→54 % MeCN over 20 min in 0.1 % aq. TFA at flow rate 1 ml/min ESI-MS: m/z: $[M+2H]^{2+}$ obsd. = 1515.9 (calc = 1516.0), $[M+3H]^{3+}$ obsd. = 1011.1 (calc = 1011.0), $[M+4H]^{4+}$ obsd. = 758.6 (calc = 758.5), $[M+5H]^{5+}$ obsd. = 607.1 (calc = 607.0), $[M+6H]^{6+}$ obsd. = 506.1 (calc = 506.0).

5.2.5.6 [$N^{\varepsilon 1}$-glyoxylyl]Lys-PNA C-Lys (22)

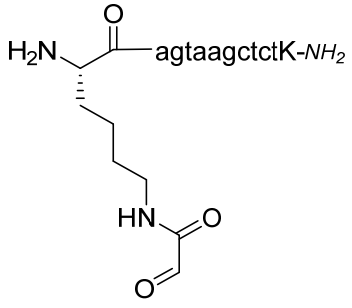

Chemical Formula: $C_{121}H_{160}N_{60}O_{34}$
Exact Mass: 2997,26
Molecular Weight: 2998,95

5.0 mg of crude **22** (1.65 μmol) was dissolved in 3 ml PBS (1×, pH 7.4). 3.5 mg sodium (meta)periodate (16.5 μmol) was dissolved in 1 ml PBS and added to the PNA solution. The

reaction mixture was handled as described for **21** (5.2.6.4) and after isolation *via* semipreparative RP-HPLC and freeze-drying of the collected product fractions, 2.6 mg of purified **22** was achieved (0.86 μmol, 52.3 %). RP-HPLC: R_t = 14.9 min, 0 % MeCN over 2 min followed by 0 %→54 % MeCN over 20 min in 0.1 % aq. TFA at flow rate 1 ml/min. ESI-MS: m/z: $[M+H_2O+3H]^{3+}$ obsd. = 1006.6 (calc = 10067.7), $[M+H_2O+4H]^{4+}$ obsd. = 755.1 (calc = 755.2), $[M+H_2O+5H]^{5+}$ obsd. = 604.3 (calc = 604.4), $[M+H_2O+6H]^{6+}$ obsd. = 503.1 (calc = 503.8).

5.2.5.7 Aha-PNA B-Lys (23)

H-Aha-catctagtgaK-NH_2

Chemical Formula: $C_{118}H_{154}N_{64}O_{32}$
Exact Mass: 2979.24
Molecular Weight: 2980.95

For the synthesis of **23**, 59.0 mg of the dried and split PNA-resin prepared in 5.2.6.3 was used (20 wt%: 0.01 mmol). After swelling of the PNA-resin and *N*-terminal deprotection, Fmoc-Aha-OH was coupled according the protocol mentioned in 5.2.1. After *N*-terminal deprotection, cleavage, and isolation, 52.0 mg of the crude PNA-peptide hybrid **23** was obtained (0.017 mmol, 69.8 %). 20 mg of the crude PNA/peptide (0.007 mmol) was purified by semipreparative HPLC yielding 8.8 mg of purified **23** (0.003 mmol, 44.0 % purification yield, 30.7 % overall yield). RP-HPLC: R_t = 14.0 min, 16.0 min, 0 % MeCN over 2 min followed by 0 %→54 % MeCN over 20 min in 0.1 % aq. TFA at flow rate 1 ml/min. ESI-MS: m/z: $[M+2H]^{2+}$ obsd. = 1491.5 (calc = 1491.5), $[M+3H]^{3+}$ obsd. = 994.6 (calc = 994.6), $[M+4H]^{4+}$ obsd. = 746.2 (calc = 746.2), $[M+5H]^{5+}$ obsd. = 597.2 (calc = 597.2).

5.2.5.8 8-(*tert*-butoxycarbonylmethyleneoxy)psoralen (24')

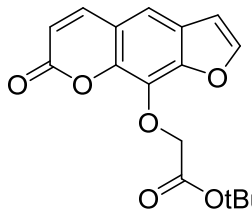

Chemical Formula: $C_{17}H_{16}O_6$
Exact Mass: 316.09
Molecular Weight: 316.31

333 mg 8-hydroxypsoralen (1.64 mmol), 1.28 g *tert*-butyl bromoacetate (6.59 mmol) and 1.67 g potassium carbonate (12.08 mmol) were dissolved in 50 ml acetone. The mixture was stirred under reflux for 2 h. The solid residue was removed by filtration and centrifugation. The supernatant was purified by flash column chromatography (silica gel 600, 0.040-0.063 mm, 230 – 300 mesh, eluent DCM, followed by MeOH). After removal of the solvent, 350.1 mg (1.11 mmol, 67,8 %) of purified **24'** was obtained. ^{1}H-NMR (300 MHz, $CDCl_3$): 7.77 (d, J=9.6 Hz, 1H), 7.67 (d, J=2.3 Hz, 1H), 7.36 (s, 1H), 6,82 (d, J=2.3 Hz, 1H), 6.38 (d, J=9.6 Hz, 1H), 5.07 (s, 2H), 1.43 (s, 9H).

5.2.5.9 8-(Carboxymethyleneoxy)psoralen (24)

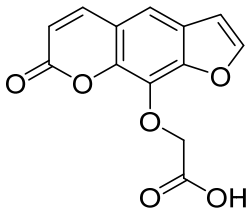

Chemical Formula: $C_{13}H_8O_6$
Exact Mass: 260.03
Molecular Weight: 260.20

350.1 mg **24'** (1.11 mmol) was given in 20 ml TFA and stirred under reflux for 2 h. TFA was removed by rotary evaporation to afford 290.2 mg **24** as a pale-brown solid (1.11 mmol, 100 %). ^{1}H-NMR (300 MHz, DMSO-d$_6$): 8.15 (d, J=9.7 Hz, 1H), 8.11 (d, J=2.2 Hz, 1H), 7.65 (s, 1H), 7.09 (d, J=2.2 Hz, 1H), 6.45 (d, J=9.6 Hz, 1H), 5.13 (s, 2H).

5.2.5.10 [$N^{\varepsilon 2}$- Gly$_3$]8-(Carboxymethyleneoxy)psoralen-Lys-PNA2-Lys-Val-Cit-Glu (25)

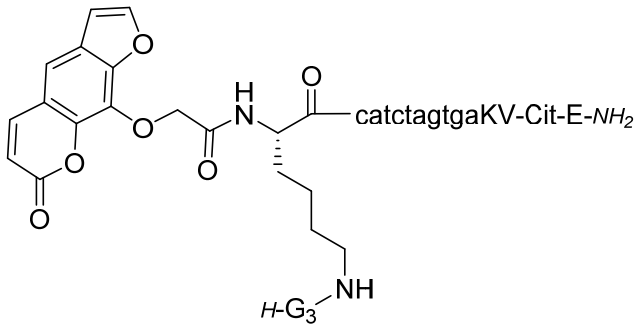

Chemical Formula: $C_{155}H_{202}N_{70}O_{46}$
Exact Mass: 3779.56
Molecular Weight: 3781.77

For the synthesis of **25**, 59.0 mg of the dried and split PNA-resin analogously prepared as described in 5.2.5.3 was used (20 wt%, 0.01 mmol). After swelling of the PNA-resin and *N*-terminal deprotection, Fmoc-Lys(Mtt)-OH and **24** was coupled according to the protocol described in 5.2.1.2 (**24** was handled as same as non-canonical amino acids: 4 eq. **24**, activation with 3.9 eq. HATU and 8 eq. DIEA). Mtt deprotection was carried out as described for 5.2.5.3. Coupling of Boc-Gly$_3$-OH to the free amine of the lysine side chain was achieved following the protocol mentioned in 5.2.1.2 (Boc-Gly$_3$-OH was handled as same as non-canonical amino acids: 4 eq. Boc-Gly$_3$-OH, activation with 3.9 eq. HATU and 8 eq. DIEA). The entire crude PNA-peptide hybrid after cleavage and isolation (5.2.1.4; 9.7 mg, 2.565 mmol, 25.6 %) was purified by semipreparative HPLC yielding 3.8 mg of purified **25** (0.001 mmol, 10.0 % overall yield). RP-HPLC: R_t = 15.7 min, 0 % MeCN over 2 min followed by 0 %→54 % MeCN over 20 min in 0.1 % aq. TFA at flow rate 1 ml/min. ESI-MS: m/z: $[M+3H]^{3+}$ obsd. = 1261.6 (calc = 1261.5), $[M+4H]^{4+}$ obsd. = 946.4 (calc = 946.4), $[M+5H]^{5+}$ obsd. = 757.3 (calc = 757.3), $[M+6H]^{6+}$ obsd. = 631.3 (calc = 631.2), $[M+7H]^{7+}$ obsd. = 541.3 (calc = 541.2).

5.2.5.11 PNA D-Lys (26)

H-tatagtagatcactK-NH_2

Chemical Formula: $C_{158}H_{202}N_{82}O_{43}$
Exact Mass: 3935.61
Molecular Weight: 3937.89

For the synthesis of **26**, 50.8 mg of the dried and split PNA-resin prepared in 5.2.5.1 was used (20 wt%, 0.01 mmol). *N*-terminal extension with the tata PNA motif was performed following the PNA extension protocol II (5.2.2.3). The entire crude PNA-peptide hybrid after cleavage and isolation (5.2.1.4; 14.8 mg, 3.758 mmol, 37.6 %) was purified by semipreparative HPLC yielding 4.0 mg of purified **26** (0.001 mmol, 10.0 % overall yield). RP-HPLC: R_t = 14.9 min, 0 % MeCN over 2 min followed by 0 %→54 % MeCN over 20 min in 0.1 % aq. TFA at flow rate 1 ml/min. ESI-MS: m/z: $[M+3H]^{3+}$ obsd. = 1313.6 (calc = 1313.6), $[M+4H]^{4+}$ obsd. = 985.5 (calc = 985.5), $[M+5H]^{5+}$ obsd. = 788.6 (calc = 788.5), $[M+6H]^{6+}$ obsd. = 657.4 (calc = 657.3), $[M+7H]^{7+}$ obsd. = 563.6 (calc = 563.5), $[M+8H]^{8+}$ obsd. = 493.4 (calc = 493.4).

5.2.5.12 Gly_5-PNA B-Lys (27)

H-GGGGGcatctagtgaK-*OH*

Chemical Formula: $C_{124}H_{163}N_{65}O_{36}$
Exact Mass: 3138,29
Molecular Weight: 3140,03

SPPS of **27** was performed on 37.0 mg AmphiSpheres® 40 RAM resin with loading capacity of 0.27 mmol/g (batch size: 0.010 mmol). For chain elongation of the PNA part and the *N*-terminal Gly_5-tag, the PNA protocol II (5.2.2.2) was applied. After cleavage of the PNA-peptide hybrid from solid support, 9.7 mg of crude **27** was isolated (0.003 mmol, 30.9 %). A purification *via* semipreparative RP-HPLC resulted in 4.9 mg of **27** (1.56 μmol, 50.4% purification yield, 15.6 % overall yield). RP-HPLC: R_t = 13.5 min, 0 % MeCN over 2 min followed by 0 %→54 % MeCN over 20 min in 0.1 % aq. TFA at flow rate 1 ml/min ESI-MS: m/z: $[M+3H]^{3+}$ obsd. = 1047.7 (calc = 1047.7), $[M+4H]^{4+}$ obsd. = 786.1 (calc = 786.0), $[M+5H]^{5+}$ obsd. = 629.1 (calc = 629.0), $[M+6H]^{6+}$ obsd. = 524.4 (calc = 524.3).

5.2.5.13 [$N^{\varepsilon 6}$-Ser]Gly_5-Lys-TEV-PNA B-Lys (28)

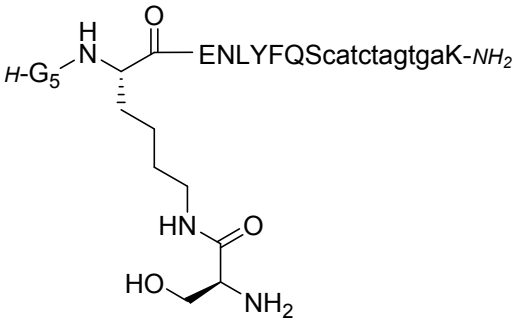

Chemical Formula: $C_{174}H_{235}N_{77}O_{52}$
Exact Mass: 4234,81
Molecular Weight: 4237,21

For the synthesis of **28**, 150.4 mg of the dried and split PNA-resin prepared in 5.2.5.3 was used (50 wt%, 0.025 mmol). *N*-terminal extension with the TEV protease cleavage site, Lys(Mtt), and Gly_5 tag was performed following the protocol for manual peptide chain elongation without microwave assistance (5.2.1.2). After coupling of Fmoc-Lys(Mtt)-OH, the Mtt protecting group was cleaved and Boc-Ser(tBu)-OH was coupled to the side chain as described for **17** (5.2.5.4). Finally, 28.6 mg of the crude PNA-peptide hybrid **28** could be isolated by cleavage and precipitation (0.007 mmol, 27.0 %). After purification *via* semipreparative RP-HPLC, isolation and freeze-drying of the collected product fractions, 15.3 mg of purified **28** was achieved (3.61 μmol, 51.5 % purification yield, 13.9 % overall yield). RP-HPLC: R_t = 15.3 min, 0 % MeCN over 2 min followed by 0 %→90 % MeCN over 20 min in 0.1 % aq. TFA at flow rate 1 ml/min. ESI-MS: m/z: $[M+3H]^{3+}$ obsd. = 1413.4 (calc = 1414.1), $[M+4H]^{4+}$ obsd. = 1060.3 (calc = 1060.8), $[M+5H]^{5+}$ obsd. = 848.5 (calc = 848.8), $[M+6H]^{6+}$ obsd. = 707.2 (calc = 707.5).

5.2.5.14 Gly_5-PNA E-Lys (29)

H-GGGGGcatctagtgaggagK-*OH*

Chemical Formula: $C_{168}H_{215}N_{93}O_{47}$
Exact Mass: 4286,73
Molecular Weight: 4289,10

29 was synthesized by manual Fmoc-SPPS. 185.0 mg of AmphiSpheres® 40 RAM resin with 0.27 mmol/g loading capacity (total batch size: 0.050 mmol) was chosen as solid support and prepared as described in 5.2.1.1. Loading and chain elongation was performed according to the PNA chain elongation protocol II (5.2.2.3). After chain elongation up to c^2, the peptide-resin was dried and 130.6 mg (1/2 of total batch, 0.025 mmol) was spilt for further synthesis. After cleavage and isolation (5.2.1.4), 47.4 mg of the strongly contaminated crude PNA-peptide hybrid **29** was obtained (0.011 mmol, 44.2 %). 42.0 mg crude **29** (9.79 μmol) was purified *via* semipreparative RP-HPLC and after isolation and freeze-drying of the collected product fractions, 5.3 mg of purified **29** was achieved (1.23 μmol, 12.6 % purification yield, 5.6 % overall yield). RP-HPLC: R_t = 11.0 min, 12.3 min, 9 % MeCN over 2 min followed by 9 %→54 % MeCN over 20 min in 0.1 % aq. TFA at flow rate 1 ml/min. ESI-MS: m/z:

$[M+4H]^{4+}$ obsd. = 1073.2 (calc = 1073.3), $[M+5H]^{5+}$ obsd. = 858.9 (calc = 858.8), $[M+6H]^{6+}$ obsd. = 715.9 (calc = 715.9), $[M+7H]^{7+}$ obsd. = 613.6 (calc = 613.7).

5.2.5.15 Gly_5-PNA2-Lys-Val-Cit-Aha (30')

H-GGGGGcatctagtgaKV-Cit-Aha-NH_2

Chemical Formula: $C_{139}H_{189}N_{73}O_{40}$
Exact Mass: 3520.50
Molecular Weight: 3522.51

SPPS of **30'** was performed on 75.0 mg AmphiSpheres® 40 RAM resin with loading capacity of 0.27 mmol/g (batch size: 0.020 mmol). Chain elongation of the *C*-terminal, peptidic part was performed according the protocol for manual microwave-assisted SPPS (5.2.1.2). For chain elongation of the PNA part and the *N*-terminal Gly_5-tag the PNA protocol I (5.2.2.2) was applied. After cleavage of the PNA-peptide hybrid from solid support, crude **30'** could be isolated in high purity, thus no further purification was required. 23.4 mg of **30'** was obtained (0.007 mmol, 33.2 %). RP-HPLC: R_t = 14.0 min, 0 % MeCN over 2 min followed by 0 %→72 % MeCN over 20 min in 0.1 % aq. TFA at flow rate 1 ml/min. ESI-MS: m/z: $[M+4H]^{4+}$ obsd. = 881.7 (calc = 881.6), $[M+5H]^{5+}$ obsd. = 705.6 (calc = 705.5), $[M+6H]^{6+}$ obsd. = 588.1 (calc = 588.1).

5.2.5.16 BCN-9-methoxycarbonyl-*N*-Ispinesib (31)

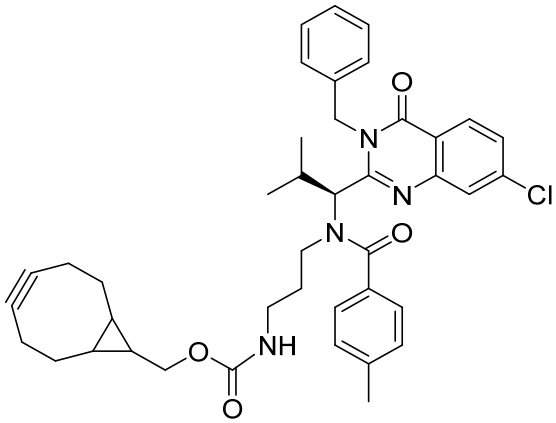

Chemical Formula: $C_{41}H_{45}ClN_4O_4$
Exact Mass: 692.31
Molecular Weight: 693.29

2.8 mg of Ispinesib (5.4 μmol) was dissolved in 1 ml DMSO. 80 μl of BCN-NHS (34 mM in DMSO, 2.7 μmol) was added and the resulting mixture was shaken at ambient temperature until conversion of Ispinesib was terminated, while monitoring the reaction progress by RP-HPLC and ESI-MS. The mixture was applied without further purification for the successive SPAAC. RP-HPLC: R_t = 19.5 min, 0 % MeCN over 2 min followed by54 %→90 % MeCN over 20 min in 0.1 % aq. TFA at flow rate 1 ml/min. ESI-MS: m/z: $[M+Na]^+$ obsd. =715.3 (calc = 716.3), $[M+H]^+$ obsd. = 693.3 (calc = 694.3).

5.2.5.17 [$C^{\gamma 19}$- ((7*R*,8s,9*S*)-5,6,7,9,10,11-hexahydro-bicyclo[6.1.0]nona[1,2,3]triazolyl)-8-methoxy)carbonyl-*N*-Ispinesib)]Gly_5-PNA B-Lys-Val-Cit-hAla (30)

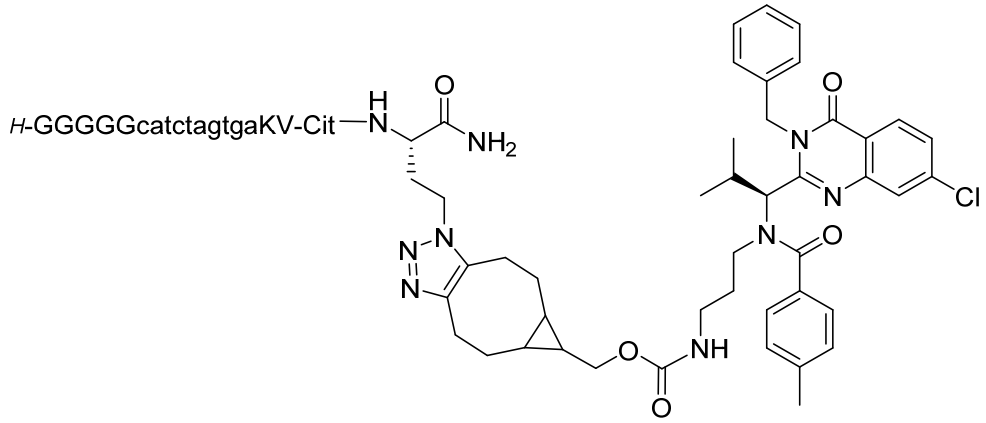

Chemical Formula: $C_{183}H_{237}ClN_{74}O_{44}$
Exact Mass: 4209,8271
Molecular Weight: 4212,7623

The loading of ispinesib to the PNA-peptide hybrid **30** was achieved *via* SPAAC. 5 mg of **30'** (1.35 μmol) was dissolved in 500 μl H_2O and 1 ml of the **31** containing mixture prepared in 5.2.6.11 was added. The resulting mixture was diluted with DMSO to 3 ml and shaken at ambient temperature for 5 h. Finally, the toxin-loaded PNA-peptide hybrid **30** was purified *via* semipreparative RP-HPLC yielding 3.8 mg of pure **30** (0.9 μmol, 66.7 %). RP-HPLC: R_t = 19.6 min, 0 % MeCN over 2 min followed by 0 %→90 % MeCN over 20 min in 0.1 % aq. TFA at flow rate 1 ml/min. ESI-MS: m/z: $[M+3H]^{3+}$ obsd. =1406.2 (calc = 1405.3), $[M+4H]^{4+}$ obsd. = 1055.0 (calc = 1054.2), $[M+5H]^{5+}$ obsd. = 844.2 (calc = 843.6), $[M+6H]^{6+}$ obsd. = 703.7 (calc = 703.1), $[M+7H]^{7+}$ obsd. = 603.3 (calc = 602.8).

5.3 Test Reactions

5.3.1 Proteolysis Experiments of Protease Inhibitors

Proteolysis experiments of the linear precursor of the inhibitors **1'**-**4'** and cyclic HNE inhibitors **3** and **4** were performed by incubation in presence of the HNE or chymotrypsin and analysis of the supernatant of the reaction mixture after protein precipitation *via* analytical RP-HPLC and ESI-MS of the collected fraction.

Setup 1. 20 μl of precursors **1'** – **4'** (1 mM in H_2O, 20 nmol) was treated with 200 μl DTT (50 mM in elastase activity buffer: 100 mM Tris/HCl, 20 mM $CaCl_2$, 500 mM NaCl, 0.005 % Triton X-100, pH 7.8; 10 μmol). 100 μl of HNE (1 μM in PBS pH 7.5, 100 pmol) was added. The reaction mixture was shaken at ambient temperature while taking 20 μl of the mixture in 10 – 60 min steps for HPLC analysis. HNE was removed by precipitation in acidic milieu: the sample solution was given in 80 μl HCl (aq. 100 mM).

Setup 2. 20 μl of precursors **1'** – **4'** (1 mM in H_2O, 20 nmol) was treated with 200 μl DTT (50 mM in chymotrypsin activity buffer: 100 mM Tris/HCl, 20 mM $CaCl_2$, 0.05 % Triton X-100, pH 7.8; 10 μmol). 100 μl of bovine chymotrypsin (1 μM in PBS pH 7.5, 100 pmol) was

added and the reaction mixture was shaken at ambient temperature. Further procedure was same as described for setup 1.

Setup 3. 100 μl of cyclic inhibitors **3** or **4** (1 mM in H_2O, 100 nmol) was diluted with 200 μl elastase activity buffer (10 μmol). 100 μl of HNE (1 μM in PBS pH 7.5, 100 pmol) was added and the reaction mixture was shaken at ambient temperature while taking 20 μl of the mixture in 10 – 60 min steps for HPLC analysis. HNE was removed by precipitation in acidic milieu: the sample solution was given in 80 μl HCl (aq. 100 mM). An excess amount of DTT (solid) was added and the samples were heated at 90 °C for 1-2 min.

5.3.2 PHIP Experiments of SFTI Derivatives

NMR PHIP experiments were performed either on a 7 T *Bruker* AVANCE® III (300 MHz) or on an 11 T *Bruker* AVANCE® HD (OXFORD, 500 MHz) spectrometer. All probes were dissolved in the NMR solvents: Methanol-d_4, Ethanol-d_6 and D_2O (*Euriso-Top*). Para-hydrogen was enriched at liquid nitrogen temperature in a home-build apparatus which was described previously.[185]

All ALTADENA experiments were performed in the terrestrial magnetic field at ambient temperature in 5 mm “screw cap” NMR tubes equipped with a silicon rubber septum. 2.5 μmol of the catalyst and 50 μmol of the Fmoc-L-Pra-OH, Fmoc-L-Tyr(*O*-propargyl)-OH and 4-pentynoic acid or 2.5 μmol of SFTI derivative **5** - **13** (respective to the amount of C-C triple bonds in the sample) were dissolved in 600 μL NMR solvent. The NMR tube was sealed and para-enriched H_2 gas was filled into the sample tube through the septum with a pressure of 2 bar. Subsequently, the sample was vigorously shaken for a short time, placed into the measuring chamber of the spectrometer, and a standard PHIP sequence (i.e. signal acquisition after a 45° pulse) was applied for irradiation. All PHIP spectra have been recorded as “single-shot experiments”, performing one scan. Full relaxation of the polarized protons products was observed at least 2 minutes after the hydrogenation normally recorded with 256 scans. Additional PHIP experiments employing peptide 7 were performed at 333K in D_2O-methanol-d_4 and D_2O-ethanol-d_6 mixture (both 1:1, v/v).

Signal enhancements (SE) were calculated from the normalized integrals of the respective signal after deconvolution using the implemented line fitting function in MestReNova 8. SE was estimated as the quotient of the integral for the polarized signals during PHIP experiments (Int (PHIP)) and the integral for the hydrogenation product at thermal equilibrium (Int (therm.)) using following equation:

$$SE \approx \frac{Int\,(PHIP)}{Int\,(therm.)} \tag{13}$$

Int (PHIP) was determined as the sum of the absolute values each of the emission and absorption area of the antiphase signals since the integral sum of the antiphase signals is equal to zero., Further information about determination and calculation of SE can be found in the recently published protocol.[50b] All PHIP experiments were performed by Grit Sauer and Dr. Marco Körner (Prof. Buntkowsky group).

5.3.2.1 Determination of T_1 Relaxation Times

Determination of T_1 times of the hydrogenation products were performed by the inversion recovery method at 500 MHz. T_1 of Fmoc-L-allylglycine, Fmoc-L-Tyr(All)-OH and 4-Pentenoic acid, were determined using commercially available substances purchased from *PolyPeptide* and *Sigma Aldrich*. T_1 time of the hydrogenation product of peptide **7** was calculated from measurement of peptide [Tyr(*O*-allyl)[1]]SFTI-1[1,14] (**13**). T_1 time of the hydrogenation product of peptide **8** was calculated from measurement of peptide [4-Pentenoic acid[1]]SFTI-1[1,14] (**14**). T_1 (H^a/H^b) represents the average relaxation time of the H^a-H^b spin system. As previously mentioned, a distinction of respective proton signals was not possible. All T_1 determination experiments were performed by Grit Sauer and Dr. Marco Körner (Prof. Buntkowsky group).

5.3.3 Strain-Promoted Cycloaddition and Nucleobase Cross-Conjugation

All strain-promoted cycloadditions were referred to modifications of reported protocols.[172-173] In general, the test reactions were performed in degassed NH_4OAc buffer (0.1 M, pH 6.5 or pH 6.0). In special cases, HEPES buffer (0.1 M, pH 6.0), NaOAc buffer (0.1 M, pH 5.0), and PBS (1×, pH 7.5) were also applied as solvent. All coiled coil and PNA-peptide hybrids were applied as 1 mM or 0.5 mM stock solutions in H_2O. All reactions were monitored *via* direct injection of the reaction mixture in LC-MS equipped with a C18 RP column or RP-HPLC and the collected fraction were analyzed by ESI-MS. For SPANC, *in situ* oxidation of side chain-coupled Ser and the application of pre-oxidized and isolated aldehyde-bearing guiding units were tried, both. The amount and equivalents of reactants, the timing and order of their addition, reaction temperature, hybridization time of the guiding units and batch size were varied

5.3.3.1 SPANC: Coiled-Coil Guiding Units

Setup 1: 150 µl of **16** (0.5 mM in H_2O, 75 nmol) and 150 µl of **17** (0.5 mM in H_2O/DMSO, 2:3, v/v, 75 nmol) were mixed and diluted with NH_4OAc buffer (0.1 M, pH 6.5) and DMSO (3:5, v/v) to a total volume of 580 µl. The mixture was shaken for 1 h at ambient temperature. 10 µl of *p*-anisidine (37.5 mM in MeCN, 375 nmol) was added and the resulting mixture was shaken for another 10 min. After addition of 10 µl of MeNOH·HCl (9 mM in NH_4OAc buffer, 90 nmol), the reaction mixture was shaken at ambient temperature, while monitoring the reaction progress *via* analytical HPLC. After a reaction time of 4 h, 74.1 % conversion regarding **17** was obtained.
Setup 2: 10 µl of **18** (1 mM in H_2O, 10 nmol) and 10 µl of **19** (1 mM in H_2O, 10 nmol) were mixed and diluted with NH_4OAc buffer (0.1 M, pH 6.5) to a total volume of 180 µl. The mixture was shaken for 1 h at ambient temperature. 10 µl of *p*-anisidine (5 mM in MeCN, 50 nmol) was added and the resulting mixture was shaken for another 10 min. After addition of 10 µl of MeNOH·HCl (1.2 mM in NH_4OAc buffer, 12 nmol), the reaction mixture was

shaken at ambient temperature, while monitoring the reaction progress *via* LC-MS equipped with a C18-RP column. Reactant conversion was not able to calculate for this setup.

Setup 3: 10 μl of **18** (1 mM in H_2O, 10 nmol) and 20 μl of **19** (0.5 mM in H_2O, 10 nmol) were mixed and diluted with NH_4OAc buffer (0.1 M, pH 6.5) to a total volume of 180 μl. The mixture was shaken for 1 h at ambient temperature. 10 μl of *p*-anisidine (5 mM in MeCN, 50 nmol) was added and the resulting mixture was shaken for another 10 min. After addition of 10 μl of MeNOH·HCl (4.8 mM in NH_4OAc buffer, 48 nmol), the reaction mixture was shaken at ambient temperature, while monitoring the reaction progress *via* LC-MS equipped with a C18-RP column. Reactant conversion was not able to calculate for this setup.

Setup 4: 10 μl of **18** (1 mM in H_2O, 10 nmol) and 20 μl of **19** (0.5 mM in H_2O, 10 nmol) were mixed and diluted with NH_4OAc buffer (0.1 M, pH 6.5) to a total volume of 180 μl. The mixture was shaken for 1 h at ambient temperature. 10 μl of *p*-anisidine (5 mM in MeCN, 50 nmol) was added and the resulting mixture was shaken for another 10 min. After addition of 10 μl of MeNOH·HCl (4.8 mM in NH_4OAc buffer, 48 nmol), the reaction mixture was shaken at ambient temperature, while monitoring the reaction progress *via* RP-HPLC and ESI-MS of the collected fractions. 69.8 % conversion regarding **19** was obtained within a reaction time of 3 h.

Setup 5: 10 μl of **18** (1 mM in H_2O, 10 nmol) and 20 μl of **19** (0.5 mM in H_2O, 10 nmol) were mixed and diluted with H_2O to a total volume of 180 μl. Further procedure was as same as described for setup 4. 61.2 % conversion regarding **19** was obtained within a reaction time of 2.5 h.

Setup 6: 10 μl of **18** (1 mM in H_2O, 10 nmol), 20 μl of **19** (0.5 mM in H_2O, 10 nmol), and 10 μl of benzaldehyde (purified *via* distillation, 1 mM in DMSO, 10 nmol) were mixed and diluted with NH_4OAc buffer (0.1 M, pH 6.5) to a total volume of 180 μl. Further procedure was as same as described for Setup 4. 80.0 % conversion regarding **19** was obtained within a reaction time of 4 h.

Setup 7: 20 μl of **18** (1 mM in H_2O, 20 nmol), 40 μl of **19** (0.5 mM in H_2O, 30 nmol), and 10 μl of benzaldehyde (purified *via* distillation, 2 mM in MeCN, 20 nmol) were mixed and diluted with NH_4OAc buffer (0.1 M, pH 6.5) to a total volume of 180 μl. The mixture was shaken for 1 h at ambient temperature. 10 μl of *p*-anisidine (8 mM in MeCN, 80 nmol) was added and the resulting mixture was shaken for another 10 min. After addition of 10 μl of MeNOH·HCl (9.6 mM in NH_4OAc buffer, 96 nmol), the reaction mixture was shaken at ambient temperature, while monitoring the reaction progress *via* RP-HPLC and ESI-MS of the collected fractions. 71.5 % conversion regarding **19** was obtained within a reaction time of 3 h.

Setup 8: 30 μl of **18** (1 mM in H_2O, 30 nmol), 60 μl of **19** (0.5 mM in H_2O, 30 nmol), and 10 μl of benzaldehyde (purified *via* distillation, 3 mM in MeCN, 30 nmol) were mixed and diluted with NH_4OAc buffer (0.1 M, pH 6.5) to a total volume of 180 μl. The mixture was shaken for 1 h at ambient temperature. 10 μl of *p*-anisidine (6 mM in MeCN, 60 nmol) was added and the resulting mixture was shaken for another 10 min. After addition of 10 μl of MeNOH·HCl (7.2 mM in NH_4OAc buffer, 72 nmol), the reaction mixture was shaken at ambient temperature, while monitoring the reaction progress *via* RP-HPLC and ESI-MS of the collected fractions. 81.5 % overall conversion regarding **19** was obtained.

Setup 9: 20 μl of **18** (1 mM in H_2O, 20 nmol) and 10 μl of benzaldehyde (purified *via* distillation, 20 mM in DMSO, 200 nmol) were mixed and diluted with NH_4OAc buffer (0.1 M,

pH 6.5) to a total volume of 170 μl. The mixture was shaken for 1 h at ambient temperature. 20 μl of *p*-anisidine (50 mM in MeCN, 1000 nmol) was added and the resulting mixture was shaken for another 10 min. After addition of 10 μl of MeNOH·HCl (20 mM in NH_4OAc buffer, 200 nmol), the reaction mixture was shaken at ambient temperature, while monitoring the reaction progress *via* RP-HPLC and ESI-MS of the collected fractions. 50.1 % conversion regarding **18** was obtained within a reaction time of 2 h.

Setup 10: 10 μl of **18** (1 mM in H_2O, 10 nmol) was mixed with 10 μl of *p*-anisidine (50 mM in MeCN, 500 nmol) and diluted with NH_4OAc buffer (0.1 M, pH 6.5) to a total volume of 90 μl. The mixture was shaken for 1 h at ambient temperature. After addition of 10 μl of MeNOH·HCl (20 mM in NH_4OAc buffer, 200 nmol), the reaction mixture was shaken at ambient temperature, while monitoring the reaction progress *via* RP-HPLC and ESI-MS of the collected fractions.

Setup 11: 20 μl of **18** (1 mM in H_2O, 20 nmol), 40 μl of **19** (0.5 mM in H_2O, 20 nmol), and 20 μl of **32** (1 mM in H_2O, 20 nmol) were mixed and diluted with NH_4OAc buffer (0.1 M, pH 6.5) to a total volume of 180 μl. The mixture was shaken for 1 h at ambient temperature. 10 μl of *p*-anisidine (4 mM in MeCN, 40 nmol) was added and the resulting mixture was shaken for another 10 min. After addition of 10 μl of MeNOH·HCl (8 mM in NH_4OAc buffer, 80 nmol), the reaction mixture was shaken at ambient temperature, while monitoring the reaction progress *via* RP-HPLC and ESI-MS of the collected fractions. 89.2 % conversion regarding **19** was obtained within a reaction time of 6 h.

Setup 12: 20 μl of **18** (1 mM in H_2O, 20 nmol) and 20 μl of **32** (1 mM in H_2O, 20 nmol) were mixed and diluted with NH_4OAc buffer (0.1 M, pH 6.5) to a total volume of 180 μl. The mixture was shaken for 1 h at ambient temperature. 10 μl of *p*-anisidine (4 mM in MeCN, 40 nmol) was added and the resulting mixture was shaken for another 10 min. After addition of 10 μl of MeNOH·HCl (8 mM in NH_4OAc buffer, 80 nmol), the reaction mixture was shaken at ambient temperature, while monitoring the reaction progress *via* RP-HPLC and ESI-MS of the collected fractions. 60.2 % overall conversion regarding **32** was obtained.

Setup 13: 40 μl of **19'** (0.5 mM in H_2O, 20 nmol) were diluted with 90 μl NH_4OAc buffer (0.1 M, pH 6.5). 11 μl $NaIO_4$ (2 mM in NH_4OAc buffer, 22 nmol) was added to the solution at 4 °C and the resulting mixture was shaken for 30 min at 4 °C. 10 μl of 4-methoxythiophenol (40 mM in MeCN, 400 nmol) was carefully added while shaking at ambient temperature. After 15 min shaking, 20 μl of **18** (1 mM in H_2O, 20 nmol) was added and the mixture was shaken for another 1 h. After addition of 10 μl *p*-anisidine (4 mM in MeCN, 40 nmol) and 10 μl MeNOH·HCl (4 mM in NH_4OAc buffer, 40 nmol), the reaction mixture was shaken at ambient temperature, while monitoring the reaction progress *via* RP-HPLC and ESI-MS of the collected fractions. 72.2 % overall conversion related to **19** was obtained.

5.3.3.2 SPANC: PNA Guiding Units

Setup 1: 30 μl of **20** (1 mM in H_2O, 30 nmol) and 30 μl of **21** (1 mM in H_2O, 30 nmol) were mixed and diluted with NH_4OAc buffer (0.1 M, pH 6.5 or pH 6.0) to a total volume of 135 μl. The mixture was shaken for 1 h at ambient temperature. 10 μl of *p*-anisidine (2 mM in MeCN, 50 nmol) was added and the resulting mixture was shaken for another 10 min. After addition of 5 μl of MeNOH·HCl (10 mM in NH_4OAc buffer, 50 nmol), the reaction mixture was shaken

at ambient temperature, while monitoring the reaction progress *via* analytical HPLC. After a reaction time of 6 h, the mixture was lyophilized over night, dissolved in 60 µl H_2O and analyzed *via* HPLC and ESI-MS. 70.5 % conversion regarding **21** was obtained.

Setup 2: 20 µl of **20** (1 mM in H_2O, 20 nmol) and 15 µl of **21** (1 mM in H_2O, 15 nmol) were mixed and diluted with NH_4OAc buffer (0.1 M, pH 6.5) to a total volume of 140 µl. The mixture was shaken for 1 h at ambient temperature. 10 µl of MeNOH·HCl (10 mM in NH_4OAc buffer, 100 nmol) was added and the reaction mixture was shaken at ambient temperature, while monitoring the reaction progress *via* analytical HPLC. After a reaction time of 5 h, the mixture was lyophilized over night, dissolved in 60 µl H_2O and analyzed *via* HPLC and ESI-MS. 52.0 % conversion regarding **21** was obtained.

Setup 3: 20 µl of **20** (1 mM in H_2O, 20 nmol) and 15 µl of **21** (1 mM in H_2O, 15 nmol) were mixed and diluted with NH_4OAc buffer (0.1 M, pH 6.5) to a total volume of 135 µl. The mixture was shaken for 1 h at ambient temperature. 10 µl of *p*-anisidine (2 mM in MeCN, 50 nmol) was added and the resulting mixture was shaken for another 10 min. After addition of 5 µl of MeNOH·HCl (10 mM in NH_4OAc buffer, 50 nmol), the reaction mixture was shaken at ambient temperature, while monitoring the reaction progress *via* analytical HPLC. After a reaction time of 2 h, the mixture was lyophilized over night, dissolved in 60 µl H_2O and analyzed *via* HPLC and ESI-MS. 57.1 % conversion regarding **21** was obtained.

Setup 4: 20 µl of **20** (1 mM in H_2O, 20 nmol) and 15 µl of **21** (1 mM in H_2O, 15 nmol) were mixed and diluted with HEPES buffer (0.1 M, pH 6.0) to a total volume of 135 µl. The mixture was shaken for 1 h at ambient temperature. 10 µl of *p*-anisidine (5 mM in MeCN, 50 nmol) was added and the resulting mixture was shaken for another 10 min. After addition of 5 µl of MeNOH·HCl (10 mM in HEPES buffer, 50 nmol), the reaction mixture was shaken at ambient temperature, while monitoring the reaction progress *via* analytical HPLC. After a reaction time of 2.5 h, the mixture was lyophilized over night, dissolved in 60 µl H_2O and analyzed *via* HPLC and ESI-MS. 66.1 % conversion regarding **21** was obtained.

Setup 5: 100 µl of **20** (1 mM in H_2O, 100 nmol) and 100 µl of **21** (1 mM in H_2O, 100 nmol) were mixed and diluted with NH_4OAc buffer (0.1 M, pH 6.0) to a total volume of 1440 µl. The mixture was shaken for 1 h at ambient temperature. 10 µl of *p*-anisidine (50 mM in MeCN, 500 nmol) was added and the resulting mixture was shaken for another 10 min. 10×5 µl of MeNOH·HCl (10 mM in NH_4OAc buffer, 10×50 nmol) was added to the mixture in 20 min steps while shaking at ambient temperature. The reaction progress was monitored *via* analytical HPLC and ESI-MS. 75.1 % overall conversion related to **21** was obtained.

Setup 6: 100 µl of **20** (1 mM in H_2O, 100 nmol) and 100 µl of **21** (1 mM in H_2O, 100 nmol) were mixed and diluted with NH_4OAc buffer (0.1 M, pH 6.0) to a total volume of 1475 µl. The mixture was shaken for 1 h at 4 °C. 10 µl of *p*-anisidine (50 mM in MeCN, 500 nmol) was added and the resulting mixture was shaken for another 10 min. 3×5 µl of MeNOH·HCl (10 mM in NH_4OAc buffer, 3×50 nmol) was added to the mixture in 20 min steps while shaking at 4 °C. The reaction progress was monitored *via* analytical HPLC and ESI-MS. After a reaction time of 6 h, the mixture was lyophilized over night, dissolved in 60 µl H_2O and analyzed *via* HPLC and ESI-MS. 75.9 % conversion regarding **21** was obtained.

Setup 7: 100 µl of **20** (1 mM in H_2O, 100 nmol) and 100 µl of **21** (1 mM in H_2O, 100 nmol) were diluted with 1275 µl NaOAc buffer (0.1 M, pH 5.0). 10 µl of *p*-anisidine (50 mM in MeCN, 500 nmol) was added and the resulting mixture was shaken for 60 min. 15 µl of MeNOH·HCl (10 mM in NaOAc buffer, 150 nmol) was added and the resulting reaction

mixture was shaken at 4 °C. The reaction progress was monitored *via* analytical HPLC and ESI-MS. The reaction progress was monitored *via* analytical HPLC and ESI-MS. After a reaction time of 7 h, the mixture was lyophilized over night, dissolved in 60 µl H_2O and analyzed *via* HPLC and ESI-MS. 55.6 % conversion regarding **21** was obtained.

Setup 8: 100 µl of **20** (1 mM in H_2O, 100 nmol) and 100 µl of **21** (1 mM in H_2O, 100 nmol) was diluted with 1275 µl PBS (137 mM NaCl, 2.7 mM KCl, 10.0 mM Na_2HPO_4, 1.76 mM KH_2PO_4, pH 7.4). 10 µl of *p*-anisidine (50 mM in MeCN, 500 nmol) was added and the resulting mixture was shaken for 60 min. 15 µl of MeNOH·HCl (10 mM in PBS, 150 nmol) was added and the mixture was shaken was shaken at 4 °C. The reaction progress was monitored *via* analytical HPLC and ESI-MS. 39.3 % overall conversion regarding **21** was obtained.

Setup 9: 120 µl of **20** (1 mM in H_2O, 120 nmol) and 100 µl of **21** (1 mM in H_2O, 100 nmol) were mixed and diluted with HEPES buffer (0.1 M, pH 6.0) to a total volume of 1440 µl. The mixture was shaken for 1 h at 4 °C. 10 µl of *p*-anisidine (50 mM in MeCN, 500 nmol) was added and the resulting mixture was shaken for another 10 min. 5×10 µl of MeNOH·HCl (10 mM in HEPES buffer, 5×100 nmol) was added to the mixture in 20 min steps while shaking at 4 °C. The reaction progress was monitored *via* analytical HPLC and ESI-MS. After a reaction time of 6 h, the mixture was lyophilized over night, dissolved in 60 µl H_2O and analyzed *via* HPLC and ESI-MS. 73.2 % conversion regarding **21** was obtained.

Setup 10: 100 µl of **20** (1 mM in H_2O, 100 nmol) was diluted with 240 µl HEPES buffer (0.1 M, pH 6.0). 20 µl of *p*-anisidine (50 mM in MeCN, 1 µmol) was added and the resulting mixture was shaken for 30 min. 10 µl of MeNOH·HCl (100 mM in HEPES buffer, 1 µmol) was added and the mixture was shaken for another 30 min. Subsequently, 100 µl of **21** (1 mM in H_2O, 100 nmol) was added and the resulting reaction mixture was shaken at 4 °C. The reaction progress was monitored *via* analytical HPLC and ESI-MS. 61.3 % conversion regarding **21** was obtained within a reaction time of 3 h.

Setup 11: 120 µl of **20** (1 mM in H_2O, 120 nmol) and 100 µl of **21** (1 mM in H_2O, 100 nmol) were mixed and diluted with NH_4OAc buffer (0.1 M, pH 6.5) to a total volume of 480 µl. The mixture was shaken for 1 h at 4 °C. 10 µl of *p*-anisidine (50 mM in THF, 500 nmol) was added and the resulting mixture was shaken for another 10 min. 10 µl of PhNOH (10 mM in NH_4OAc buffer, 100 nmol) was added to the mixture while shaking at 4 °C. The reaction progress was monitored *via* analytical HPLC and ESI-MS. After a reaction time of 3.5 h, the mixture was lyophilized over night, dissolved in 60 µl H_2O and analyzed *via* HPLC and ESI-MS. 50.9 % conversion regarding **21** was obtained.

Setup 12: 160 µl of **20** (1 mM in H_2O, 160 nmol) and 40 µl of **21** (1 mM in H_2O, 40 nmol) were mixed and diluted with NH_4OAc buffer (0.1 M, pH 6.5) and THF (5:4, v/v) to a total volume of 480 µl. The mixture was shaken for 1 h at 4 °C. 10 µl of *p*-anisidine (16 mM in THF, 160 nmol) was added and the resulting mixture was shaken for another 10 min. 10 µl of PhNOH·HCl (16 mM in NH_4OAc buffer, 100 nmol) was added to the mixture while shaking at 4 °C. The reaction progress was monitored *via* analytical HPLC and ESI-MS. 68.5 % overall conversion regarding **21** was obtained.

Setup 13: 20 µl of **20** (1 mM in H_2O, 20 nmol) and 20 µl of **21** (1 mM in H_2O, 20 nmol) were mixed and diluted with NH_4OAc buffer (0.1 M, pH 6.0) to a total volume of 93 µl. The mixture was shaken for 1 h at ambient temperature. 6 µl of *p*-anisidine (17 mM in THF, 100 nmol) was added and the resulting mixture was shaken for another 10 min. 1 µl of

MeNOH·HCl (100 mM in NH_4OAc buffer, 100 nmol) was added to the mixture while shaking at ambient temperature. The reaction progress was monitored *via* analytical HPLC and ESI-MS. 73.1 % conversion regarding **21** was obtained within a reaction time of 4.5 h.

Setup 14: 20 μl of **20** (1 mM in H_2O, 20 nmol), 20 μl of **21** (1 mM in H_2O, 20 nmol), and 20 μl of **22** (1 mM in H_2O, 20 nmol) were mixed and diluted with NH_4OAc buffer (0.1 M, pH 6.0) to a total volume of 193 μl. The mixture was shaken for 1 h at ambient temperature. 12 μl of *p*-anisidine (17 mM in THF, 200 nmol) was added and the resulting mixture was shaken for another 10 min. 2 μl of MeNOH·HCl (100 mM in NH_4OAc buffer, 200 nmol) was added to the mixture while shaking at ambient temperature. The reaction progress was monitored *via* analytical HPLC and ESI-MS. 54.0 % conversion regarding **21+22** was obtained within a reaction time of 3.5 h.

Setup 15: 20 μl of **21** (1 mM in H_2O, 20 nmol) were diluted with 130 μl NH_4OAc buffer (0.1 M, pH 6.5). 11 μl $NaIO_4$ (2 mM in NH_4OAc buffer, 22 nmol) was added to the solution at 4 °C and the resulting mixture was shaken for 30 min at 4 °C. 10 μl of 4-methoxythiophenol (40 mM in MeCN, 400 nmol) was carefully added while shaking at ambient temperature. After 15 min shaking, 20 μl of **21** (1 mM in H_2O, 20 nmol) was added and the mixture was shaken for another 1 h. After addition of 10 μl *p*-anisidine (4 mM in MeCN, 40 nmol) and 10 μl MeNOH·HCl (4 mM in NH_4OAc buffer, 40 nmol), the reaction mixture was shaken at ambient temperature while monitoring the reaction progress *via* RP-HPLC and ESI-MS of the collected fractions. 51.0 % conversion regarding **21** was obtained within a reaction time of 5 h.

Setup 16: 100 μl of **21** (1 mM in H_2O, 100 nmol) were diluted with 140 μl NH_4OAc buffer (0.1 M, pH 6.5). 50 μl $NaIO_4$ (2.2 mM in NH_4OAc buffer, 110 nmol) was added to the solution at 4 °C and the resulting mixture was shaken for 30 min at 4 °C. 50 μl of 4-methoxythiophenol (40 mM in MeCN, 2 μmol) was carefully added while shaking at ambient temperature. After 15 min shaking, 100 μl of **20** (1 mM in H_2O, 100 nmol) was added and the mixture was shaken for another 1 h. After addition of 10 μl *p*-anisidine (20 mM in MeCN, 200 nmol) and 50 μl MeNOH·HCl (2 mM in NH_4OAc buffer, 100 nmol), the reaction mixture was shaken at ambient temperature while monitoring the reaction progress *via* RP-HPLC and ESI-MS of the collected fractions. 51.9 % conversion regarding **21** was obtained within a reaction time of 7 h.

Setup 17: 100 μl of **21** (1 mM in H_2O, 100 nmol) were diluted with 240 μl 0.1 M NH_4OAc buffer/THF (7:5, v/v). 50 μl $NaIO_4$ (2.2 mM in NH_4OAc buffer, 110 nmol) was added to the solution at 4 °C and the resulting mixture was shaken for 30 min at 4 °C. 50 μl of 4-methoxythiophenol (40 mM in THF, 2 μmol) was carefully added while shaking at ambient temperature. After 15 min shaking, 100 μl of **20** (1 mM in H_2O, 100 nmol) was added and the mixture was shaken for another 1 h. After addition of 10 μl *p*-anisidine (20 mM in THF, 200 nmol) and 50 μl MeNOH·HCl (2 mM in NH_4OAc buffer, 100 nmol), the reaction mixture was shaken at ambient temperature while monitoring the reaction progress *via* RP-HPLC and ESI-MS of the collected fractions. 49.5 % overall conversion regarding **21** was obtained.

Setup 18: 100 μl of **21** (1 mM in H_2O, 100 nmol) were diluted with 240 μl 0.1 M NH_4OAc buffer/THF (7:5, v/v). 50 μl $NaIO_4$ (2.2 mM in NH_4OAc buffer, 110 nmol) was added to the solution at 4 °C and the resulting mixture was shaken for 30 min at 4 °C. 50 μl of ethylene glycol solution (20 mM in THF, 1 μmol) was carefully added while shaking at ambient

temperature. Further procedure is as same as described for setup x. 76.6 % overall conversion regarding **21** was obtained.

5.3.3.3 SPAAC: PNA Guiding Units

Setup 1: 30 μl of **20** (1 mM in H_2O, 30 nmol) and 40 μl of **23** (1 mM in H_2O, 40 nmol) were mixed and diluted with NH_4OAc buffer (0.1 M, pH 6.5) to a total volume of 500 μl. The mixture was shaken at ambient temperature and the reaction progress was monitored *via* analytical HPLC and ESI-MS. 54.4 % conversion regarding **23** was obtained within a reaction time of 6 h.
Setup 2: 100 μl of **20** (1 mM in H_2O, 100 nmol) and 100 μl of **23** (1 mM in H_2O, 100 nmol) were mixed and diluted with NH_4OAc buffer (0.1 M, pH 6.5) to a total volume of 300 μl. The mixture was shaken at ambient temperature and the reaction progress was monitored *via* analytical HPLC and ESI-MS. 28.1 % conversion regarding **23** was obtained within a reaction time of 3 h.

5.3.4 Psoralen Cross-Linkage

The psoralen cross-linking test reaction of PNA/DNA oligomers were referred to a modification of a reported protocol.[186] For UVA irradiation, an 8 W UV hand lamp with λ = 366 nm in distance of 5 – 10 cm to reaction tube surface was used. The irradiation was performed while cooling on ice without stirring. All reactions were monitored *via* direct injection of the reaction mixture in LC-MS equipped with a C18 RP column or RP-HPLC and the collected fraction were analyzed by ESI-MS.

5.3.4.1 PNA-PNA Cross-Linkage with Free Psoralen

50 μl of **20'** (1 mM in H_2O, 50 nmol) and 50 μl of **21'** (1 mM in H_2O, 50 nmol) were mixed and diluted with NH_4OAc buffer (0.1 M, pH 6.5) to a total volume of 450 μl. The mixture was shaken on ice for 1 h. After addition of 50 μl of psoralen (10 mM in DMSO, 500 nmol), the resulting mixture was shaken for another 10 min on ice and subsequently exposed to UVA irradiation in a darkened room. For monitoring the reaction progress, HPLC probes were taken from the reaction mixture in 15 or 30 min steps, respectively.

5.3.4.2 PNA-DNA Cross-Linkage with Psoralen-loaded PNA Guiding Unit

40 μl of **25** (1 mM in H_2O, 40 nmol) and 30 μl of **33** (1 mM in H_2O, 30 nmol) were mixed and diluted with Tris-HCl buffer (0.05 M, pH 7.5), NH_4OAc buffer (0.1 M, pH 6.5), or NaOAc buffer (0.1 M, pH 5.0) to a total volume of 300 μl. The resulting mixture was shaken for 1 h on ice and subsequently exposed to UVA irradiation in a darkened room. For monitoring the reaction progress, HPLC probes were taken from the reaction mixture in 15 or 30 min steps,

respectively. 99.1 % conversion regarding **25** was obtained within an irradiation time of 90 min.

5.3.4.3 PNA-PNA Cross-Linkage with Psoralen-loaded PNA Guiding Unit

40 μl of **25** (1 mM in H_2O, 40 nmol) and 30 μl of **26** (1 mM in H_2O, 30 nmol) were mixed and diluted with Tris-HCl buffer (0.05 M, pH 7.5), NH_4OAc buffer (0.1 M, pH 6.5), or NaOAc buffer (0.1 M, pH 5.0) to a total volume of 300 μl. The resulting mixture was shaken for 1 h on ice and subsequently exposed to UVA irradiation in a darkened room. For monitoring the reaction progress, HPLC probes were taken from the reaction mixture in 15 or 30 min steps, respectively.

5.3.5 Sortase-Mediated Ligation

PNA-Fc conjugates **34** and its derivatives were synthesized upon sortase A-mediated transpeptidation. An evolved permutant of sortase A (eSrtA) with improved catalytic activity was produced and purified as described by Chen et al.[176] 10 μM Fc fragment produced according a published protocol[171] were supplemented with 10 – 100 eq. (25 eq. for preparative batch) of PNA-peptide hybrids **27** - **30** in sortase reaction buffer (50 mM Tris, 150 mM NaCl, 5 mM $CaCl_2$, pH 7.5 adjusted with HCl). Reaction was initiated by addition of 10 μM eSrtA and incubated for 30 min at 22 °C. Controls included reactions without either Fc fragment, eSrtA, or counterparts **27** - **30**.

5.3.5.1 PAGE

Protein samples and Fc-PNA conjugate were analyzed by SDS-PAGE (15 %, w/v) under reducing conditions as described elsewhere.[187] Prior to electrophoresis, samples were supplemented with 5×sample buffer (250 mM Tris/HCl pH 8.0, 7.5 % SDS, 25 % glycerol, 0.25 mg/mL bromophenol blue, 12.5 % 2-mercaptoethanol) and heated to 95 °C for 10 min. For non-reducing gels sample buffer without 2-mercaptoethanol was used. Proteins conjugated with fluorescent dyes were visualized under UV-light. Protein bands were stained with Coomassie brilliant blue R-250 solution.

Reaction monitoring of PNA-guided ligation approaches (SPANC, SPAAC, psoralen cross-linkage) were tested by a SDS-PAGE with highly concentrated polyacrylamide gel (20 %, w/v). Same sample loading buffer was used as described for standard SDS-PAGE and sample preparation as well as experimental procedure were same as described above.

Further PNA-guided ligation approaches were tested in urea-PAGE using a modified version of a reported protocol.[174] Urea gels were prepared with 26 % (w/v) polyacrylamide and 1.6 % (w/v) bisacrylamide. In a typical experiment 7.4 g urea were dissolved in 10.3 ml of polyacrylamide (40 %, w/v) and 39 mg bisacrylamide was added. 925 μl glacial acetic acid and 50 μl concentrated aqueous ammonia were added and the volume was adjusted to 15 ml. After degassing under reduced pressure, the polymerization was initiated by the addition of

300 μl ammonium persulfate (aqueous, 10 %, w/v) and 90 μl tetramethylethylendiamine (TEMED). Resulting gels were pre-electrophoresed at a constant voltage of 10 V/cm for 4 – 5 h at ambient temperature. Electrophoresis running buffer consisted of 1 M acetic acid with 0.1 M glycine. Gel overlay buffer consisted of 8M urea, 10 % (w/v) PEG-8000, 1 M acetic acid, and 50 mM ammonium hydroxide. Samples were mixed prior to electrophoresis with an equivalent volume ($\sim$ 10 μl) of loading solution consisting of 1 % methylene blue, 5 % acetic acid and 8 M urea and heated at 90 °C for 1 – 2 min.

5.4 Enzyme Kinetic Assays

Kinetic curves were recorded by photometrical monitoring of protease-catalyzed hydrolysis of the corresponding chromogenic substrates in 96-well-plates (NUNC, round bottom, clear) at 405 nm in defined intervals at ambient temperature. All experiments were performed in triplicate.

5.4.1 Trypsin

Trypsin from bovine pancreas (*Sigma-Aldrich*) was standardized by active-site titration with *p*-nitrophenyl-*p*'-guanidinobenzoate (NPGB) in phosphate buffered saline (PBS: 137 mM NaCl, 2.7 mM KCl, 10.0 mM Na_2HPO_4, 1.76 mM KH_2PO_4, pH 7.4). The kinetic assays were performed in trypsin activity buffer (50 mM Tris/HCl, 150 mM NaCl, 0.01 % Triton X-100, 0.01 % sodium azide, pH 7.6), in non-buffered water (pH 6.9), or D_2O (pH/pD 7.4).

5.4.1.1 Determination of Michaelis-Menten Constant (K_M) for Boc-QAR-pNA

The initial reaction rate (v_i) of the proteolytic degradation of Boc-QAR-pNA (*Bachem*) by bovine trypsin (100 nM) was determined for a series of concentrations ($[S]_i$) of the chromogenic substrate. The Michaelis-Menten constant (K_M) was calculated *via* Hanes-Woolf plot (quotient of substrate concentration and initial reaction rate: $[S]_i/v_i$ against the substrate concentration $[S]_i$) and linear regression of the resulting data. K_M was determined as 58.89$\pm$7.34 μM for this system in trypsin activity buffer, 114.27$\pm$27.36 μM for non-buffered water and 51.27$\pm$18.32 μM for non-buffered D_2O (arithmetic mean, standard deviation given as error).

5.4.1.2 Determination of Apparent Inhibition Constant (K_i^{app}) of Trypsin Inhibitors 5 – 13

The normalized residual trypsin reaction ratio (v/v_0) towards the chromogenic substrate Boc-QAR-pNA at different concentrations of the synthesized trypsin inhibitors was determined at a constant concentration of trypsin (E_0 = 0.9 nM) and substrate (S_0 = 0.25 mM). The apparent inhibition constants (K_i^{app}) were calculated by fitting the Morrison equation for tight-

binding inhibitors (14) onto the resulting kinetic data with the Marquardt-Levenberg algorithm of SigmaPlot 11®.

$$\frac{v}{v_0} = 1 - \frac{(E_0+I_0+K_i^{app}) - \sqrt{(E_0+I_0+K_i^{app})-4E_0I_0}}{2E_0} \tag{14}$$

5.4.1.3 Calculation of Substrate-Independent Inhibition Constant (K_i) of Trypsin Inhibitors 5 – 13

Substrate-independent inhibition constant K_i was calculated from K_i^{app} and K_M using the equation 15 (with S_0 ≡ concentration of chromogenic substrate Boc-QAR-*p*NA used for K_i^{app} determination).

$$K_i = \frac{K_i^{app}}{\left(1+\frac{S_0}{K_M}\right)} \tag{15}$$

The error of K_i (ΔK_i) was calculated by propagation of errors of K_i^{app} and K_M using the following approach:

$$\rightarrow \Delta K_i{}^2 = \left|\frac{\partial K_i}{\partial K_i^{app}}\right|^2 \cdot \left(\Delta K_i^{app}\right)^2 + \left|\frac{\partial K_i}{\partial K_M}\right|^2 \cdot (\Delta K_M)^2$$

$$\rightarrow \Delta K_i = \sqrt{\left|\frac{\partial K_i}{\partial K_i^{app}}\right|^2 \cdot \left(\Delta K_i^{app}\right)^2 + \left|\frac{\partial K_i}{\partial K_M}\right|^2 \cdot (\Delta K_M)^2}$$

Differentiation of K_i with respect to K_i^{app} yields:

$$\rightarrow \frac{\partial K_i}{\partial K_i^{app}} = \frac{1}{\left(1+\frac{S_0}{K_M}\right)}$$

Differentiation of K_i with respect to K_M:

using $K_i = K_i^{app}\left(1+\frac{S_0}{K_M}\right)^{-1}$ and chain rule for differentiation yields:

$\frac{\partial K_i}{\partial K_M} = \left(-\frac{K_i^{app}}{\left(1+\frac{[S]}{K_M}\right)^2}\right)\cdot\left(-\frac{S_0}{K_M{}^2}\right)$ and thus:

$$\rightarrow \frac{\partial K_i}{\partial K_M} = \frac{K_i^{app}\cdot S_0}{\left(1+\frac{[S]}{K_M}\right)^2 \cdot (K_M)^2}$$

Combination of respective equations gives the final formula for calculating the error of K_i:

$$\rightarrow \Delta K_i = \sqrt{\left(\frac{1}{\left(1+\frac{S_0}{K_M}\right)}\right)^2 \cdot \left(\Delta K_i^{app}\right)^2 + \left(\frac{K_i^{app}\cdot[S]}{\left(1+\frac{S_0}{K_M}\right)^2\cdot(K_M)^2}\right)^2 \cdot (\Delta K_M)^2} \tag{16}$$

5.4.2 Chymotrypsin

Chymotrypsin from bovine pancreas (*Sigma-Aldrich*) was standardized by active-site titration with *p*-nitrophenylacetate (NPA) and dissolved in NaOAc (100 mM, pH 5.0) and diluted with 2.5 mM HCl with 0.05 % triton X-100. The kinetic assays were performed in chymotrypsin activity buffer (100 mM Tris/HCl, 20 mM $CaCl_2$, 0.05 % Triton X-100, pH 7.8). As chromogenic substrate Suc-AAPF-pNA (*Sigma-Aldrich*) with a reported K_M of 60.0±7.0 μM for this system was used.[151]

5.4.2.1 Determination of K_i^{app} and the K_i of the Chymotrypsin Inhibitor 1

The normalized residual chymotrypsin reaction ratio (v/v_0) towards the chromogenic substrate Suc-AAPF-pNA at different concentrations of **1** was determined at a constant concentration of chymotrypsin (E_0 = 0.8 nM) and substrate (S_0 = 0.25 mM, in 70 % DMF). K_i^{app} and K_i were calculated as described for the trypsin inhibitors (5.4.1.2 and 5.4.1.3).

5.4.3 Elastase

Human neutrophil elastase (HNE, *Serva Electrophoresis*) was standardized by active-site titration with *p*-nitrophenylacetate (NPA) and dissolved in PBS (137 mM NaCl, 2.7 mM KCl, 10.0 mM Na_2HPO_4, 1.76 mM KH_2PO_4, pH 7.4). The kinetic assays were performed in elastase activity buffer (100 mM Tris/HCl, 20 mM $CaCl_2$, 500 mM NaCl, 0.005 % Triton X-100, pH 7.8).

5.4.3.1 Determination of K_M for MeO-Suc-AAPV-pNA

v_i of the proteolytic degradation of MeO-Suc-AAPV-pNA (*Sigma-Aldrich*) by HNE (100 nM) was determined for a series of concentrations ($[S]_i$) of the chromogenic substrate. The experimental procedure and data processing was performed as described for trypsin (5.4.1.1). K_M was determined as 47.7±5.8 μM for this system.

5.4.3.2 Determination of K_i^{app} and the Substrate K_i of the Elastase Inhibitor 2-4

The normalized residual HNE reaction ratio (v/v_0) towards the chromogenic substrate Suc-AAPV-pNA at different concentrations of the synthesized elastase inhibitors **2** – **4** were determined at a constant concentration of HNE (E_0 = 10 nM) and substrate (S_0 = 0.25 mM, in 70 % DMF). K_i^{app} and K_i were calculated as described for the trypsin inhibitors (chapters 5.4.1.2 and 5.4.1.3).

5.5 *In Silico* Modeling

All 3D computational models of synthesized or only designed compounds were derived from the crystal structure or NMR structure of the parental peptides, proteins, or protein-ligand co-complexes. PDB numbers of parental structures are given in the main text or in figure descriptions. 3D modeling and all *in silico* experiments were realized with the YASARA® structure package applying the YASARA 2 force field.[188] After modeling of the designed structure using the "build" function of respective software, each structure was energy minimized individually or as co-complex with its target enzyme, first *in vacuo*, then in 0.9 M NaCl (aq.) at pH 7.4 and 298.16 K. Generally, the simulation cell was set with the distance of 5 Å around all atoms of the inhibitor structure, thus only the binding region of enzymes was included to the simulation when simulating an enzyme-inhibitor co-complex.
For alignment and superposition of the energy minimized structures, the multiple structural alignment algorithm MUSTANG were applied, normally on the backbone structure of modeled peptides and proteins. Thereby, the flipping of side chains was allowed to minimize RMSD values. Alternations from this general protocol are mentioned in the main text or in the figure descriptions. All graphics were rendered with POVRay$_{TM}$. In few cased, the resulted image was post-processed with a graphical tools as Adobe® Photoshop® for better presentation (schemes, concept sketches, etc).

6 References

[1] R. N. Young, *Pure Appl. Chem.* **1999**, *71*, 1655-1661.

[2] a) P. Li, S. Jiang, S.-L. Lee, C. Y. Lin, M. D. Johnson, R. B. Dickson, C. J. Michejda, P. P. Roller, *J. Med. Chem.* **2007**, *50*, 5976-5983; b) J. Fan, I. A. M. de Lannoy, *Biochem. Pharmacol.* **2014**, *87*, 93-120; c) H. van de Waterbeemd, E. Gifford, *Nat Rev Drug Discov* **2003**, *2*, 192-204; d) L. D. E. H. Kerns, *Drug-like Properties: Concepts, Structure Design and Methods*, Elsavier, UK, **2008**; e) V. Frecer, F. Berti, F. Benedetti, S. Miertus, *Journal of Molecular Graphics and Modelling* **2008**, *27*, 376-387.

[3] G. E. Means, R. E. Feeney, *Bioconjugate Chem.* **1990**, *1*, 2-12.

[4] a) D. H. Spackman, W. H. Stein, S. Moore, *Anal. Chem.* **1958**, *30*, 1190-1206; b) W. H. S. S. Moore, *Methods Enzymol.* **1963**, *6*, 819-831.

[5] a) O. Vesterberg, *J Chromatogr A* **1989**, *480*, 3-19; b) T. Keough, M. P. Lacey, G. M. Trakshel, T. N. Asquith, *Int. J. Mass Spectrom. Ion Processes* **1997**, *169–170*, 201-215.

[6] L. Wofsy, H. Metzger, S. J. Singer, *Biochemistry* **1962**, *1*, 1031-1039.

[7] G. Schoellmann, E. Shaw, *Biochemistry* **1963**, *2*, 252-255.

[8] a) W. M. Hunter, F. C. Greenwood, *Nature* **1962**, *194*, 495-496; b) M. Morrison, *Methods Enzymol.* **1970**, *17*, 653-664; c) H. J. Sinn, H. H. Schrenk, E. A. Friedrich, D. P. Via, H. A. Dresel, *Anal. Biochem.* **1988**, *170*, 186-192.

[9] a) T. B. Rogers, T. Boerresen, R. E. Feeney, *Biochemistry* **1978**, *17*, 1105-1109; b) J. F. Riordan, *Biochemistry* **1973**, *12*, 3915-3923; c) R. B. Yamasaki, A. Vega, R. E. Feeney, *Anal. Biochem.* **1980**, *109*, 32-40.

[10] a) G. D. Markham, C. Satishchandran, *J. Biol. Chem.* **1988**, *263*, 8666-8670; b) A. M. Crestfield, S. Moore, W. H. Stein, *J. Biol. Chem.* **1963**, *238*, 622-627.

[11] H. C. Kolb, M. G. Finn, K. B. Sharpless, *Angewandte Chemie International Edition* **2001**, *40*, 2004-2021.

[12] R. B. Merrifield, *J. Am. Chem. Soc.* **1963**, *85*, 2149-2154.

[13] a) M. Mutter, S. Vuilleumier, *Angewandte Chemie International Edition in English* **1989**, *28*, 535-554; b) V. Aucagne, I. E. Valverde, P. Marceau, M. Galibert, N. Dendane, A. F. Delmas, *Angewandte Chemie International Edition* **2012**, *51*, 11320-11324.

[14] a) M. Tischler, D. Nasu, M. Empting, S. Schmelz, D. W. Heinz, P. Rottmann, H. Kolmar, G. Buntkowsky, D. Tietze, O. Avrutina, *Angew. Chem., Int. Ed.* **2012**, *51*, 3708-3712; b) M. Cristau, C. Devin, C. Oiry, O. Chaloin, M. Amblard, N. Bernad, A. Heitz, J.-A. Fehrentz, J. Martinez, *J. Med. Chem.* **2000**, *43*, 2356-2361.

[15] T. Takenaka, *BJU Int* **2001**, *88*, 7-10.

[16] C. You, Y. H. Percival Zhang, *Anal. Biochem.* **2012**, *428*, 7-12.

[17] S. Mandal, M. n. Moudgil, S. K. Mandal, *Eur. J. Pharmacol.* **2009**, *625*, 90-100.

[18] S. Yurtkuran, G. Kırlı, Y. Taneli, *Procedia - Social and Behavioral Sciences* **2013**, *89*, 633-639.

[19] Y. Bar-Cohen, *Biomimetics: Nature-Based Innovation*, CRC Press, USA, **2011**.

[20] A. Grauer, B. König, *Eur. J. Org. Chem.* **2009**, *2009*, 5099-5111.

[21] R. Kharb, R. Rana, P. C. Sharma, M. S. Yar, *J. Chem. Pharm. Res.* **2011**, *3*, 173-186.

[22] D. J. Abraham, *Burger's Medicinal Chemistry and Drug Discovery, 6th edition, Vol. 1*, John Wiley and Sons, England, **2003**.

[23] a) K. M. Yamada, S. S. Yamada, I. Pastan, *Proc. Natl. Acad. Sci. U. S. A.* **1976**, *73*, 1217-1221; b) S. E. D'Souza, M. H. Ginsberg, E. F. Plow, *Trends Biochem. Sci.* **1991**, *16*, 246-250.

[24] S. Kagami, S. Kondo, M. Urushihara, K. Loster, W. Reutter, T. Saijo, A. Kitamura, S. Kobayashi, Y. Kuroda, *Kidney Int* **2000**, *58*, 1088-1097.

[25] a) M. J. Fisher, B. Gunn, C. S. Harms, A. D. Kline, J. T. Mullaney, A. Nunes, R. M. Scarborough, A. E. Arfsten, M. A. Skelton, S. L. Um, B. G. Utterback, J. A. Jakubowski, *J. Med. Chem.* **1997**, *40*, 2085-2101; b) V. Rerat, G. Dive, A. A. Cordi, G. C. Tucker, R. Bareille, J. Amédée, L. Bordenave, J. Marchand-Brynaert, *J. Med. Chem.* **2009**, *52*, 7029-7043.
[26] R. M. Keenan, W. H. Miller, C. Kwon, F. E. Ali, J. F. Callahan, R. R. Calvo, S.-M. Hwang, K. D. Kopple, C. E. Peishoff, J. M. Samanen, A. S. Wong, C.-K. Yuan, W. F. Huffman, *J. Med. Chem.* **1997**, *40*, 2289-2292.
[27] P. N. Aarsen, *Br. J. Pharmacol.* **1977**, *61*, 523-532.
[28] C. G. Smith, J. R. Vane, *The FASEB Journal* **2003**, *17*, 788-789.
[29] P. E. Nielsen, *Pseudo-peptides in Drug Discovery, Vol. 1*, John Wiley & Sons, England, **2006**.
[30] H. C. Kolb, K. B. Sharpless, *Drug Discov Today* **2003**, *8*, 1128-1137.
[31] I. E. Valverde, A. Bauman, C. A. Kluba, S. Vomstein, M. A. Walter, T. L. Mindt, *Angewandte Chemie International Edition* **2013**, *52*, 8957-8960.
[32] N. Terasaka, H. Suga, *Chem. Lett.* **2014**, *43*, 11-19.
[33] a) X. Wu, J. L. Stockdill, P. Wang, S. J. Danishefsky, *J. Am. Chem. Soc.* **2010**, *132*, 4098-4100; b) R. M. Wenger, *Angewandte Chemie International Edition in English* **1985**, *24*, 77-85.
[34] J. Dittmann, R. M. Wenger, H. Kleinkauf, A. Lawen, *J. Biol. Chem.* **1994**, *269*, 2841-2846.
[35] a) H. Neumann, *FEBS Lett.* **2012**, *586*, 2057-2064; b) L. Davis, J. W. Chin, *Nat Rev Mol Cell Biol* **2012**, *13*, 168-182.
[36] S. Roosenburg, P. Laverman, L. Joosten, M. S. Cooper, P. K. Kolenc-Peitl, J. M. Foster, C. Hudson, J. Leyton, J. Burnet, W. J. G. Oyen, P. J. Blower, S. J. Mather, O. C. Boerman, J. K. Sosabowski, *Mol. Pharm.* **2014**, *11*, 3930-3937.
[37] N. C. Gassner, B. W. Matthews, *Acta Crystallographica Section D* **1999**, *55*, 1967-1970.
[38] D. E. Milenic, E. D. Brady, M. W. Brechbiel, *Nat Rev Drug Discov* **2004**, *3*, 488-499.
[39] M. Mitsunaga, M. Ogawa, N. Kosaka, L. T. Rosenblum, P. L. Choyke, H. Kobayashi, *Nat Med* **2011**, *17*, 1685-1691.
[40] M. Kainosho, T. Torizawa, Y. Iwashita, T. Terauchi, A. Mei Ono, P. Güntert, *Nature* **2006**, *440*, 52-57.
[41] M. Sastry, C. Bewley, P. Kwong, in *Isotope labeling in Biomolecular NMR, Vol. 992* (Ed.: H. S. Atreya), Springer Netherlands, **2012**, pp. 197-211.
[42] F. Castellani, B. van Rossum, A. Diehl, M. Schubert, K. Rehbein, H. Oschkinat, *Nature* **2002**, *420*, 98-102.
[43] G. S. Rule, T. K. Hitchens, *Fundamentals of Protein NMR Spectroscopy, Vol. 1*, Springer Science & Business Media, Netherlands, **2006**.
[44] L. Frydman, *Nat Chem* **2009**, *1*, 176-178.
[45] R. A. de Graaf, *In Vivo NMR Spectroscopy: Principles and Techniques, Vol. 1*, John Wiley & Sons, England, **2013**.
[46] a) A. Kastler, *J. Phys. Radium* **1950**, *11*, 255-265; b) M. A. Bouchiat, T. R. Carver, C. M. Varnum, *Phys. Rev. Lett.* **1960**, *5*, 373-375.
[47] F. D. Colegrove, P. A. Franken, *Physical Review* **1960**, *119*, 680-690.
[48] A. Abragam, M. Goldman, *Reports on Progress in Physics* **1978**, *41*, 395.
[49] R. Graf, M. R. Hansen, D. Hinderberger, K. Muennemann, H. W. Spiess, *Phys. Chem. Chem. Phys.* **2014**, *16*, 9700-9712.
[50] a) W. S. Warren, E. Jenista, R. T. Branca, X. Chen, *Science* **2009**, *323*, 1711-1714; b) G. Sauer, D. Nasu, D. Tietze, T. Gutmann, S. Englert, O. Avrutina, H. Kolmar, G. Buntkowsky, *Angewandte Chemie International Edition* **2014**, *53*, 12941-12945.
[51] C. R. Bowers, D. P. Weitekamp, *Phys. Rev. Lett.* **1986**, *57*, 2645-2648.

[52] C. R. Bowers, D. P. Weitekamp, *J. Am. Chem. Soc.* **1987**, *109*, 5541-5542.
[53] J. Natterer, J. Bargon, *Prog. Nucl. Magn. Reson. Spectrosc.* **1997**, *31*, 293-315.
[54] T. C. Eisenschmid, R. U. Kirss, P. P. Deutsch, S. I. Hommeltoft, R. Eisenberg, J. Bargon, R. G. Lawler, A. L. Balch, *J. Am. Chem. Soc.* **1987**, *109*, 8089-8091.
[55] M. G. Pravica, D. P. Weitekamp, *Chem. Phys. Lett.* **1988**, *145*, 255-258.
[56] C. R. Bowers, D. H. Jones, N. D. Kurur, J. A. Labinger, M. G. Pravica, D. P. Weitekamp, in *Advances in Magnetic and Optical Resonance, Vol. Volume 14* (Ed.: W. Warren S), Academic Press, **1990**, pp. 269-291.
[57] R. W. Adams, J. A. Aguilar, K. D. Atkinson, M. J. Cowley, P. I. P. Elliott, S. B. Duckett, G. G. R. Green, I. G. Khazal, J. López-Serrano, D. C. Williamson, *Science* **2009**, *323*, 1708-1711.
[58] M. M. Spence, E. J. Ruiz, S. M. Rubin, T. J. Lowery, N. Winssinger, P. G. Schultz, D. E. Wemmer, A. Pines, *J. Am. Chem. Soc.* **2004**, *126*, 15287-15294.
[59] H. R. Ward, *Acc. Chem. Res.* **1972**, *5*, 18-24.
[60] a) F. Reineri, D. Santelia, A. Viale, E. Cerutti, L. Poggi, T. Tichy, S. S. D. Premkumar, R. Gobetto, S. Aime, *J. Am. Chem. Soc.* **2010**, *132*, 7186-7193; b) M. Roth, A. Koch, P. Kindervater, J. Bargon, H. W. Spiess, K. Münnemann, *J. Magn. Reson.* **2010**, *204*, 50-55; c) F. Gruppi, X. Xu, B. Zhang, J. A. Tang, A. Jerschow, J. W. Canary, *Angewandte Chemie International Edition* **2012**, *51*, 11787-11790.
[61] J. A. Baccile, M. A. Morrell, R. M. Falotico, B. T. Milliken, D. L. Drew, F. M. Rossi, *Tetrahedron Lett.* **2012**, *53*, 1933-1935.
[62] S. Ulrich, D. Boturyn, A. Marra, O. Renaudet, P. Dumy, *Chemistry – A European Journal* **2014**, *20*, 34-41.
[63] S. S. Ghosh, P. M. Kao, A. W. McCue, H. L. Chappelle, *Bioconjugate Chem.* **1990**, *1*, 71-76.
[64] E. Saxon, J. I. Armstrong, C. R. Bertozzi, *Org. Lett.* **2000**, *2*, 2141-2143.
[65] a) G. J. Bodwell, Z. Pi, I. R. Pottie, *Synlett* **1999**, *1999*, 477-479; b) M. L. Blackman, M. Royzen, J. M. Fox, *J. Am. Chem. Soc.* **2008**, *130*, 13518-13519.
[66] M. Grammel, H. C. Hang, *Nat Chem Biol* **2013**, *9*, 475-484.
[67] K. V. Gothelf, K. A. Jørgensen, *Chemical Reviews* **1998**, *98*, 863-910.
[68] F. Himo, T. Lovell, R. Hilgraf, V. V. Rostovtsev, L. Noodleman, K. B. Sharpless, V. V. Fokin, *J. Am. Chem. Soc.* **2005**, *127*, 210-216.
[69] *Proceedings of the Chemical Society* **1961**, 357-396.
[70] a) C. W. Tornøe, C. Christensen, M. Meldal, *The Journal of Organic Chemistry* **2002**, *67*, 3057-3064; b) V. V. Rostovtsev, L. G. Green, V. V. Fokin, K. B. Sharpless, *Angewandte Chemie International Edition* **2002**, *41*, 2596-2599.
[71] J. McNulty, K. Keskar, R. Vemula, *Chemistry – A European Journal* **2011**, *17*, 14727-14730.
[72] L. Zhang, X. Chen, P. Xue, H. H. Sun, I. D. Williams, K. B. Sharpless, V. V. Fokin, G. Jia, *J. Am. Chem. Soc.* **2005**, *127*, 15998-15999.
[73] a) S. G. Hansen, H. H. Jensen, *Synlett* **2009**, *2009*, 3275-3276; b) M. Empting, O. Avrutina, R. Meusinger, S. Fabritz, M. Reinwarth, M. Biesalski, S. Voigt, G. Buntkowsky, H. Kolmar, *Angew. Chem., Int. Ed.* **2011**, *50*, 5207-5211.
[74] a) W. S. Horne, C. D. Stout, M. R. Ghadiri, *J. Am. Chem. Soc.* **2003**, *125*, 9372-9376; b) W. S. Horne, M. K. Yadav, C. D. Stout, M. R. Ghadiri, *J. Am. Chem. Soc.* **2004**, *126*, 15366-15367.
[75] a) N. J. Agard, J. A. Prescher, C. R. Bertozzi, *J. Am. Chem. Soc.* **2005**, *127*, 11196-11196; b) M. Cortizo, M. Lorenzo de Mele, *Biol. Trace Elem. Res.* **2004**, *102*, 129-141.
[76] a) B. M. Swarts, C. M. Holsclaw, J. C. Jewett, M. Alber, D. M. Fox, M. S. Siegrist, J. A. Leary, R. Kalscheuer, C. R. Bertozzi, *J. Am. Chem. Soc.* **2012**, *134*, 16123-16126; b) J. C. Jewett, E. M. Sletten, C. R. Bertozzi, *J. Am. Chem. Soc.* **2010**, *132*, 3688-3690; c) P.

V. Chang, D. H. Dube, E. M. Sletten, C. R. Bertozzi, *J. Am. Chem. Soc.* **2010**, *132*, 9516-9518; d) J. A. Codelli, J. M. Baskin, N. J. Agard, C. R. Bertozzi, *J. Am. Chem. Soc.* **2008**, *130*, 11486-11493.

[77] C. S. McKay, J. Moran, J. P. Pezacki, *Chem. Com.* **2010**, *46*, 931-933.

[78] M. Yang, A. S. Jalloh, W. Wei, J. Zhao, P. Wu, P. R. Chen, *Nat Commun* **2014**, *5*.

[79] V. B. Klimovich, *Biochemistry (Moscow)* **2011**, *76*, 534-549.

[80] C. Fasting, C. A. Schalley, M. Weber, O. Seitz, S. Hecht, B. Koksch, J. Dernedde, C. Graf, E.-W. Knapp, R. Haag, *Angewandte Chemie International Edition* **2012**, *51*, 10472-10498.

[81] P. I. Kitov, D. R. Bundle, *J. Am. Chem. Soc.* **2003**, *125*, 16271-16284.

[82] S. Fabritz, D. Heyl, V. Bagutski, M. Empting, E. Rikowski, H. Frauendorf, I. Balog, W.-D. Fessner, J. J. Schneider, O. Avrutina, H. Kolmar, *Org. Biomol. Chem.* **2010**, *8*, 2212-2218.

[83] R. Alleti, V. Rao, L. Xu, R. J. Gillies, E. A. Mash, *The Journal of Organic Chemistry* **2010**, *75*, 5895-5903.

[84] C. Wängler, G. Moldenhauer, R. Saffrich, E. M. Knapp, B. Beijer, M. Schnölzer, B. Wängler, M. Eisenhut, U. Haberkorn, W. Mier, *Chemistry – A European Journal* **2008**, *14*, 8116-8130.

[85] M. L. Uhrig, J. Kovensky, in *Click Chemistry in Glycoscience*, John Wiley & Sons, Inc., **2013**, pp. 107-142.

[86] a) J. McCombs, S. Owen, *AAPS J* **2015**, *17*, 339-351; b) F. Kratz, *J. Controlled Release* **2008**, *132*, 171-183.

[87] a) S. Fabritz, S. Horner, D. Konning, M. Empting, M. Reinwarth, C. Dietz, B. Glotzbach, H. Frauendorf, H. Kolmar, O. Avrutina, *Org. Biomol. Chem.* **2012**, *10*, 6287-6293; b) S. Horner, S. Fabritz, H. D. Herce, O. Avrutina, C. Dietz, R. W. Stark, M. C. Cardoso, H. Kolmar, *Org. Biomol. Chem.* **2013**, *11*, 2258-2265.

[88] P. Dumy, I. M. Eggleston, S. Cervigni, U. Sila, X. Sun, M. Mutter, *Tetrahedron Lett.* **1995**, *36*, 1255-1258.

[89] M. Galibert, O. Renaudet, P. Dumy, D. Boturyn, *Angewandte Chemie International Edition* **2011**, *50*, 1901-1904.

[90] H. S. Choi, W. Liu, P. Misra, E. Tanaka, J. P. Zimmer, B. I. Ipe, M. G. Bawendi, J. V. Frangioni, *Nat. Biotechnol.* **2007**, *25*, 1165-1170.

[91] E. Hurwitz, R. Arnon, E. Sahar, Y. Danon, *Ann. N. Y. Acad. Sci.* **1983**, *417*, 125-136.

[92] J. Y. Axup, K. M. Bajjuri, M. Ritland, B. M. Hutchins, C. H. Kim, S. A. Kazane, R. Halder, J. S. Forsyth, A. F. Santidrian, K. Stafin, Y. Lu, H. Tran, A. J. Seller, S. L. Biroc, A. Szydlik, J. K. Pinkstaff, F. Tian, S. C. Sinha, B. Felding-Habermann, V. V. Smider, P. G. Schultz, *Proc. Natl. Acad. Sci. U. S. A.* **2012**, *109*, 16101-16106.

[93] P. Dennler, A. Chiotellis, E. Fischer, D. Brégeon, C. Belmant, L. Gauthier, F. Lhospice, F. Romagne, R. Schibli, *Bioconjugate Chem.* **2014**, *25*, 569-578.

[94] a) M. P. Madej, G. Coia, C. C. Williams, J. M. Caine, L. A. Pearce, R. Attwood, N. A. Bartone, O. Dolezal, R. M. Nisbet, S. D. Nuttall, T. E. Adams, *Biotechnol. Bioeng.* **2012**, *109*, 1461-1470; b) J. H. Davis, C. Aperlo, Y. Li, E. Kurosawa, Y. Lan, K.-M. Lo, J. S. Huston, *Protein Engineering Design and Selection* **2010**, *23*, 195-202; c) J. B. B. Ridgway, L. G. Presta, P. Carter, *Protein Eng.* **1996**, *9*, 617-621.

[95] T. J. Marks, D. R. Stojakovic, *J. Am. Chem. Soc.* **1978**, *100*, 1695-1705.

[96] D. Black, R. Srivastava, *Aust. J. Chem.* **1969**, *22*, 1439-1447.

[97] S. Tsukiji, M. Miyagawa, Y. Takaoka, T. Tamura, I. Hamachi, *Nat Chem Biol* **2009**, *5*, 341-343.

[98] Z. Song, Y. Takaoka, Y. Kioi, K. Komatsu, T. Tamura, T. Miki, I. Hamachi, *Chem. Lett.* **2015**, *44*, 333-335.

[99] M. F. Schmidt, J. Rademann, *Trends Biotechnol.*, *27*, 512-521.

[100] a) G. von Kiedrowski, *Angewandte Chemie International Edition in English* **1986**, *25*, 932-935; b) P. Luo, J. C. Leitzel, Z.-Y. J. Zhan, D. G. Lynn, *J. Am. Chem. Soc.* **1998**, *120*, 3019-3031; c) Y. Xu, N. B. Karalkar, E. T. Kool, *Nat Biotech* **2001**, *19*, 148-152.
[101] X. Li, D. R. Liu, *Angewandte Chemie International Edition* **2004**, *43*, 4848-4870.
[102] A. Roloff, O. Seitz, *Bioorg. Med. Chem.* **2013**, *21*, 3458-3464.
[103] J. Michaelis, G. J. van der Heden van Noort, O. Seitz, *Bioconjugate Chem.* **2014**, *25*, 18-23.
[104] a) H.-K. S. Leiros, B. O. Brandsdal, O. A. Andersen, V. Os, I. Leiros, R. Helland, J. Otlewski, N. P. Willassen, A. O. Smalås, *Protein Sci.* **2004**, *13*, 1056-1070; b) L. Polgár, *Cellular and Molecular Life Sciences CMLS* **2005**, *62*, 2161-2172.
[105] M. J. P. O'Connell T. P., *Biochem. J.* **1995**, *307* 353-359.
[106] B. Korkmaz, M. S. Horwitz, D. E. Jenne, F. Gauthier, *Pharmacol Rev* **2010**, *62*, 726-759.
[107] S. R. Presnell, G. S. Patil, C. Mura, K. M. Jude, J. M. Conley, J. A. Bertrand, C.-M. Kam, J. C. Powers, L. D. Williams, *Biochemistry* **1998**, *37*, 17068-17081.
[108] a) N. D. Rawlings, A. J. Barrett, in *Methods Enzymol., Vol. Volume 244* (Ed.: J. B. Alan), Academic Press, **1994**, pp. 461-486; b) M. Laskowski, I. Kato, *Annu. Rev. Biochem.* **1980**, *49*, 593-626.
[109] A. E. Nixon, C. R. Wood, *Curr Opin Drug Discov Devel.* **2006**, *9*, 261-268.
[110] Y. Pan, M. Ye, L. Zhao, K. Cheng, M. Dong, C. Song, H. Qin, F. Wang, H. Zou, *Angewandte Chemie International Edition* **2013**, *52*, 9205-9209.
[111] Y. V. Wu, D. J. Sessa, *J. Agric. Food Chem.* **1994**, *42*, 2136-2138.
[112] N. L. Daly, Y. K. Chen, F. M. Foley, P. S. Bansal, R. Bharathi, R. J. Clark, C. P. Sommerhoff, D. J. Craik, *J. Biol. Chem.* **2006**, *281*, 23668-23675.
[113] K. Hilpert, G. Hansen, H. Wessner, R. Volkmer-Engert, W. Höhne, *Journal of Biochemistry* **2005**, *138*, 383-390.
[114] A. M. Jaulent, R. J. Leatherbarrow, *Protein Engineering Design and Selection* **2004**, *17*, 681-687.
[115] M. L. J. Korsinczky, H. J. Schirra, K. J. Rosengren, J. West, B. A. Condie, L. Otvos, M. A. Anderson, D. J. Craik, *J. Mol. Biol.* **2001**, *311*, 579-591.
[116] a) A. B. E. Brauer, G. J. Domingo, R. M. Cooke, S. J. Matthews, R. J. Leatherbarrow, *Biochemistry* **2002**, *41*, 10608-10615; b) J. D. McBride, E. M. Watson, A. B. E. Brauer, A. M. Jaulent, R. J. Leatherbarrow, *Peptide Science* **2002**, *66*, 79-92.
[117] N. L. Daly, Y.-K. Chen, F. M. Foley, P. S. Bansal, R. Bharathi, R. J. Clark, C. P. Sommerhoff, D. J. Craik, *J. Biol. Chem.* **2006**, *281*, 23668-23675.
[118] F. H. C. Crick, *Acta Crystallographica* **1953**, *6*, 689-697.
[119] D. A. D. Parry, R. D. B. Fraser, J. M. Squire, *J Struct Biol* **2008**, *163*, 258-269.
[120] H. Chao, M. E. Houston, S. Grothe, C. M. Kay, M. O'Connor-McCourt, R. T. Irvin, R. S. Hodges, *Biochemistry* **1996**, *35*, 12175-12185.
[121] a) W. Landschulz, P. Johnson, S. McKnight, *Science* **1988**, *240*, 1759-1764; b) K. Struhl, *Trends Biochem. Sci.* **1989**, *14*, 137-140; c) B. Brodsky, A. V. Persikov, in *Adv. Protein Chem., Vol. Volume 70* (Eds.: A. D. P. David, M. S. John), Academic Press, **2005**, pp. 301-339.
[122] J. R. Litowski, R. S. Hodges, *J. Biol. Chem.* **2002**, *277*, 37272-37279.
[123] H. Dong, J. D. Hartgerink, *Biomacromolecules* **2006**, *7*, 691-695.
[124] N. E. Zhou, C. M. Kay, R. S. Hodges, *J. Mol. Biol.* **1994**, *237*, 500-512.
[125] W. D. Kohn, R. S. Hodges, *Trends Biotechnol.* **1998**, *16*, 379-389.
[126] U. Reinhardt, J. Lotze, S. Zernia, K. Mörl, A. G. Beck-Sickinger, O. Seitz, *Angewandte Chemie International Edition* **2014**, *53*, 10237-10241.
[127] a) Z. Chen, B. V. Popp, C. L. Bovet, Z. T. Ball, *ACS Chem. Biol.* **2011**, *6*, 920-925; b) B. V. Popp, Z. T. Ball, *J. Am. Chem. Soc.* **2010**, *132*, 6660-6662.

[128] P. E. Nielsen, M. Egholm, *Curr Issues Mol Biol* **1999**, *1*, 89-104.
[129] P. E. Nielsen, M. Egholm, O. Buchardt, *Bioconjugate Chem.* **1994**, *5*, 3-7.
[130] K. L. Dueholm, M. Egholm, C. Behrens, L. Christensen, H. F. Hansen, T. Vulpius, K. H. Petersen, R. H. Berg, P. E. Nielsen, O. Buchardt, *The Journal of Organic Chemistry* **1994**, *59*, 5767-5773.
[131] a) P. Nielsen, M. Egholm, R. Berg, O. Buchardt, *Science* **1991**, *254*, 1497-1500; b) M. Egholm, P. E. Nielsen, O. Buchardt, R. H. Berg, *J. Am. Chem. Soc.* **1992**, *114*, 9677-9678.
[132] a) S. Tomac, M. Sarkar, T. Ratilainen, P. Wittung, P. E. Nielsen, B. Nordén, A. Gräslund, *J. Am. Chem. Soc.* **1996**, *118*, 5544-5552; b) U. Giesen, W. Kleider, C. Berding, A. Geiger, H. Ørum, P. E. Nielsen, *Nucleic Acids Res.* **1998**, *26*, 5004-5006.
[133] a) P. E. Nielsen, M. Egholm, O. Buchardt, *J. Mol. Recognit.* **1994**, *7*, 165-170; b) B. P. B. D Y Cherny, M D Frank-Kamenetskii, M Egholm, O Buchardt, R H Berg, P E Nielsen, *Proc Natl Acad Sci U S A* **1993**, *90*, 1667–1670.
[134] T. Sugiyama, A. Kittaka, *Molecules* **2012**, *18*, 287-310.
[135] K. K. Jensen, H. Ørum, P. E. Nielsen, B. Nordén, *Biochemistry* **1997**, *36*, 5072-5077.
[136] D. Sun, A. L. Stadler, M. Gurevich, E. Palma, E. Stach, D. van der Lelie, O. Gang, *Nanoscale* **2012**, *4*, 6722-6725.
[137] T. Bentin, P. Nielsen, in *Peptide Nucleic Acids, Vol. 208* (Ed.: P. Nielsen), Springer New York, **2002**, pp. 111-118.
[138] A. S. Lygina, K. Meyenberg, R. Jahn, U. Diederichsen, *Angewandte Chemie International Edition* **2011**, *50*, 8597-8601.
[139] P. E. Nielsen, T. Shiraishi, *Artificial DNA, PNA & XNA* **2011**, *2*, 90-99.
[140] U. C. Marx, M. L. J. Korsinczky, H. J. Schirra, A. Jones, B. Condie, L. Otvos, D. J. Craik, *J. Biol. Chem.* **2003**, *278*, 21782-21789.
[141] P. Fabbrizzi, G. Menchi, A. Guarna, A. Trabocchi, *Curr. Med. Chem.* **2014**, *21*, 1467-1477.
[142] a) H. Fittler, O. Avrutina, B. Glotzbach, M. Empting, H. Kolmar, *Org. Biomol. Chem.* **2013**, *11*, 1848-1857; b) H. Fittler, O. Avrutina, M. Empting, H. Kolmar, *J. Pept. Sci.* **2014**, *20*, 415-420.
[143] a) J. Monteseirín, I. Bonilla, M. J. Camacho, P. Chacón, A. Vega, A. Chaparro, J. Conde, F. Sobrino, *Int. Arch. Allergy Appl. Immunol.* **2003**, *131*, 174-181; b) H. Koga, N. Miyahara, Y. Fuchimoto, G. Ikeda, K. Waseda, K. Ono, Y. Tanimoto, M. Kataoka, E. Gelfand, M. Tanimoto, A. Kanehiro, *Respiratory Research* **2013**, *14*, 8.
[144] a) K. Hilpert, H. Wessner, J. Schneider-Mergener, K. Welfle, R. Misselwitz, H. Welfle, A. C. Hocke, S. Hippenstiel, W. Höhne, *J. Biol. Chem.* **2003**, *278*, 24986-24993; b) J. D. McBride, H. N. M. Freeman, R. J. Leatherbarrow, *Eur. J. Biochem.* **1999**, *266*, 403-412; c) E. Zabłotna, A. Jaśkiewicz, A. Łęgowska, H. Miecznikowska, A. Lesner, K. Rolka, *J. Pept. Sci.* **2007**, *13*, 749-755.
[145] M. Korner, G. Sauer, A. Heil, D. Nasu, M. Empting, D. Tietze, S. Voigt, H. Weidler, T. Gutmann, O. Avrutina, H. Kolmar, T. Ratajczyk, G. Buntkowsky, *Chem. Com.* **2013**, *49*, 7839-7841.
[146] O. Avrutina, M. Empting, S. Fabritz, M. Daneschdar, H. Frauendorf, U. Diederichsen, H. Kolmar, *Org. Biomol. Chem.* **2009**, *7*, 4177-4185.
[147] T. Trantzschel, M. Plaumann, J. Bernarding, D. Lego, T. Ratajczyk, S. Dillenberger, G. Buntkowsky, J. Bargon, U. Bommerich, *Applied Magnetic Resonance* **2012**, *44*, 267-278.
[148] M. W. Jones, G. Mantovani, C. A. Blindauer, S. M. Ryan, X. Wang, D. J. Brayden, D. M. Haddleton, *J. Am. Chem. Soc.* **2012**, *134*, 7406-7413.
[149] Lundquist, J. C. Pelletier, *Org. Lett.* **2001**, *3*, 781-783.
[150] G. J. Roth, B. Liepold, S. G. Müller, H. J. Bestmann, *Synthesis* **2004**, *2004*, 59-62.

[151] J. Ermolieff, C. Boudier, A. Laine, B. Meyer, J. G. Bieth, *J. Biol. Chem.* **1994**, *269*, 29502-29508.
[152] K. Nakajima, J. C. Powers, B. M. Ashe, M. Zimmerman, *J. Biol. Chem.* **1979**, *254*, 4027-4032.
[153] R. A. Copeland, in *Evaluation of Enzyme Inhibitors in Drug Discovery*, John Wiley & Sons, Inc., **2013**, pp. 245-285.
[154] A. Legowska, D. Debowski, R. Lukajtis, E. Sztabkowska, M. Aneta, K. Brzozowski, M. Wysocka, A. Lesner, K. Rolka, *Protein Pept. Lett.* **2011**, *18*, 1158-1167.
[155] W. Dall'Acqua, C. Halin, M. L. Rodrigues, P. Carter, *Protein Eng.* **1999**, *12*, 981-987.
[156] a) M. L. J. Korsinczky, R. J. Clark, D. J. Craik, *Biochemistry* **2005**, *44*, 1145-1153; b) O. Avrutina, H. Fittler, B. Glotzbach, H. Kolmar, M. Empting, *Org. Biomol. Chem.* **2012**, *10*, 7753-7762.
[157] T. Gutmann, M. Sellin, H. Breitzke, A. Stark, G. Buntkowsky, *Phys. Chem. Chem. Phys.* **2009**, *11*, 9170-9175.
[158] S. Aime, D. Canet, W. Dastru, R. Gobetto, F. Reineri, A. Viale, *J. Phys. Chem. A* **2001**, *105*, 6305-6310.
[159] M. Körner, G. Sauer, A. Heil, D. Nasu, M. Empting, D. Tietze, S. Voigt, H. Weidler, T. Gutmann, O. Avrutina, H. Kolmar, T. Ratajczyk, G. Buntkowsky, *Chem. Comm.* **2013**, *49*, 7839-7841.
[160] a) R. B. Yamasaki, D. T. Osuga, R. E. Feeney, *Anal. Biochem.* **1982**, *126*, 183-189; b) K. F. Geoghegan, J. G. Stroh, *Bioconjugate Chem.* **1992**, *3*, 138-146.
[161] D. A. Lindhout, J. R. Litowski, P. Mercier, R. S. Hodges, B. D. Sykes, *Biopolymers* **2004**, *75*, 367-375.
[162] M. M. Fabani, C. Abreu-Goodger, D. Williams, P. A. Lyons, A. G. Torres, K. G. C. Smith, A. J. Enright, M. J. Gait, E. Vigorito, *Nucleic Acids Res.* **2010**, *38*, 4466-4475.
[163] a) B. R. Scott, M. A. Pathak, G. R. Mohn, *Mutation Research/Reviews in Genetic Toxicology* **1976**, *39*, 29-74; b) J. A. Parrish, T. B. Fitzpatrick, L. Tanenbaum, M. A. Pathak, *N. Engl. J. Med.* **1974**, *291*, 1207-1211.
[164] a) G. P. Wiesehahn, J. E. Hyde, J. E. Hearst, *Biochemistry* **1977**, *16*, 925-932; b) C. Hanson, C. Shen, J. Hearst, *Science* **1976**, *193*, 62-64.
[165] A. Okamoto, K. Tanabe, I. Saito, *Org. Lett.* **2001**, *3*, 925-927.
[166] K.-H. Kim, X.-J. Fan, P. E. Nielsen, *Bioconjugate Chem.* **2007**, *18*, 567-572.
[167] A. Boltz, B. Piater, L. Toleikis, R. Guenther, H. Kolmar, B. Hock, *J. Biol. Chem.* **2011**, *286*, 21896-21905.
[168] L. Lad, L. Luo, J. D. Carson, K. W. Wood, J. J. Hartman, R. A. Copeland, R. Sakowicz, *Biochemistry* **2008**, *47*, 3576-3585.
[169] C. C. Lee, E. R. Samuels, *Can. J. Chem.* **1964**, *42*, 168-170.
[170] J. Dommerholt, S. Schmidt, R. Temming, L. J. A. Hendriks, F. P. J. T. Rutjes, J. C. M. van Hest, D. J. Lefeber, P. Friedl, F. L. van Delft, *Angewandte Chemie International Edition* **2010**, *49*, 9422-9425.
[171] S. Dickgiesser, N. Rasche, D. Nasu, S. Middel, S. Hörner, O. Avrutina, U. Diederichsen, H. Kolmar, *ACS Chem. Biol.* **2015**.
[172] R. P. Temming, L. Eggermont, M. B. van Eldijk, J. C. M. van Hest, F. L. van Delft, *Org. Biomol. Chem.* **2013**, *11*, 2772-2779.
[173] a) X. Ning, R. P. Temming, J. Dommerholt, J. Guo, D. B. Ania, M. F. Debets, M. A. Wolfert, G.-J. Boons, F. L. van Delft, *Angewandte Chemie International Edition* **2010**, *49*, 3065-3068; b) D. A. MacKenzie, A. R. Sherratt, M. Chigrinova, L. L. W. Cheung, J. P. Pezacki, *Curr. Opin. Chem. Biol.* **2014**, *21*, 81-88.
[174] D. W. Dodd, R. H. E. Hudson, *Electrophoresis* **2007**, *28*, 3884-3889.
[175] R. C. Beavis, B. T. Chait, *Anal. Chem.* **1990**, *62*, 1836-1840.

[176] I. Chen, B. M. Dorr, D. R. Liu, *Proceedings of the National Academy of Sciences* **2011**, *108*, 11399-11404.
[177] a) S. K. Mazmanian, G. Liu, H. Ton-That, O. Schneewind, *Science* **1999**, *285*, 760-763; b) M. W.-L. Popp, H. L. Ploegh, *Angewandte Chemie International Edition* **2011**, *50*, 5024-5032.
[178] S. Möhlmann, C. Mahlert, S. Greven, P. Scholz, A. Harrenga, *ChemBioChem* **2011**, *12*, 1774-1780.
[179] L. Kuhn, J. Bargon, in *In situ NMR Methods in Catalysis, Vol. 276* (Eds.: J. Bargon, L. Kuhn), Springer Berlin Heidelberg, **2007**, pp. 25-68.
[180] M. H. Levitt, *Annu. Rev. Phys. Chem.* **2012**, *63*, 89-105.
[181] N. Zhang, R. Chen, N. Young, D. Wishart, P. Winter, J. H. Weiner, L. Li, *Proteomics* **2007**, *7*, 484-493.
[182] M. Empting, O. Avrutina, R. Meusinger, S. Fabritz, M. Reinwarth, M. Biesalski, S. Voigt, G. Buntkowsky, H. Kolmar, *Angew. Chem. Intl. Ed.* **2011**, *50*, 5207-5211.
[183] K. Holland-Nell, M. Meldal, *Angew. Chem.* **2011**, *123*, 5310-5312.
[184] E. Vivès, B. Lebleu, *Tetrahedron Lett.* **2003**, *44*, 5389-5391.
[185] T. Gutmann, M. Sellin, H. Breitzke, A. Stark, G. Buntkowsky, *Phys. Chem. Chem. Phys.* **2009**, *11*, 9170-9175.
[186] G. D. Cimino, H. B. Gamper, S. T. Isaacs, J. E. Hearst, *Annu. Rev. Biochem.* **1985**, *54*, 1151-1193.
[187] S. P. Fling, D. S. Gregerson, *Analytical Biochemistry* **1986**, *155*, 83-88.
[188] a) Y. Duan, C. Wu, S. Chowdhury, M. C. Lee, G. Xiong, W. Zhang, R. Yang, P. Cieplak, R. Luo, T. Lee, J. Caldwell, J. Wang, P. Kollman, *J. Comput. Chem.* **2003**, *24*, 1999-2012; b) E. Krieger, T. Darden, S. B. Nabuurs, A. Finkelstein, G. Vriend, *Proteins* **2004**, *57*, 678-683.

7 Appendix

List of Abbreviations

2-Cl-Trt	2-Chlorotrityl
Å	Ångström
aa	Amino acid
AAC	Alkyne-azide cycloaddition
Ab	Antibody
Ac	Acetate
ADC	Antibody-drug conjugate
ADMET	Absorption, distribution, metabolism, excretion, toxicity
aeg	*N*-(2-ethyl)glycine
Aha	Azidohomoalanine
Ala	Alanine
All	Allyl
AgAAC	Silver(I)-catalyzed alkyne-azide cycloaddition
AGD	Affinity-guided DMAP
ALTADENA	Adiabatic longitudinal transport after dissociation engenders nuclear alignment
Arg	Arginine
Asp	Aspartic acid
B	Magnetic field
BARAC	Biarylazacyclooctynone
BBI	Bowman-Birk inhibitor
BCN	(1*R*,8*S*,9*s*)-bicyclo[6.1.0]non-4-yn
Bhoc	Benzhydryloxycarbonyl
BLI	Biolayer interferometry
Boc	*tert*-butoxycarbonyl
BPP_{5a}	bradykinin potentiating peptide
°C	Degrees Celsius
CIDNP	Chemically induced dynamic nuclear polarization
Cit	Citrulline
CL	Cross-linkage
cm	Centimeter
COD	Cyclooctadiene
COSS	Cube-octametric silsequioxane

cp	Cyclopentadiene
CuAAC	Copper(I)-catalyzed alkyne-azide cycloaddition
Cys	Cysteine
d	Day
DA	Diels-Alder
Da	Dalton
DAR	Drug-to-antibody ratio
DCM	Dichloromethane
DIBAH	Dibuthylaluminium hydride
DIEA	*N*,*N*-diisopropylethylamine
DMAP	*N*,*N*-dimethyl-4-aminopyridine
DMF	*N*,*N*'-dimethyl formamide
DMSO	Dimethyl sulfoxide
DNA	Deoxyribonucleic acid
DNP	Dynamic nuclear polarization
DOTA	1,4,7,10-tetraazacyclododecane-1,4,7,10-tetraacetic acid
DTS	DNA-templated synthesis
DTT	Dithiothreitol
E	Magnetic quantum energy
[*E*]	Enzyme concentration
EF	Enhancement factor
ESI	Electrospray ionization
eSrtA	Evolved sortase A
EtOH	Ethanol
Fab	Antigen-binding fragment
Fc	Fragment crystallizable
FGE	Formylglycine-generating enzyme
Fmoc	9-Fluorenylmethyloxycarbonyl
FRET	Fluorescence polarization energy transfer
G	Free Energy
g	Gram
Glu	Glutamic acid
Gly	Glycine
GRAB	Group replacement assisted binding
h	Hour

HATU	2-(1H-7-azabenzotriazol-1-yl)-1,1,3,3-tetramethyl uronium hexafluorophosphate
HBTU	2-(1H-benzotriazol-1-yl)-1,1,3,3-tetramethyluronoium hexafluorophosphate
His	Histidine
HNE	Human neutrophil elastase
HOBt	1-hydroxybenzotriazole
HP/Xe	Hyperpolarized Xenon biosensor
HPLC	High-performance liquid chromatography
HTS	High-throughput screening
I	Nuclear spin quantum number
$[I]$	Inhibitor concentration
IgG	Immunoglobulin G
IgM	Immunoglobulin M
Ile	Isoleucine
Int	Intensity
IR	Infrared
J	NMR J-coupling
K	Kelvin
k_B	Boltzmann constant
kcal	Kilocalories
kDa	Kilodalton
K	Binding/affinity/equilibrium constant
k_2	Second-order kinetic constant
K_a	Association constant
K_{avid}	Affinity constant wit avidity effect
K_D	Dissociation constant
K_i	ınhibition constant
K_i^{app}	Apparent inhibition constant
K_M	Michaelis-Menten constant
LDT	Ligand-directed tosyl
Leu	Leucine
Lys	Lysine
λ	Wavelength
M	Mol per liter
M	Magnetization
mAB	Monoclonal antibody

MALDI	Matrix-assisted laser desorption/ionization
MBHA	4-Methyl benzhydrylamine
Me	Methyl
MeCN	Acetonitrile
MeOH	Methanol
Met	Methionine
min	Minute
mm	Millimeter
MRI	Magnetic resonance imaging
mRNA	Messenger ribonucleic acid
MS	Mass spectrometry
MTBE	Methyl tert-butyl ether
MW	Microwave
m/z	Mass to charge signal
μ	Magnetic moment
μl	Microliter
μM	Micromol per liter
μmol	Micoromol
N	Number of nuclei
NCL	Native chemical ligation
NHS	*N*-succinimidyl carbonate
Nle	Norleucine
nM	Nanomol per liter
nm	Nanometer
nmol	Nanomol
NMP	*N*-methyl pyrrolidone
NMR	Nuclear magnetic resonance
NPA	*p*-nitrophenylacetate
v	Wave number
P	Polarization
Ψ	Wave function
PASADENA	Parahydrogen and synthesis allow dramatically enhanced nuclear alignment
PAGE	Polyacrylamide gel electrophoresis
PBS	Phosphate-buffered saline
PET	Positron emission tomography

Phe	Phenylalanine
PHIP	Parahydrogen induced polarization
pmol	Picomol
PNA	Peptide nucleic acid
pNA	para-nitro aniline
POE, PEG	Polyethylene glycol
ppm	Parts per million
Pra	Propargylglycine
Pro	Proline
Pso	Psoralen
R	Ideal gas constant
R^2	Regression coefficient of trend line
RAFT	Regioselectively addressable functionalized templates
RAM	Rink amide MBHA
RMSD	Root mean square derivation
RP-HPLC	Reversed-phase HPLC
R_t	Retention time
RuAAC	Ruthenium(II)-catalyzed alkyne-azide cycloaddition
S	Signal
s	Second
[S]	Substrate concentration
S1 pocket	Specificity-site pocket
SABRE	Signal amplification by reversible exchange
SDS	Sodium dodecyl sulfonate
SE	Signal enhancement
SEC	Size exclusion chromatography
Sem	Selenomethionine
Ser	Serine
SFTI	Sunflower trypsin inhibitor
SNR	Signal-to-noise-ratio
SPAAC	Strain-promoted alkyne-azide cycloaddition
SPANC	Strain-promoted alkyne-nitrone cycloaddition
SPECT	Single-photon emission computed tomography
SPPS	Solid-phase peptide synthesis
SPS	Solid-phase synthesis
ssNMR	Solid-state nuclear magnetic resonance

Su, Suc	Succinimide
T	Tesla
T	Temperature
t	*trans*
T_1	Spin relaxation time
TAMRA	Carboxytetramethylrhodamine
TASP	Template assembled synthetic proteins
t	Time
TES	Triethyl silane
TFA	Trifluoroacetic acid
TFE	2,2,2,-Trifluoroehtanol
Thr	Threonine
T_m	Melting temperature
TPCK	Tosyl phenylalanyl chloromethyl ketone
tRNA	Transfer ribonucleic acid
Trp	Tryptophan
ts	Transition state
Tyr	Tyrosine
Tyr(*O*-propargyl)	*O*-Propargyltyrosine
Val	Valine
v	Reaction rate
Xaa	Any canonical amino acid

Enlarged version of ***Figure 34***

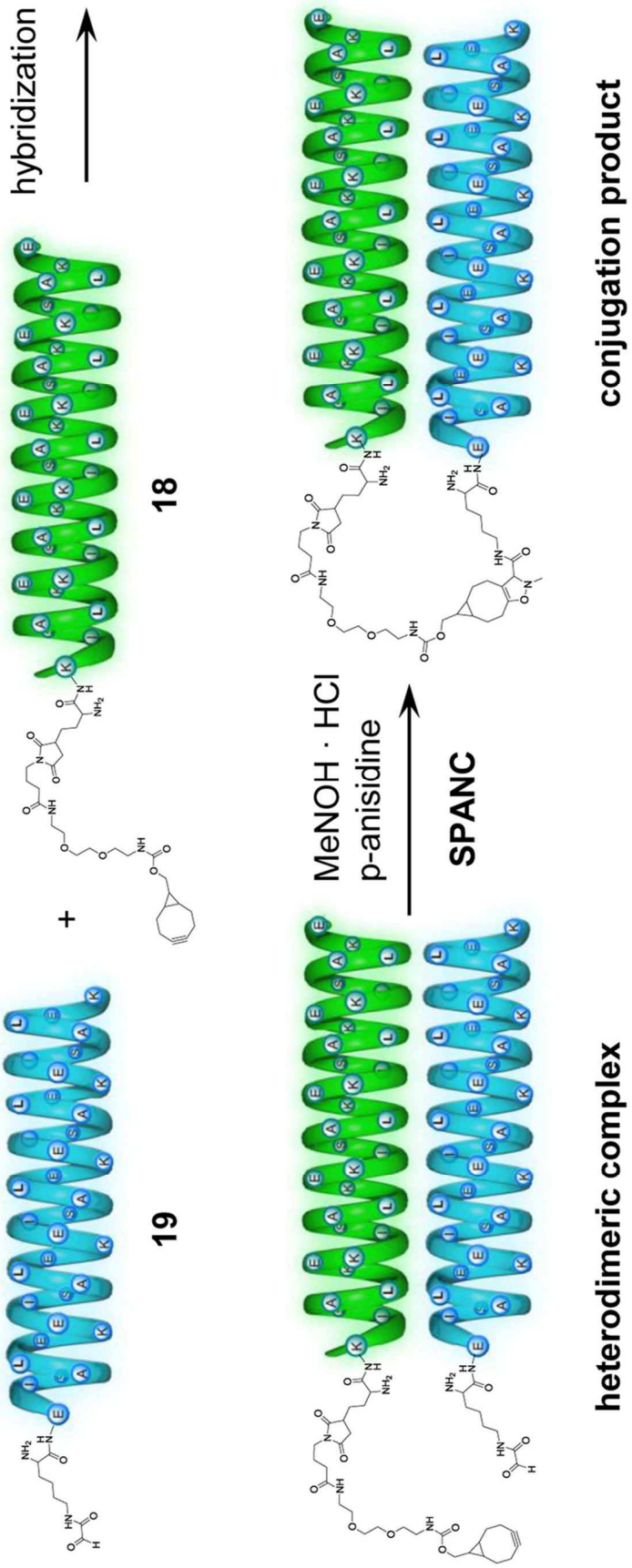

Summary of test reaction setups of coiled coil-guided SPANC

Setup	A[a]	B[b]	C[c]	Eq. A:B:C	[A] [μM]	Analysis	Conversion[d] [%]
1	**16**	**17**	-	1:1	125	HPLC, ESI-MS	74.1[f]
2	**18**	**19**	-	1:1	50	ESI-MS	*n. c.*
3	**18**	**19**	-	1:1	50	ESI-MS	*n. c.*
4	**18**	**19**	-	1:1	50	HPLC, ESI-MS	69.8
5[f]	**18**	**19**	-	1:1	50	HPLC, ESI-MS	61.2
6	**18**	**19**	benzaldehyde	1:1:1	50	HPLC, ESI-MS	80.0
7	**18**	**19**	benzaldehyde	2:3:2	100	HPLC, ESI-MS	71.5
8	**18**	**19**	benzaldehyde	1:1:1	150	HPLC, ESI-MS	79.3
9[g]	**18**	-	benzaldehyde	1:0:10	100	HPLC, ESI-MS	50.1
10[h]	**18**	-	-	-	50	HPLC, ESI-MS	-
11	**18**	**19**	**32**	1:1:1	100	HPLC, ESI-MS	89.2
12[i]	**18**	-	**32**	1:0:1	100	HPLC, ESI-MS	60.2
13[j]	**18**	**19'**	-	1:1	100	HPLC, ESI-MS	72.2

a: BCN-decorated guiding unit.
b: Aldehyde-bearing guiding unit.
c: Competitive aldehyde component.
d: Conversion calculated from decrease in HPLC traces of aldehyde-bearing guiding unit.
e: Reaction performed in water pH 7.0.
f: Mean value of conversions of two reaction batches using same setup.
g: Control experiment using **18** and benzaldehyde. Conversion calculated from consumption of **18**.
h: Control experiment with only **18** and MeNOH.
i: Control experiment using **18** and **32**. Conversion calculated from consumption of **32**.
j: *In situ* aldehyde-formation strategy was applied.
n.c.: conversion not calculated.

Summary of test reaction setups of coiled coil-guided SPANC

Setup	A[a]	B[b], C[c]	Eq. A:B:C	[A[a]] [μM]	Main solvent (pH)	t_{comp} [min]	T_{rct}	Conversion[d] [%]
1	**20**	**21**	1:1	200	NH_4OAc_{aq} (6.5)	60	rt	51.0
2	**20**	**21**	4:3	130	NH_4OAc_{aq} (6.5)	60	rt	52.0
3	**20**	**21**	4:3	130	NH_4OAc_{aq} (6.5)	60	rt	57.1
4	**20**	**21**	4:3	130	$HEPES_{aq}$ (6.0)	60	rt	66.1
5	**20**	**21**	1:1	67	NH_4OAc_{aq} (6.0)	60	rt	75.1
6	**20**	**21**	1:1	67	NH_4OAc_{aq} (6.0)	60	4°C	75.9
7	**20**	**21**	1:1	67	$NaOAc_{aq}$ (5.0)	0	4°C	55.6
8	**20**	**21**	1:1	67	PBS_{aq} (7.4)	0	4°C	39.3
9	**20**	**21**	6:5	80	$HEPES_{aq}$ (6.0)	60	4°C	73.2
10	**20**	**21**	1:1	220	$HEPES_{aq}$ (6.0)	0	4°C	61.3
11[e]	**20**	**21**	6:5	240	NH_4OAc_{aq} (6.5)	60	4°C	50.9
12[e]	**20**	**21**	4:1	320	NH_4OAc_{aq} (6.5)	60	4°C	68.5
13	**20**	**21**	1:1	200	NH_4OAc_{aq} (6.0)	60	rt	73.1
14	**20**	**21, 22**	1:1:1	100	NH_4OAc_{aq} (6.0)	60	rt	54.0[f]
15[f]	**20**	**21'**	1:1	100	NH_4OAc_{aq} (6.5)	60	rt	51.0
16[f]	**20**	**21'**	1:1	200	NH_4OAc_{aq} (6.5)	60	rt	51.9
17[e,f]	**20**	**21'**	1:1	200	NH_4OAc/THF	60	rt	49.5
18[e,i]	**20**	**21'**	1:1	200	NH_4OAc/THF	60	rt	76.6

a: BCN-decorated guiding unit.
b: Aldehyde-bearing guiding unit.
c: Competitive aldehyde component.
d: Conversion calculated from decrease in HPLC traces of aldehyde-bearing guiding unit.
e: PhNOH was applied as nitrone-forming agent.
f: *In situ* aldehyde-formation strategy was applied. Reaction quenched with MeOPhSH.
i: *In situ* aldehyde-formation strategy was applied. Reaction quenched with ethylene glycol.

List of conjugation products of cycloaddition experiments

Conjugation product	Reaction type	Reaction equation	M [g/mol]
cp1	**SPANC**	**16** + **17** $\xrightarrow{\text{MeNOH}}$ **cp1**	5979.2
cp2	**SPANC**	**18** + **19** $\xrightarrow{\text{MeNOH}}$ **cp2**	8543.0
cp3	**SPANC**	**18** + benz-aldehyde $\xrightarrow{\text{MeNOH}}$ **cp3**	4593.5
cp4	-	**18** + MeNHOH $\longrightarrow$ **cp4**	4506.0
cp5	**SPANC**	**18** + **32** $\xrightarrow{\text{MeNOH}}$ **cp5**	6181.4
cp6	**SPANC**	**20** + **21** $\xrightarrow{\text{MeNOH}}$ **cp6**	6515.6
cp7	**SPANC**	**20** + **22** $\xrightarrow{\text{MeNOH}}$ **cp7**	6475.6
cp8	-	**20** + MeNHOH $\longrightarrow$ **cp8**	3494.5
cp9	-	**20** + PhNOH $\longrightarrow$ **cp9**	3556.6
cp10	**SPAAC**	**20** + **23** $\longrightarrow$ **cp10**	6428.4
cp11	**Pso-CL**	**20'** + **21'** $\xrightarrow[\text{UVA}]{\text{psoralen}}$ **cp11**	6183.1
cp12	**Pso-CL**	**25** + **26** $\xrightarrow{\text{UVA}}$ **cp12**	7717.7
cp13	**Pso-CL**	**25** + **33** $\xrightarrow{\text{UVA}}$ **cp13**	8047.0

Hanes-Woolf Plots of Protease Activity Assays

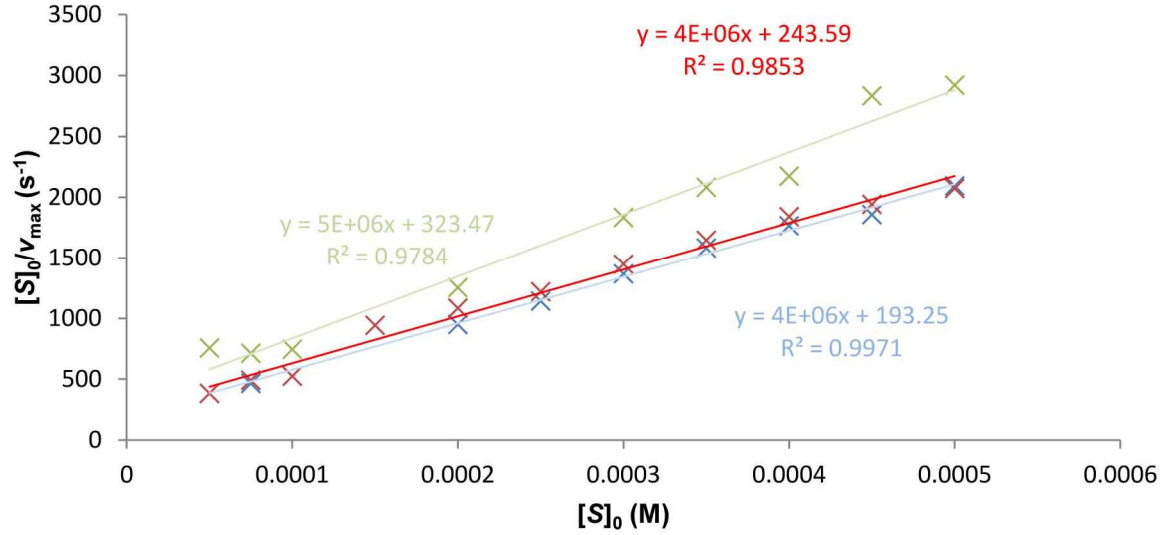

Hanes-Woolf plot of trypsin activity assays against Boc-QAR-pNA in trypsin activity buffer in triplicate. Data points, trend lines of linear regressions, linear equation of trend lines, and associated regression coefficient of each measurement series are marked in individual colors.

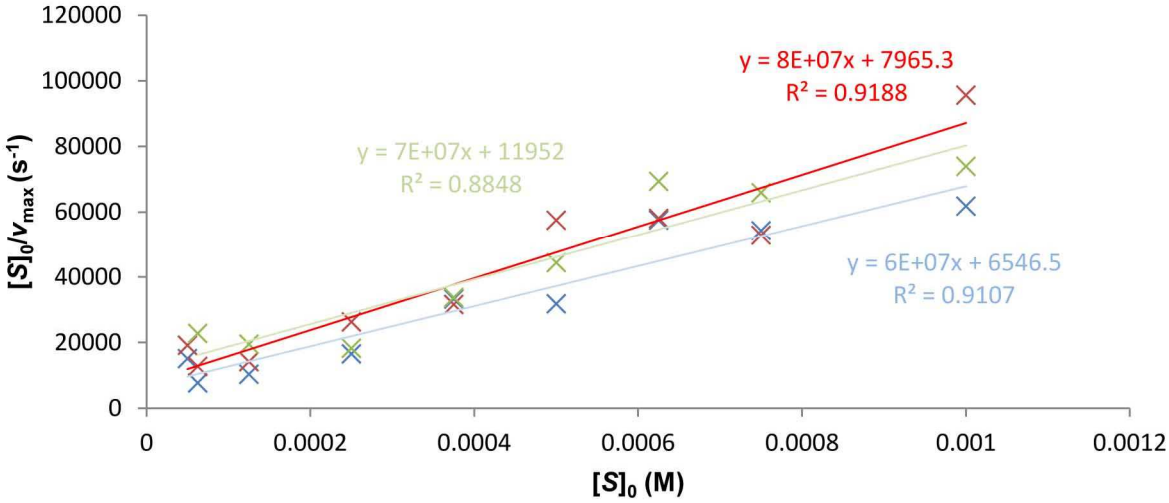

Hanes-Woolf plot of trypsin activity assays against Boc-QAR-pNA in non-buffered water in triplicate. Data points, trend lines of linear regressions, linear equation of trend lines, and associated regression coefficient of each measurement series are marked in individual colors.

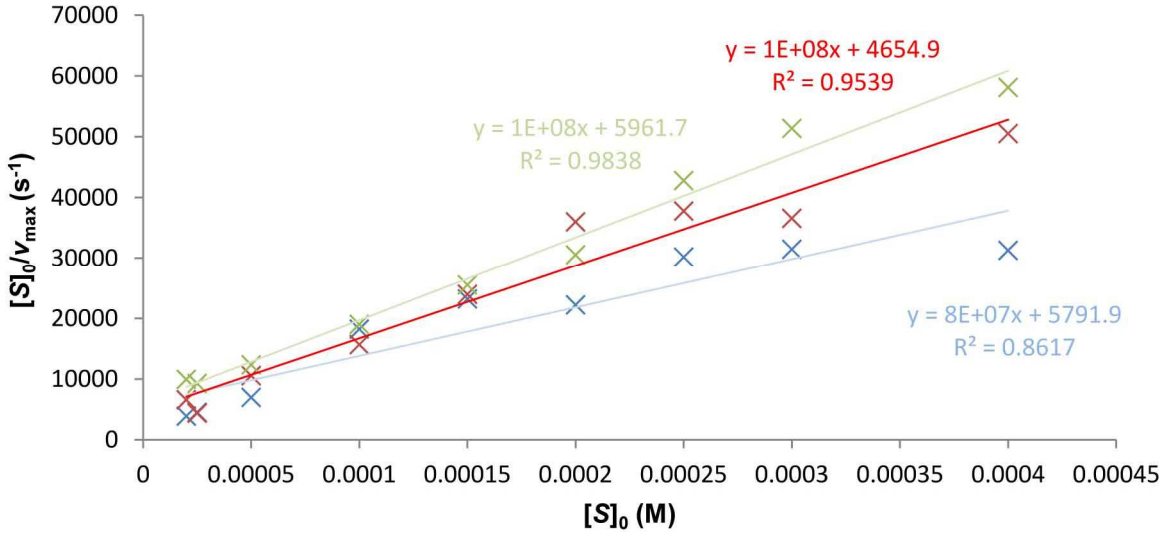

Hanes-Woolf plot of trypsin activity assays against Boc-QAR-pNA in non-buffered D_2O in triplicate. Data points, trend lines of linear regressions, linear equation of trend lines, and associated regression coefficient of each measurement series are marked in individual colors.

Dixon Plots of Enzyme Inhibition Assays

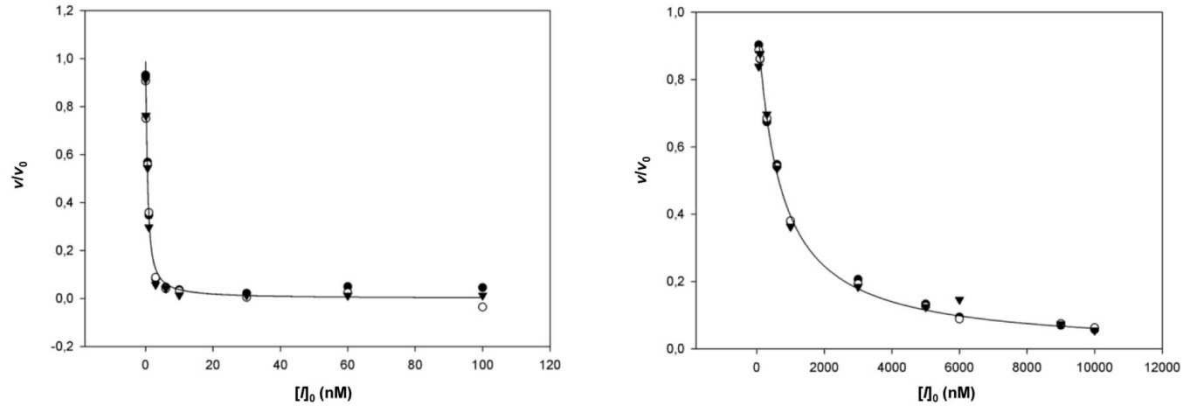

Dixon plots of inhibition assays of **1** against chymotrypsin (left) and **2** against HNE (right) with trend curves of global fittings of triplicate measurements.

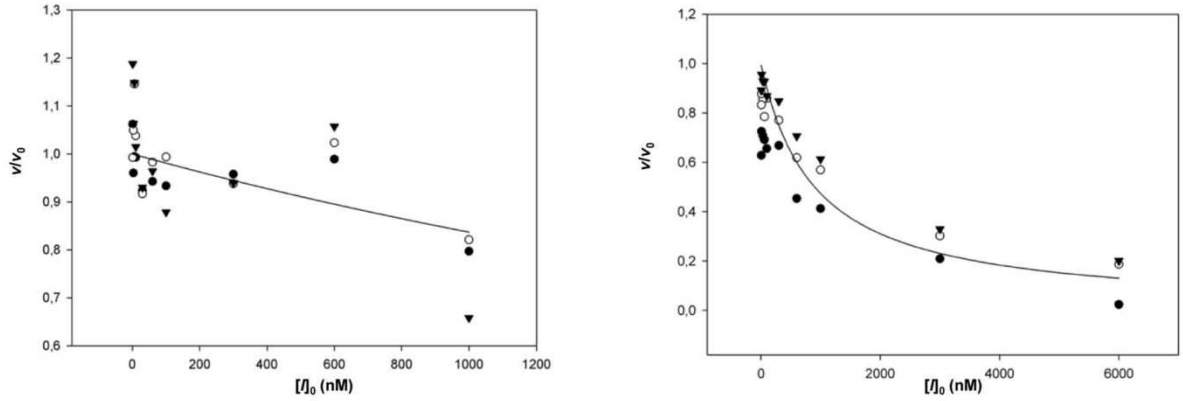

Dixon plots of inhibition assays of **2** against trypsin (left) and **3** against HNE (right) with trend curves of global fittings of triplicate measurements.

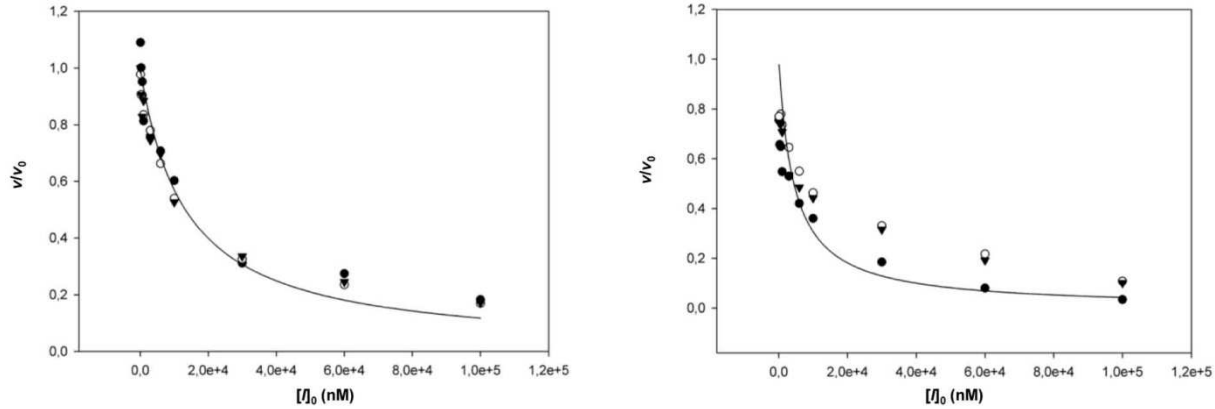

Dixon plot of inhibition assays of **3'** against HNE after 2 h incubation of the inhibitor with enzyme (left) and **4** against HNE (right) with trend curves of global fittings of triplicate measurements.

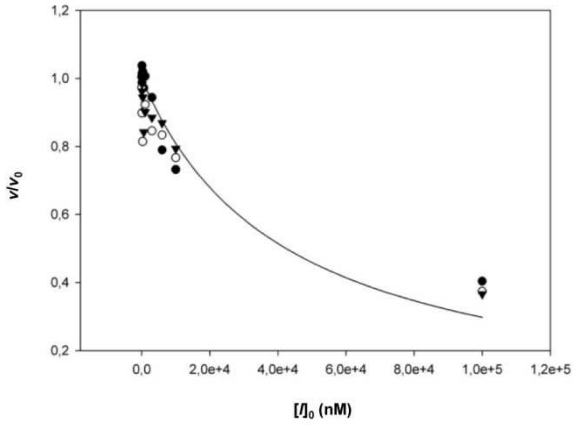

Dixon plot of inhibition assays of **4'** against HNE upon 2 h incubation of the inhibitor with enzyme with trend curves of global fittings of the triplicate measurement.

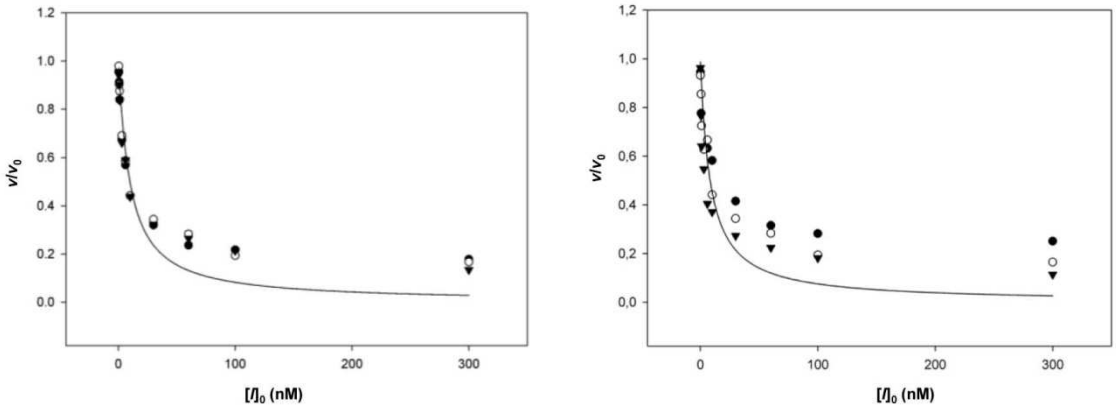

Dixon plots of inhibition assays of **5** against trypsin (left) and **6** against trypsin (right) in trypsin activity buffer with trend curves of global fittings of triplicate measurements.

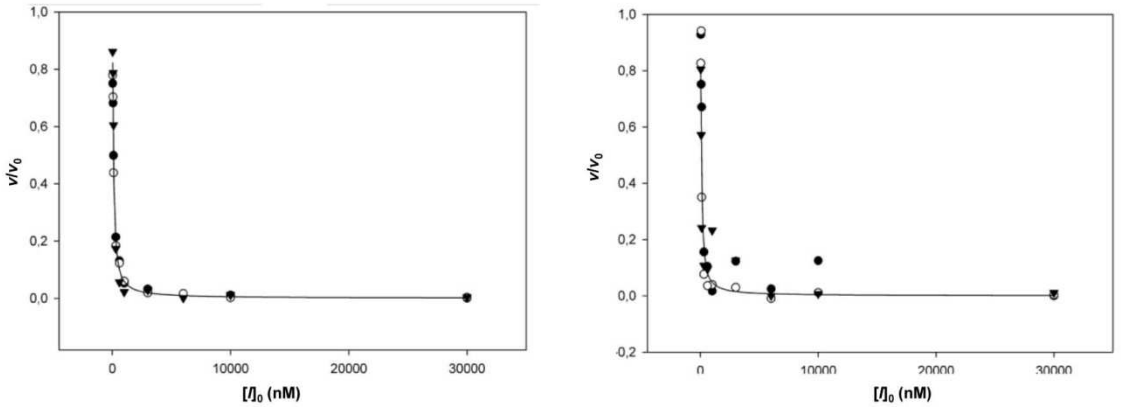

Dixon plots of inhibition assays of **6** against trypsin in non-buffered water (left) and **6** against trypsin in non-buffered D_2O (right) with trend curves of global fittings of triplicate measurements.

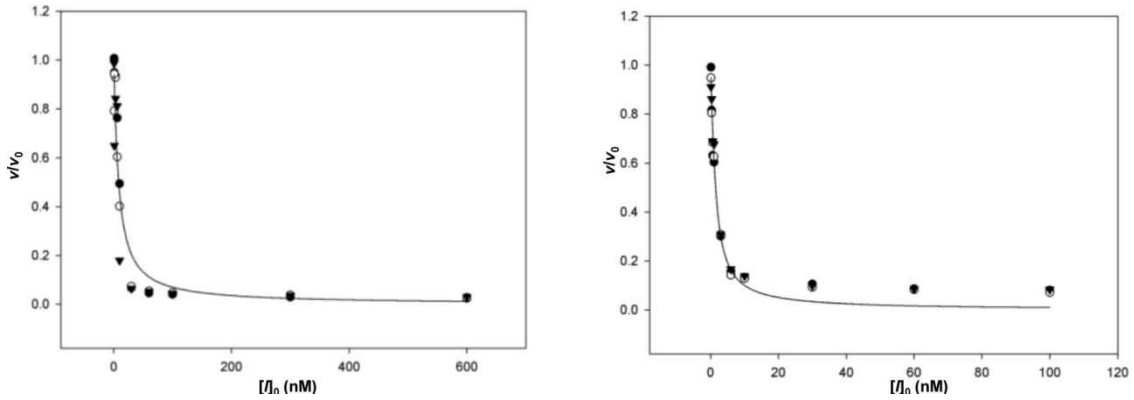

Dixon plots of inhibition assays of **7** against trypsin (left) and **8** against trypsin (right) in trypsin activity buffer with trend curves of global fittings of triplicate measurements.

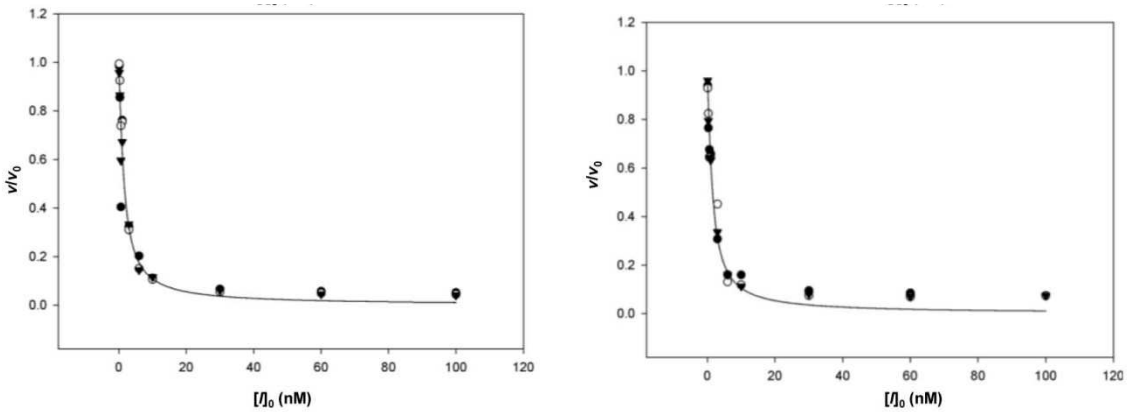

Dixon plots of inhibition assays of **9** against trypsin (left) and **10** against trypsin (right) in trypsin activity buffer with trend curves of global fitting of triplicate measurements.

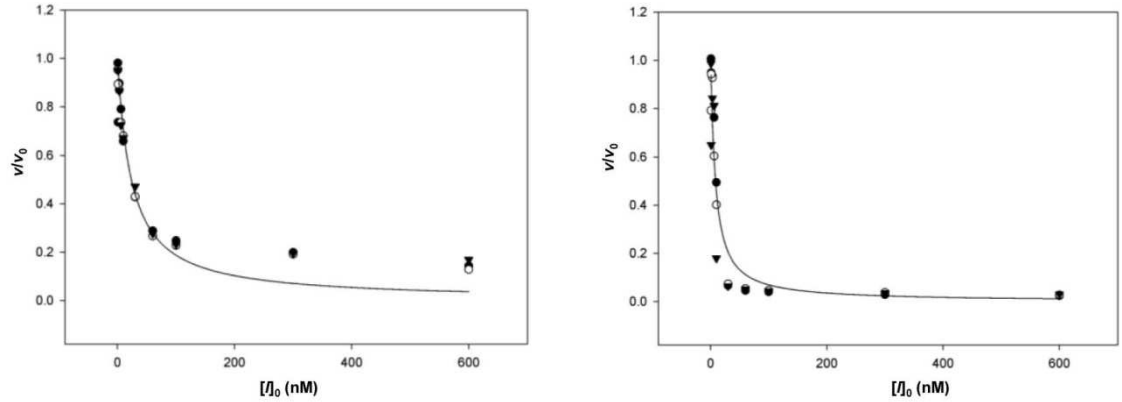

Dixon plots of inhibition assays of **11** against trypsin (left) and **12** against trypsin (right) in trypsin activity buffer with trend curves of global fitting of triplicate measurements.

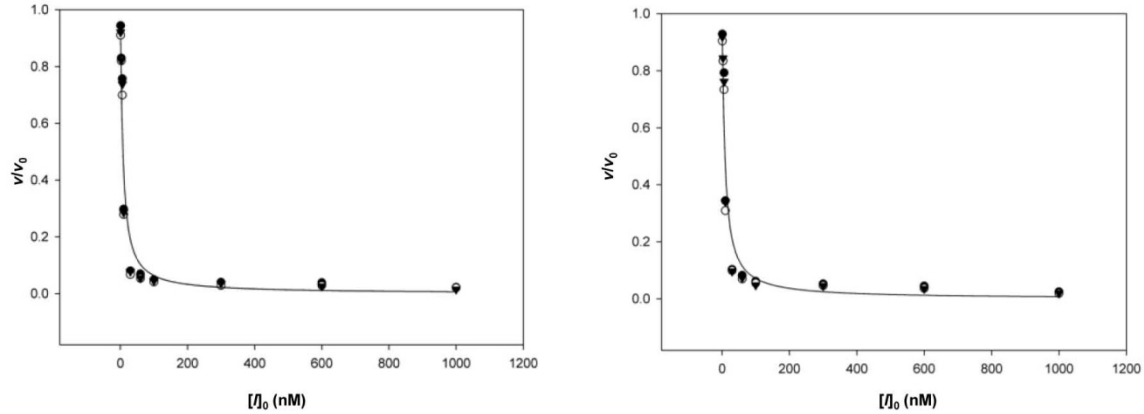

Dixon plots of inhibition assays of **13** against trypsin (left) and **13** against trypsin upon incubation of **13** at 65 °C for 30 min (right) in trypsin activity buffer with trend curves of global fittings of triplicate measurements.

Kinetic Plots of Bioorthogonal Conjugations

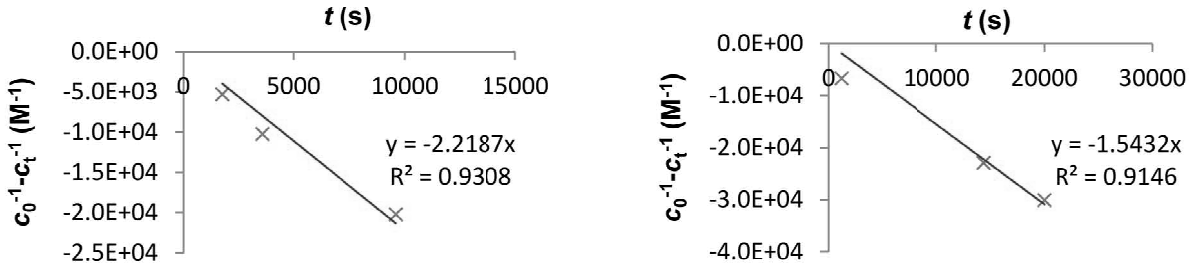

Integrated second-order kinetic plots of coiled coil-guided SPANC using setup 1(experiment was performed in duplicate). Difference between reciprocal initial aldehyde concentration and time-dependent concentration (c_0^{-1}-c_t^{-1}) is plotted against the time t. Slope of trend line corresponds to negative value of k_2.

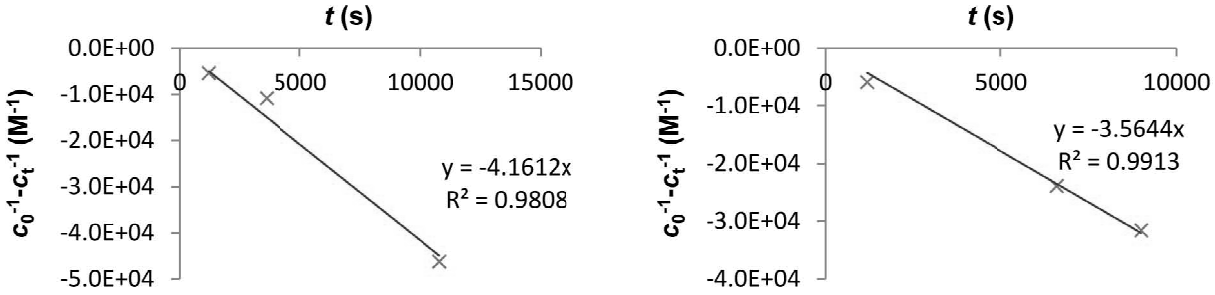

Integrated second-order kinetic plot of coiled coil-guided SPANC using setup 4 (left) and setup 5 (right).

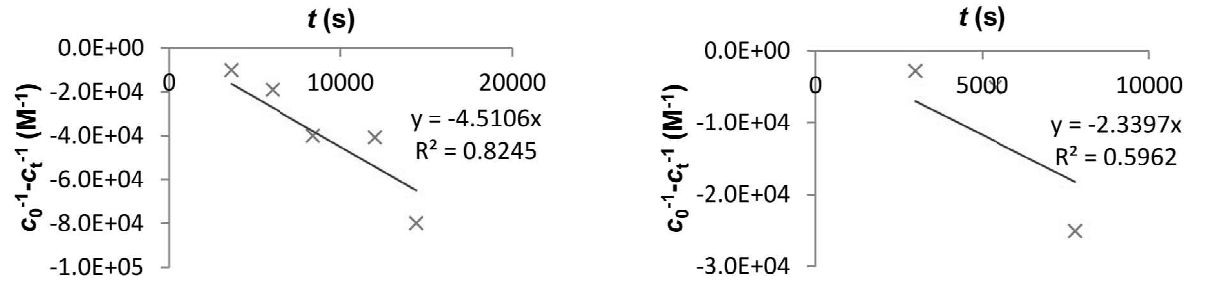

Integrated second-order kinetic plot of coiled coil-guided SPANC using setup 6 (left) and setup 7 (right).

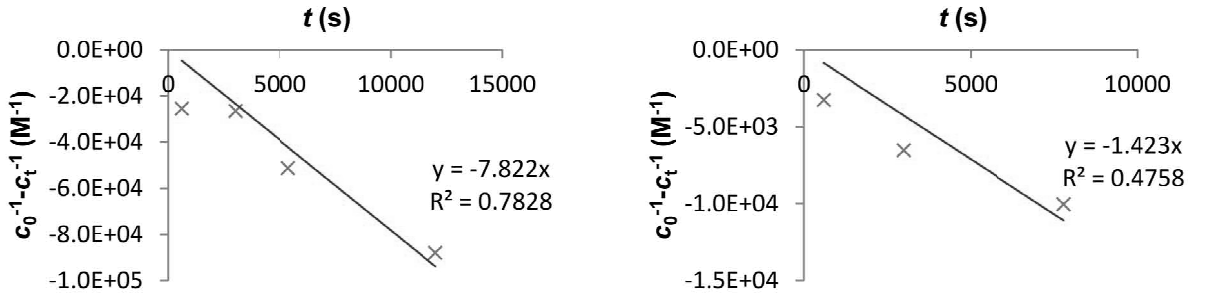

Integrated second-order kinetic plot of coiled coil-guided SPANC using setup 8 (left) and setup 9 (right).

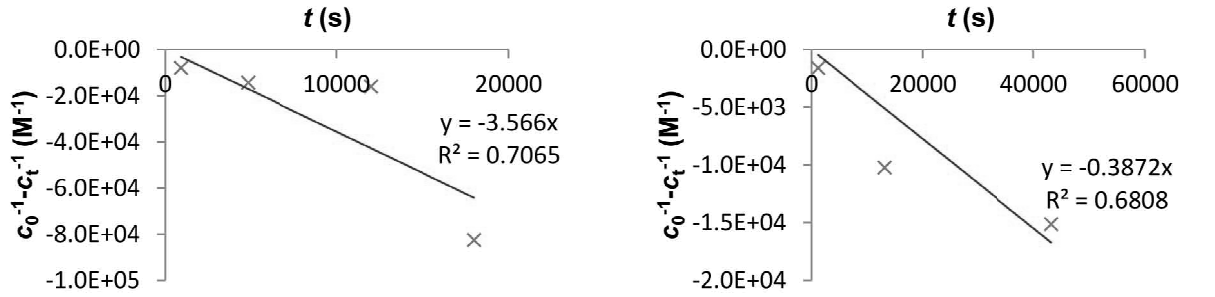

Integrated second-order kinetic plot of coiled coil-guided SPANC using setup 11 (left) and setup 12 (right).

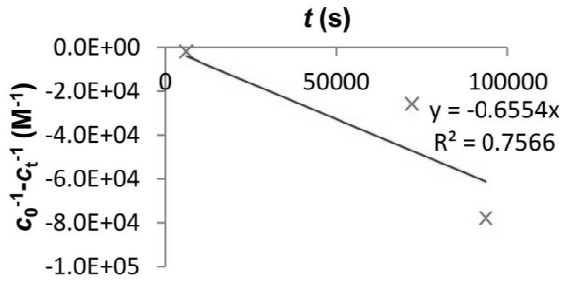

Integrated second-order kinetic plot of coiled coil-guided SPANC using setup 13.

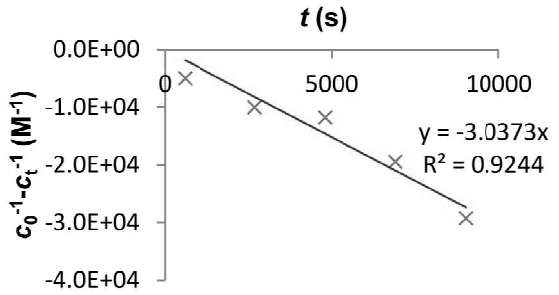

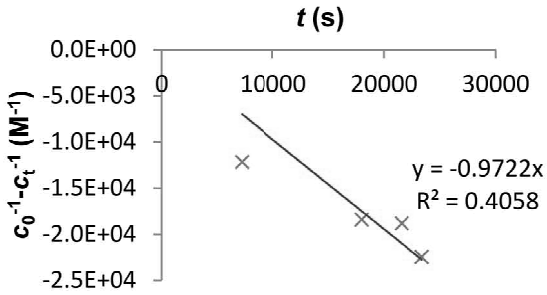

Integrated second-order kinetic plot of PNA-guided SPANC using setup 4 (left) and setup 6 (right).

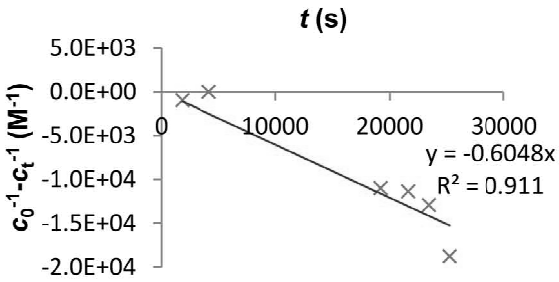

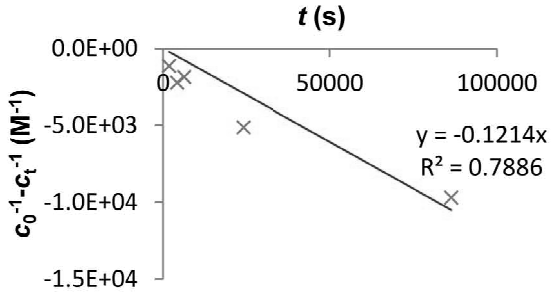

Integrated second-order kinetic plot of PNA-guided SPANC using setup 7 (left) and setup 8 (right).

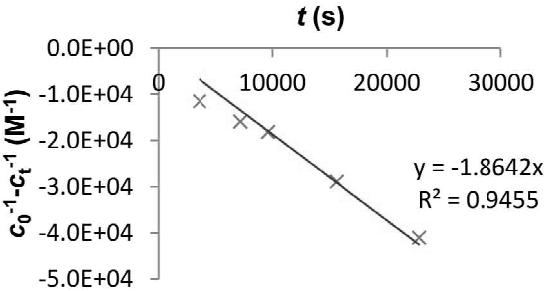

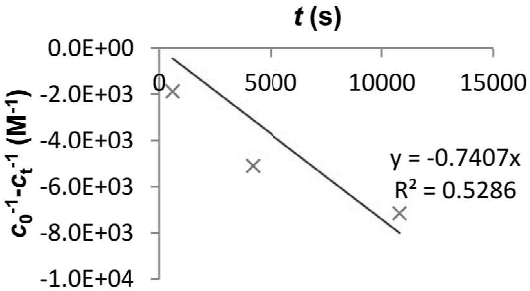

Integrated second-order kinetic plot of PNA-guided SPANC using setup 9 (left) and setup 10 (right).

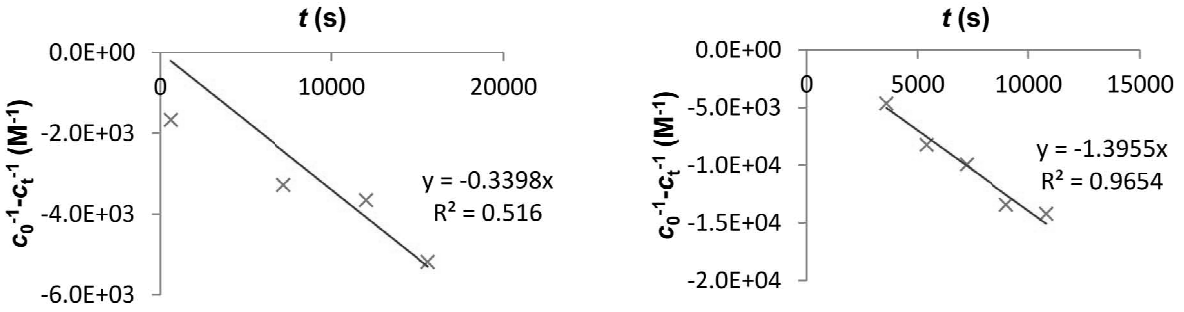

Integrated second-order kinetic plot of PNA-guided SPANC using setup 11 (left) and setup 12 (right).

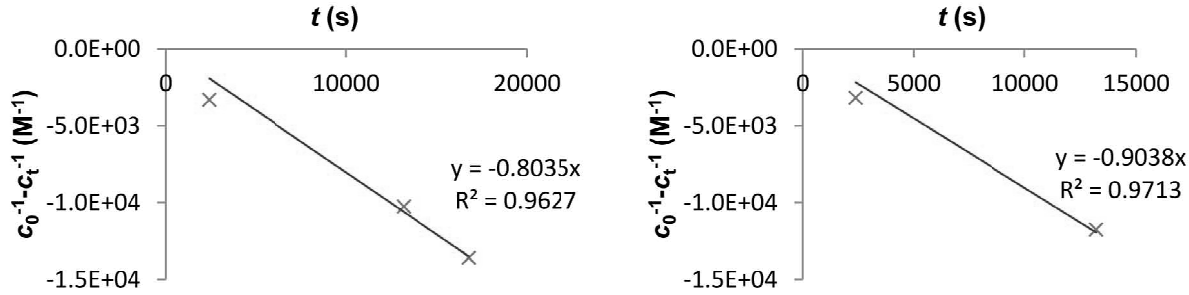

Integrated second-order kinetic plot of PNA-guided SPANC using setup 13 (left) and setup 14 (right).

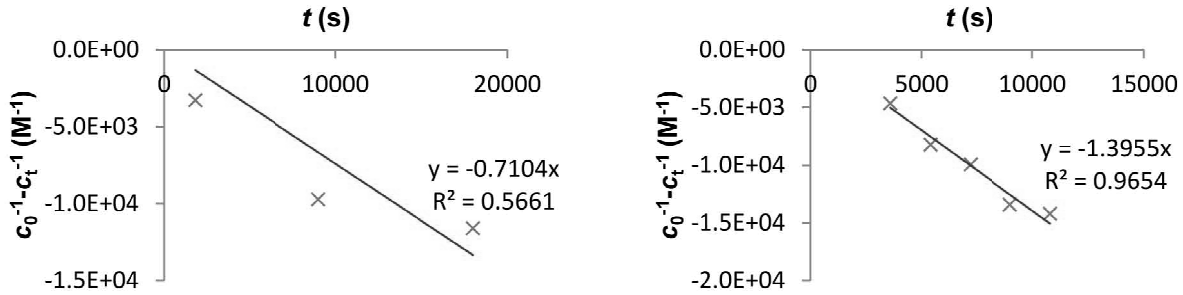

Integrated second-order kinetic plot of PNA-guided SPANC using setup 16 (left) and setup 17 (right).

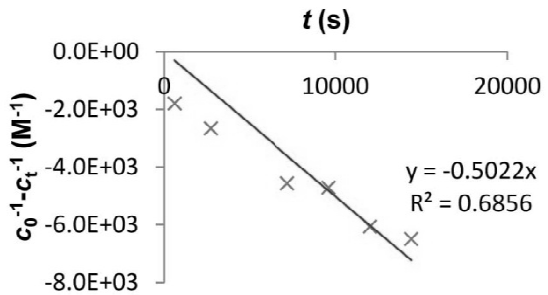

Integrated second-order kinetic plot of PNA-guided SPANC using setup 13.

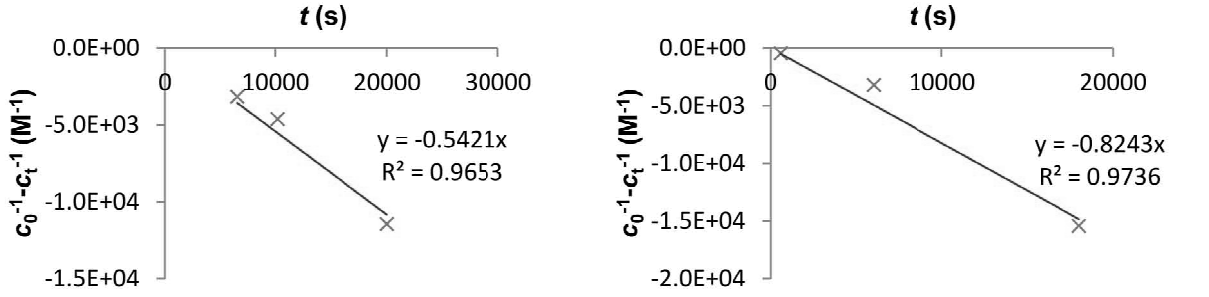

Integrated second-order kinetic plot of PNA-guided SPAAC using setup 1 (left) and setup 2 (right).

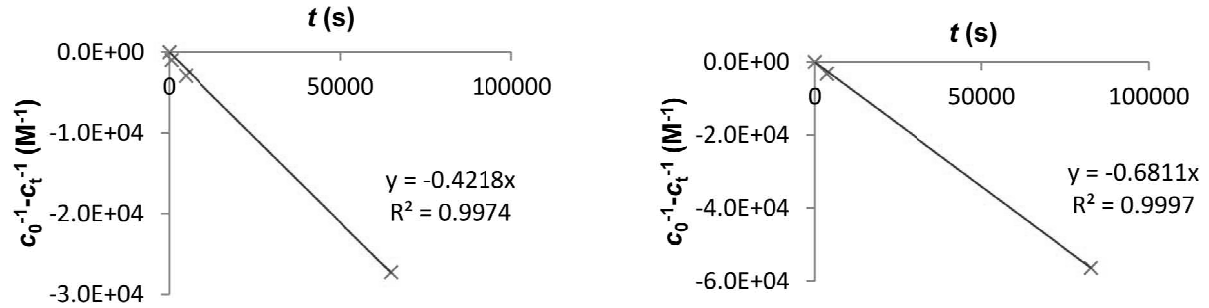

Integrated second-order kinetic plot of non-guided SPAAC between **30'** and **31** (Experiment was performed in duplicate).

HPLC Traces

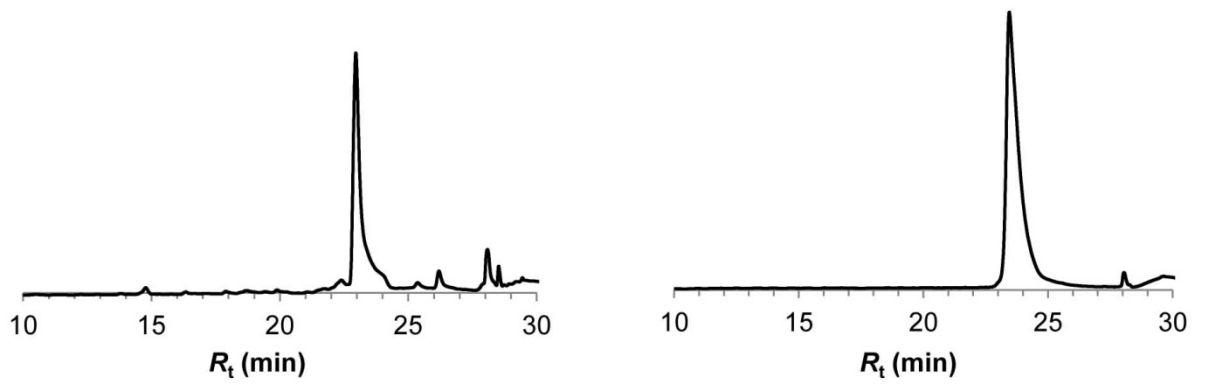

Chromatographic profiles of **1** (left) and **2** (right). UV detection at λ = 220 nm; eluent: 18→40.5 % acetonitrile in 0.1 % aq. TFA over 20 minutes at flow rate 1 ml/min.

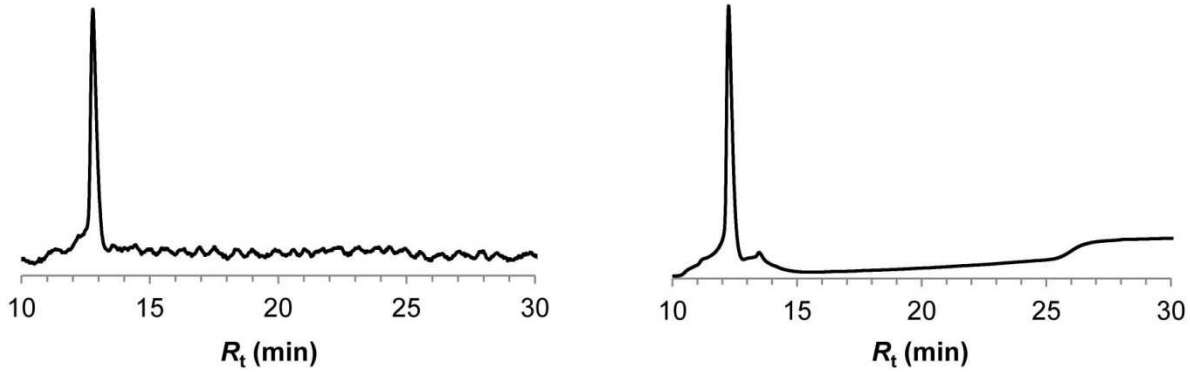

Chromatographic profiles of **3** (left) and **4** (right). UV detection at λ = 220 nm; eluent: 18→72 % acetonitrile in 0.1 % aq. TFA over 20 minutes at flow rate 1 ml/min.

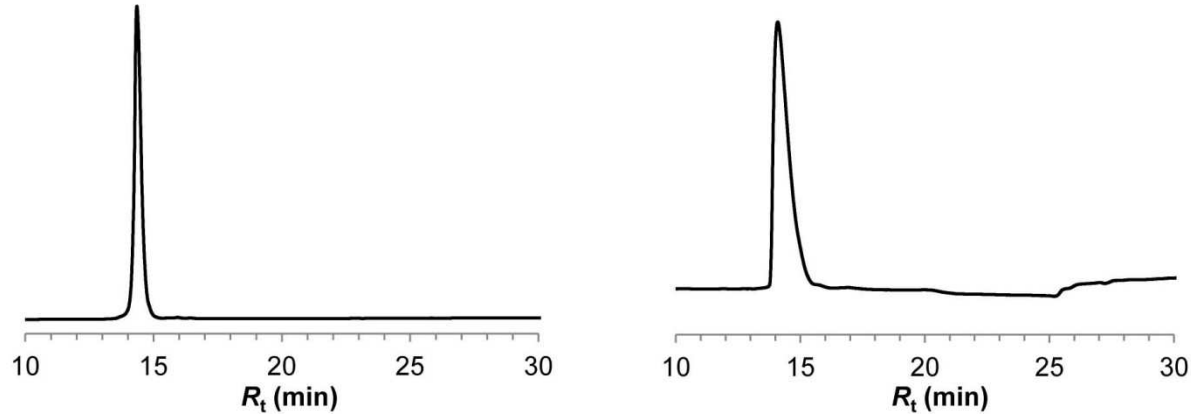

Chromatographic profiles of **5** (left) and **6** (right). UV detection at λ = 220 nm; eluent (left): 9→90 % acetonitrile in 0.1 % aq. TFA over 20 minutes at flow rate 1 ml/min; eluent (right): 18→40.5 % acetonitrile in 0.1 % aq. TFA over 20 minutes at flow rate 1 ml/min.

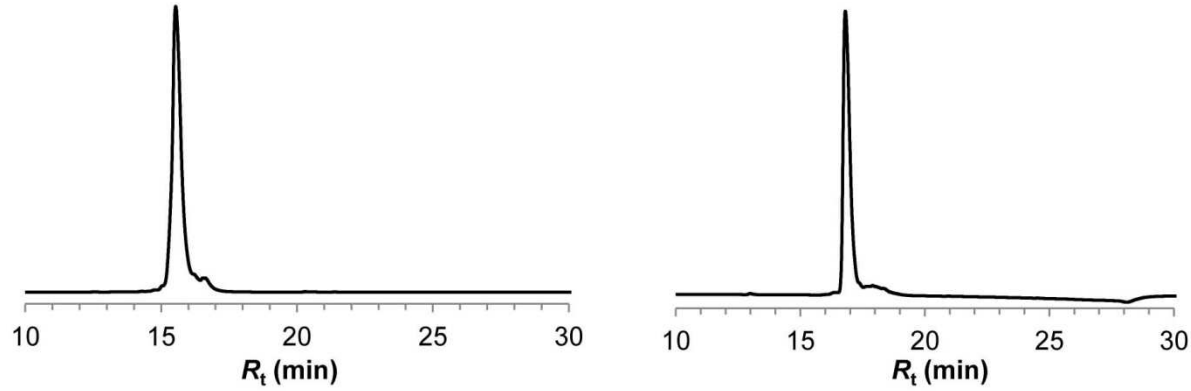

Chromatographic profiles of **7** (left) and **8** (right). UV detection at λ = 220 nm; eluent (left): 9→90 % acetonitrile in 0.1 % aq. TFA over 20 minutes at flow rate 1 ml/min; eluent (right): 9→72 % acetonitrile in 0.1 % aq. TFA over 20 minutes at flow rate 1 ml/min.

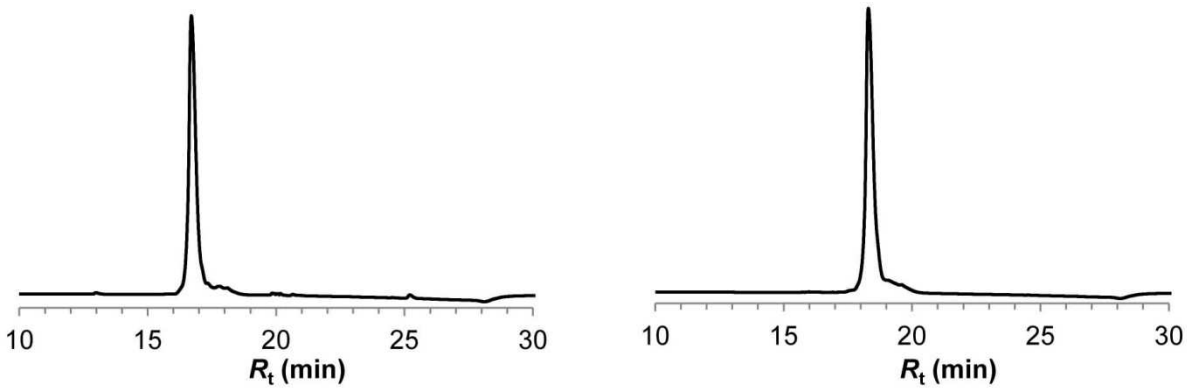

Chromatographic profiles of **9** (left) and **10** (right). UV detection at λ = 220 nm; eluent : 9→72 % acetonitrile in 0.1 % aq. TFA over 20 minutes at flow rate 1 ml/min.

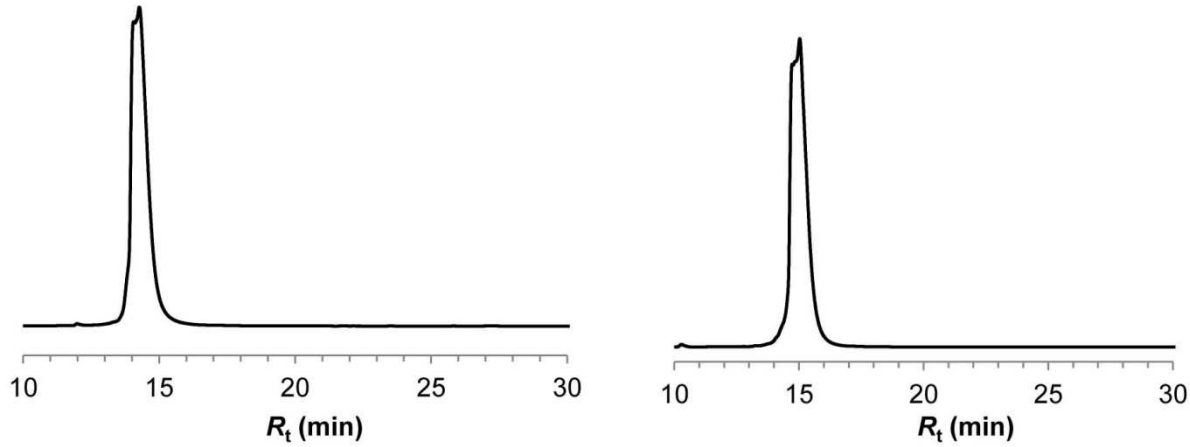

Chromatographic profiles of **11** (left) and **12** (right). UV detection at λ = 220 nm; eluent: 9→90 % acetonitrile in 0.1 % aq. TFA over 20 minutes at flow rate 1 ml/min.

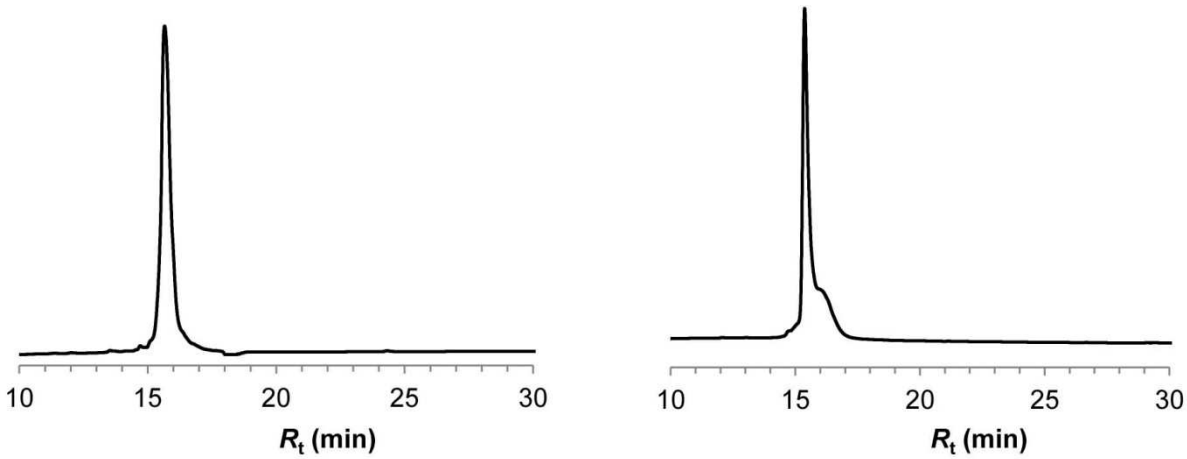

Chromatographic profiles of **13** (left) and **14** (right). UV detection at λ = 220 nm; eluent: 9→90 % acetonitrile in 0.1 % aq. TFA over 20 minutes at flow rate 1 ml/min.

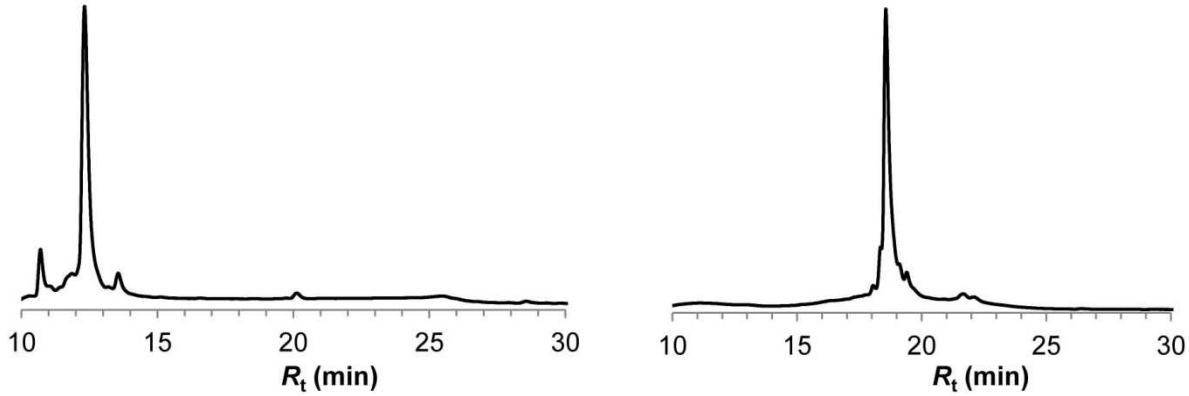

Chromatographic profiles of **16** (left) and **17** (right). UV detection at λ = 220 nm; eluent (left): 27→72 % acetonitrile in 0.1 % aq. TFA over 20 minutes at flow rate 1 ml/min; eluent (right): 9→90 % acetonitrile in 0.1 % aq. TFA over 20 minutes at flow rate 1 ml/min.

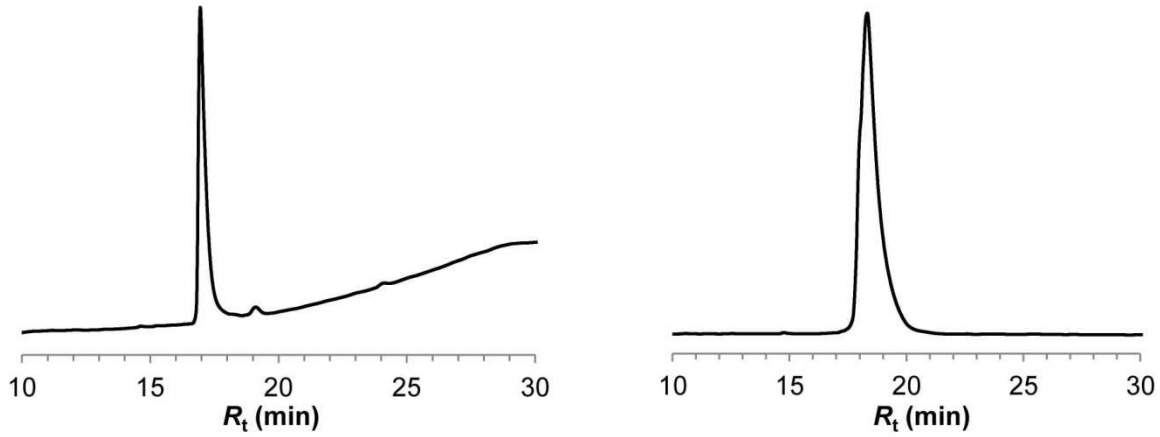

Chromatographic profiles of **18** (left) and **19** (right). UV detection at λ = 220 nm; eluent: 9→90 % acetonitrile in 0.1 % aq. TFA over 20 minutes at flow rate 1 ml/min.

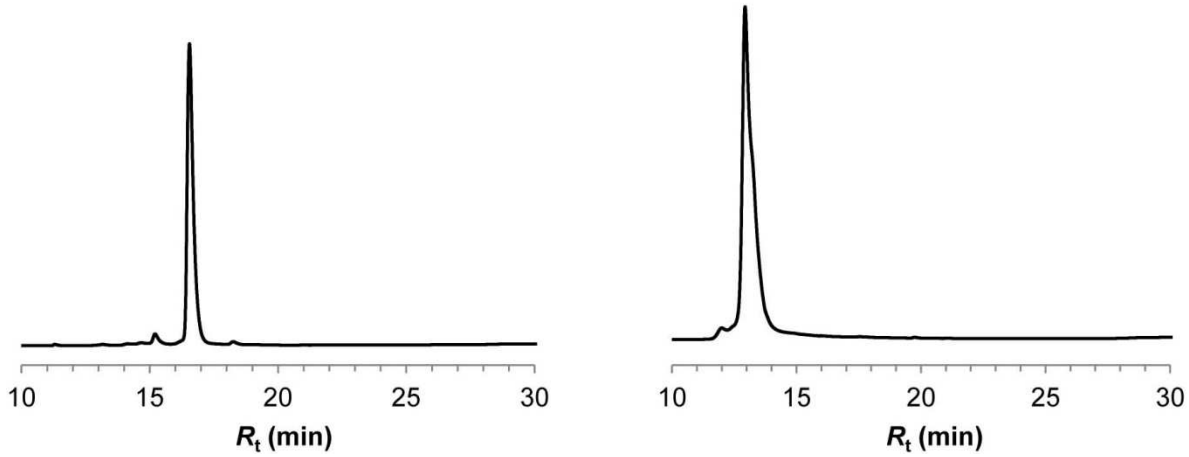

Chromatographic profiles of **20** (left) and **21** (right). UV detection at λ = 260 nm; eluent: 0→72 % acetonitrile in 0.1 % aq. TFA over 20 minutes at flow rate 1 ml/min.

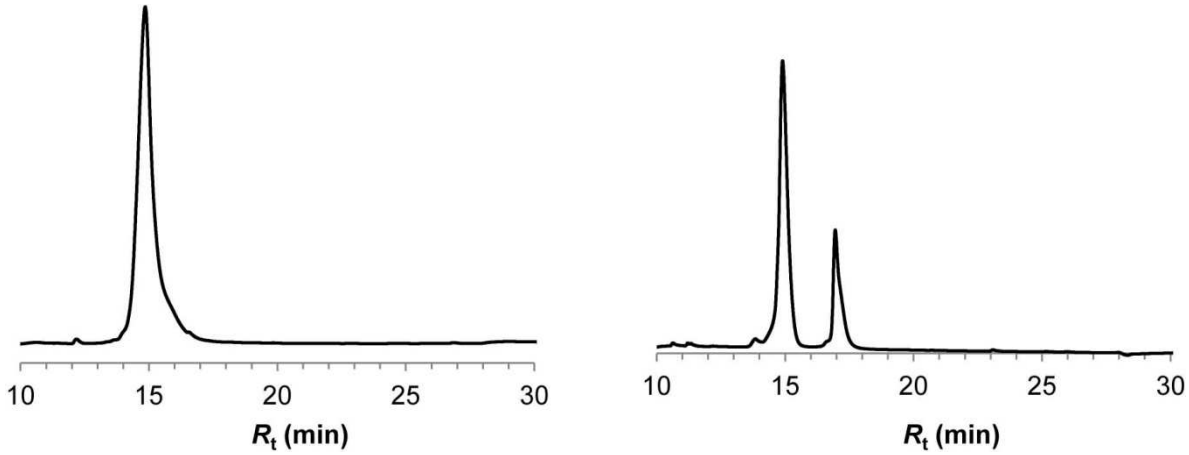

Chromatographic profiles of **22** (left) and **23** (right). UV detection at λ = 260 nm; eluent: 0→54 % acetonitrile in 0.1 % aq. TFA over 20 minutes at flow rate 1 ml/min.

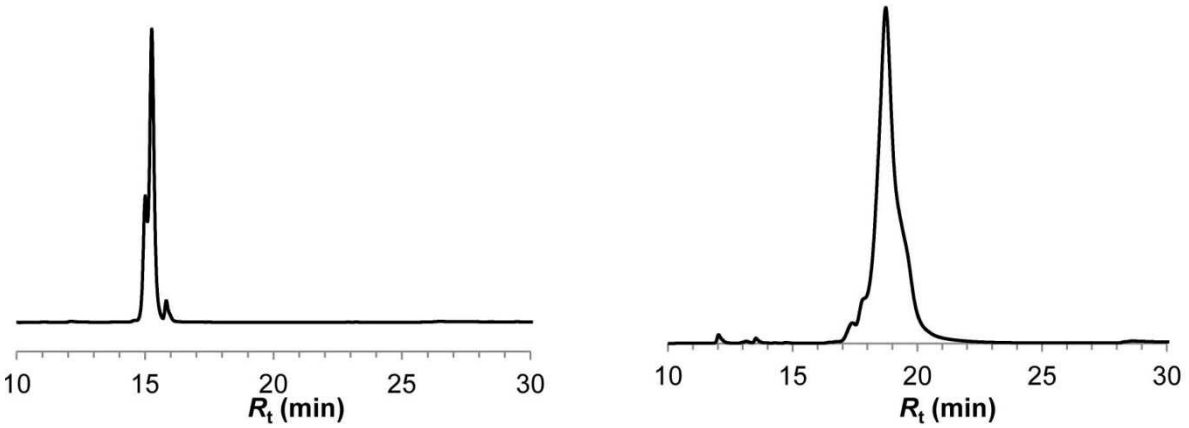

Chromatographic profiles of **25** (left) and **26** (right). UV detection at λ = 260 nm; eluent (left): 0→72 % acetonitrile in 0.1 % aq. TFA over 20 minutes at flow rate 1 ml/min; eluent (right): 0→36 % acetonitrile in 0.1 % aq. TFA over 20 minutes at flow rate 1 ml/min.

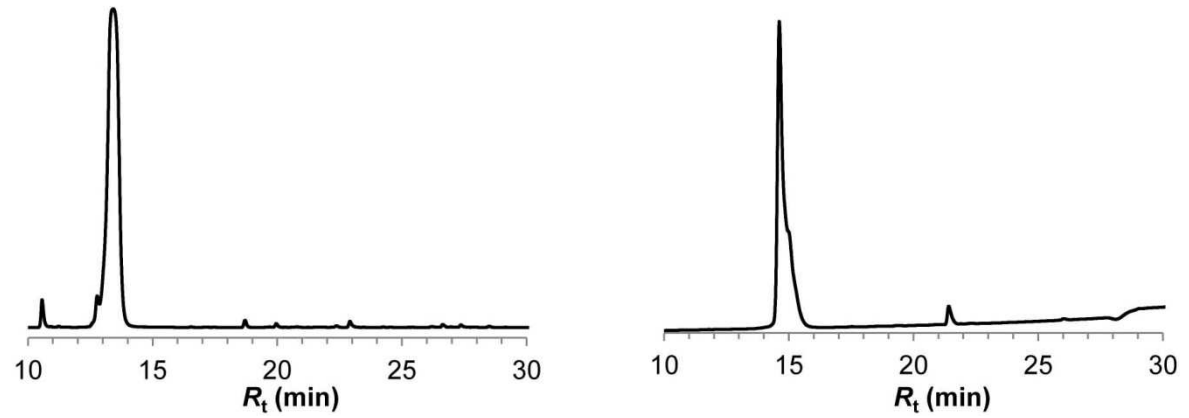

Chromatographic profiles of **27** (left) and **28** (right). UV detection at λ = 260 nm; eluent: 0→72 % acetonitrile in 0.1 % aq. TFA over 20 minutes at flow rate 1 ml/min.

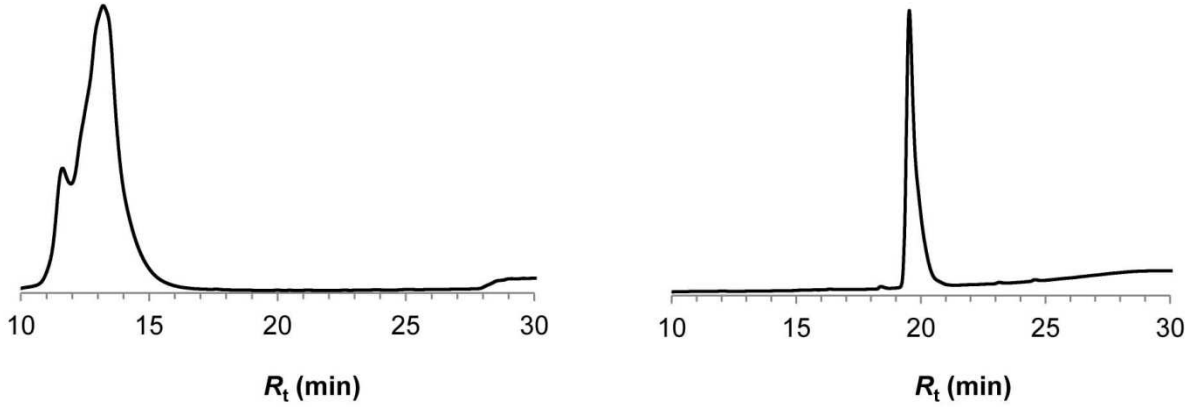

Chromatographic profiles of **29** (left) and **30** (right). UV detection at λ = 260 nm; eluent (left): 9→54 % acetonitrile in 0.1 % aq. TFA over 20 minutes at flow rate 1 ml/min, eluent (right): 0→90 % acetonitrile in 0.1 % aq. TFA over 20 minutes at flow rate 1 ml/min.

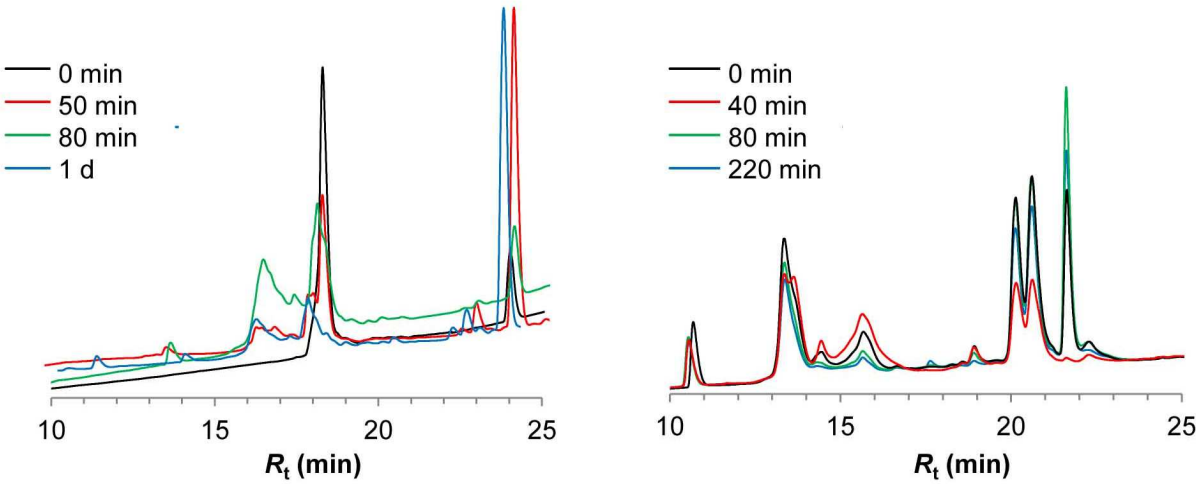

Chromatographic profiles of reaction mixtures of coiled coil-guided SPANC (left, setup 13) and PNA-guided SPANC (right, setup 19), both applying the *in situ* aldehyde formation strategies. UV detection at λ = 220 nm (left) or 260 nm (right); eluent (left): 0→90 % acetonitrile in 0.1 % aq. TFA over 20 minutes at flow rate 1 ml/min, eluent (right): 0→72 % acetonitrile in 0.1 % aq. TFA over 20 minutes at flow rate 1 ml/min.

SEC Traces

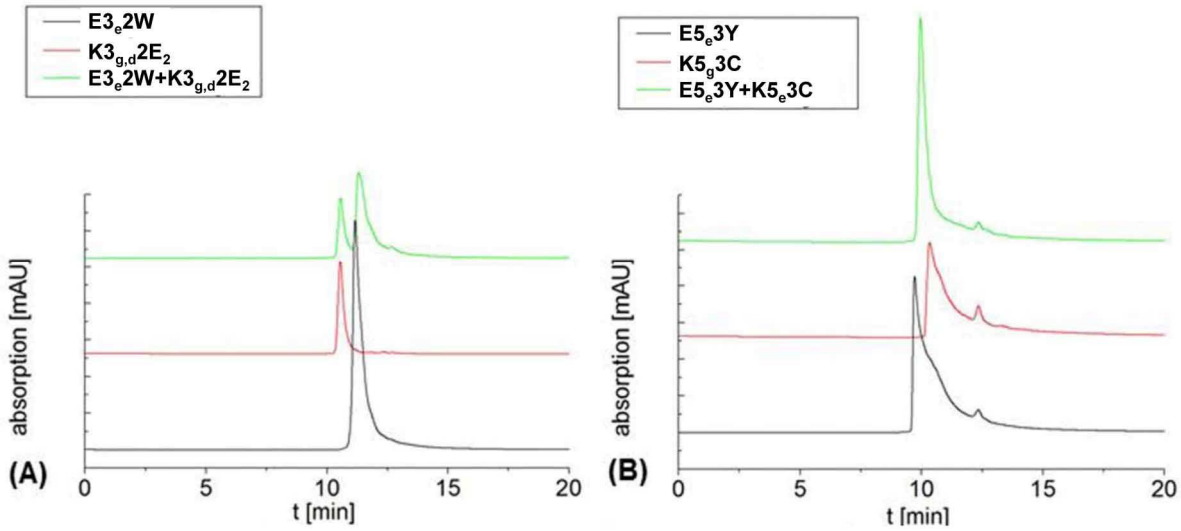

SEC profiles of three-heptad coiled coils $E3_e2W/K3_{g,d}2E_2$ (**A**) and five-heptad coiled coils $E5_e3Y/K5_g3C$ (**B**) as 1:1 mixture and individual peptides. Recorded with *Varian* 920-LC system equipped with a *Phenomenex* BioSep-SEC-S2000TM column (300×7.8 mm, 5 μm, 145 Å). Absorption detected at 220 nm and 280 nm, eluent: degassed 1× PBS at pH 7, flow rate 1 ml/min.

Summary of dimerization experiments of three-heptad coiled coils $E3_e2W/K3_{g,d}2E_2$ and five-heptad coiled coils $E5_e3Y/K5_g3C$ *via* SEC with molecular mass and retention time of reference proteins/peptides using same analytical setup.

Reference/Sample	Molecular mass [kDa]	R_t [min]
Lysozyme	14.3	10.8
Ribonuclease A	13.7	10.0
Aprotinin	6.5	10.8
MCoTI-II	3.5	12.5
$E3_e2W$	2.4	11.2
$K3_{g,d}2E_2$	2.3	10.6
$E3_e2W$ + $K3_{g,d}2E_2$	4.7	10.6 & 11.2
$E5_e3Y$	3.9	9.7
$K5_g3C$	3.8	10.3
$E5_e3Y$ + $K5_g3C$	7.7	10.0

MS Spectra

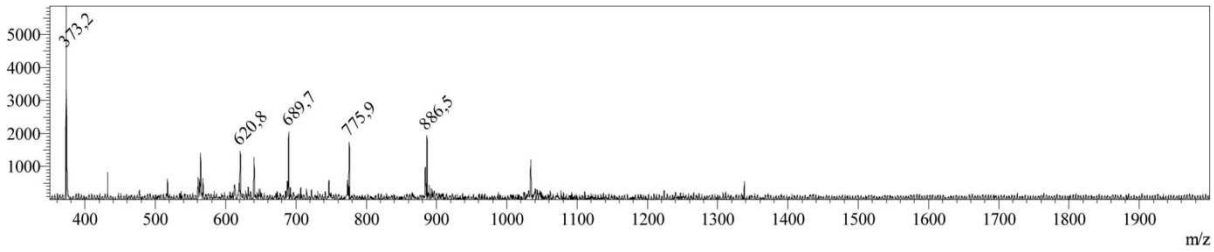

ESI mass spectrum of collected HPLC fraction (R_t = 16.8 min) of a control SPANC reaction between **18** and **32** (setup 12) towards **cp5** after 2 h. Spectrum is in positive mode.

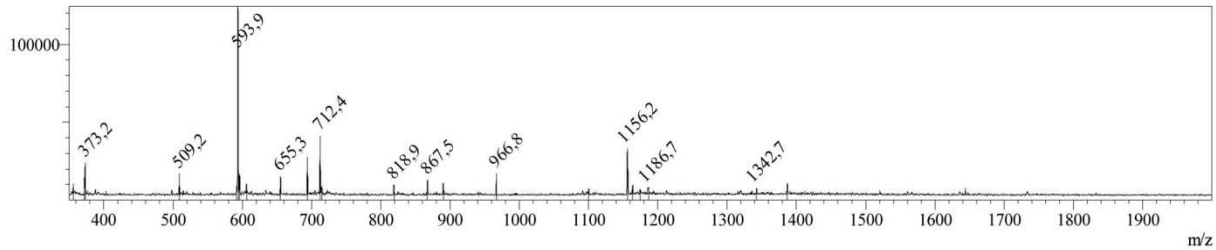

ESI mass spectrum of collected HPLC fraction (R_t = 14.8 min) of SPANC between **20** and **21** using PhNOH as nitrone-forming agent (setup 11) towards **cp6** after 2 h. m/z corresponding to **cp9** are also observed. Spectrum is in positive mode.

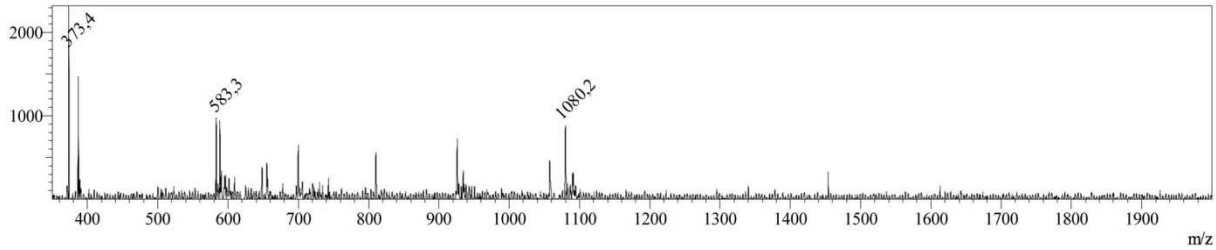

ESI mass spectrum of collected HPLC fraction (R_t = 16.1 min) of a control SPANC reaction between **20** and **22** (applied in equimolar ratio) towards **cp7** after 24 h. Spectrum is in positive mode.

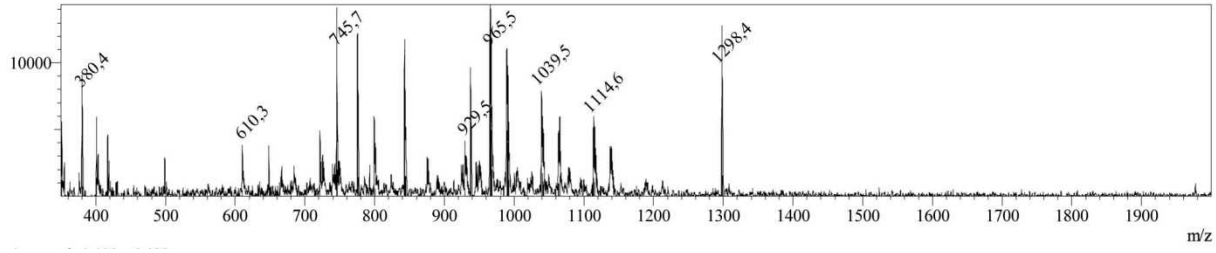

ESI mass spectrum of reaction mixture of UVA-mediated cross-linkage between **25** and **26** (applied in equimolar ratio) towards **cp12** after 2 h irradiation. Spectrum is in positive mode.

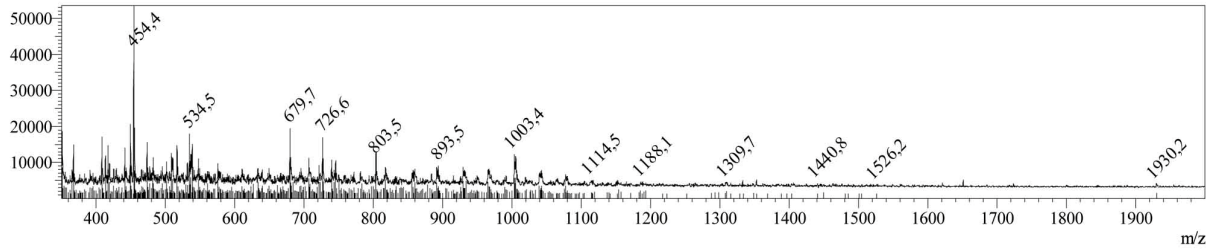

ESI mass spectrum of reaction mixture of UVA-mediated cross-linkage between **25** and **33** (applied in equimolar ratio) towards **cp13** after 2 h irradiation. Spectrum is in positive mode.

NMR Spectra

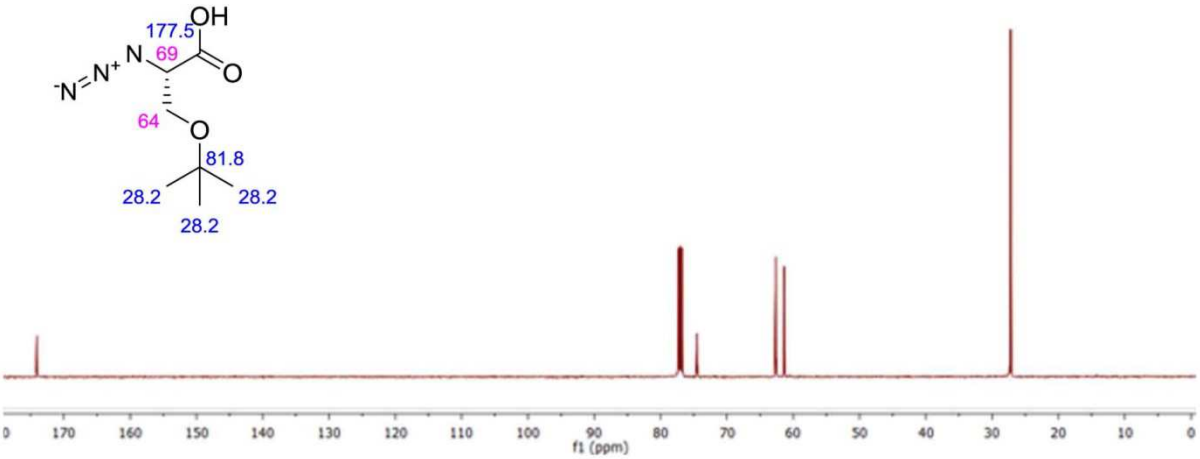

^{13}C NMR spectrum of isolated compound **4a** with structure and predicted chemical shifts. Sample was dissolved in $CDCl_3$.

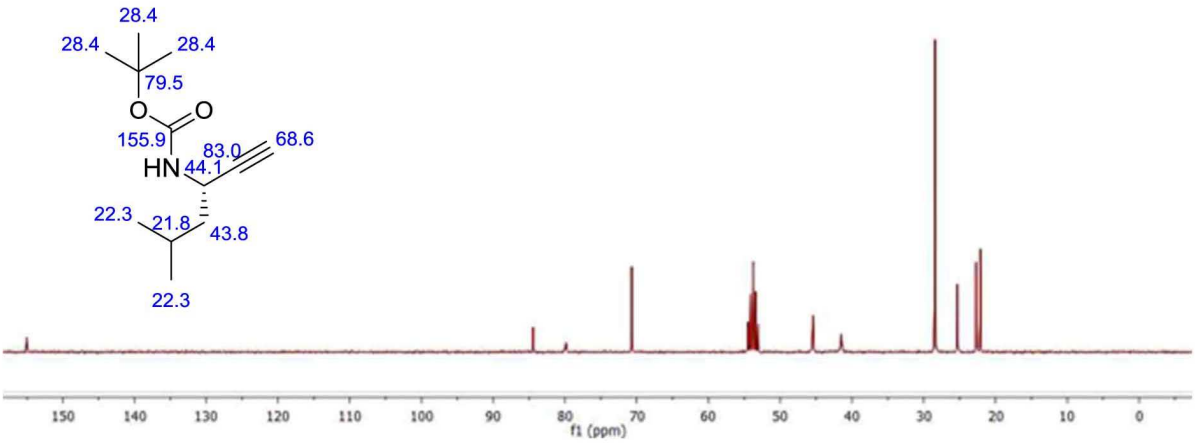

^{13}C NMR spectrum of isolated compound **4b** and predicted chemical shifts. Sample was dissolved in $CDCl_3$.

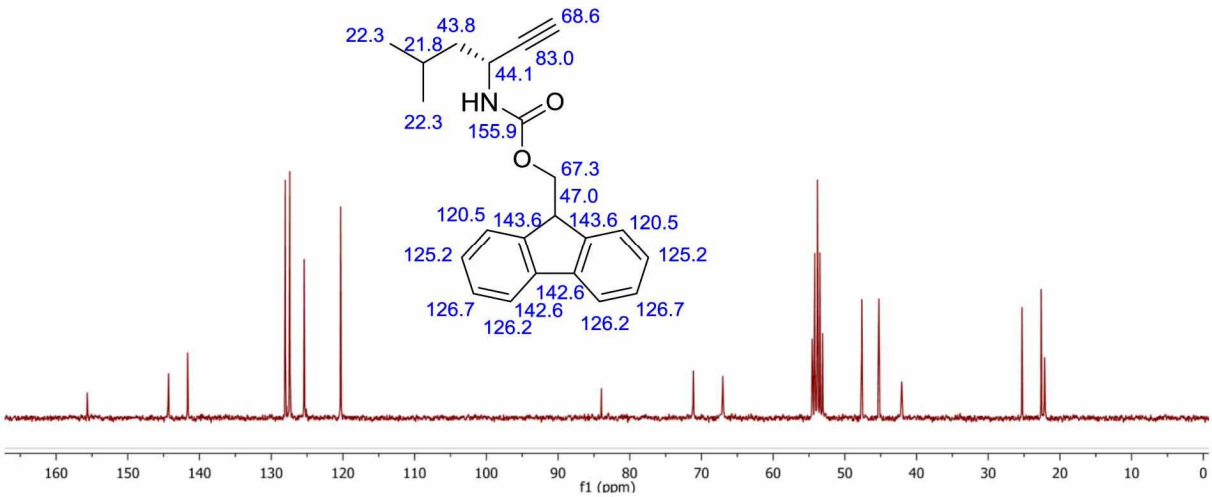

^{13}C NMR spectrum of isolated compound **4c** and predicted chemical shifts. Sample was dissolved in $CDCl_3$.

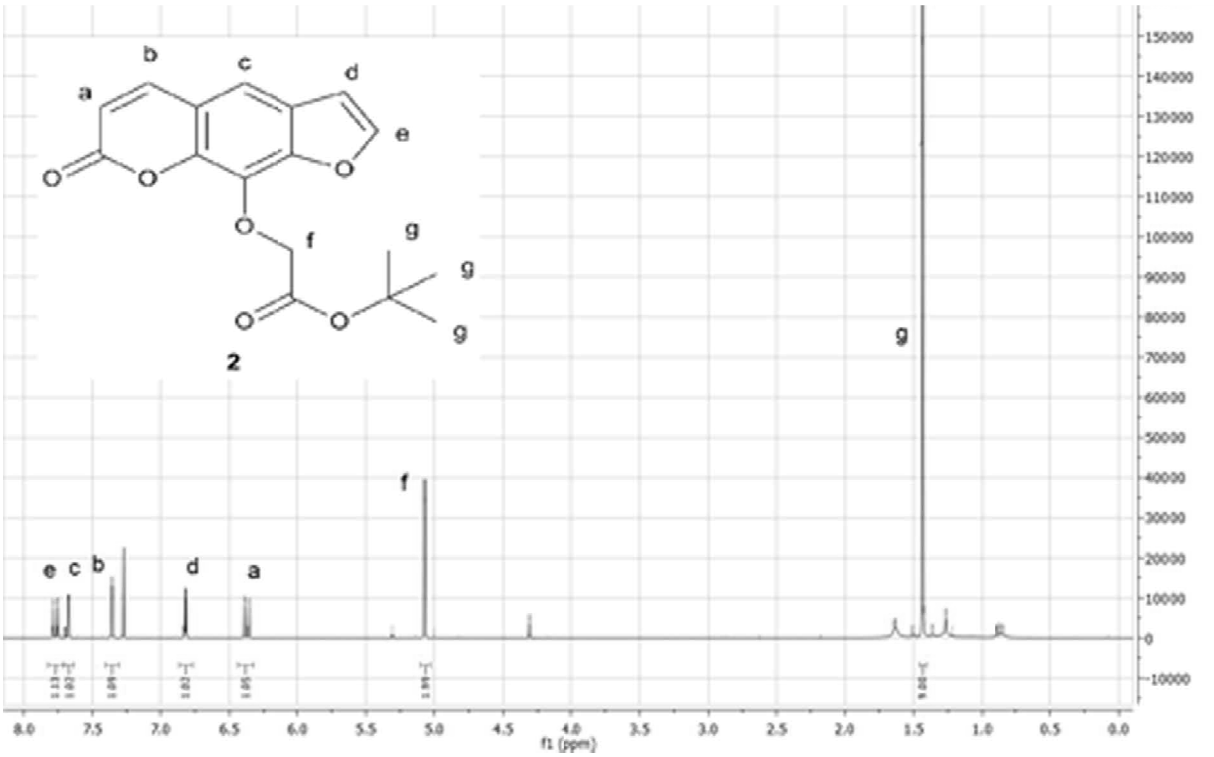

^{1}H NMR spectrum of isolated compound **24'**. Sample was dissolved in $CDCl_3$.

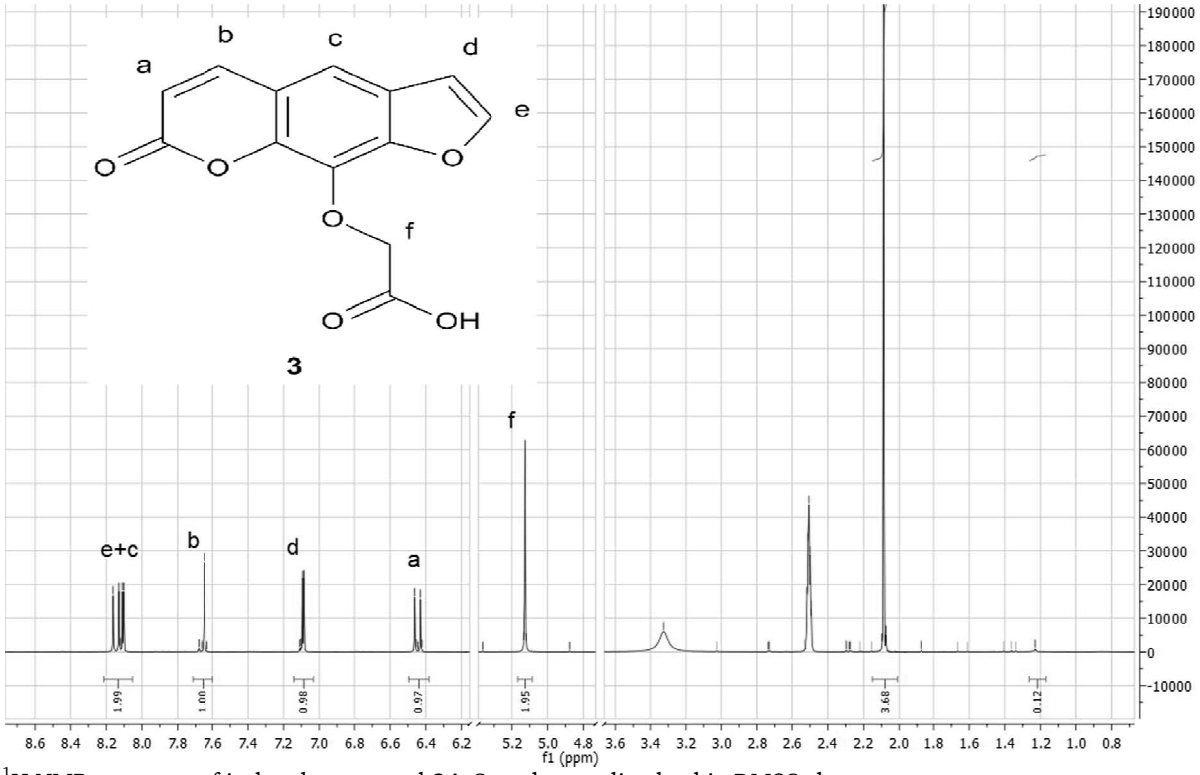

^{1}H NMR spectrum of isolated compound **24**. Sample was dissolved in DMSO-d_6.

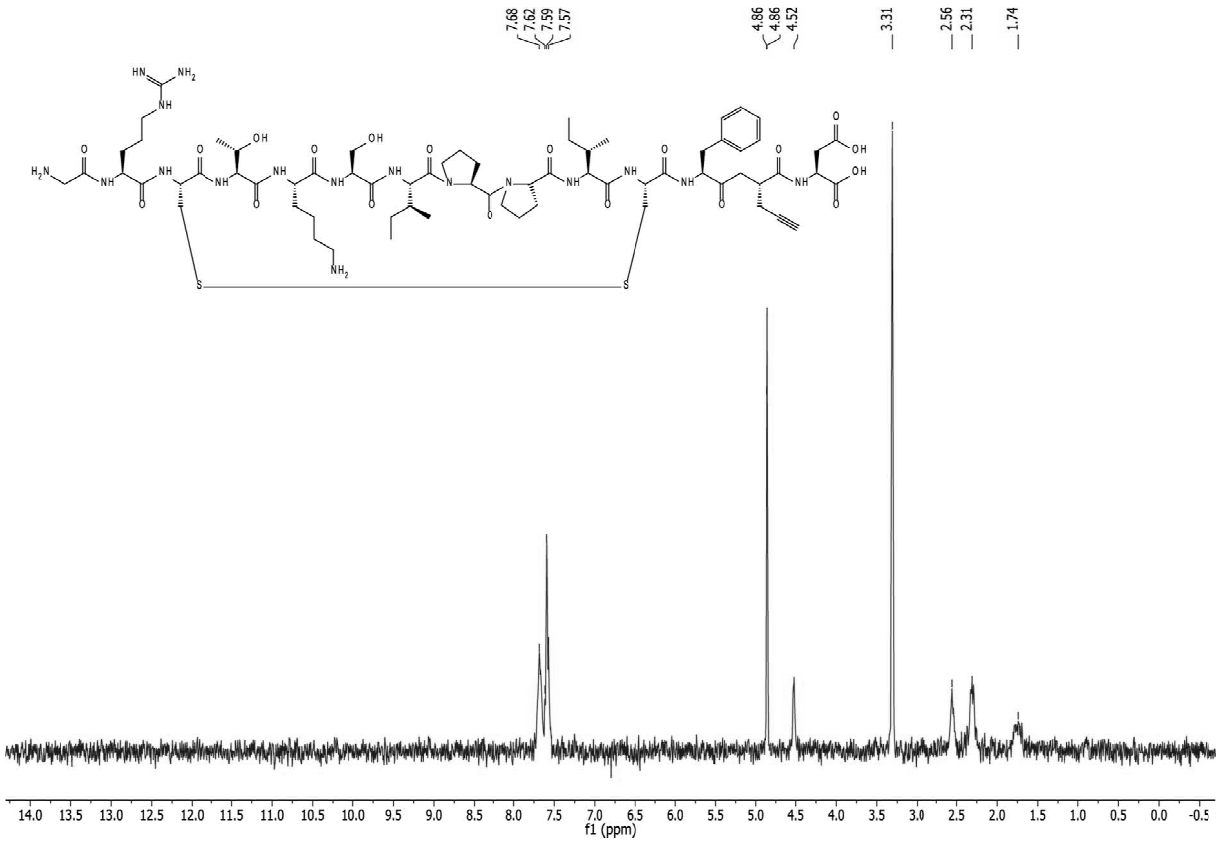

^{1}H NMR spectrum of**6** at ground state. Sample was dissolved in MeOH-d_4.

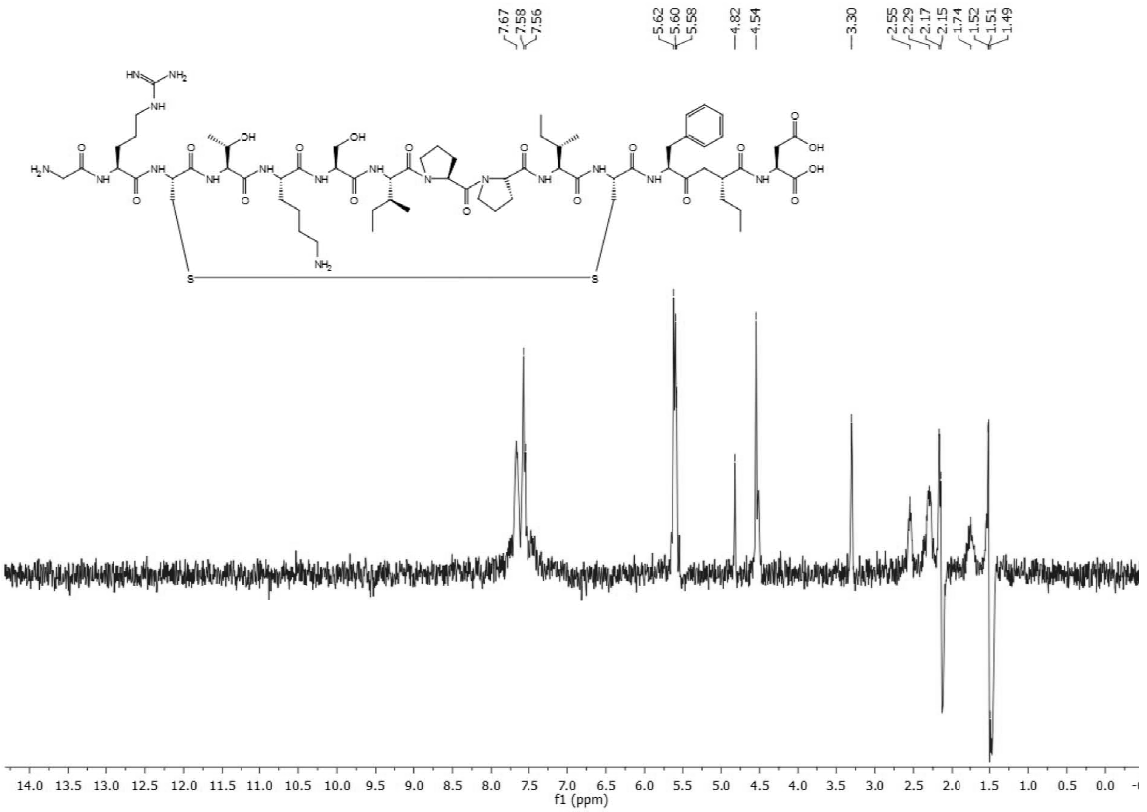

^{1}H NMR spectrum of**6** upon hydrogenation. (PHIP spectrum) Sample was dissolved in MeOH-d_4.

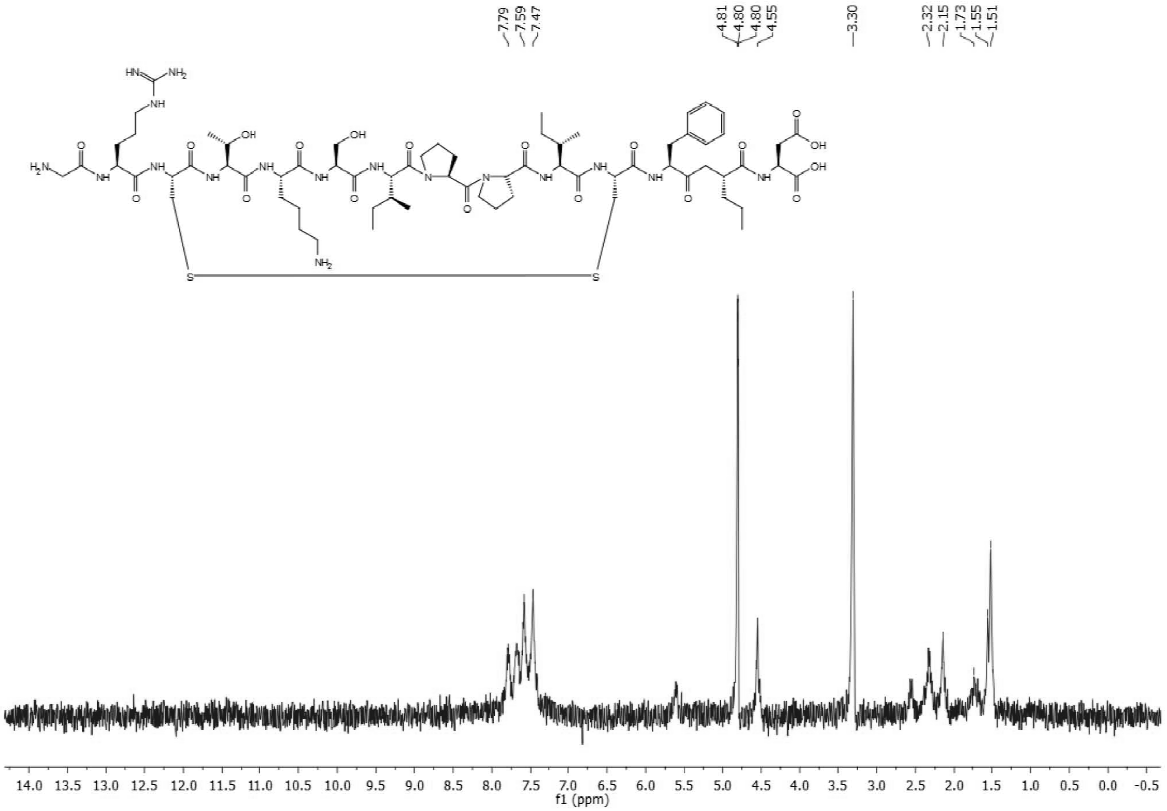

^{1}H NMR spectrum of**6** after relaxation. Sample was dissolved in MeOH-d_4.

Further PHIP NMR spectra (compounds **5**, **7** – **13**) can be found in respective publication.[50b]

Dipl.-Ing.
Daichi Nasu
Gervinusstraße 59
64287 Darmstadt

Darmstadt, den 28.10.2015

Erklärung

Ich erkläre hiermit, noch keinen Promotionsversuch unternommen zu haben.

_____

Dipl.-Ing. Daichi Nasu

Dipl.-Ing.
Daichi Nasu
Gervinusstraße 59
64287 Darmstadt

Darmstadt, den 28.10.2015

Eidesstattliche Erklärung

Ich erkläre hiermit ein Eides Statt, dass ich meine Dissertation selbstständig und nur mit den angegebenen Hilfsmitteln angefertigt habe.

_____

Dipl.-Ing. Daichi Nasu

Lebenslauf

Dipl.-Ing.
Daichi Nasu

Gervinusstraße 59
64287 Darmstadt
Mobile: 0173-6739801
Email: nasu@biochemie-TUD.de

Persönliche Daten

Geburt: 07.07.1985 in Frankfurt am Main
Nationalität: japanisch
Familienstand: ledig

Akademischer Werdegang

11. 2011 – 12. 2015	**Promotion** am Clemens-Schöpf-Institut für Organische Chemie und Biochemie der Technischen Universität Darmstadt unter der Betreuung von Prof. Dr. Harald Kolmar
10.2005 – 09.2011	**Diplomstudium in Chemie** an der Technischen Universität Darmstadt. Abschluss: Dipl.-Ing. Chemie (Note: 1.5) Titel der Diplomarbeit: *"Disubsituted triazoles: Application to bioactive peptidomimetics"* Betreuer: Prof. Dr. Harald Kolmar

Schulausbildung

1996 – 2005	Schillerschule (Gymnasium), Frankfurt am Main Abschluss: Abitur (Note: 2.6)
1998 – 2001	Japanisches Institut Frankfurt am Main e. V. Abschluss: japanischer Junior-High School Abschluss
1992 – 1998	Japanisches Institut Frankfurt am Main e. V. Abschluss: japanischer Elementary School Abschluss
1992 – 1996	Textorschule (Grundschule), Frankfurt am Main

Darmstadt, den _____. 10. 2015

Dipl.-Ing. Daichi Nasu